Correlation of particle fluxes and film properties deposited by vacuum arc

Dissertation

Von der Fakultät für Physik
der Universität Duisburg-Essen
zur Erlangung des akademischen Grades eines
Doktors der Naturwissenschaften (Dr. rer. Nat.)
genehmigten Dissertation
von

Oleksiy Filipov

geboren am 17. August 1977
in Charkiw / Ukraine

Tag der Disputation:	08. Mai 2013
Prüfungsvorsitzender:	Prof. Dr. Peter Kratzer
Erster Gutachter:	Prof. Dr. Volker Buck
Zweiter Gutachter:	Prof. Dr. Dieter Mergel

Murphy's First Laboratory Law:

Hot glass looks exactly the same as cold glass.

Dedicated to my beloved parents

for their love, endless support

and encouragement

Table of Contents

Acknowledgments 8

1 Introduction 10

2 Fundamentals 15

2.1 Carbon 15

2.1.1 Electronic Structure of Carbon 15

2.1.2 Hybridization of Atomic Orbitals 16

2.1.2.1 sp^3 Hybridization 16

2.1.2.2 sp^2 Hybridization 17

2.1.2.3 sp^1 Hybridization 17

2.1.2.4 σ and π Bonds 18

2.2 Carbon Allotropes 19

2.2.1 Diamond 20

2.2.2 Graphite 21

2.2.3 Fullerene 22

2.2.4 Nanotubes 22

2.2.5 Graphene 23

2.2.6 Amorphous Carbon 24

2.3 DLC Models 26

3 DLC Deposition Techniques 28

4 DC Discharge in the Vacuum 29

5 Arc Discharge 32

5.1 Cathodic Arc 34

5.2 Macroparticle Filtering 38

5.3 Anodic Arc 40

5.4 Transition From Cathodic to Anodic Arc 40

6 Diagnostics 41

6.1 Plasma Diagnostics 41

6.1.1 Retarding Field Energy Analyzer (RFEA) 41

6.2 Film Diagnostics 44

6.2.1 Nuclear Reaction Analysis (NRA) 44

6.2.2 Spectroscopic Diagnostic Methods 45
6.2.2.1 UV-VIS Spectroscopy 45
6.2.3 Physical Structure 46
6.2.3.1 X-Ray Diffraction (XRD) and Williamson-Hall Method 46
6.2.4 Mechanical Properties 50
6.2.4.1 Residual Stress 50
6.2.4.2 SSIOD 54
7 Experimental Setup 56
7.1 Experimental Setup for DLC Film Deposition 56
7.2 Experimental Setup for Magnesium Film Deposition 60
8 Experimental Results 64
8.1 Plasma Diagnostics 64
8.1.1 Influence of Deposition Parameters on Plasma Properties 64
8.1.1.1 Mass-spectroscopy During DLC Film Deposition 64
8.1.2 Influence of Electrode Material on Plasma Composition 67
8.1.2.1 Electrode Degasation 67
8.1.2.2 Electrode Material Impurity 69
8.1.3 Influence of Deposition Parameters on Plasma Properties 71
8.1.3.1 Mass Spectroscopy During Magnesium Film Deposition 71
8.1.4 Particle Energy Measurement During DLC Film Deposition 73
8.1.4.1 Influence of Different Arc Modes on the Ion Energy 73
8.1.4.2 Influence of Different Hydrogen Flow Rates on the Ion Energy 76
8.1.4.3 Degree of Ionisation as a Function of Different Arc Modes 77
8.1.5 Particle Energy Measurement During Magnesium Film Deposition 79
8.1.5.1 Influence of Different Hydrogen Flow Rates on the Ion Energy 79
8.2 Film Diagnostics 81
8.2.1 Arc Modes 81
8.2.2 Deposition Rate 83
8.2.3 Structural Properties 84
8.2.3.1 Film Morphology 84
8.2.3.1.1 Influence of Different Arc Modes on Film Morphology 85
8.2.3.1.2 Influence of Bias Voltage on Film Morphology 89
8.2.3.1.3 Influence of Different Hydrogen Flow Rates on Film Morphology 92

8.2.3.2 Hydrogen Content in the DLC Film 97
8.2.3.2.1 Hydrogen to Carbon Ratio 97
8.2.3.2.2 Nuclear Reaction Analysis (NRA) 99
8.2.3.2.3 Adhesion Coefficient 102
8.2.4 Optical Properties and Electronic Structure of DLC Films 103
8.2.4.1 Film Transmittance 103
8.2.4.1.1 Influence of Different Arc Modes on Film Transmittance 103
8.2.4.1.2 Influence of Different Hydrogen Flow Rates on Film Transmittance 105
8.2.4.2 The Optical Band Gap 109
8.2.4.2.1 Influence of Different Arc Modes on the Band Gap 109
8.2.4.2.2 Influence of Different Hydrogen Flow Rates on the Band Gap 110
8.2.4.3 DLC Band Model 111
8.2.4.4 The sp^3 Content in DLC Film as a Function of Deposition Parameters 114
8.2.4.4.1 Influence of Different Arc Modes on sp^3 Content 114
8.2.4.4.2 Influence of Different Deposition Parameters on sp^3 Content 115
8.2.4.5 The Complex Dielectric Function 116
8.2.4.5.1 Influence of Different Arc Modes on ε_2 119
8.2.4.5.2 Influence of Different Hydrogen Flow Rates on ε_2 120
8.2.4.5.3 Influence of Bias Voltage on ε_2 122
8.2.5 Raman Spectroscopy 126
8.2.5.1 The G-Peak Position 127
8.2.5.1.1 Influence of Different Arc Modes on the G- Peak Position 128
8.2.5.1.2 Influence of Bias Voltage and Different Hydrogen Flow Rates on the G-Peak Position 129
8.2.5.2 The I_D/I_G Ratio 131
8.2.5.2.1 Influence of Different Arc Modes on the I_D/I_G Ratio 132
8.2.5.2.2 Influence of Bias Voltage and Different Hydrogen Flow Rates on the I_D/I_G Ratio 133
8.2.5.3 The Full Width at Half Maximum of G-Peak (FWHM G) 135
8.2.5.3.1 Influence of Different Arc Modes on FWHM G 135
8.2.5.3.2 Influence of Bias Voltage and Different Hydrogen Flow Rates on FWHM G 136
8.2.5.4 The G-Peak Dispersion ($Disp_G$) 137

8.2.5.5 Correlation between Results from Raman and UV-VIS Spectroscopy 139
8.2.5.5.1 The Optical Band Gap and Raman Parameters 139
8.2.5.5.2 The Imaginary Part ε_2 of the Dielectric Function and Raman Parameters 140
8.2.6 Mechanical Properties 141
8.2.6.1 Residual Stress Measurements 141
8.2.6.1.1 Thermal Stress 141
8.2.6.1.2 Influence of Different Arc Modes on Residual Stress 142
8.2.6.1.3 Influence of Bias Voltage on Residual Stress 143
8.2.6.1.4 Influence of Different Hydrogen Flow Rates on Residual Stress 144
8.3 DLC Film Classification 148
8.4 Magnesium Films Deposition 150
8.4.1 Energy-Dispersive X-Ray Spectroscopy (EDX) 150
8.4.2 Grain size by SEM 154
8.4.3 Grain Size by XRD 155
9 Results And Outlook 157
10 References 160
Appendix I 171

Acknowledgments

I am very grateful and would like to express my acknowledgement to

My supervisor Prof. Dr. Volker Buck for welcoming me into his group, his guidance in my scientific work, providing outstanding working facilities and friendly working atmosphere, always ready to help in finding a solution to any problem,

Prof. Dr. Dieter Mergel my second reviewer for good advices, attention to details, and useful comments,

Dr. Alexei Poukhovoi for his friendship all the time, willingness to help, companionship in many good activities inside and outside the office,

Dr. Nicolas Wöhrl for his help in stress measurements, scientific advices, good old days together when we were young and a robot,

Dr. Stefan Reuter for his kindness and his cooperation during my work, good times and conversations which I’m missing now,

Sebastian Schipporeit for his help, friendly conversations, readiness to correct my English grammar,

Dr. Viktor Kadetov for his friendly support at the beginning of my time in Germany,

Dr. Werner Becker for providing data from NRA measurements,

Dr. Nebati Abdelkader for his help with XRD measurements,

Dipl.-Ing. Smail Boukercha for his help in SEM measurements and friendly conversations,

Dipl.-Phys. Marcus Neubert for his friendly advices and cooperation,

Dipl.-Phys. Matthias Haase for willingness to discuss any encountered problems and his opinion,

Dipl.-Phys. Klaus Pärschke for his readiness to help and useful advices,

Dipl.-Phys. Victoria Khlopyanova for her smile, kindly provided data for missing experiments,

Dipl.-Phys.Ing. Martin Jerman his help with the vacuum arc chamber,

Dipl.-Ing. Monika Timpner for many friendly conversations,

Mrs. Heidi Pärschke for her help especially with German office bureaucracy,

Peter Walter and Heinz Loffeld for their technical assistance,

co-workers of the Essen mechanic workshop (especially to prematurely deceased Frank Matthies) for help and advices in construction activities, on time and accurate manufacturing,

Dietrich Tönnes and Dr. Bärbel Maullu for their help, friendly conversations and support,

My family who always believe in me, for their love, whom I owe everything I have...

Abstract

Despite the fact that diamond-like carbon (DLC) films have been known for a long time and widely used in various fields of science and technology, they are still the subject of permanent scientific interest. These films are a whole class of carbon based amorphous films which properties are strongly defined by the deposition parameters. In the first place, the film properties are determined by plasma parameters (particle energy and plasma chemistry). In order to demonstrate this influence, it is necessary to examine these parameters separately. But there are only a few plasma sources capable to perform this separation. One of them is the vacuum arc. Vacuum arc is a well-known deposition technique which can be operated in different modes (cathodic or anodic). Up to now, these modes were investigated separately. However, these modes and the transition between them were never investigated in one complex.

The aim of this work is to investigate the influence of the deposition parameters on the chemical, optical and mechanical properties of DLC films by the help of vacuum arc plasma source adjustable from cathodic to anodic arc modes.

Trotz der Tatsache, dass diamantähnliche Kohlenstoffschichten (DLC) seit langer Zeit bekannt und in verschiedenen Gebieten der Wissenschaft und Technik weit verbreitet sind, sind Sie immer noch Gegenstand ständigen wissenschaftlichen Interesses. Sie sind eine ganze Klasse von auf Kohlenstoff basierenden amorphen Schichten deren Eigenschaften stark von den Abscheidungs-Parametern definiert werden. In erster Linie werden die Filmeigenschaften durch Plasmaparameter (Teilchenenergie und Plasmachemie) bestimmt. Um diesen Einfluss zu demonstrieren, ist es notwendig diese Parameter getrennt zu prüfen. Jedoch gibt es nur wenige Plasmaquellen die fähig sind, diese Trennung durchzuführen. Einer von ihnen ist der Vakuumlichtbogen. Es ist eine wohlbekannte Abscheidetechnik, die in unterschiedlichen Betriebsarten arbeiten kann (kathodisch oder anodisch). Bisher sind diese Betriebsartem nur separat untersucht worden. Allerdings sind beide Betriebsarten und der Übergang zwischen ihnen nie in einem Komplex untersucht worden. Das Ziel dieser Arbeit ist es, den Einfluss der Abscheidungsparameter von Vakuumlichtbogen-Plasmaquellen, die von kathodischen zur anodischen Betriebsart einstellbar sind, auf die chemischen, optischen und mechanischen Eigenschaften von diamantähnlichen Kohlenstoffschichten zu untersuchen.

Introduction

Since the beginning of mankind, humans have been creating new tools and new devices in order to improve the existing ones and create more efficient and durable ones. Each era is determined by its technology, from the simplest bronze cutting tools to high-tech lasers and multilayered ceramic cutters. Science has been looking deeper and deeper and opened up newer and newer horizons. And the time when there was a requirement for new materials with new properties has come. During the last century, thin film technology has become more and more popular. This technology stands for whole new materials with the special properties which may differ from those of bulk ones. Using such technology we are able to intentionally modify bulk material properties only by coating it with a very thin layer of another material. These materials can be deposited directly onto any required surface in order to confer special properties or a set of properties. Such technology requires a new means of production: vacuum technology and plasma technology. The most rapidly developing and growing technique is plasma deposition. This technology allows us to operate with another state of matter – plasma, and create hitherto unknown metastable conditions in which a new kind of chemical processes and reactions is possible. These processes are not possible under standard conditions but we are able to use common materials and give them new functional properties.

The functional properties – macroscopic properties, of deposited films usually determine their application area. In some cases, films should be hard or soft, hydrophilic or hydrophobic, or multilayered with different optical properties. These properties usually appear to be a product of *trial and error* in industrial researches to receive the films with desired macroscopic parameters. Usually these thin film deposition methods are "*empirically*" developed without understanding the physical processes which lie under the surface. In order to optimize the existing methods and to develop a modern one it is necessary to gain the knowledge and comprehension of film deposition processes and factors affecting these processes. Only thin film technology is able to give a comprehensive answer to this question. The tailoring of microscopic properties will give us the means to tune up the macroscopic properties of the deposited films.

The following figure shows the influence of different parameters onto functional properties of deposited films [Buck93].

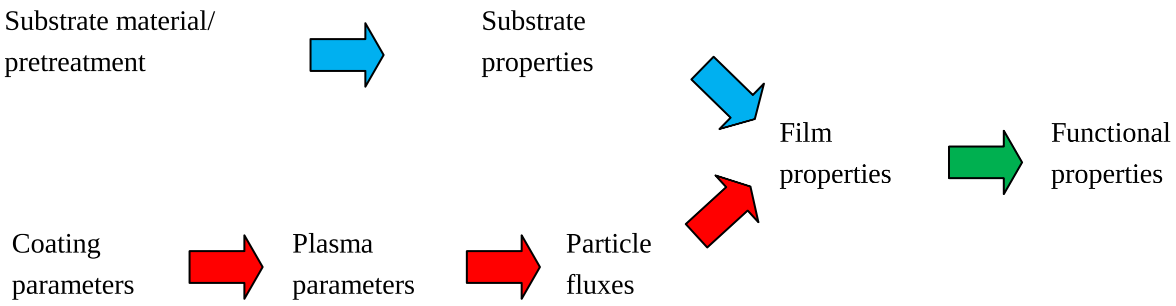

Fig. 1.1: *Tailoring the thin films properties [Buck93].*

In order to understand the microscopic parameters we need to take a closer look onto film properties at atomic level. Film properties at microlevel are determined by two factors: substrate properties (the most important parameters are the substrate surface and temperature) and particle fluxes arriving to the substrate surface.

But in many cases information about these microscopic parameters is very limited, and only macroscopic information is available. For instance, a substrate material or substrate pretreatment process; deposition parameters: working pressure, current and voltage of plasma source. To optimize the process, fundamental physical understanding is necessary. The main aim is to clarify the influence of each part of the diagram (see Fig.1.1) onto functional properties. To understand this influence it is better to divide the processes influencing the functional properties into two branches: first – particle fluxes, second – substrate properties. The particle fluxes are usually determined by which type of the plasma is used (plasma parameters). These parameters determine particle energy, degree of ionisation, etc.

Particle energy is an important but often neglected parameter determining the film properties. Therefore we have used carbon – because it is the most particle energy dependent material, to investigate differences between different modes of an arc plasma source.

Carbon is a well-known material, it has a lot of modifications like diamond or graphite and their properties are very different. One stands for maximum hardness but low conductivity, another one for very high conductance but very poor mechanical properties. All these so different materials are still made of the same carbon atoms but arranged under different conditions and energies. For some applications we need highly energetic particles to embed them under the substrate surface, or to have the particle energy as low as possible, in order to avoid damage of very sensitive substrate. Here we meet the second branch – substrate, it should be taken into account which type of substrate material is used (plastic or metal), its surface condition (roughness, oxide layers) and temperature.

As one can see there are many parameters influencing deposition processes, in addition these parameters are also interacting with each other and causing more complex effects. It is necessary to consider “hidden parameters”. These indeterminate parameters can be only detected after series of similar experiments [Buck93].

Diamond-like carbon (*DLC*) stands for a whole class of materials based on carbon (amorphous carbon, hydrogenated carbon, tetrahedral amorphous carbon, etc.), where the properties can be varied in an unusually large area – e.g. from conductive to isolating or from hydrophilic to hydrophobic [Grill03]. Also be gradually changed in hardness, intrinsic mechanical stress, E-module, roughness, gas permeability, etc. – and these properties can be varied by choosing suitable coating parameters. In order to influence the film properties it is necessary to control particle energy but it is only possible for charged particles and the amount of the charged particles (ionisation rate) is a crucial parameter. Very interesting material properties are expected for films produced with particle energy in the range *10 eV – 100 eV* [Robertson02], but there are only a few plasma sources that deliver high fluxes at these energies, the hybrid radiofrequency source and the *DC* arc source seems to be the most promising for this purpose. But these sources are rather different in the way of plasma generation, ionisation rate and deposition rates. Therefore, the obtained films have differences in structure and chemical composition, consequently film properties differ.

The cathodic arc is the most commonly used deposition method in a vacuum technology. Such arc is a powerful plasma source with high deposition rate, but the biggest problem is macroparticle or droplet formation. Usually macroparticles are formed by the materials with the low melting temperature like *Al, Cu* where amount of ions evaporated is very low. When a materials with the high melting temperature like *C, W, Mo* or the sublimation materials are used it is possible to reduce macroparticle content and to increase the amount of ions evaporated [Eckhardt75]. But for some applications where the surface properties like the roughness or the film transparency are very important, the amount of macroparticles does not allow to use this method. In that case there is a possibility to keep the advantages of the cathodic vacuum arc like high degree of ionisation and very high deposition rate, but avoid macroparticles generation. There have been several attempts [Aksenov78, Karpov97, Anders99,] one of them is an anodic vacuum arc. The anodic arc can be more successfully used especially in thin films technology applications instead of the cathodic arc deposition method.

An arc plasma source adjustable from cathodic to anodic mode allows us to customize plasma properties in order to obtain nanostructured coatings with reduced droplet incorporation.

In order to adjust film properties, *DLC* films were deposited by using different deposition regimes of a *DC* vacuum arc plasma source. The variation in process parameters such as substrate bias and gas admixture is used to influence the film properties. The plasma parameters were monitored during deposition by mass-spectrometer and ion energy by retarding field energy analyzer. The films were deposited on polished *(100) Si*, *BK-7* glass and steel substrates in order to investigate their mechanical, chemical and optical properties. For the film morphology analysis and surface roughness evaluation of deposited films, scanning electron microscopy (*SEM)* and atomic force microscopy (*AFM)* were used. Nuclear reaction analysis *(NRA)* was used to evaluate hydrogen content in the films. The optical properties of the films were *ex-situ* examined by *UV-VIS* spectroscopy and from these data details of the band structure were modelled. The Raman spectroscopy was used to investigate the chemical composition of the obtained films. The relation between particle energy and deposited film properties is determined.

The residual stress is a significant parameter for growing films. It influences adhesion of the growing films and therefore their application areas. The residual stress in the deposited films was *ex-situ* measured using Surface Stress Induced Optical Deflection (*SSIOD*) method [Woehrl10]. The custom made anodic arc plasma source with graphite electrodes, which was used in order to investigate the transition between the cathodic and anodic arc modes, is not suitable for the metallic film deposition. Therefore another anodic arc modification with different electrode configuration and exchangeable electrode material was used. This was also made to demonstrate the flexibility of the anodic vacuum arc in comparison to the cathodic arc, where only materials with a high melting temperature can be used [Eckhardt75]. In order to demonstrate the influence of particle energy onto grain size of growing metallic films, magnesium has been used. This metal was chosen also because magnesium is a very promising, widely available and cheap material for the energy-storage technologies, especially hydrogen. It is known that physical storage of hydrogen, as a highly pressurized gas or in liquid phase at low temperature, is associated with significant security risks and energy losses [Zecchina05]. Furthermore, physical adsorption of hydrogen onto lightweight nanomaterials, such as zeolites, carbon nanotubes, and activated carbons, yields only low storage densities and also needs low temperature [Bogdanovic85, Rudy05, Schlapbach01, Schimmel03 and Zuttel04]. The alternative is chemical storage: the reversible absorption of hydrogen into another material [Hirscher01]. Especially metal hydrides offer a promising and safe alternative to storage in compressed or liquid form [Dillon97, Dillon01]. Magnesium hydride MgH_2 has a high hydrogen storage capacity of *7.6 wt %* [Nijkamp01, Huot01 and Rudy05] and exceeds all known reversible metal hydrides. The crucial parameter for storage capacity is magnesium hydride grain size. In comparison with the common reactive ball milling [Imamura10, Varin06, Darriet80 and Zaluska99] of magnesium, where hydrogen is stored only on the surface, anodic vacuum arc deposition of magnesium films in vacuum chamber with controlled hydrogen atmosphere, allows us to introduce hydrogen directly into deposited magnesium films layer by layer at any necessary surface and material.

In this work the influence and correlation between different deposition parameters (especially particle energy) using different modes of an arc plasma source and obtained film properties are shown.

2 Fundamentals

2.1 Carbon

Carbon (L*at.* - carbo), C, is a chemical element of group IV in the periodic table, atomic number - *6*, atomic mass – *12.011*. There are two stable isotopes: *12C* (*98.892%*) and *13C* (*1.108%*). Carbon has been known since ancient times as coal and diamond, but as a chemical element it was discovered at *1789* by the chemist Antoine Lavoisier.

There are four crystalline carbon modifications: diamond, graphite, lonsdaleite and carbyne. All the carbon modifications are resistant to alkalis and acids; they are also insoluble in common organic and inorganic solvents.

The unique ability of carbon atoms connected together to build strong and long chains and cycles leads to appearance of an enormous number of various carbon modifications.

2.1.1 Electronic Structure of Carbon

Carbon has such electronic configuration: $1s^2 2s^2 2p^2$ (see Fig. 2.1). The outer L-shell of the carbon atom contains four electrons: $2s^2 2p^2$, two of which occupy $2s$ orbital, which has a spherical shape, and two other electrons occupy $2p$ orbital with dumbbell shape. Due to this the neutral carbon atom is bivalent (in this case an atom valence is determined by the p electron shell). Carbon forms four covalent bonds, therefore carbon can equally draw and give electrons. Chemical bonding can occur at the expense of sp^3, sp^2 and sp^1 hybrid orbital respectively. The number of valence electrons and valence orbitals of carbon is the same and this is one of the reasons for the bond stability between carbon atoms.

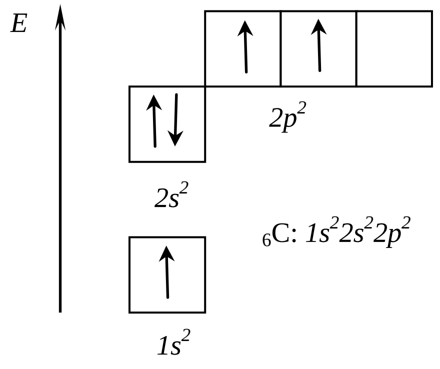

Fig. 2.1: *Electronic structure of carbon.*

2.1.2 Hybridization of Atomic Orbitals

It is known that carbon atoms can exist in three states corresponding to sp^3, sp^2 and sp^1 hybridization of their valence orbitals.

2.1.2.1 sp^3 Hybridization

In case of sp^3 hybridization, three *p* orbitals and one *s* orbital interact thereby to form energetically similar and symmetrically oriented configurations. By sp^3 hybridization the total number of orbitals stays the same but the energy and shape are changed. The four hybrid orbitals are extended from the center to the top of regular tetrahedron at the angles of $109^\circ 28'$ (see Fig. 2.2). The bonds which are formed by hybrid electrons (for instance s-sp^3 bond) are much stronger than the bonds formed by unhybridized *p* electrons (for instance *s*-*p* bond). The hybrid sp^3orbital provides a bigger overlapping area of electron orbitals then an unhybridized *p* orbital. Molecules with sp^3 hybridisation have a tetrahedral structure. The coordination number in such structure is equal to four (4NN).

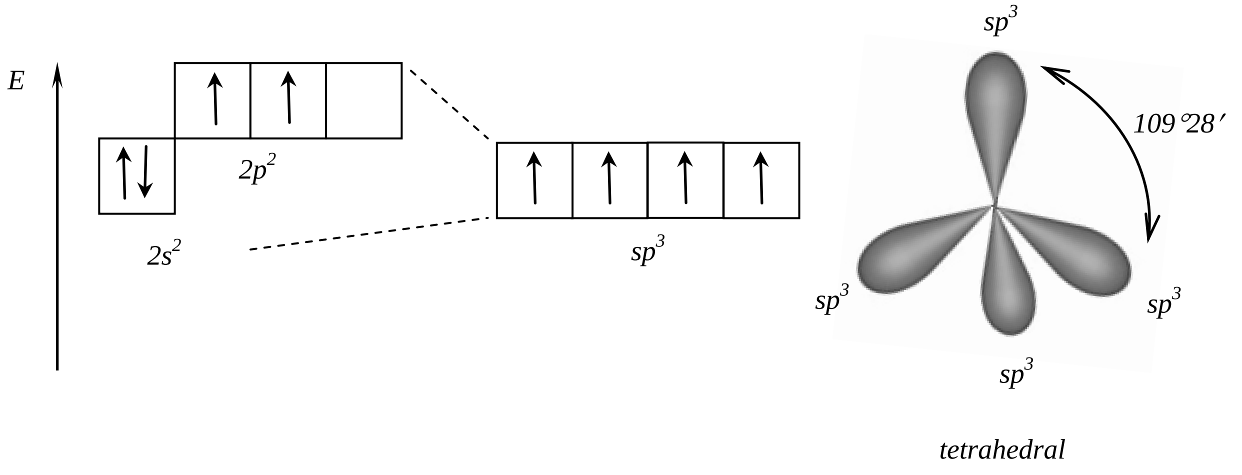

Fig. 2.2: *Hybridization of s and p orbitals into* sp^3 *orbitals.*

2.1.2.2 *sp*^{2} Hybridization

sp^2 Hybridization occurs in case of overlapping of one *2s* and two *2p* orbitals. Thus obtained *sp*^{2} orbitals are lying in the same plane at the angle of *120°* to each other, and unhybridized *p* orbital lies perpendicular to this plane (see Fig. 2.3). The total number of the orbitals stays the same – four. The coordination number in such structure is equal to three (3NN).

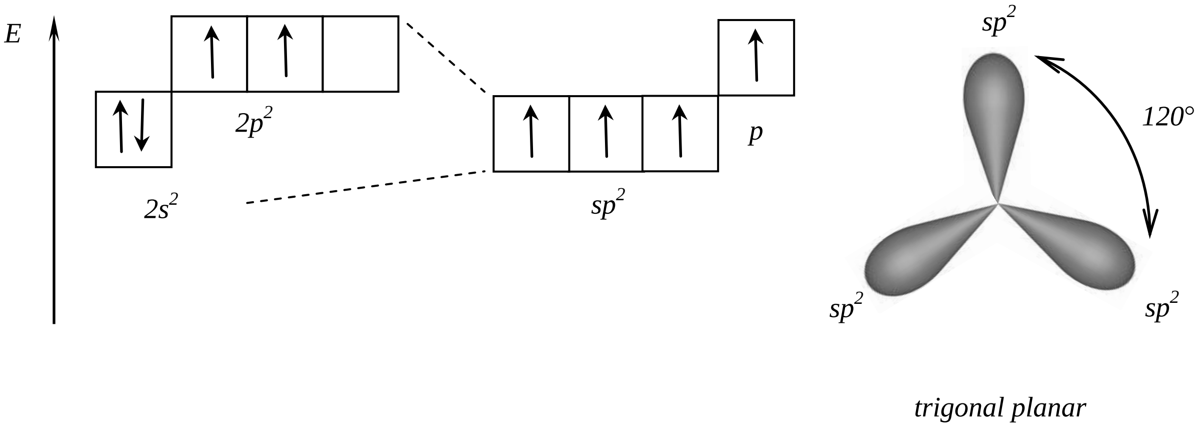

Fig. 2.3: *Hybridization of s and p orbitals into sp*^{2} *orbitals*.

2.1.2.3 *sp* ^{1} Hybridization

In a state of *sp*^{1} hybridization a carbon atom has two *sp*- hybrid orbitals linearly arranged at an angle of *180°* to each other, and two non-hybridized *p* orbitals at the two mutually transverse planes, as shown in Fig. 2.4. The coordination number in such structure is equal to two (2NN).

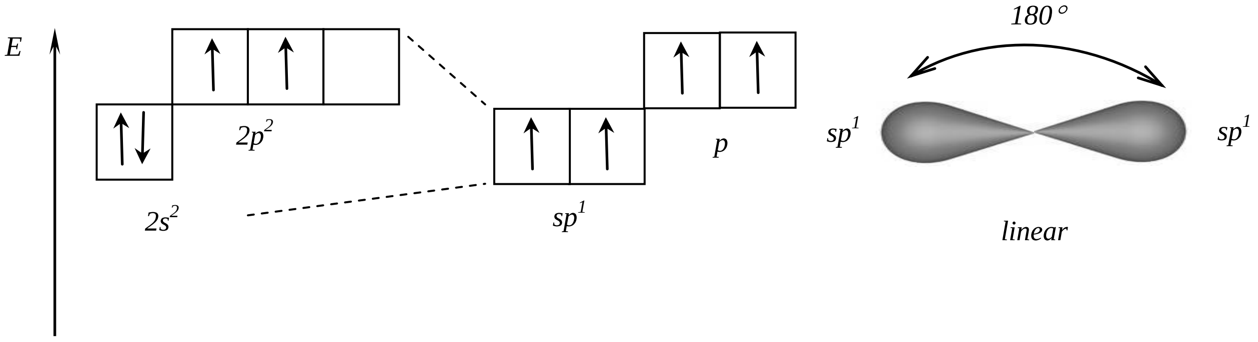

Fig. 2.4: *Hybridization of s and p orbitals into sp orbitals*.

2.1.2.4 σ and π Bonds

Hybridized carbon atoms form also σ and π bonds. Covalent σ bond is formed by overlap of two carbon valence electrons. The π bond is usually formed by overlap of unhybridized *p* orbital on each carbon atom (see Fig. 2.5). Generally speaking, any σ bond is characterized by the fact that electron orbitals of two bonded atoms overlap on the line-of-centres joining the two atoms. The σ bonds usually respond to a maximum possible overlap of atomic orbitals, therefore they are strong enough. A characteristic feature of the π bond is that the electron orbitals overlap goes beyond the line connecting two atoms.

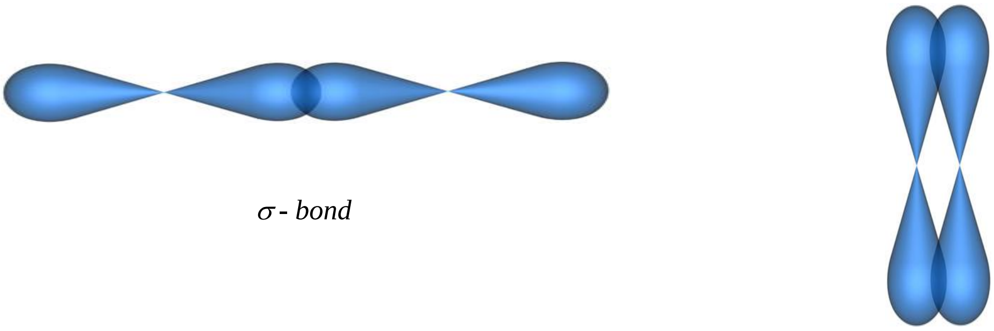

σ *- bond*

π *- bond*

Fig. 2.5: *σ and π bonds formation in carbon atoms.*

The combination of a σ bond and a π bond spreading between the same pair of atoms forms the double bond in molecules. Since the overlap area of unhybridized *p* orbitals in π bonds is smaller than overlap area in σ bonds, it leads to the fact that π bonds are weaker than σ bonds and easily can be broken in chemical reactions.

2.2 Carbon Allotropes

According to the hybridization type, carbon allotropes can be arranged in the following classes, see Fig. 2.6.

Carbon Allotropes

sp^3:

- Diamond
- Lonsdaleite

sp^2:

- Graphite
- Fullerene
- Nanotubes
- Graphene

sp:

- Linear acytelenic carbon
- Carbyne

sp^3/sp^2:

- Amorphous carbon
- Carbon nanofoam

Fig. 2.6: *Carbon allotropes*.

Due to diversity of carbon form their properties of allotropes also very diverse. Some allotropes extremely hard but some are very soft, some are good conductors but other are dielectric, some are amorphous but other are crystalline. Some carbon allotropes are known for many decades but some were discovered only few years ago. To avoid some difficulties in the future with the film classification it is better to take a look at the few carbon allotropes and their characteristics.

2.2.1 Diamond

Diamond (G*reek* αδαμαζ – *adamas* “unbreakable”) is one of the most famous configurations of carbon atoms. It is a colourless, transparent (due to large band gap *5.5 eV*) crystalline material with very strong refraction of visible light. Diamond is the typical representative of sp^3 hybridized atoms. Diamond atoms form *FCC* (face-centered cubic) lattice, with lattice constant $a = 0.3559\ nm$ [Pierson93]. Carbon atoms in a diamond structure are placed in the corners of tetrahedron as shown in Fig. 2.7.

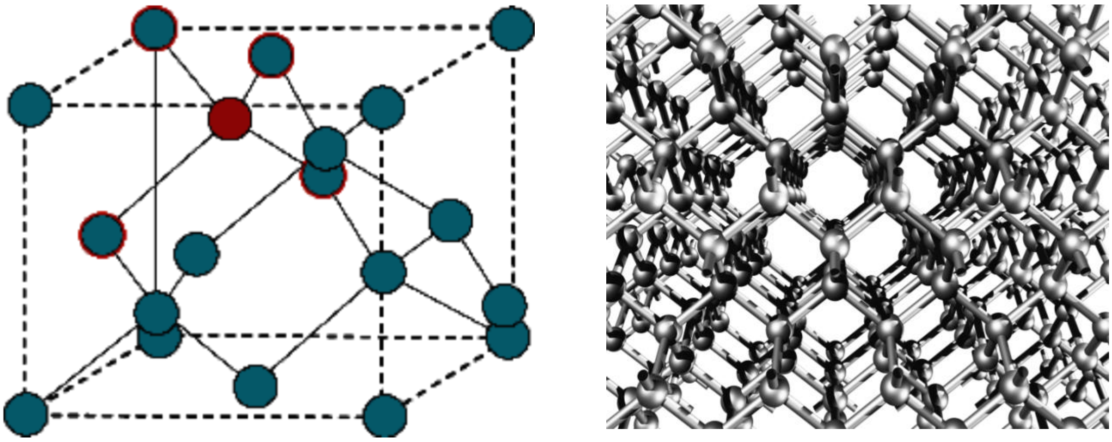

Fig. 2.7: *Diamond FCC lattice and diamond structure*.

The strength of all the bonds is identical. Thus, atoms in diamond structure are “packed” very tightly. Diamond density is $3.52\ g/cm^3$. Diamond is the hardest material in the nature, it has a highest hardness on the Mohs scale, see Fig. 2.8.

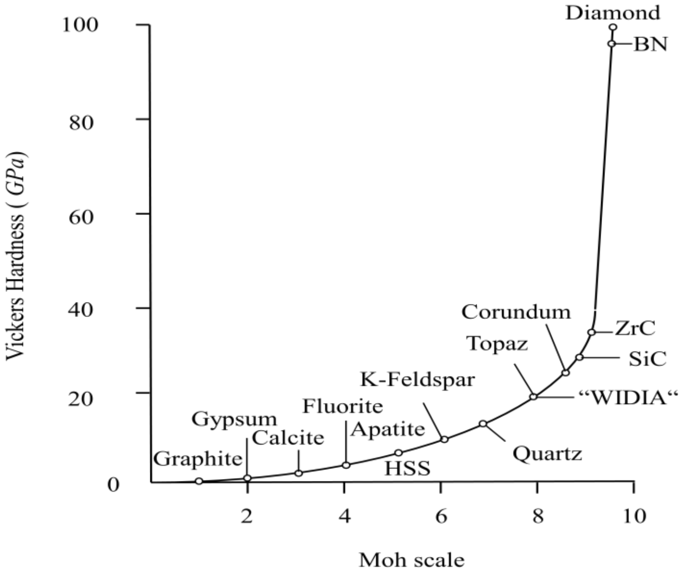

Fig. 2.8: *Hardness diagram for different materials [Buck06].*

Covalent bonded diamond atoms have no free electrons; therefore diamond is an insulator with band gap around *5.5 eV*.

2.2.2 Graphite

Graphite (G*reek* $\gamma\rho\alpha\varphi\omega$ *– grapho “*to write”) – gray-black crystalline substance with metallic glitter, was named by Abraham Werner in 1789. Graphite is the second most known carbon allotrope. Graphite has a low density of $2.27 g/cm^3$. The carbon atoms in graphite are sp^2 hybridized, they have strong σ bond and oriented in one plane, forming hexagonal layers and very weak π bond perpendicular to this plane Fig. 2.9. The presence of π bond leads to shortening of the single bond length from *0.154 nm* for diamond to *0.142 nm* for graphite and an increase of binding energy. The presence of free electrons in non-localized π bond leads to appearance of metallic conductivity in graphite.

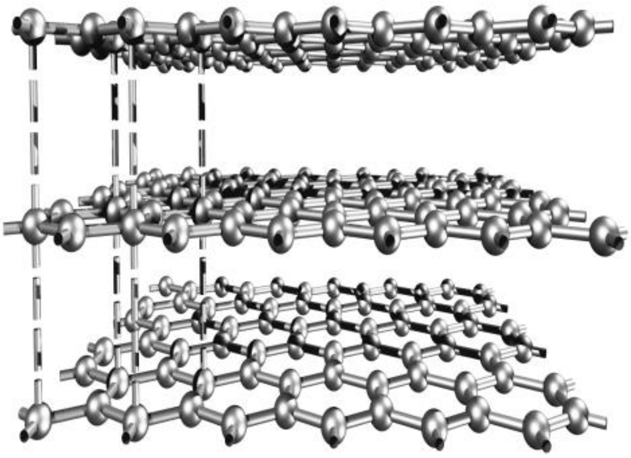

Fig. 2.9: *Graphite structure*.

The hexagonal layers in the graphite are bonded only due to the weak Van der Waals forces. Therefore there is a big distance *0.335 nm* between graphite layers [Pierson93], what cause bad mechanical properties of graphite (small micro hardness, ease of slipping planes between each other and weak conductivity across the planes).

2.2.3 Fullererne

Fullerene is a three-dimensional carbon modification. It is a molecule which atoms arranged in hexagons and pentagons forming spherical surface. The atoms at the vertices are sp^2 hybridized carbon atoms, see Fig. 2.10.

In 1971 Ejii Osawa predicted the existence of C_{60} in a Japanese magazine [Osawa70]. He proposed that the carbon atoms may be located in the lattice sites of truncated icosahedron, and he made the hypothesis that a full ball shape could also exist. His idea was reported in Japanese magazines, but did not reach Europe or America. In 1973 for the first time soviet theoreticians D. Bovchar and E. Galperin performed quantum-chemical computation of such hypothetical molecule, confirming it high energetic stability and possibility of its natural occurrence. [Bovchar73]. But only in 1985 it was found by Kroto and co-workers [Kroto85].

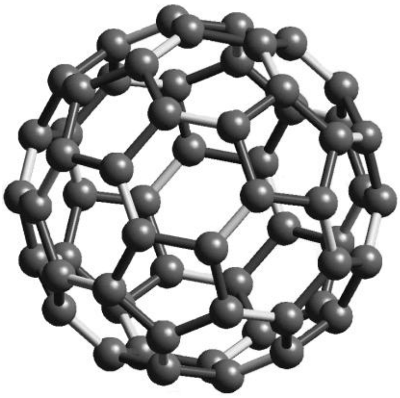

Fig. 2.10: *Fullerene* C_{60}.

Due to their structure fullerenes are used in many areas of science and technology (low friction materials, semiconductive materials)

2.2.4 Nanotubes

Nanotubes, in principle, are another three-dimensional modification of graphite hexagonal plane. At this time such plane rolled in to a cylinder, see Fig. 2.11. The atoms in nanotubes are sp^2 hybridized. During the growth process the nanotubes can form single-walled (SWNT) or multi-walled (MWNT) structures. Such carbon modification was discovered in 1991 by Iijima [Iijima91]. But for many years before such structures were observed by soviet scientists

Radushkevich L. V. and co-workers [Radushkevich52]. Unfortunately results were reported in Soviet magazines and did not reach Europe or America.

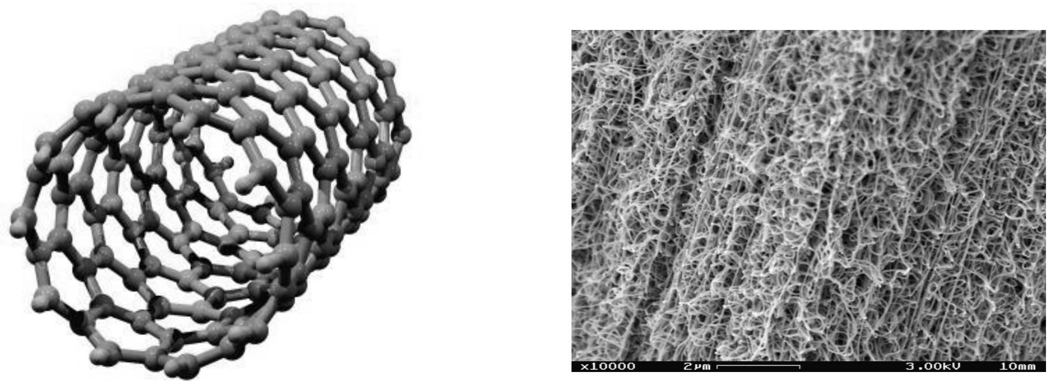

Fig. 2.11: *Nanotubes*.

Due to special structure and length to diameter ratio nanotubes found application in microelectronics, they can be used as composite materials with unique properties; also they are subject of medical interest.

2.2.5 Graphene

This carbon allotrope is one of the newly discovered carbon forms [Novoselov04]. It is two-dimensional carbon modification. It can be described as a single graphite plane one atom thick, see Fig. 2.12. The grapheme atoms are sp^2 hybridized.

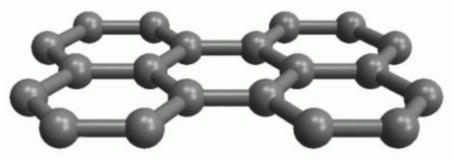

Fig. 2.12: *Graphene*.

Graphene have outstanding mechanical properties and extremely high thermal conductivity ~ 5×10^3 $W\cdot m^{-1}\cdot K^{-1}$ [Balandin08]. Due to high electron mobility in graphene this material can be very perspective for nanoelectronics [Bunch07].

2.2.6 Amorphous carbon

The name “amorphous carbon films” or diamond-like carbon (*DLC*) stands for a whole class of carbon-based films, where properties can be varied in an unusually large area – e.g. from conductive to isolating or from hydrophilic to hydrophobic as well as gradually changed in hardness, mechanical stress, roughness etc. The concept “amorphous carbon” already means that there is no organized structure like in diamond or graphite. DLC films are kind of mixture between sp^3 and sp^2 hybridized carbon atoms [Robertson87], see Fig. 2.13. Therefore the properties of such carbon structures are poorer than diamond or graphite. But nevertheless they can combine the best qualities of one and another.

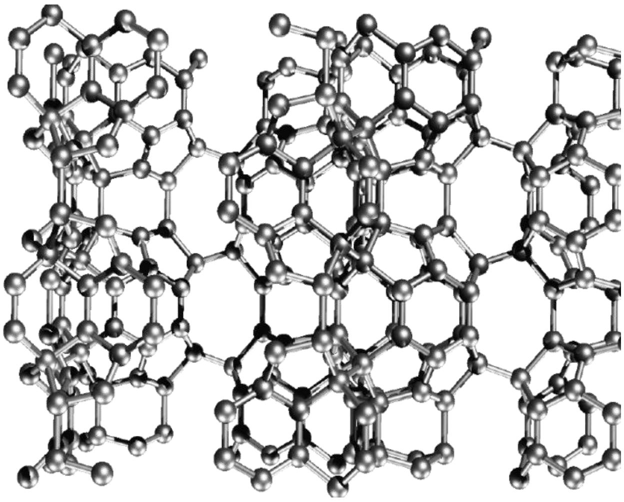

Fig. 2.13: *Amorphous carbon structure*.

The properties of carbon coatings strongly depend on the deposition parameters: particle fluxes, particle energy and impurities. By variation of the deposition parameters it is possible to influence amorphous carbon structure and to obtain the desired properties. In the Table 2.1 one can see summarized experimental data on DLC films deposited by different deposition techniques at various deposition conditions.

Table 2.1: Physical and chemical properties of various carbon modifications and DLC films deposited by the different techniques [Robertson02].

	Density [g/cm^3]	***Hardness [Gpa]***	***sp^3 [%]***	***H [at. %]***	***Band gap [eV]***
Diamond	*3.515*	*100*	*100*	*0*	*5.5*
Graphite	*2.267*	–	*0*	*0*	*– 0.04*
Glassy C	*1.3 – 1.55*	*2 – 3*	*0*	–	*0.01*
a-C (evaporated)	*1.8 – 2.0*	*2 – 5*	*< 5*	–	*0.4 – 0.7*
a-C (MSIB)	*2.5 – 3.0*	*≤ 100*	*90 ± 5*	*9*	*1.5 – 2.5*
a-C (sputtered)	*2.0 – 2.4*	*10 – 14*	*95*	–	*0.5*
ta-C	*2.9 – 3.4*	*< 80*	*~ 85*	*< 5*	*1.5 – 2.1*
ta-C:H	*2.0 – 2.9*	*30 – 60*	*< 75*	*~ 30*	*1.5 – 2.0*
Laser nc-C	–	*40*	–	–	–
a-C:H (hard)	*1.6 – 2.2*	*10 – 40*	*30 – 60*	*20 – 40*	*0.8 – 1.5*
a-C:H (soft)	*0.9 – 1.6*	*< 5*	*50 – 80*	*40 – 65*	*1.5 – 4*
Polythene	*0.92*	*0.01*	*100*	*67*	*6*

As one can see with the diversity of different DLC modifications there were some attempts to describe DLC properties by the help of various models.

2.3 DLC Models

The common method to produce diamond like carbon films is a physical vapour deposition technique (*PVD*). The films produced by this method usually show a strong correlation between sp^3/sp^2 ratio and H-content as explained by the "Fully Constrained Network" (*FCN*) model [Angus88, Angus91], Fig. 2.14.

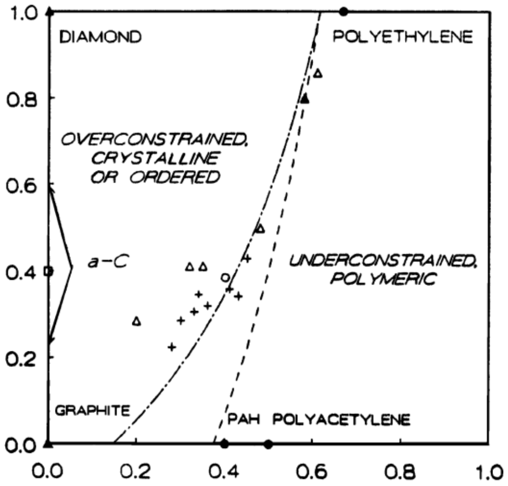

Fig. 2.14: *Fully constrained network diagram.*

Films with properties besides this *FCN*-regime can be produced using plasma source with well defined particle energies, especially films with very high sp^3-content and vanishing or small content of hydrogen can be obtained using particle energies near *100 eV* as explained by the "subplantation model" [Robertson02], Fig. 2.15.

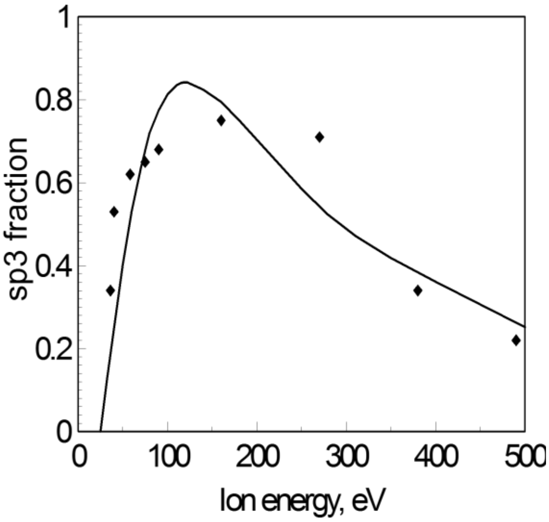

Fig. 2.15: *Diagram presenting the influence of deposited ions energy onto DLC films properties [Robertson02].*

According to the hydrogen content *sp*^{3} and *sp*^{2} content all DLC films can be divided into classes, like shown on "*Ternary phase diagram*", see Fig. 2.16 [Robertson02].

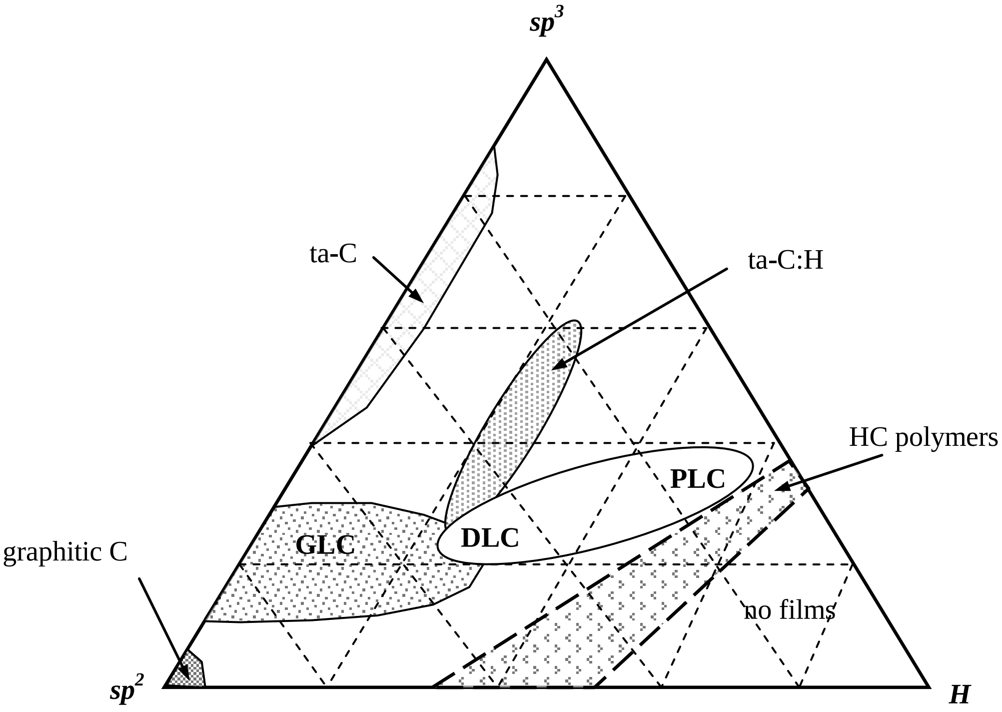

Fig. 2.16:. *Ternary phase diagram for different DLC films. Each corner corresponds to diamond, graphite and hydrogenated amorphous carbons.*

***GLC** – graphite-like carbon, **DLC** – diamond-like carbon, **PLC** – polymer-like carbon.*

3 DLC Deposition Techniques

Diamond like carbon films are usually produced by vacuum deposition technique and in some cases by liquid electrochemical technique [He11]. The deposition methods can be divided in two groups according to the phase of matter of ion source:

CVD – Chemical Vapour Deposition *(gaseous phase)*
PVD – Physical Vapour Deposition *(solid phase)*

These methods are differing in many parameters one of them is a particle fluxes (ion energy, plasma chemistry) and therefore the deposited DLC films properties depend on these parameters. According to [Robertson02] very interesting material properties are expected for films produced with particle energy in the range *10 eV – 100 eV*, but there are only a few deposition techniques that deliver high fluxes at these energies, Radio Frequency Plasma Enhanced Chemical Vapour Deposition (*RFPECVD*) [Kadetov04] technique and the DC vacuum arc PVD method [Buck91] seems to be the most promising for this purpose. But these deposition techniques are rather different in the way of plasma generation, ionisation rate and deposition rates. Therefore, the obtained films have differences in structure and chemical composition. But the main advantage of PVD vacuum arc is that it is able to operate without any gases. This allows investigating the influence of plasma parameters on film properties separately.

In order to know better the properties of vacuum arc discharge it is necessary to have a closer look at those processes in a vacuum.

4 DC Discharge in the Vacuum

In order to understand the processes in the vacuum arc it is necessary to consider the simplified situation with two electrodes in a vacuum. The term “vacuum” means absence of particles and pressure much lower than the atmospheric pressure, but inside the vacuum there are some gas particles, which are playing the key role in described processes.

The electrodes are connected to the dc power supply and have a gap between cathode and anode, as shown in Fig. 4.1.

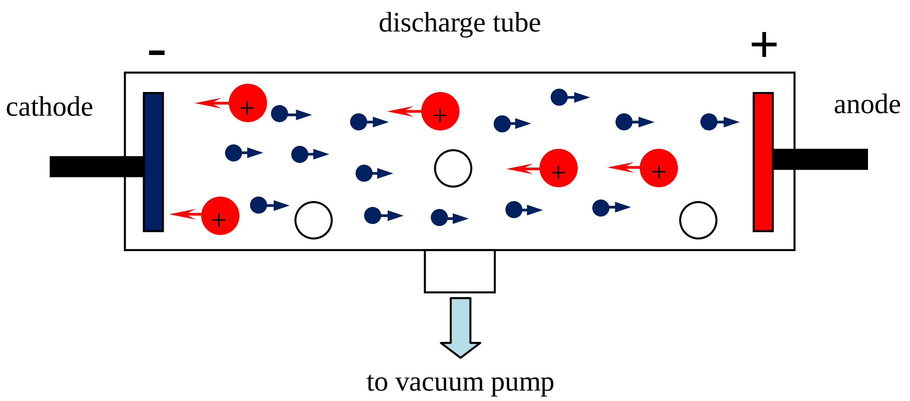

Fig. 4.1: *Schematic diagram of the discharge tube with two electrodes in a vacuum.*

By the gradual increase of the external field $E= V/d$ (where V – is applied voltage and d – is an electrodes gap) and at the certain values of the electric field the electric breakdown is occurs. It is characterized by transformation of nonconducting material into conductor by producing the ionized states in times from $10^{-9}s$ to several seconds [Raizer01]. This ionisation reaches certain values so breakdown is accompanied by the emission of light. If the external electric field is applied for continuous time, the breakdown may transform itself into a discharge, as long as the external electric field is present. The electric breakdown is a threshold process. It means that it could occur only in case of some conditions are fulfilled.

The main part of the breakdown process is an electron avalanche, which occurs in the gap between the electrodes if a sufficiently strong electric field is applied. Usually there are electrons in the gap between the electrodes. The electrons are gaining energy from the applied electric field reaching energies higher then ionisation potential. Then they are able to ionize the gas molecules in the gap. After the ionization they are losing energy, then again accelerating by the external field and ionizing more gas molecules and producing more and more electrons.

Electrons lose energy to excite molecules and atoms; on impacts. Due to the applied electric field the electrons are moved towards the anode and disappear after the breakdown. The processes of electrons creation and disappearance are competing processes. The electron creation rate is described by the ionization frequency and strongly depends on the external field strength. The electron disappearance rate also depends on the field [Raizer01]. As a result of all the processes above-mentioned the electric current *i* appear to flow between the electrodes. According to the values of the electric current flowing between the electrodes, the current-voltage (*i*-*V*) dependence can be divided into few regions, as shown in Fig. 4.2.

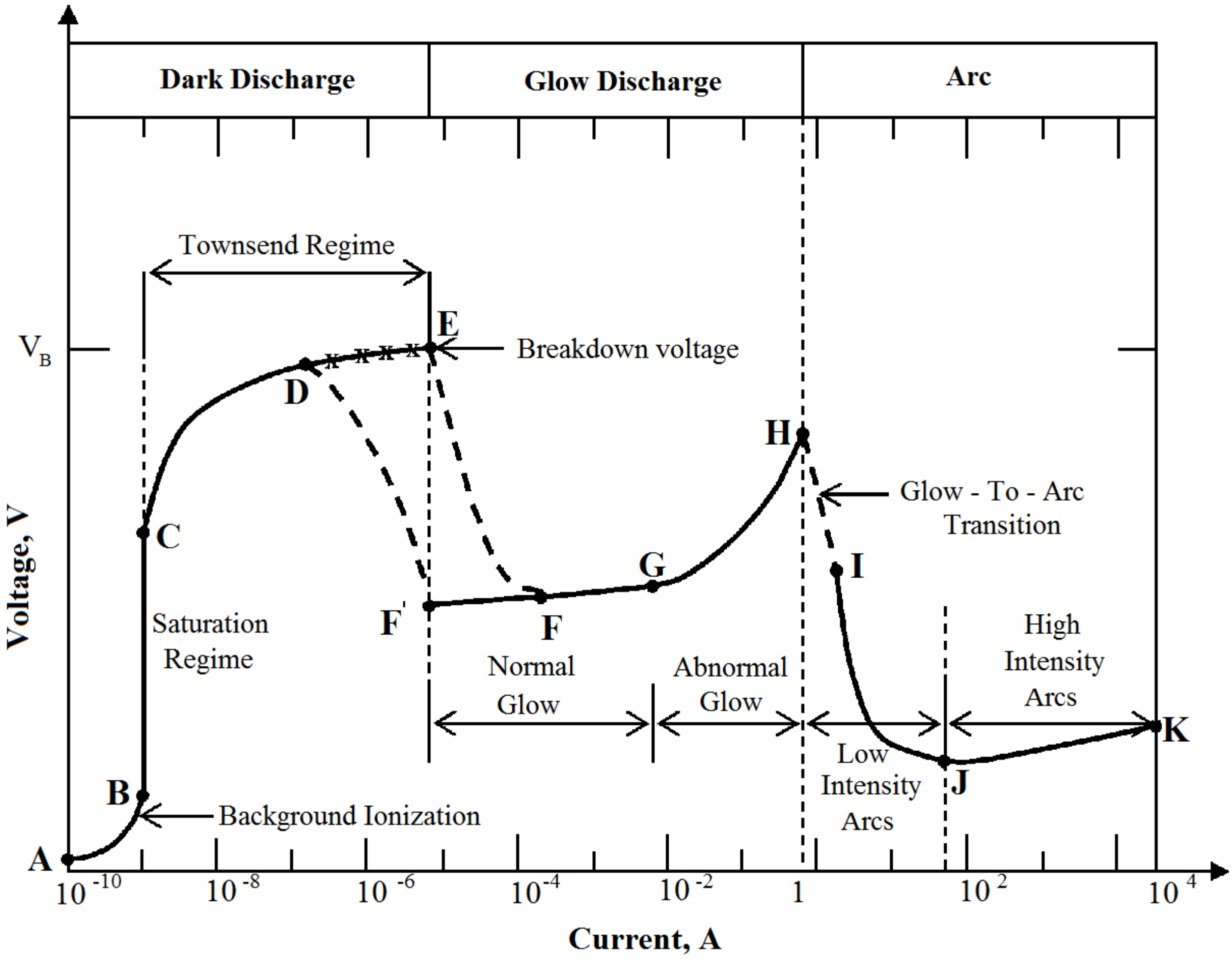

Fig. 4.2: *Current-voltage (i-V) characteristic of discharge between the electrodes [Roth01].*

A – C – Non-self-sustaining discharge

A – B is a region in which the current *i* in the circuit depends on the amount of charged particles flowing towards the electrodes and it increases with increasing voltage *V*.

B – C is a region in which, at a certain voltage, all the charged particles reach electrodes. The current *i* reaches saturation regime and become independent on *V*. The region ***A – C*** is called *non-self-sustaining*, its current-voltage characteristic is shown in Fig. 4.2. Since it corresponds to a steady state, it is static.

C – E – Townsend dark discharge

After the breakdown voltage V_B is reached, the discharge transfer into *self-sustaining* regime. The voltage V_B provides stable reproduction of electrons emitted from the cathode towards the anode. As long as the external electric field is independent on carrier densities the current-voltage (*i*-*V*) characteristic is constant $V = constant = V_B$, it corresponds to the area ***B* – *C*** on Fig. 4.2. There is virtually no light radiation due to the very small ionization rates. This regime is called *Townsend dark discharge*.

E – G – Normal glow discharge

When a certain value of the current *i* is reached, the voltage across the electrodes decreases what corresponds to the ***E* – *F*** section. After the voltage falls, the current *i* become almost constant. This region corresponds to the ***F* – *G*** section in Fig. 4.2. This regime is called *normal glow discharge*. It has a special feature: the discharge density at the cathode is still constant independently from discharge current. Only the current flow area is changing. The *glow discharge* is characterized by high cathode potential fall, which can be around hundreds of volts, and low currents $i \approx 10^{-5} – 10^{-2}\ A$.

G – H – Abnormal glow discharge

In case when no more free surface is left on the cathode, then current *i* is increased by an increase of voltage and the cathode current density is growing. This region is called *abnormal glow discharge* **- *G* – *H*** section of Fig.4.2. It is characterized by currents $i \approx 10^{-2} – 1\ A$.

H – I – Transition to arc

When the current *i* reaches values around *1 A*, the glow discharge conversed into the *arc regime*.

I – K – Arc

The *arc regime* is a self-sustaining discharge which is characterized by low cathode potential fall and high discharge current $i \approx 1 – 10^4\ A$. [Raizer01].

5 Arc Discharge

The *arc discharge* is known for almost 100 years, it is characterized by rather high currents $i \approx 1 - 10^4\ A$ and low voltages $V \approx 20 - 40\ V$. The small value of the potential fall is explained by the cathode emission mechanism, due to the high electron current from the cathode. This current is the result of emission processes such as a thermionic emission and field emission or their combination. In the case of *arc discharge*, electrodes because of the ohmic resistance transfer the high current to the surface into the heat, which leads to the strong heating of the electrodes material. This effect can occur locally or over the whole cathode area, usually for a short time. The electrodes sustain erosion and evaporation. The eroded material immediately fills up the discharge gap between the electrodes. The *arc discharge* is burning in the vapour of the vaporized material, its parameters strongly depend on working gas pressure, and characterized by high degree of ionisation due to the high burning current. The arc temperature reaches the value around $10^5\ K$.

There are several arc discharge ignition methods [Boxman95]. The easiest method is to bring two electrodes which are connected to the power supply into contact and separate from each other after some time. The electrodes due to the high resistance and high current at the contact point, owing to the ohmic resistance, become very hot and reach vaporization temperature in local points. This leads to the emission of neutral atoms and charged particles (electrons and ions) and at the separation moment arc ignites between the electrodes. The vaporized electrode material is much easier to be ionized (because of their high temperature) then the neutral gas molecules. After the arc ignition the working gas molecules afterwards replace vaporized molecules originated from the electrodes. The high temperature in the arc leads to the destruction of the working gas molecular bonds and participation of these atoms in the deposition processes.

The next method is to use an auxiliary electrode. This small electrode is brought into contact with the cathode. After applying the voltage to the stationary electrodes, this auxiliary electrode is separated from the cathode, which leads to the vaporization of the auxiliary electrode material and formation of arc discharge.

Another method is to connect two stationary electrodes using thin wire, after applying the voltage, due to the high ohmic resistance of thin wire it evaporates and this evaporated material ignites the *arc discharge*.

Additional method is to ionize the electrodes gap by some external ionization source (this can be done by *UV* – radiation, laser ionisation or another electron source).

Another possibility is to apply high voltage which should be enough for gas breakdown between stationary electrodes. In this case the arc discharge ignition occurs according to the current-voltage characteristic of discharge between the electrodes as shown in Fig.4 2. First it forms the *glow discharge*, which transforms into the *arc discharge* as cathode reachs sufficient temperature for the vaporisation.

The typical representative of the *arc discharge* is a carbon arc. The arc ignited between two carbon rods. This discharge gained its name due to the effect that the particle current bends upward due to the Archimedean force [Raizer01], see the Fig.5.1.

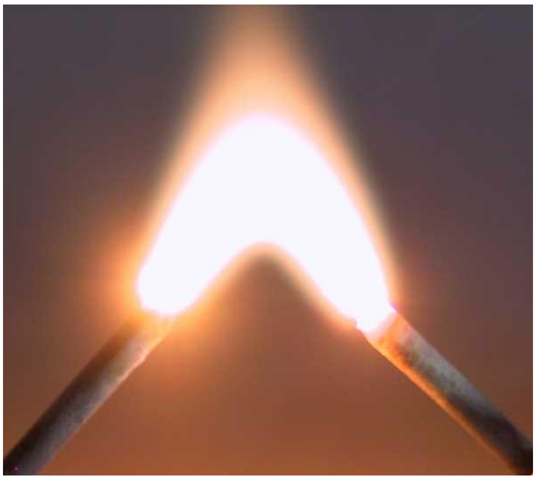

Fig. 5.1: *An electric arc demonstrating "arch" effect [Web12].*

The *arc discharge* can be divided into two types, depending on the source of the deposited material: *cathodic arc* (material is coming from the cathode) and the *anodic arc* (material is coming from the anode) correspondingly.

5.1 Cathodic Arc

There are different mechanisms and theories describing particle generation during the *cathodic arc* [Boxman95]. But the common is that the particles are originated from localized small surface areas (around few micrometers) so-called – *cathode spots*, see Fig. 5.2. At a certain period of time the current density at the surface area is high enough, which leads to the rapid rise of temperature in an extremely small volume and explosive evaporation of the electrode material due to the high pressure of the overheated electrode material. This process happens so quickly that not all the material has time to evaporate, what leads to the macroparticle (microclusters) or droplets (molten electrode material) formation see Fig. 5.2, 5.3.

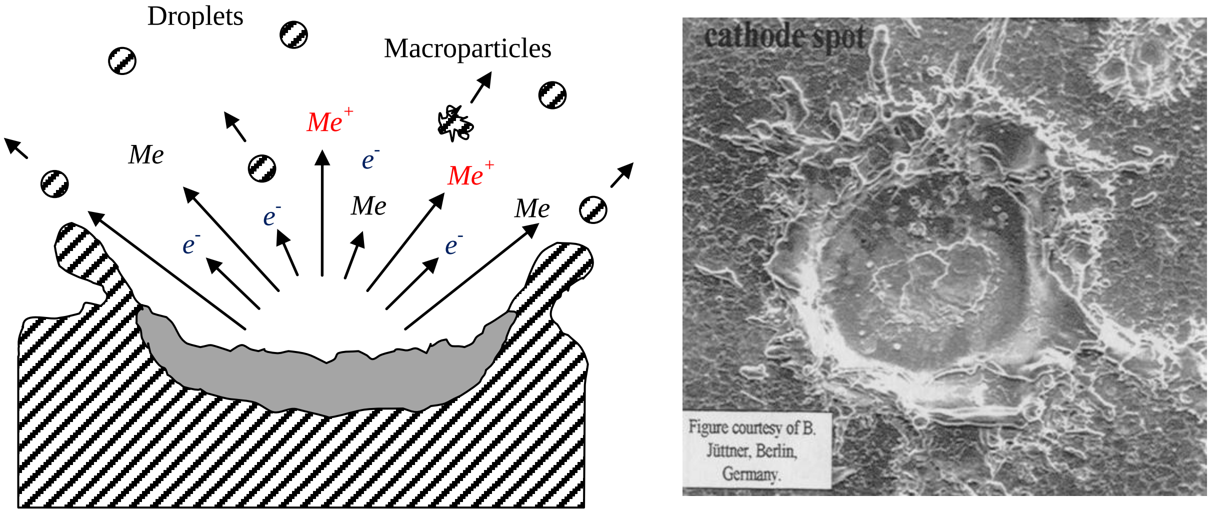

Fig. 5.2: *a) – Evaporation process from the cathode surface, where Me and Me^+ are atoms and ions correspondingly, b) – [Jüttner01].*

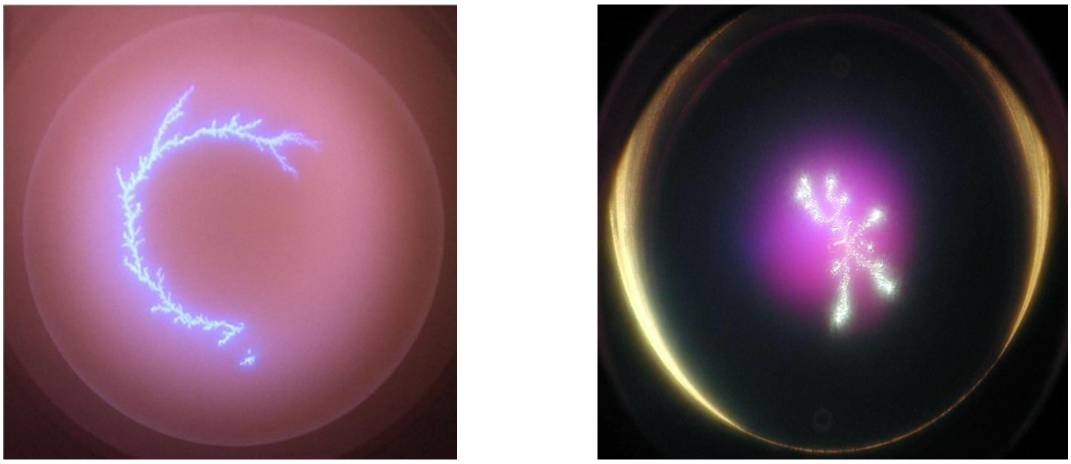

Fig. 5.3: *Cathode spot evolution.*

The arc discharge between the electrodes can be divided into three regions: cathodic, interelectrode and anodic region, see Fig. 5.3.

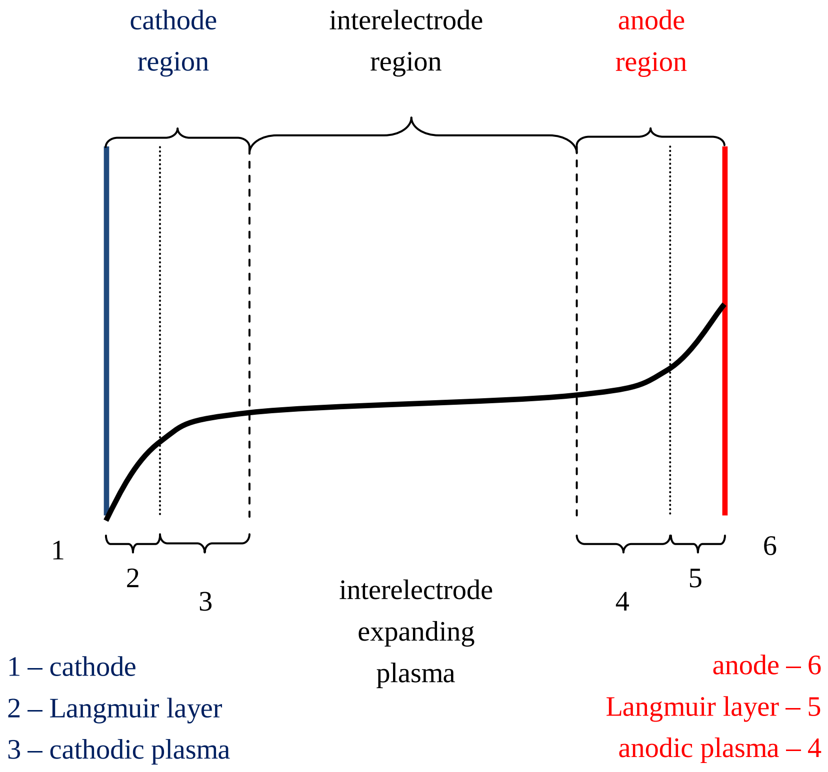

Fig. 5.3: *Potential distribution between the electrodes in discharge area.*

The potential distribution between the cathode and anode can be divided into smaller regions. The *cathode sheath* is a small layer (10^{-4} – 10^{-3} *mm*) in front of the cathode surface is about *10* to *20 V*, where ions are accelerated towards cathode. Then potential distribution in cathode region goes up and reaches the maximum [Plyutto65]. In the cathode boundary layer which is about 1 to several mm, the widening of the arc happens which leads to the decrease of current density. Then potential distribution stays almost constant in the whole interelectrode region – *arc column*. In anodic region the plasma potential is higher than in the interelectrode region, anode boundary layer is about *1* to *2 mm*. The *anode fall* region is also called Langmuir layer, is responsible for the reduction of the charge carrier current toward the anode surface. As a result the current to the anode become equal to the applied one. As mentioned above the cathode emits not only ions, electrons and neutrals but also molten electrode material and microclusters. The electrons, accelerated in Langmuir layer, and through the impact ionisation producing the charge carriers and thereby cathodic plasma. The obtained ions passing through the Langmuir layer and with the high speed striking the cathode surface thereby causing electrode material evaporation. The

cathodic plasma expands into interelectrode region toward anode. The interelectrode plasma is weakly active plasma which is supported only by the expanding electrode plasmas. Electrons are losing their energy due to elastic and inelastic collisions with the atoms and ions in near electrode plasma regions. These regions are also called energy-loss regions. Near the electrodes a particle densities and temperatures are reaching their maximum. Due to the high excitation and recombination rates these areas are visible as a plasma spots. The dimensions of those plasma spot are much bigger than the mean free path for excitation and ionisation. Expanding plasma ions reach the energy which may lie above the ion sound speed $c_s = (T_e/M)^{1/2}$ [Hasse92].
The cathodic arc, due to the high concentration of highly energetic ions inside the expanding cathodic plasma, is used as a coating source [Boxman95].

The films, obtained by such deposition method contain some inclusions in form of macroparticles and small droplets, originated from the cathode spot [Anders99], Fig. 5.4.

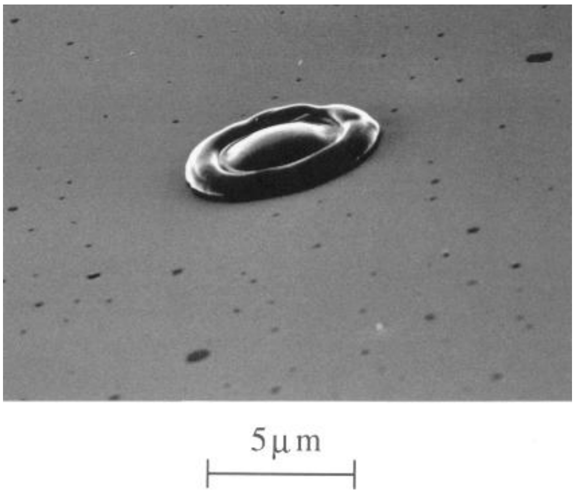

Fig. 5.4: *Tungsten droplet on a silicon substrate [Anders99].*

This is a big drawback of cathodic arcs where only materials with a high melting temperature can be used [Eckhardt75], Fig. 5.6.

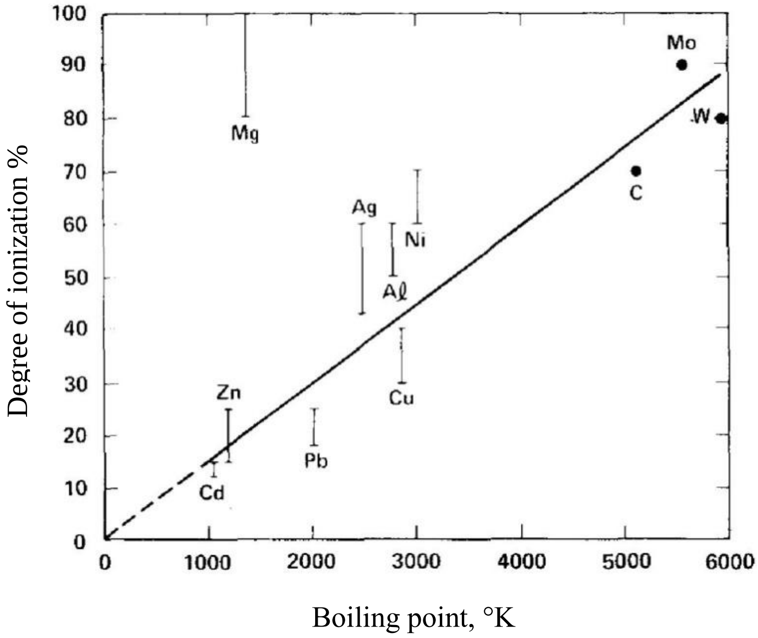

Fig. 5.6: *Degree of ionisation as a function of boiling point [Eckhardt75]*

The materials with low melting temperaturehave low degree of ionisation and in the cathodic arc produce too many macroparticles and microdroplets, which reduce their application areas.

5.2 Macroparticle Filtering

The presence of macroscopic inclusions in the films deposited by cathodic arc has significantly reduced the range of application of such deposition technique.

In order to reduce the negative influence of the macroparticles on to thin films properties some types of filters were used [Aksenov78, Anders99, Karpov97].

The common feature for all of them is the mechanical separation of macroparticles and droplets from the arc plasma.

One solution is to turn the substrate at 90° to the expanding plasma, so the macroparticles will be simply flying along the substrate. But the probability to reach the substrate surface still very high. The growing film becomes inhomogeneous due to film thickness gradient.

The next solution is to place the grounded protective shield in front of the substrate. The shield must be larger than the substrate. But the biggest drawback is that such shield protects the substrate surface from all kind of particles, even the charged one. A large amount of ions needed for the film deposition are lost on the shield surface. Nevertheless the macropaticles due to their high speed can rebound from the chamber walls and finally reach the substrate, see Fig. 5.7.

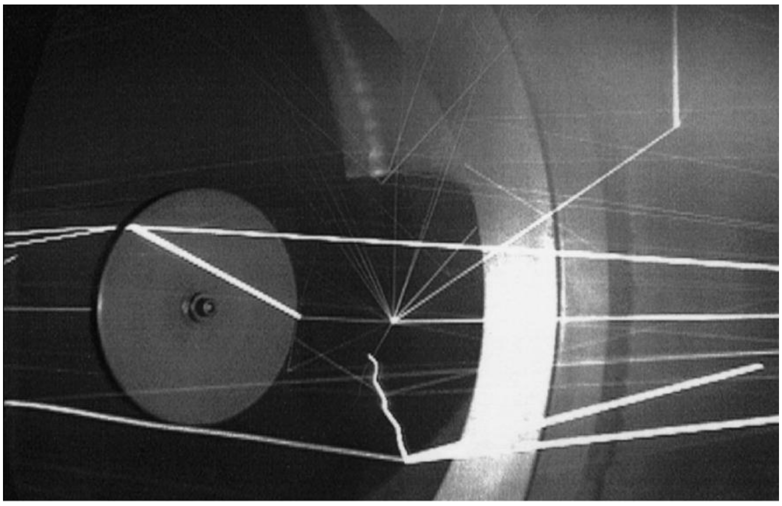

Fig. 5.7: *Picture showing the macroparticles reflection from the vacuum chamber parts*.

Another solution is to bias the substrate then the ions can be collected by the substrate behind the shield. Next modification of such protection is to place the magnet behind the shield – “magnetic island” to guide the charged particles or to have an electro-magnetic coil [Boxman95].

The most widely used way to separate the arc plasma from the macroparticles is to use curved electro-magnetic filters [Aksenov78]. The plasma deflected by electromagnetic field and then the separation of the macroparticle trajectories from the plasma trajectory can be reached [Karpov97], see Fig. 5.9. In most cases the arc and the substrate are still in the same vacuum chamber.

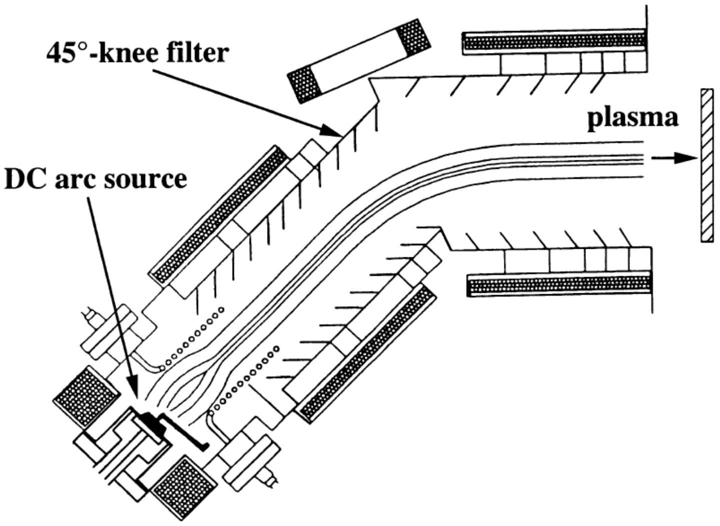

Fig. 5.9: *Schematic diagram of a 45°- knee filter.*

To improve this method the plasma source can be separated from the deposition chamber, and then guide the plasma toward the substrate (Fig. 5.10).

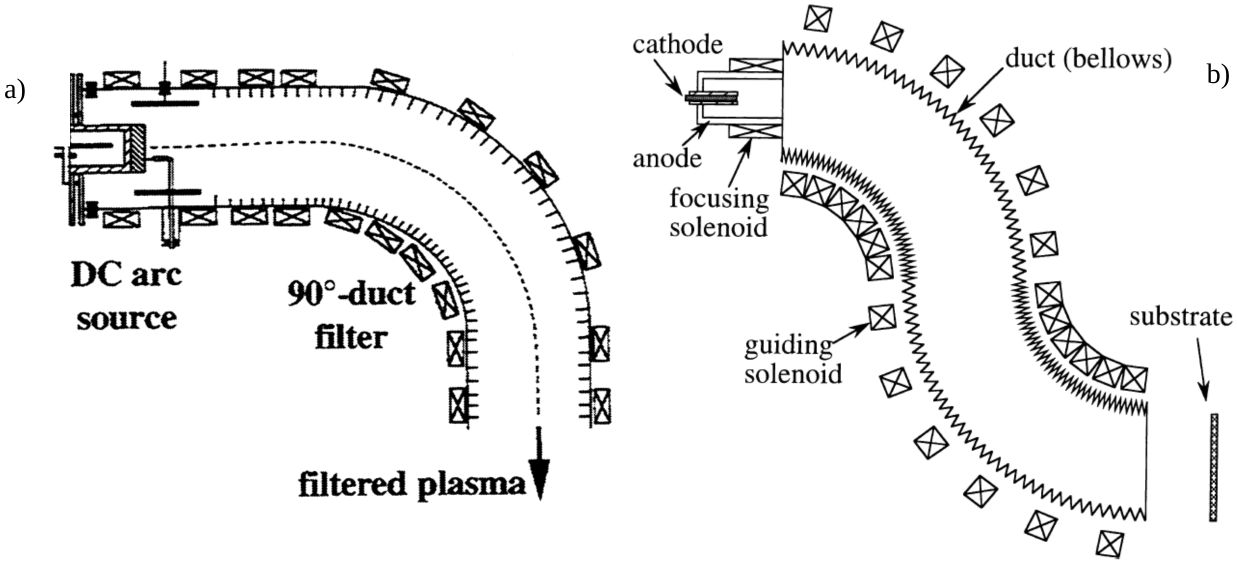

Fig. 5.10: *Schematic diagram of a filters: a) – 90°- duct filter, b) – "S"-shaper filter [Aksenov93].*

The main drawback of all filtering system is a significant reduction of deposition rate. But there is another vacuum arc source which has adwantages of the cathodic arc but no drawbacks.

5.3 Anodic Arc

With an active anode, which occurs only in special vacuum arc discharges, the anodic plasma can be produced due to the ionisation of the evaporated electrode material.

The anodic arc is different from well-known cathodic arc mainly because the evaporated material is originated from the anode. The anodic arc phenomenon was found and investigated by [Ehrich88]. And the main advantage of anodic arc plasma in comparison with the cathodic arc is that the anodic arc produces no macroparticles or droplets [Ehrich90]. Therefore an anodic arc can be more successfully used especially in thin films technology applications instead of the cathodic arc deposition technique.

5.4 Transition from Cathodic To Anodic Arc

The cathodic and anodic vacuum arcs are well-explored deposition techniques [Boxman95, Buck91]. But the transition from anodic to cathodic arc is still not studied yet. The main aim of the present work is to fulfil this gap and to have a more detailed description of this transition using most suitable plasma source for this purpose. This plasma source has the possibility to vary the anode and cathode diameter ratio $\varnothing_A/\varnothing_C$ and thereby realize the transition between “cathodic” and “anodic” vacuum arc modes.

6 Diagnostics

In order to know the influence of plasma parameters on the film parameters first the plasma properties should be investigated.

6.1 Plasma Diagnostics

Plasma diagnostic is the main method to know plasma properties like chemical composition and particle energy. For the chemical composition a mass-spectrometry is used. To measure the particle energy an energy analyzer is used.

6.2 Retarding Field Energy Analyzer (RFEA)

The key role in every plasma deposition process is played by ions. To know and to control the deposition parameters it is necessary to monitor the ion energy during the deposition process.

Energy resolved ion current measurements were performed by retarding field plasma analysis [Stephanakis68, Musa94]. The schematic diagram of the analyzer is shown in Fig. 6.1.

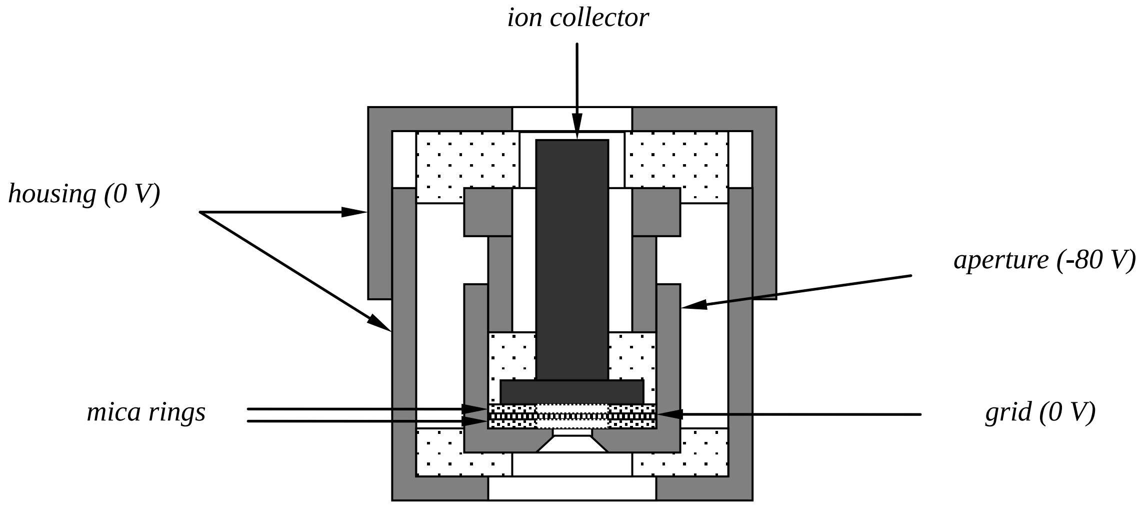

Fig. 6.1: *Schematic diagram of retarding field energy analyzer.*

The energy analyzer consists of the entrance aperture, screening grid with small spacing and a ion collector. The housing and ion collector were made of stainless steel. The grid was kept under *0 V* potential. To avoid additional distortion of ion current measurements by the plasma, the housing was additionally grounded. The grid has a mesh size of $20\ \mu m \times 20\ \mu m$ (such size was chosen in order to be smaller than the Debye length of the metal vapor plasma [Musa97, Schuhmann00]), see Fig. 6.2.

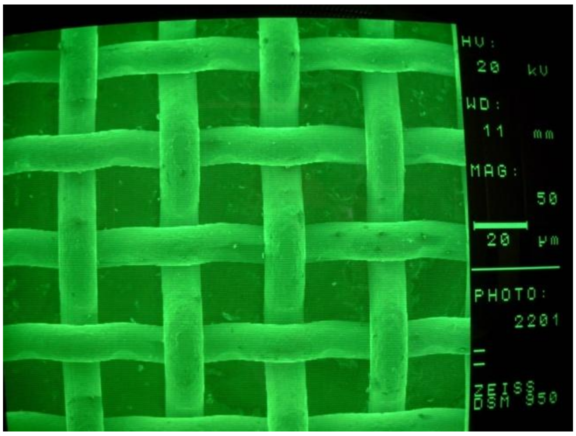

Fig. 6.2: *The SEM picture of the grid used in energy analyser.*

The grid is used to protect the ion collector from the plasma. It was shielded by an aperture of *4 mm* in diameter, which was additionally set under *- 80 V* potential to accelerate ions and deflect electrons from the plasma, see [Ingram88, Musa97, Surdu-Bob07], (see Fig.6.3). The energy analyzer was mounted at the substrate position, which allows monitoring of the deposition process near the substrate.

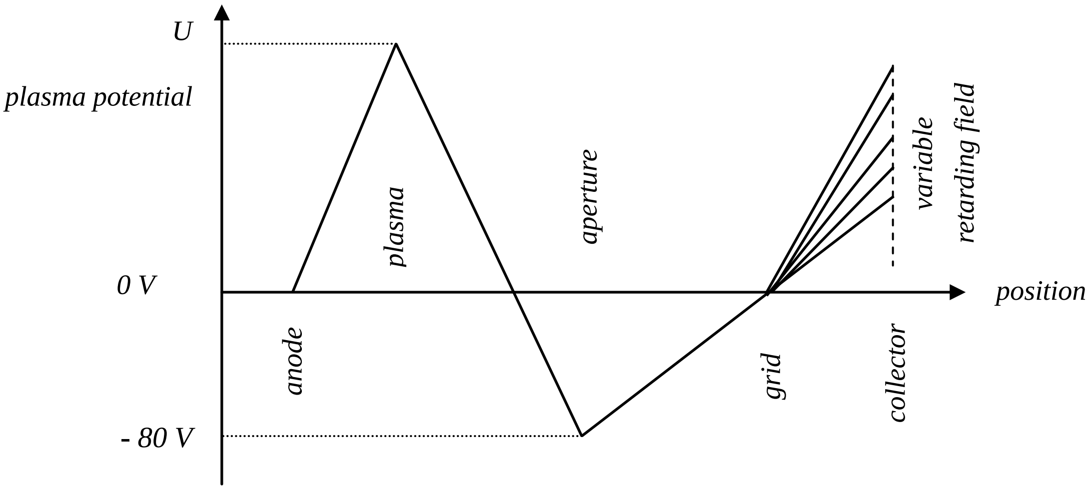

Fig. 6.3: *Potential distribution during ion energy measurements.*

In a work of [Jaeger98] was shown that the particle flux from the plasma to the analyzer is identical to the particle flux to the grounded substrate during deposition. Ions which pass the grid are repelled by positive collector bias. Only ions with sufficient kinetic energy are neutralized at the collector surface. Thus, the collector current decreases monotonically with increasing collector bias. The dependence of the collector current on applied potential barrier $E_{\mathrm{min}} = eU_{\mathrm{coll}}$ is given by Eq. 6.1 [Jaeger98]:

$$I_{coll}(E_{min}) - I_{SE} = Ae\int_{E_{min}}^{\infty} n(E)v(E)dE, \tag{6.1}$$

where A is the effective area with respect to the transmittance of the grids and I_{SE} is the current caused by secondary electron emission, $n(E)$ is the ion energy distribution function (IEDF) and $v(E)$ the velocity of the ions. Using Eq. 6.1, IEDF can be written as:

$$n(E) = -\frac{1}{Aev(E)}\frac{dI_{coll}}{dE} \ . \tag{6.2}$$

This method is well suited for energy-resolved measurements of positive ions.

6.2 Film Diagnostics

The film diagnostics begins with the film weight, thickness measurements. Then the film morphology is analyzed by Scanning Electron Microscopy (*SEM*) and Atomic Force Microscopy (*AFM*). To know the chemical composition Energy-dispersive X-ray Spectroscopy (*EDX*) and Nuclear Reaction Analysis (*NRA*) were used.

6.2.1 NRA (Nuclear Reaction Analysis)

NRA is well-known analytical method for material characterization [Lanford95]. NRA is a non-destructive nuclear method to measure the chemical composition and concentration of specified chemical elements, which is widely used in solid state physics. In this method the incident nuclei, accelerated to certain energies from *100 keV* to *10 MeV*, interact with the sample material and initiate a nuclear reaction with elements in the investigated sample. The product of such nuclear reaction is an excited nucleus with very short decay period. During the decay this nucleus emits ionizing radiation (α and γ - particle). The resulting radiation is characteristic for the analysed element. The intensity of the emitted radiation is proportional to the concentration of this certain chemical element. NRA is usually used for surface analysis. The depth resolution of NRA is energy bound; it is growing with the incident nuclei energy and decreasing with atomic number. At some special conditions depth resolution can be around micromeres. By the variation of incident nuclei energy it is possible to obtain information about depth profile for specified chemical element in the investigated sample.

NRA is widely used for the concentration measurements of the elements with low nuclear masses (hydrogen, carbon, nitrogen, oxygen...).

The most important NRA application is hydrogen concentration quantification. This method has sensitivity around 100 ppm and depth resolution around 10 nm.

The ^{15}N hydrogen profiling method uses such reaction $^{15}N + {}^{1}H \rightarrow {}^{12}C + {}^{4}He + \gamma\,(4{,}43\ MeV)$ to measure the hydrogen concentration. This reaction is schematically shown in Fig. 6.4.

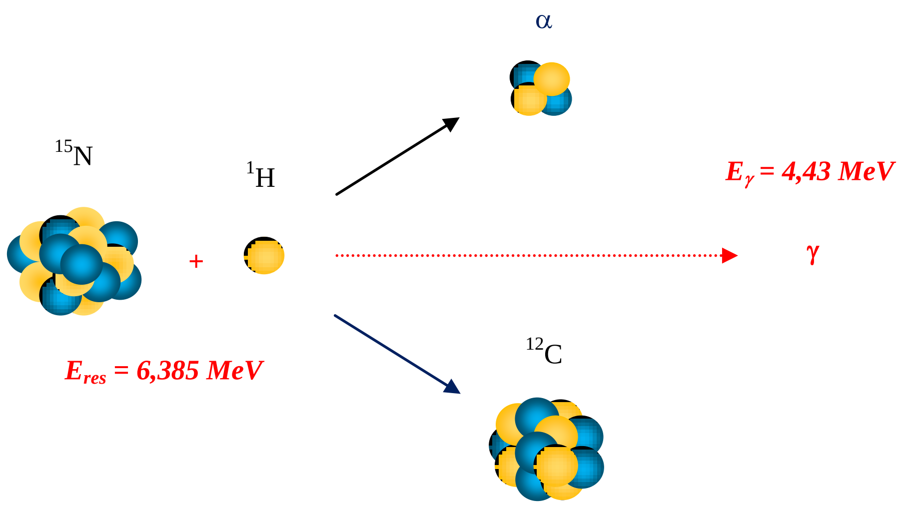

Fig. 6.4: *Schematic diagram showing principle of hydrogen detection in the films by nuclear reaction.*

6.2.2 Spectroscopic Diagnostic Methods

6.2.2.1 UV-VIS Spectroscopy

Diamond-like carbon coatings are amorphous films and usually spectroscopic methods are used to obtain more detailed information about their structure and chemical composition. These methods also have a big advantage: they are non-destructive, so coated samples which are analyzed by Ultraviolet-Visible Spectroscopy (*UV-VIS*) can be used for further tests. UV-VIS spectroscopy was used in order to investigate optical film properties *ex-situ*.

This spectroscopic method is very informative and at the same time fairly simple and accessible analysis of DLC coatings. For this analysis electromagnetic radiation in the range of ultraviolet and visible light is used to excite electrons in the valence band of DLC films. It is well-known that absorption frequency and absorption intensity of a C-H bond depends not on elementary or phase composition at large, but only on state of a carbon atom connected to hydrogen (hybridization type sp^3, sp^2 or sp^1).

UV-VIS spectroscopy allows obtaining information about the band gap of the deposited films and information about the refractive index. The optical spectra were recorded in a range from *200* to *2500 nm* using *UV-VIS-NIR Lambda-9* spectrometer by PerkinElmer Company. The spectrometer was operated in transmittance mode.

The obtained optical spectra were converted by commercial *SCOUT 2.3™* simulation program, where they were fitted using dielectric function, for interband transitions and for the band gap transitions. In this dielectric function two types of harmonic oscillators for interband transitions were used. For the band gap calculation the *OJL* (O'Leary, Johnson, Lim [O'Leary97]) interband transition model was used.

In order to know the chemical composition the Raman spectroscopy was used [Ferrari00].

6.2.3 Physical Structure

To know the physical structure of the deposited films X-Ray Diffraction (*XRD*) technique is used.

6.2.3.1 X-Ray Diffraction (XRD) and Williamson-Hall Method

The Bragg's law [Bragg13] determines the essential condition which must be fulfilled if diffraction is to occur:

$$n\lambda=2d\sin\theta \tag{6.3}$$

where n is the order of diffraction (is an integer), λ is the x-ray wavelength, d is the distance between the planes in the atomic lattice, and θ is the angle measured between the incident ray and the particular crystal planes under consideration (Bragg's angle). It also assumes that incident beam consist of perfectly parallel and monochromatic x-rays. This leads to the formation of a sharp diffraction maximum. But in a real situation, these flawless conditions are never fulfilled. Small crystallite size and crystal imperfection or defects (vacancies, dislocations, grain boundaries and voids) are commonly considered to be a reason for broadening of the peaks in the diffraction pattern.

Broadening of diffraction peaks arises mainly due to two factors: small crystallite size and lattice strain. These factors transform perfect peak (peak without width) into observed broadened peak (see Fig. 6.5).

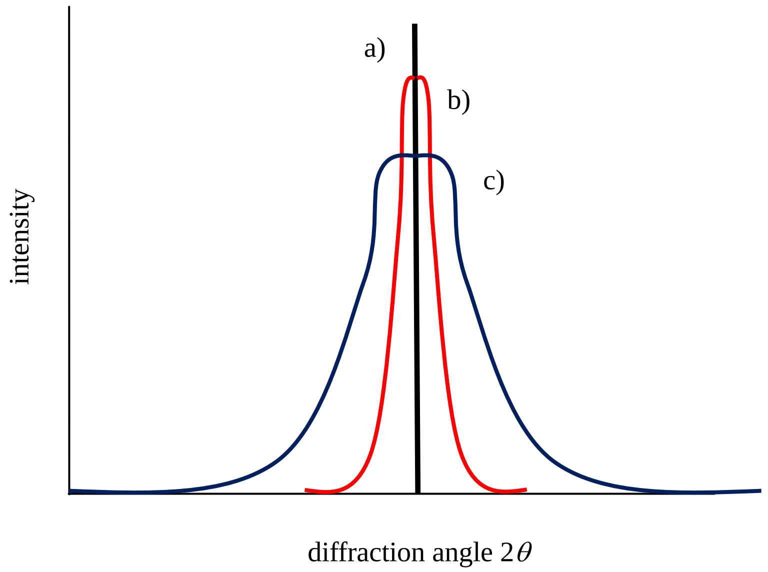

Fig. 6.5: *Broadening of x-ray diffraction peaks: a) perfect peak, b) peak broadening due to small crystallite size, c) peak broadening caused by lattice strain effects. For details see [Suryanarayana98].*

However, there is a method to separate these factors. Scherrer [Scherrer18] has derived an equation for broadening of x-ray diffraction peaks due to small crystallite size:

$$B_{crystallite} = \frac{k \times \lambda}{G \times cos\theta} \ , \tag{6.4}$$

where λ is the wavelength of x-rays used (λ = *0,15406* nm), θ is the Bragg angle, G is the “average” crystallite size, k is a constant (in our case k = *0,94)*.

The lattice strain in the films deposited also causes broadening of the diffraction peaks, which can be described by [Cowley75]:

$$B_{strain} = \varepsilon \times tan\theta, \tag{6.5}$$

where $\varepsilon = \Delta d/d$ is the strain in the material.

Using equations *(6.4)* and *(6.5)*, one can see that peak broadening increases rapidly with increasing θ, but separation between these two factors is clearer at smaller θ values (see Fig. 6.6). The width B_{Γ}, the Full Width at Half Maximum (FWHM) of diffraction peak, could be considered as the sum of widths due to small crystallite sizes and lattice strains:

$$B_{\Gamma} = B_{crystallite} + B_{strain} \tag{6.6}$$

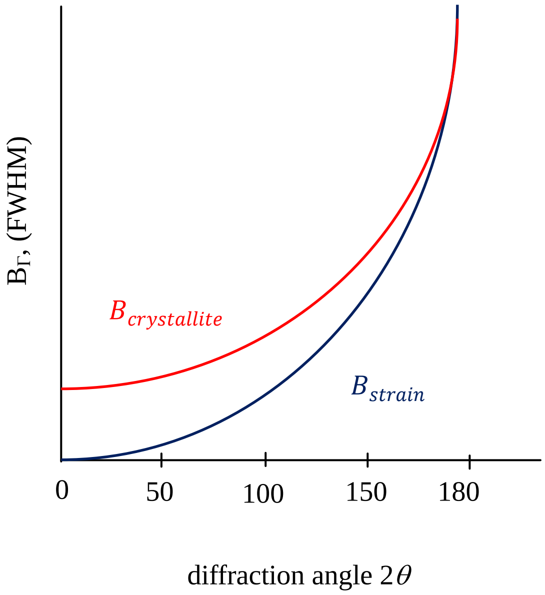

Fig. 6.6: *Dependence of FWHM caused by small crystallite size and lattice strain on the diffraction angle [Suryanarayana98].*

From equations *(6.4)*, *(6.5)* and *(6.6)* we get:

$$B_\Gamma = \frac{k\times\lambda}{G\times cos\theta} + \varepsilon\times tan\theta. \qquad (6.7)$$

Multiplying Eq. *(6.7)* by $cos\theta$, obtain:

$$B_\Gamma cos\theta = \frac{k\times\lambda}{G} + \varepsilon\times sin\theta. \qquad (6.8)$$

If we plot now $B_\Gamma cos\theta$ against $sin\theta$ we obtain a straight line with slope ε and intercept $k\cdot\lambda/G$. This method is called Williamson-Hall Plot [Williamson53]. The smaller the value of ε, the flatter the straight line, the smaller is the amount of strain in the sample.

The crystallite size *G* can be calculated from the intercept by using already known values of *k* and λ. Fig. 6.7 shows the XRD spectrum for a magnesium coating. Fig. 6.8 shows the evaluation of XRD profiles obtained.

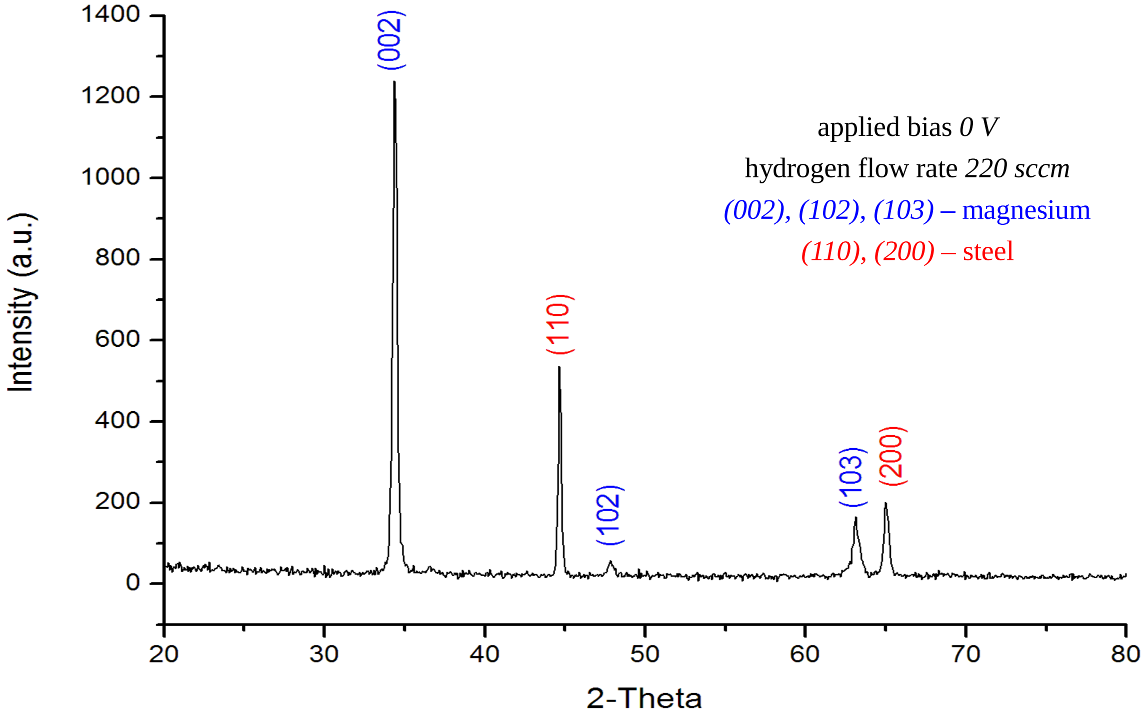

Fig. 6.7: *XRD pattern of Magnesium coated steel specimen, with peaks evaluation.*

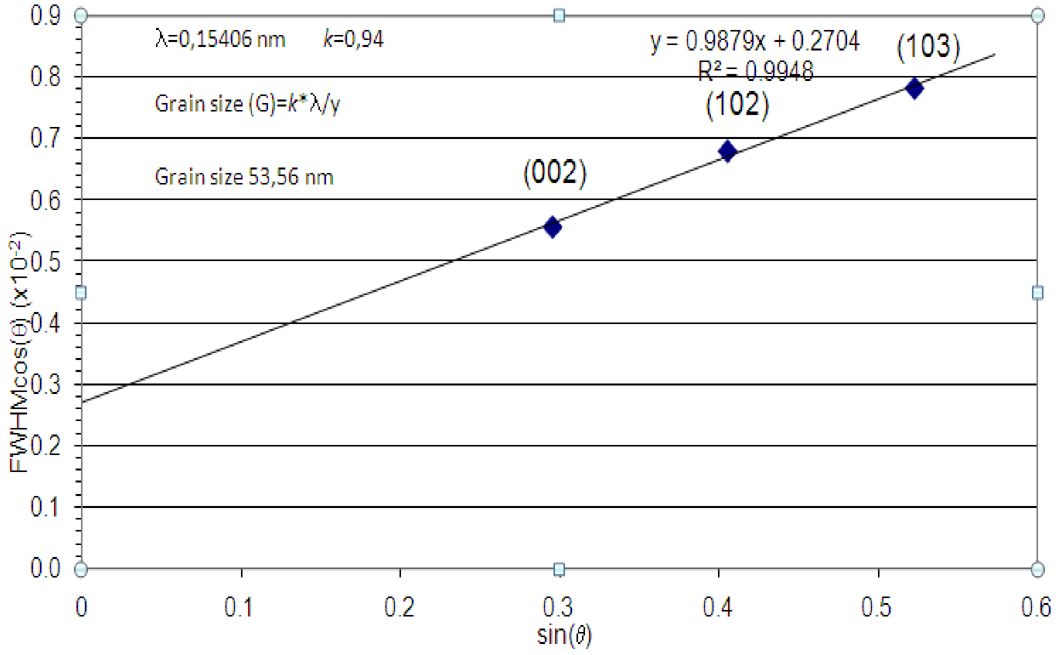

Fig. 6.8: *XRD pattern grain size evaluation.*

6.2.4 Mechanical Properties

The mechanical properties of DLC films mainly determined by the residual stress in the growing films.

6.2.4.1 Residual Stress

One of the most significant parameters for growing films is the residual stress. It determines the thin film properties and therefore their application areas. In the most cases, two factors are responsible for stress formation:

- substrate material properties;
- deposition parameters.

It is common in thin film technology that the substrate is pre-specified by a customer or by the application area. The task is then to adjust the deposition parameters for optimal results.

For instance, the substrate can have different crystal lattice orientation or different thermal expansion coefficient, which leads to stress formation in the substrate-film boundary. The plasma deposition parameters can also cause stress due to the different particle energies or high deposition temperatures. As one can see there are a lot of effects influencing the film properties which have to be taken into account.

The pioneering work in the film stress investigation was done by Stoney [Stoney09] when he observed growth processes of metallic films and found their delamination after they reached certain thickness. He also found the possibility to determine the residual film stress. This method is based on the fact that growing films can bend thin substrates because of residual stress, and by substrate curvature evaluation the stress values can be calculated.

The residual stress σ in thin films consists of the following components:

$$\sigma = \sigma_{th} + \sigma_{lat} + \sigma_{int}, \tag{6.9}$$

where σ_{th} is component caused by the thermal stress, σ_{lat} is the lattice mismatch component caused by the mismatch between the growing film and the substrate lattice and σ_{int} is the component arising from the intrinsic stress [Woehrl06]. The thermal stress σ_{th} can be described as:

$$\sigma_{th} = E_C(\alpha_C - \alpha_S)(T_C - T_M), \tag{6.10}$$

where E_C is the elastic modulus of the coating, α_C and α_S are the thermal expansion coefficients for the coating and for the substrate, T_C is the temperature during the coating process and T_M is the one during the stress measurement [Windischmann91].

The thin film's intrinsic stress in turn has two different components responsible for two different stress types, there are two models describing these components:

- grain boundaries mismatch model: describes the "tensile stress" [Hoffman76];
- ion-peening model: describes the "compressive stress" [Windischmann92].

Tensile stress

At the early stages of thin film deposition, films are forming insulated islands on the substrate, with different voids between them. Then the growing islands overlap or touch each other and form a closed film. During the island growth the voids become smaller and smaller. But the probability that these voids have the same diameter as a condensed atom is very small. Most likely is that these voids have a bigger diameter. The presence of the void between the islands is energetically more unfavourable then the closed film. Therefore atoms attract each other and cover the void and a close film. These attractive forces lead to the tensile stress origination in the deposited thin film, as shown in Fig. 6.9.

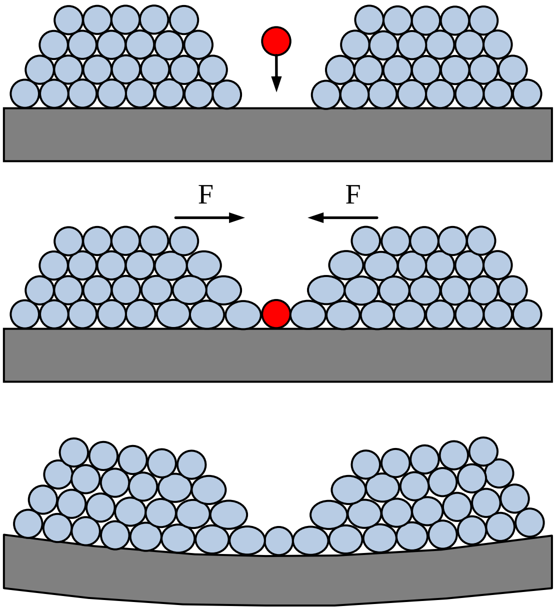

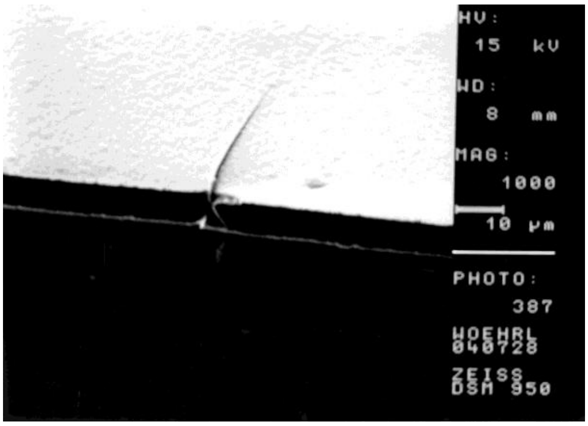

Fig. 6.9: *Tensile stress formation in the thin film*. **Fig. 6.10:** *Tensile stress in a thin film [Woehrl06].*

Fig. 6.10 shows the SEM picture of the UltraNanoCrystalline Diamond (*UNCD*) thin film grown under high tensile stress, what leads to substrate damage.

Compressive stress

The source for the compressive stress is an interaction between the energetic atom and the growing film. The charged particle with a certain energy level arrives at the growing film surface and due to high energy can not only condense onto the film surface, but also penetrate it. As it was mentioned above, during the film growth, the voids between the island become smaller and smaller and sometimes the void size is smaller than the diameter of a condensed atom. But the atom has enough kinetic energy to squeeze between the two neighbouring islands. The excess of energy leads to the transformation of the kinetic energy of the incoming atoms into motion energy of surrounding atoms and film densification, see Fig. 6.11, as a result the particles in such films are packed more tightly. The compressive stress therefore is proportional to the particle energy. This parameter is crucial for the residual stress determination.

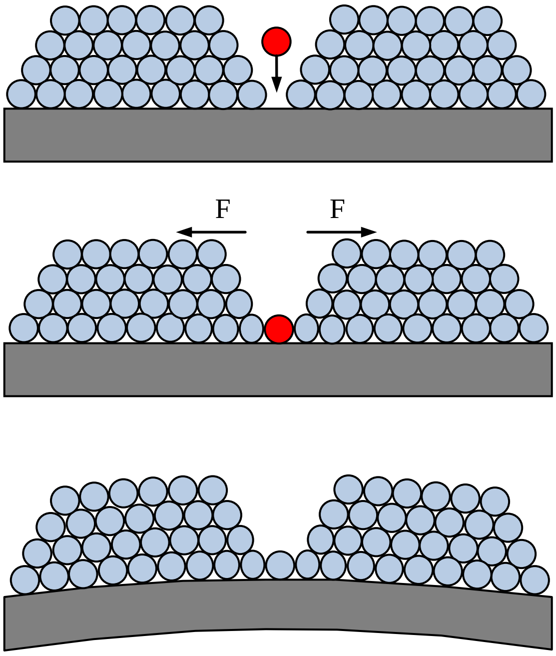

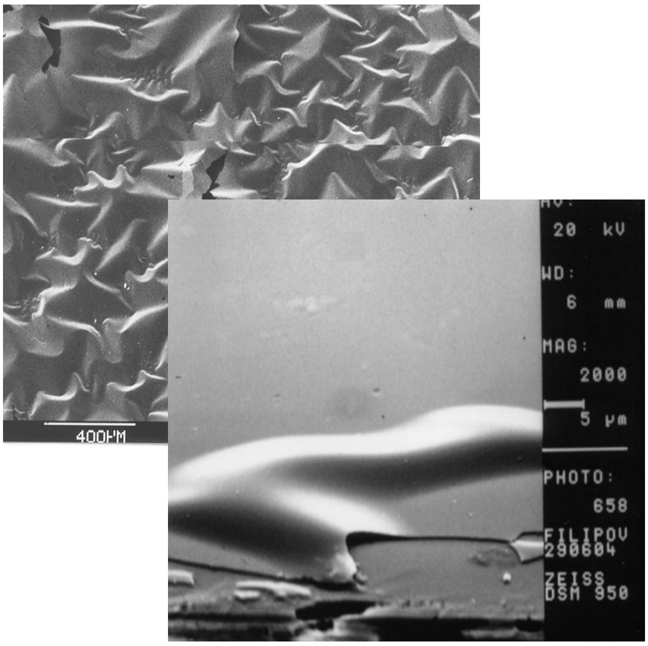

Fig. 6.11: *Compressive stress formation in a thin film.* **Fig. 6.12:** *Compressive stress in a thin film.*

Fig.6.12 shows the SEM picture of the DLC thin film grown under the high compressive stress, which leads to the film delamination.

In [Windischmann92] the statement about the dependence between microstructure and intrinsic stress in growing thin films was made. In Fig. 6.13 three areas can be seen:

- Low particle energy area, where porous coatings are growing. The coatings in this area are grown under “tensile stress”.
- Mean energy area, where the transition between “tensile stress” and “compressive stress” take place. The coatings in this area are almost dense and without pores.
- High energy area, where dense coatings are growing. In this area the “compressive stress” prevails.

According to this theory the same material, with the same chemical composition, can have different properties depending on the deposition parameters (particle energy, working pressure). The microstructure determines optical, mechanical and chemical properties of the thin films [Buck00]. Therefore the plasma deposition techniques are promising methods where by the variation of the deposition parameters new desirable material properties can be obtained. This can be done by the variation of the particle fluxes toward the substrate surface.

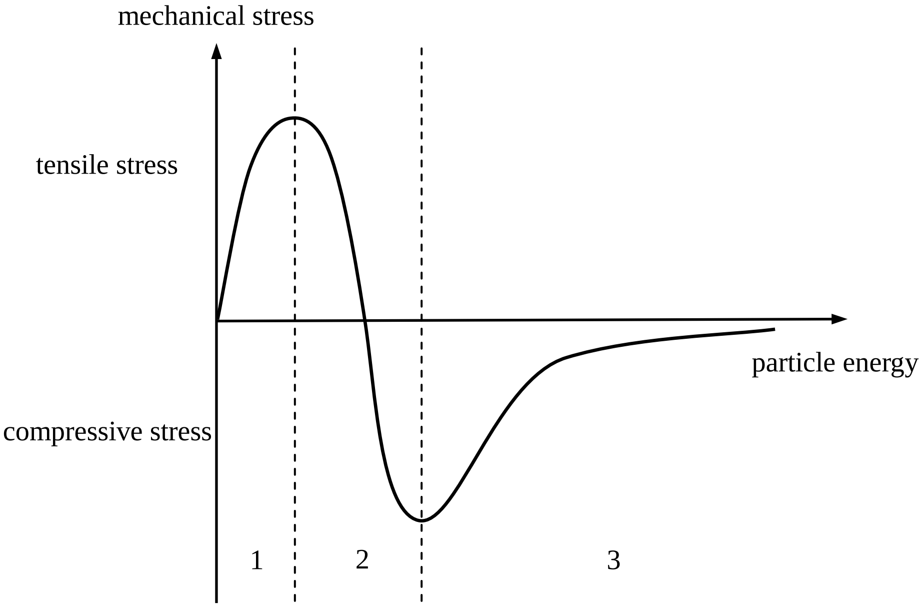

Fig. 6.13 : *Correlation between residual stress and ion energy according to the grain boundaries mismatch model (1) and ion-peening model (2), where (3) is a relaxation area.*

In a case of low-energy ions the grain boundaries mismatch model gives description for the residual stress in the thin films. With increase of energy the ion-peening model describes the stress behaviour [Woehrl10]. After the ion energy exceeds a certain value the residual stress is reduced to the smaller values due to the annealing processes. Compressive stress is the opposite of tensile stress and as agreed the compressive stress is negative and tensile stress is positive.

6.2.4.2 SSIOD (Surface Stress Induced Optical Deflection)

There are many stress measurement methods such as optical: shift of the Raman peaks, Tolansky interferometry; or mechanical: stylus profilometry; or even method based on X-ray diffraction lines broadening. But these methods have a lot of limitations and special conditions which should be fulfilled, and they are not able to give information about the total film stress. In comparison to these methods the Surface Stress Induced Optical Deflection (*SSIOD*) method can be easily used with different substrates, *in-situ* or *ex-situ,* transparent or opaque films.

This method is based on the fact that the residual stress in the growing films bends the substrate and this substrate curvature can be measured by position sensing diode.

SSIOD method is based on the Stoney approach [Stoney09]:

$$\sigma = \frac{E_{sub}}{(1-\nu)} \frac{t_{sub}^2}{6 \cdot t_{film}} \left(\frac{1}{R_a} - \frac{1}{R_b} \right), \qquad (6.11)$$

where E_{sub} is the substrate elastic modulus, ν is the substrate Poisson ratio, t_{sub} is substrate thickness, t_{film} is the deposited film thickness and ΔR is the difference in the substrate curvature (measured before the deposition R_b and after R_a). The only information which is necessary to know is the film thickness.

In order to determine film stress more precisely the SSIOD method should fulfil some conditions such as: substrate thickness should be smaller than the curvature radius, as well as substrate length at least two times bigger than the substrate width.

In Fig .6.14 one can see the schematic diagram of SSIOD method for curved and flat substrates and principle of mechanic stress determination. During the scan over the substrate laser beam is deflected at certain angle to the position sensing diode (defined by the substrate curvature). In Fig. 6.15 the schematic diagram of stress measurement system is shown.

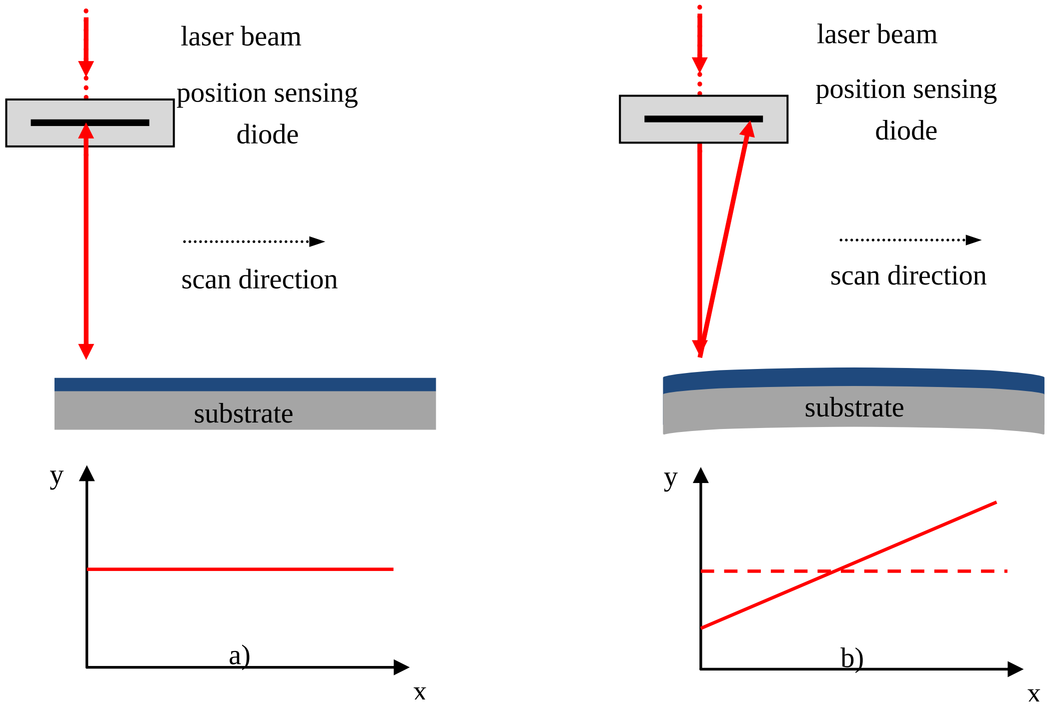

Fig. 6.14: *Schematic representation of SSIOD measurement method: a) flat substrate, b) curved substrate.*

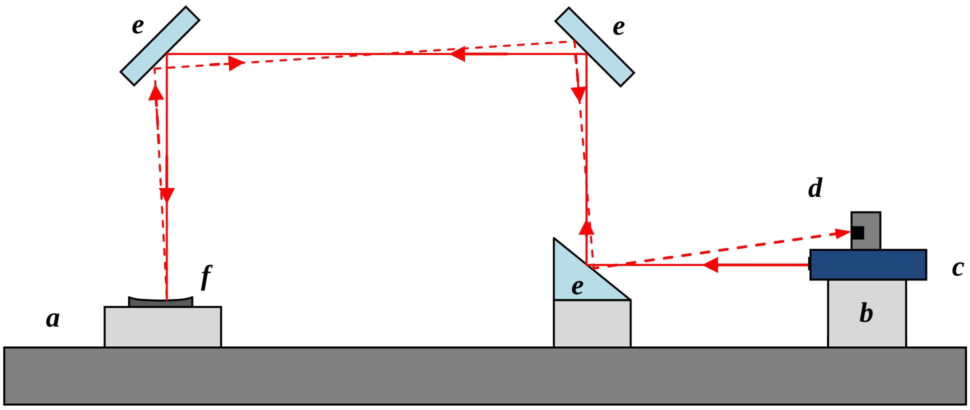

Fig. 6.15: *Stress measurement system schematic diagram:* ***a*** *– optical table,* ***b*** *– linear positioning table,* ***c*** *– laser,* ***d*** *– position sensing diode,* ***e*** *– mirrors,* ***f*** *– substrate [Woehrl06].*

7 Experimental Setup

7.1 Experimental Setup for DLC Film Deposition

A schematic diagram of the vacuum arc deposition apparatus is shown in Fig. 7.1.

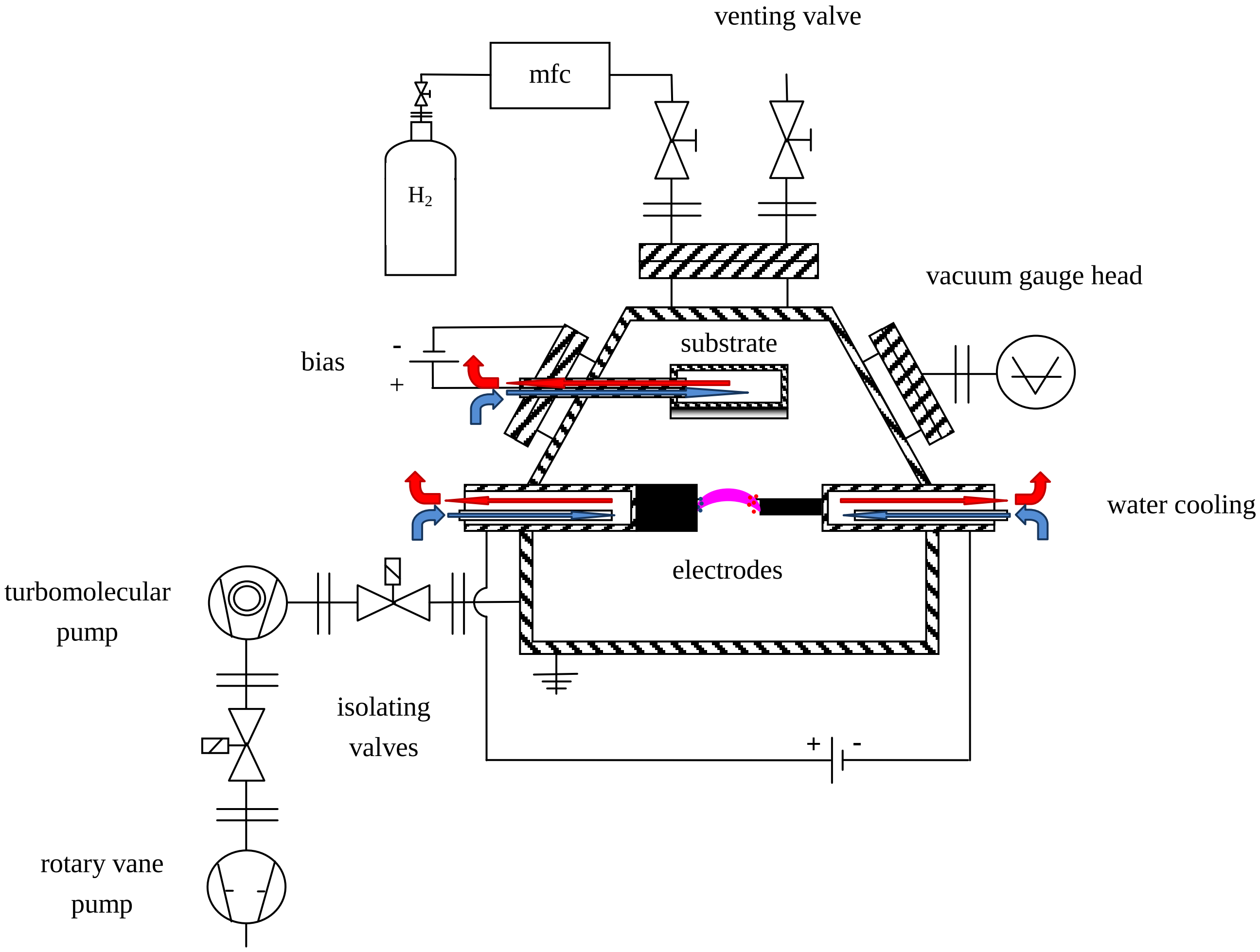

Fig. 7.1: *Vacuum chamber schematic diagram.*

Hydrogenated and non-hydrogenated DLC films were deposited in a high vacuum chamber in controlled atmosphere. The vacuum chamber is equipped with CF (ConFlat) flanges that allow reaching high vacuum. The working pressure was maintained by a two–stage vacuum system. To obtain fore–vacuum an *EDWARDS RV 8* dual stage rotary vane pump was used. In the rotary vane pump, *Fomblin® 06/6 PFPE* chemical inert vacuum oil was used. The *RV 8* rotary vane pump has an ultimate pressure of 2×10^{-3} *mbar*. In the second vacuum stage, a

TPU-240 turbomolecular high vacuum pump by *Pfeiffer Vacuum* was used. Using these two pumps, a residual gas pressure of 10^{-7} *mbar* was achieved.

Gas pressure was measured by *PKR 251* Pfeiffer Compact Full Range™ Pirani / cold cathode gauge (CCG). Due to the fact that most of the vacuum gauges can not accurately measure the pressure in a hydrogen atmosphere an *MKS Baratron Type 615A* high accuracy absolute capacitance manometer was used.

Cylindrical spectral pure graphite rods *RINGSDORFF*® type *RW 003* were used as electrodes, the ratio of the anode to cathode diameter $\varnothing_A/\varnothing_C$ was varied from *1/3* to *3/1*. The electrodes were water–cooled. In order to maintain a vacuum arc, two TCR 3 Phase power supplies *LAMBDA EMI* with *4 kW* maximum output power were used.

Double–side polished *2 cm × 1 cm Si* $\langle 100 \rangle$ wafers and *BK 7* optical glass discs were used as substrate material. The substrates were immersed in acetone and treated in an ultrasonic bath for *15 min* and then dried in nitrogen atmosphere. Such procedure was performed in order to clean the substrates from possible organic contamination. The deposition conditions were monitored with *QMS-200 Prisma* by *Balzers*™ mass-spectrometer. The deposition parameters used are given in Table 7.1.

Table 7.1: *Deposition parameters.*

Working pressure at 0 sccm gas flow	$< 10^{-6}$ *mbar*
Working pressure at 100 sccm gas flow	9×10^{-3} *mbar*
Arc current	*80 A*
Arc voltage	*20 V*
Deposition time	*180 s*
$d_{source\text{-}substrate}$	*20 cm*
Graphite electrodes	*Type RW 003, quality RW*
$\varnothing_A/\varnothing_C$	*3/1, 2/1, 1/1, 1/2, 1/3*

The DLC films were obtained using a vacuum arc system adjustable from cathodic to anodic mode, where the carbon plasma is produced by the graphite electrodes. The arc is ignited by placing two graphite electrodes (with similar purity) connected to the power supply into contact and then separating them when the sufficient electrode temperature is achieved. Fig. 7.2 shows the measured voltage-current characteristic of the arc discharge.

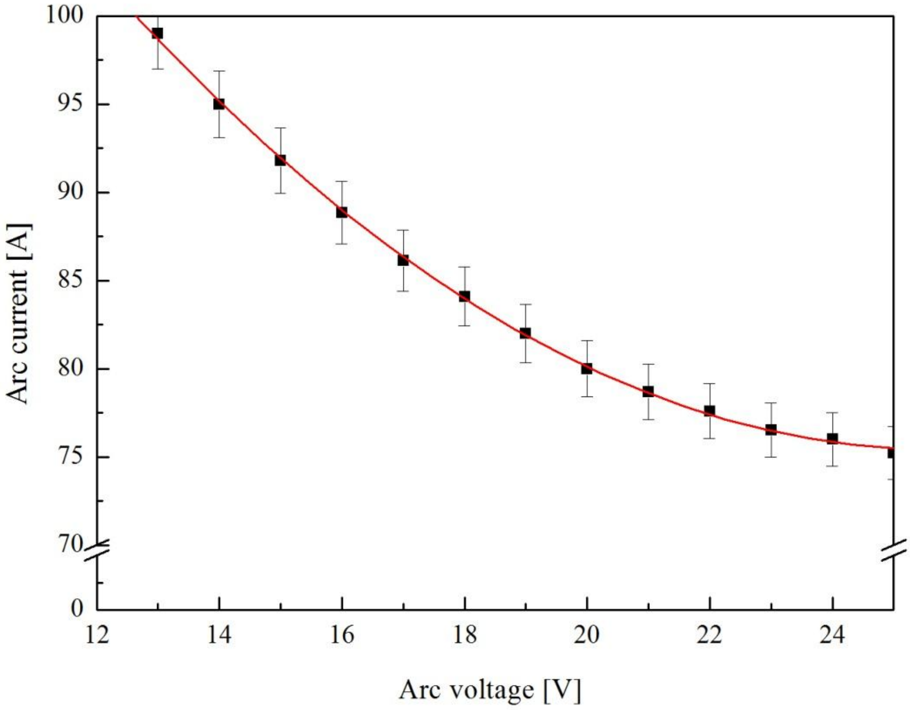

Fig. 7.2: *Measured voltage-current characteristic of the vacuum arc.*

The arc voltage and the arc current were set to $U_A = 80\ V$ and $I_A = 20\ A$. Such values correspond to the working distance of *5 mm* between two electrodes at which the arc burns in a stable regime. The stabilized power supply was set to fixed current so the arc current was kept constant during the deposition time. In order to keep the constant arc current the working distance between two electrodes was kept constant at *5 mm* during the deposition.

After the arc stabilize and to reaches the operating mode a shutter between the arc and the substrate was removed in order to start the carbon deposition. The substrates were placed upside down and fixed to the water–cooled copper block. This was made in order to reduce the plasma temperature influence onto the growing carbon films and to reduce the thermal stress in growing films [Woehrl10]. Another purpose for such substrate position is to avoid contamination of the growing film by dust particles and graphite macroclusters which are falling down due to gravity.

The carbon ions energies were varied by applying a (pulsed bipolar) bias dc voltage to the substrate holder. The substrate was connected to the *Magtron MAGPULS 1000/10/60-BP* power supply by *Magtron GmbH*. Therefore, the incident carbon ion energy is the sum of the plasma emitted ions energy and the applied bias voltage. The ion energy was measured near the substrate position using a retarding field energy analyzer. The substrate temperature was measured by a thermocouple attached to the backside of the substrate. The distance between substrate and electrodes was chosen to be *20 cm*, after the substrate temperature measurements during the plasma deposition. This distance corresponds to the optimum deposition rate and especially the substrate temperature, see Fig. 7.3.

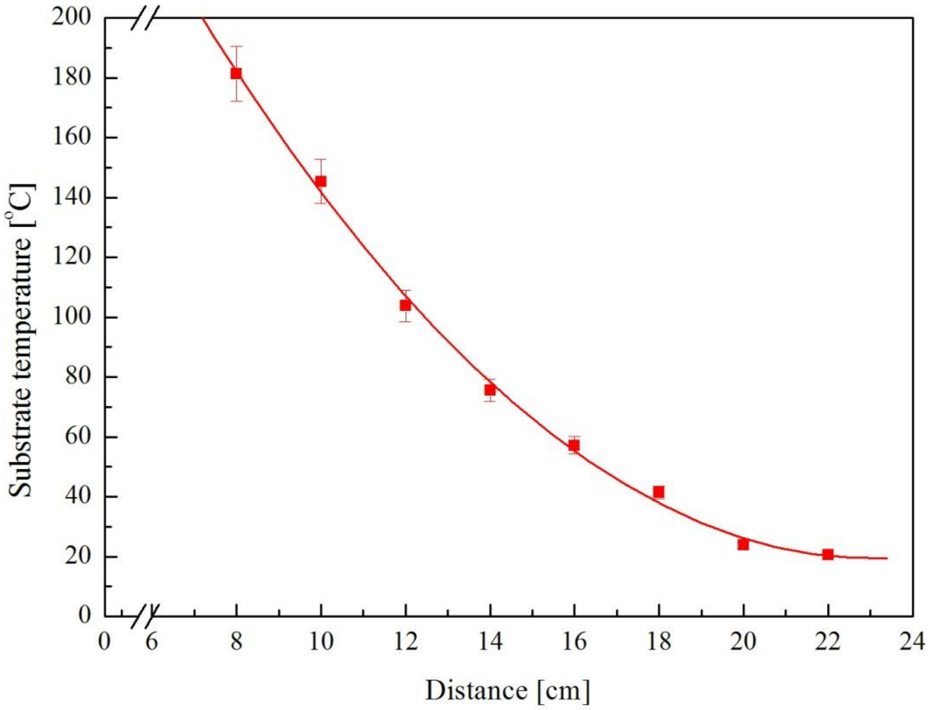

Fig. 7.3: *Substrate temperature as a function of the substrate to plasma distance.*

The custom made arc source is equipped with graphite electrodes, which were used to deposit DLC films, thus is not suitable for metallic film deposition. Therefore we used another anodic arc modification with different electrode configuration and exchangeable electrode material was used.

7.2 Experimental Setup for Magnesium Film Deposition

In the experiments, an industrial high vacuum chamber *PLS Classic 500* (*Pfeiffer Vacuum*) equipped with an anodic vacuum arc was used. The arc discharge can be operated in any vacuum condition where it is independent on operation gases, allowing to operate in high vacuum and to obtain impurities–free coatings [Ehrich88a].

A schematic diagram of the vacuum chamber and electrodes is shown in Fig. 7.4.

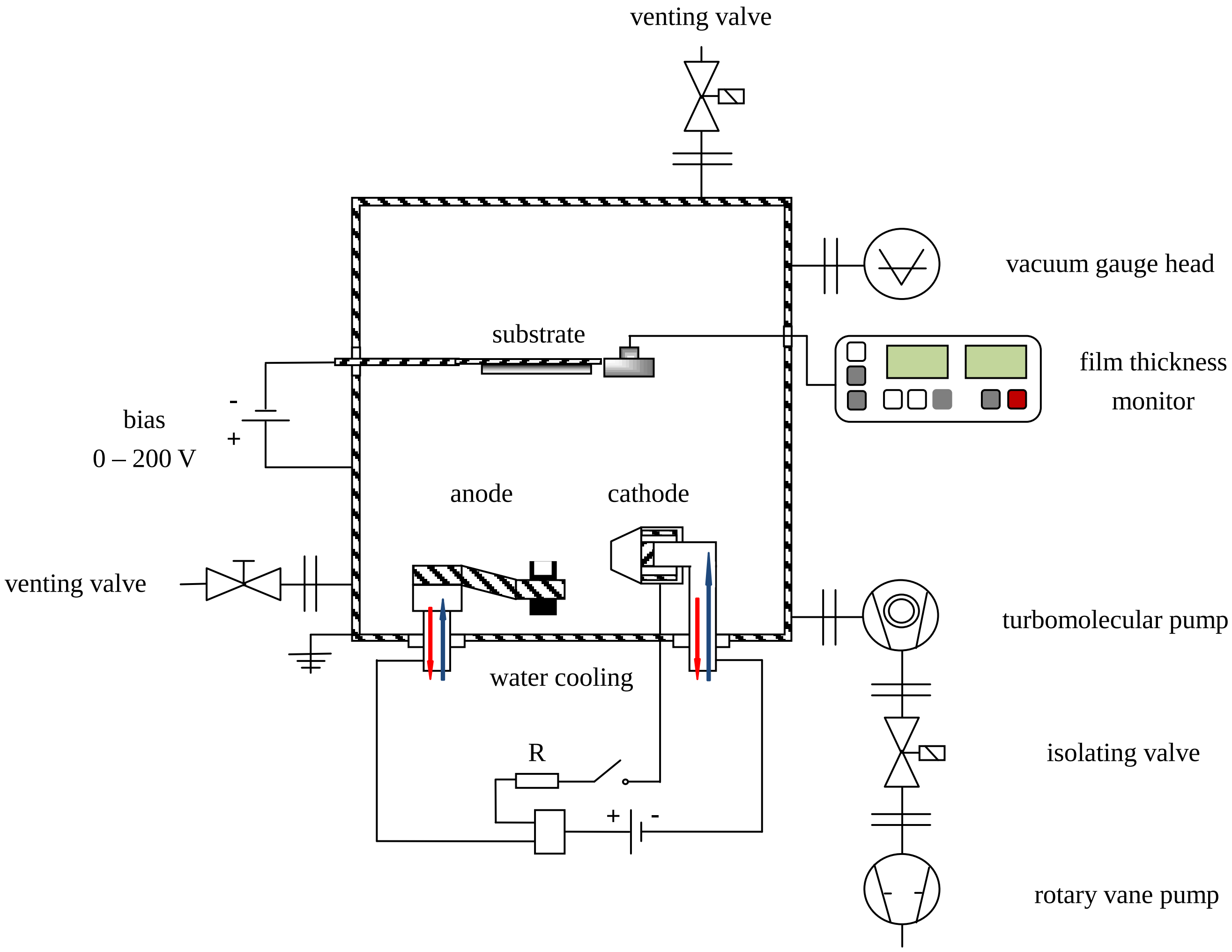

Fig. 7.4: *Vacuum chamber schematic diagram.*

Cathode and anode are located in a vacuum chamber and connected to a water cooling system. The electrodes are insulated from the grounded chamber as shown in Fig. 7.5.

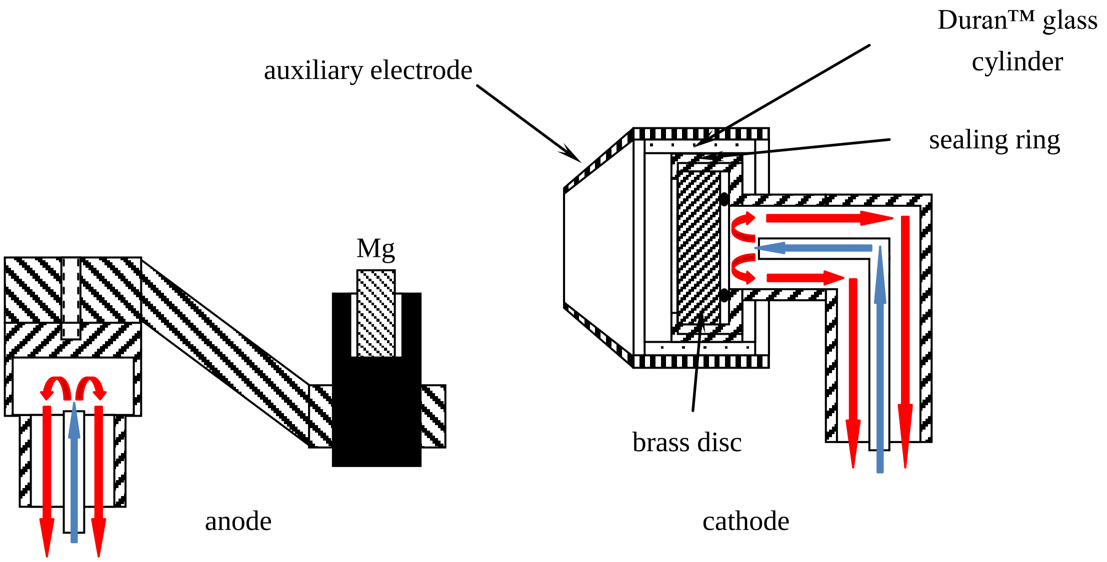

Fig. 7.5: *Schematic diagram of electrode construction.*

The cathode consists of a water cooled metallic disc (brass), sealing ring, metal coated *Duran™* glass cylinder and the cone-shaped auxiliary electrode. The auxiliary electrode is separated by a glass cylinder from the cathode potentially.

The anode consists of a crucible mounted on the water-cooled electrical feed through. Anodic arc means that the deposited material is vaporized only from the anode, while the cathode is used as ionization source. Cathode activity is needed to transport the current from the cathode to the anodic plasma. In order to have a constant deposition rate from the anode it is necessary to keep a constant power flux to the anode. For this purpose it is necessary to restrict the surface of the cathodic spots inside the central part of the cathode disc. This could be done by two ways: by restriction of the cathodic spots using a sealing ring or by magnetic control of the cathodic spot [Ehrich88a, Ehrich90]. The material of the sealing ring should have much higher ignition voltage than the cathodic material. In this work brass as a cathode material was used, because of low ignition current, effective cooling and the correspondence between evaporated cathodic material and its stochiometric composition [Ehrich90]. The restriction of the cathodic spot at the brass cathode is done by a molybdenum auxiliary electrode which is separated through a Duran™ glass cylinder from cathode potential. Molybdenum was used due to its high melting point; therefore burning voltage of the cathodic spot is much higher in comparison to the cathodic material. It was shown by [Hasse92] that cathodic spot restriction is so effective that no magnetic control is necessary. In order to reduce the erosion of the cathodic material and to decrease the influence of the cathodic plasma onto the expanding anodic arc, the cone-shaped auxiliary electrode orifice was made as small as possible. During the plasma operation the temperature inside the auxiliary electrode was so high that even backward evaporation of zinc onto the cathode surface occurred, this leads to the reduction of cathode material erosion. It was found [Filipov05] during the anodic arc deposition the evaporated anodic material is also deposited onto the cathode surface, what on its part decreases the plasma and films contamination by the cathode material, see Fig. 8.89. As indicated below, the anodic plasma and in turn the deposited magnesium film have no contamination from the evaporated cathodic material, see Fig. 8.87.

In comparison with the cathodic arc deposition, the anodic arc has a significant advantage: there are no macroparticles produced during the deposition due to the evaporation of the metal from the anodic crucible [Ehrich88a].

To ignite the plasma, it was necessary to use an auxiliary electrode. After applying current between molybdenum auxiliary electrode and the cathode, the thin metallic layer on the Duran™ glass cylinder evaporates due to the ohmic heating. This ignites an auxiliary arc. After the auxiliary arc ignition, the electrons which leave the cathode due to the potential difference between the electrodes move toward the anode. This results in rapid evaporation of the anode material and also its ionization. The anodic arc ignites when a critical evaporation rate is reached. Then the auxiliary arc electric circuit is turned off. By using auxiliary arc ignition, the cathodic material erosion could be avoided and thus film contamination. During the deposition, the power input to the anode is concentrated on the molten material. Intense and bright color of the evaporated metal in the plasma cloud around the anode, prove strong activation (excitation and ionization) of the produced anodic arc plasma [Ehrich88b].

In order to prevent contamination of the magnesium coatings, a carbon crucible was used because of its high melting temperature and absence of chemical reactions between magnesium and a carbon crucible. Due to the physical-chemical properties of magnesium it sublimates during the evaporation and passes liquid phase formation what prevents formation of magnesium melts and to contaminate expanding anodic plasma.

The films were deposited on $50\,mm \times 50\,mm$ steel substrates. These substrates were pretreated in an ultrasonic bath with acetone to remove surface contamination. After the cleaning procedure the substrates were transferred into the vacuum chamber. The chamber was pumped down to $10^{-7}\,mbar$. The variation of process parameters, such as substrate bias (from $0\,V$ to $-200\,V$) and hydrogen admixture (from $0\,sccm$ to $1000\,sccm$), is used to influence the film properties. According to different hydrogen flow rates different deposition pressures were obtained. As described in the literature, the amount of stored hydrogen is proportional to the working pressure [Varin06]. This parameter is very important for plasma chemistry, because of the influence on particle energy and in turn particle activity and therefore film properties [Raizer01].

In Table 7.2 the corresponding deposition parameters are listed.

Table 7.2: *Working pressure as a function of hydrogen flow rate.*

Hydrogen flow rate, (sccm)	*0*	*220*	*700*	*1000*
Working pressure, (mbar)	5×10^{-7}	1×10^{-4}	5×10^{-4}	1×10^{-3}

During deposition, the plasma parameters were monitored by retarding field energy analyzer and mass-spectrometer.

8 Experimental Results

8.1 Plasma Diagnostics

8.1.1 Influence of Deposition Parameters on Plasma Properties

In order to characterize the deposition process and properties of the films deposited, it is necessary to know and control plasma parameters. One of the most important plasma parameters is gas composition. Before every deposition process and during the deposition, the gas composition was monitored by the *QMS-200 Prisma* by *Balzers*™ mass-spectrometer.

8.1.1.1 Mass-spectroscopy During DLC Film Deposition

The *QMS-200 Prisma* by *Balzers*™ Rest gas analyser (*RGA*) was used to monitor the DLC film deposition processes. Fig. 8.1 shows a characteristic residual gas spectrum before deposition.

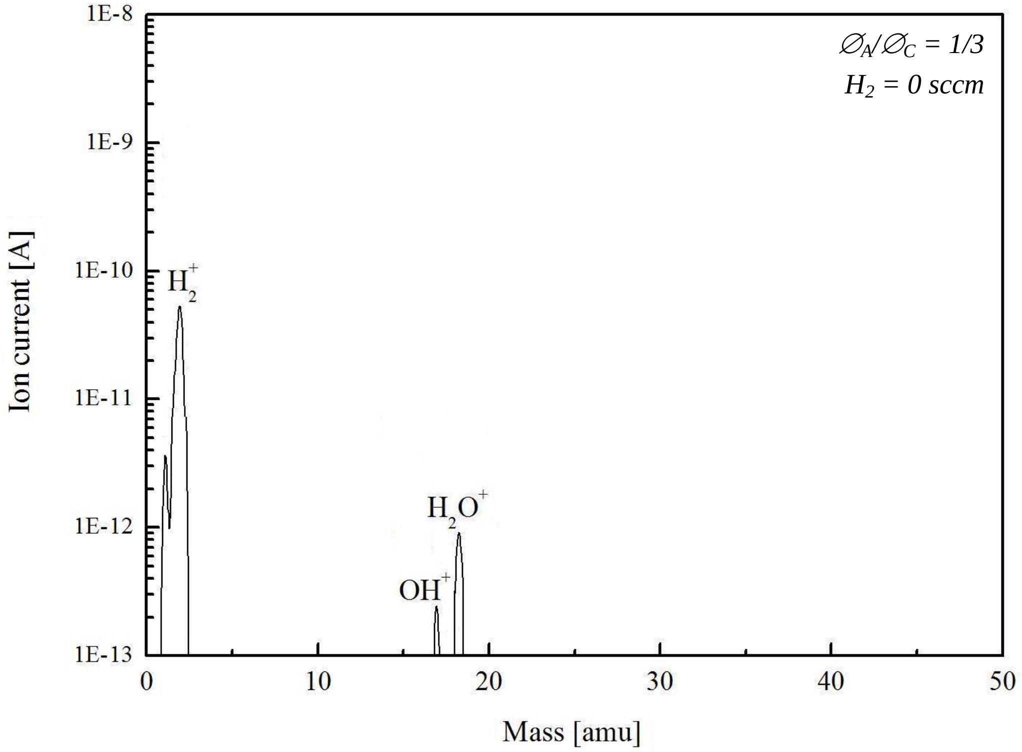

Fig. 8.1: *Sample of residual gas mass-spectrum before DLC deposition.*

Only hydrogen and water can be found in the mass-spectrum. This is a typical high vacuum residual gas spectrum.

By-turn Fig. 8.2 shows the mass-spectrum during the DLC films deposition at *50 sccm* hydrogen flow rate.

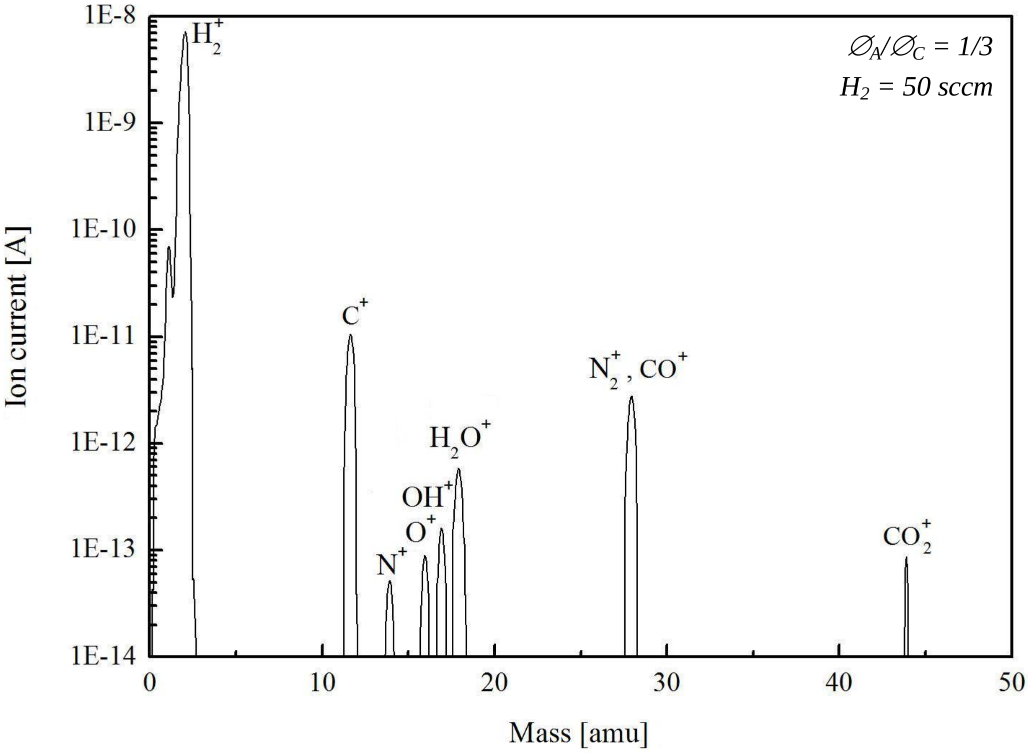

Fig. 8.2: *Sample mass-spectrum during the DLC film deposition (50 sccm hydrogen flow rate).*

As one can see, the presence of the nitrogen peak is stipulated by surface adsorption of nitrogen during chamber operation at atmospheric pressure. The absence of argon and oxygen peaks at *40* and *32 amu* correspondingly also proves that there is no leak or contamination coming from the gas transport system. The carbon peak intensity is rather low for carbon plasma, but here should be taken into account that a high amount of carbon atoms do not reach the mass-spectrometer due to their condensation on the walls.

Using mass-spectrometer, it was possible to monitor the gas composition before and during the plasma deposition. Fig. 8.3 shows the variation of the hydrogen peak intensity as a function of the deposition time.

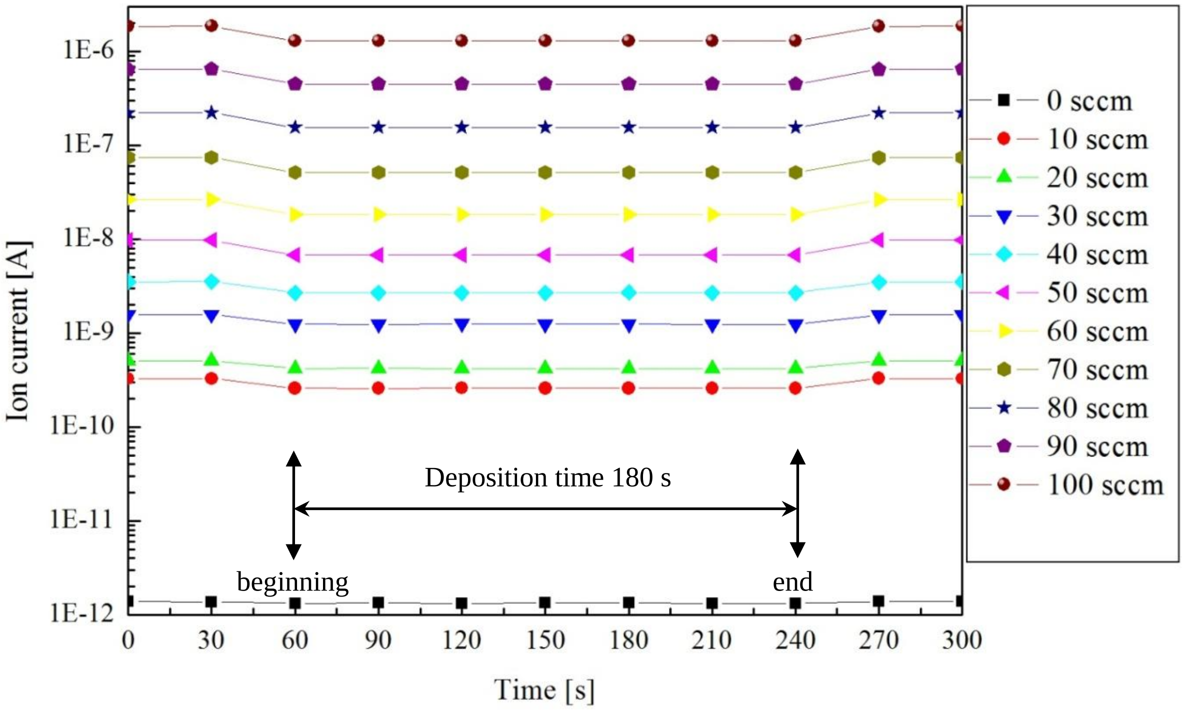

Fig. 8.3: *Measured hydrogen peak intensity as a function of the deposition time at different hydrogen flow rates.*

Fig. 8.3 shows a decrease of hydrogen peak intensity during deposition. By the help of *RGA* module, it was possible to calculate the hydrogen partial pressure in the vacuum chamber during the deposition process, see Fig. 8.4.

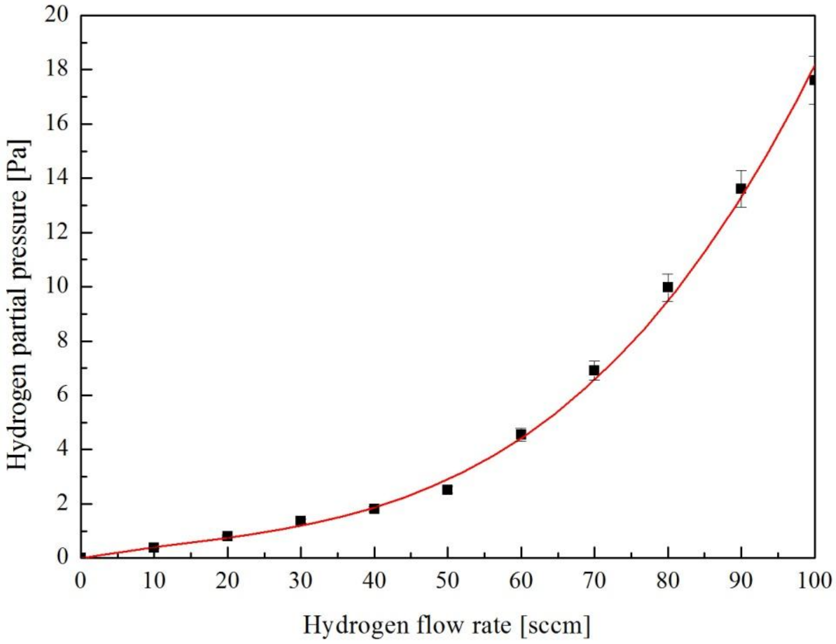

Fig. 8.4: *Hydrogen partial pressure with the plasma as a function of the hydrogen flow rate.*

8.1.2 Influence of Electrode Material on Plasma Composition

8.1.2.1 Electrode Degasation

In this work several commercially manufactured graphite electrodes were used. This was done to compare their chemical composition during the deposition and to choose the purest one. Usually, commercial graphite contains impurities. It happens because of the low annealing temperature during graphite manufacture, that virtually all impurities which can be found in the raw material are still present.

According to the feed stock and working process, the electro graphite can contain from *0.01* to *0.3 %* ash content. It can be divided into three purity gradations:

1) high purity electro graphite – *0.02 – 0.03 %* ash content
2) repurified electro graphite – maximum *0.007 %* ash content
3) highest purity (spectrographic) electro graphite – maximum *0.001 %* ash content

The electro graphite also contains non-volatile elements, their concentrations for the different purity gradations are shown in Table 8.1 and Table 8.2.

Table 8.1: *Elements content in repurified and high purity electro graphite [Schunk80].*

Ca	30 – 50 $\mu g/g$
Si, Ti, S	10 – 20 $\mu g/g$
B, V, Fe	5 – 10 $\mu g/g$
Al, Cu, Mn, Pb, Sn, Mg	5 $\mu g/g$

Table 8.2: *Element contents in spectrographic electro graphite [Schunk80].*

B	< 0.01 $\mu g/g$
Ca	< 0.2 $\mu g/g$
Cu	< 0.8 $\mu g/g$
Fe	0.2 $\mu g/g$
Mg	0.1 $\mu g/g$
Si	0.5 $\mu g/g$
Ti	< 0.5 $\mu g/g$
V	< 0.2 $\mu g/g$

There are also volatile elements inside electro graphite. The high purity electro graphite has volatile elements content around *100 – 300 μg/g*. This gas content consists of different gases like: CO, CO_2, H_2, O_2, N_2 and water vapour. For the next graphite purity classes the gas content is reduced by degasation till values around *1 μg/g*, see Fig. 8.5.

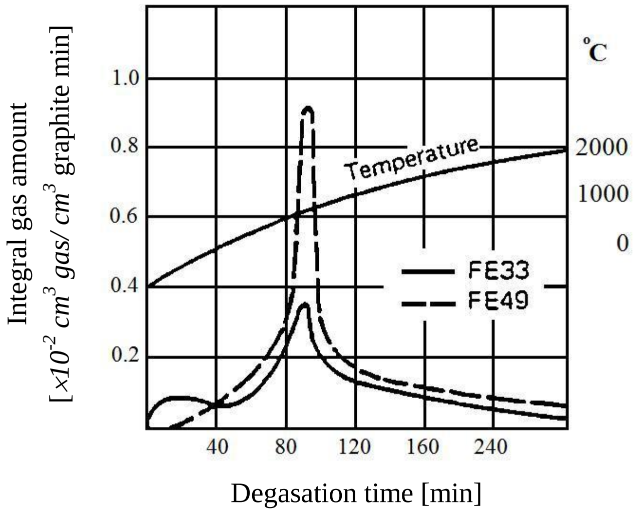

Fig. 8.5: *Graphite degasation in vacuum for different graphite electrodes [Schunk80].*

For degasation measurement two graphite electrodes were put into contact in the vacuum and then warmed up by ohmic heating, and the desorbed gases were monitored by mass-spectroscopy. In this work, the degasation measurements were performed with different degasation times, the maximum measured degasation time was *60* minutes, see Fig. 8.6. It was found that during the degasation some new gas peaks come into existence: nitrogen and oxygen. The nitrogen peak is coming from the electrodes; the nitrogen gas was adsorbed on the electrode surface during chamber ventilation by the nitrogen. This peak is only present during the electrodes heating, and disappears after degasation. The oxygen peak comes from the water decomposition. After chamber ventilation, the chamber usually operated in air (electrodes replacement, substrate exchange) and therefore some water vapours adsorbed on the electrodes surface. The oxygen peak also disappears after degasation. The short increase of the oxygen peak means only decomposition of the water adsorbed on the electrodes surface.

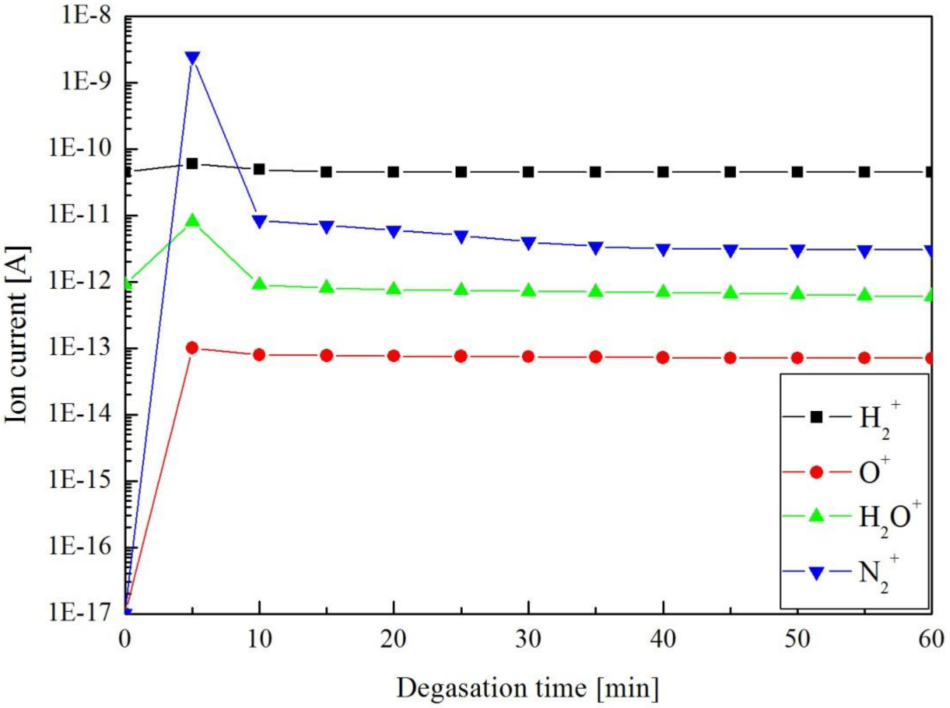

Fig. 8.6: *Graphite electrode degasation in vacuum as a function of the degasation time.*

It was found that after *10* minutes of degasation most adsorbed gases can be removed from the atmosphere, see Fig.8.6. Therefore before every deposition process, degasation with *10 min* duration was performed.

8.1.2.2 Electrode Material Impurity

In order to choose the electrodes with the lowest impurity level, in this work few sets of electrodes from different manufacturers were used. A pair of similar electrodes was mounted in a vacuum chamber, and the chamber was evacuated till working pressure $< 10^{-6}$ *mbar*. The quadrupole mass-spectrometer *QMS-200 Prisma* by *Balzers™* was used to monitor the electrodes degasation process. First we took the residual gas spectum and then monitored the gas composition during the arc deposition. As one can see below there is not only the difference in gas composition during the degasation time but also during the residual gas measurement, see Fig. 8.7.

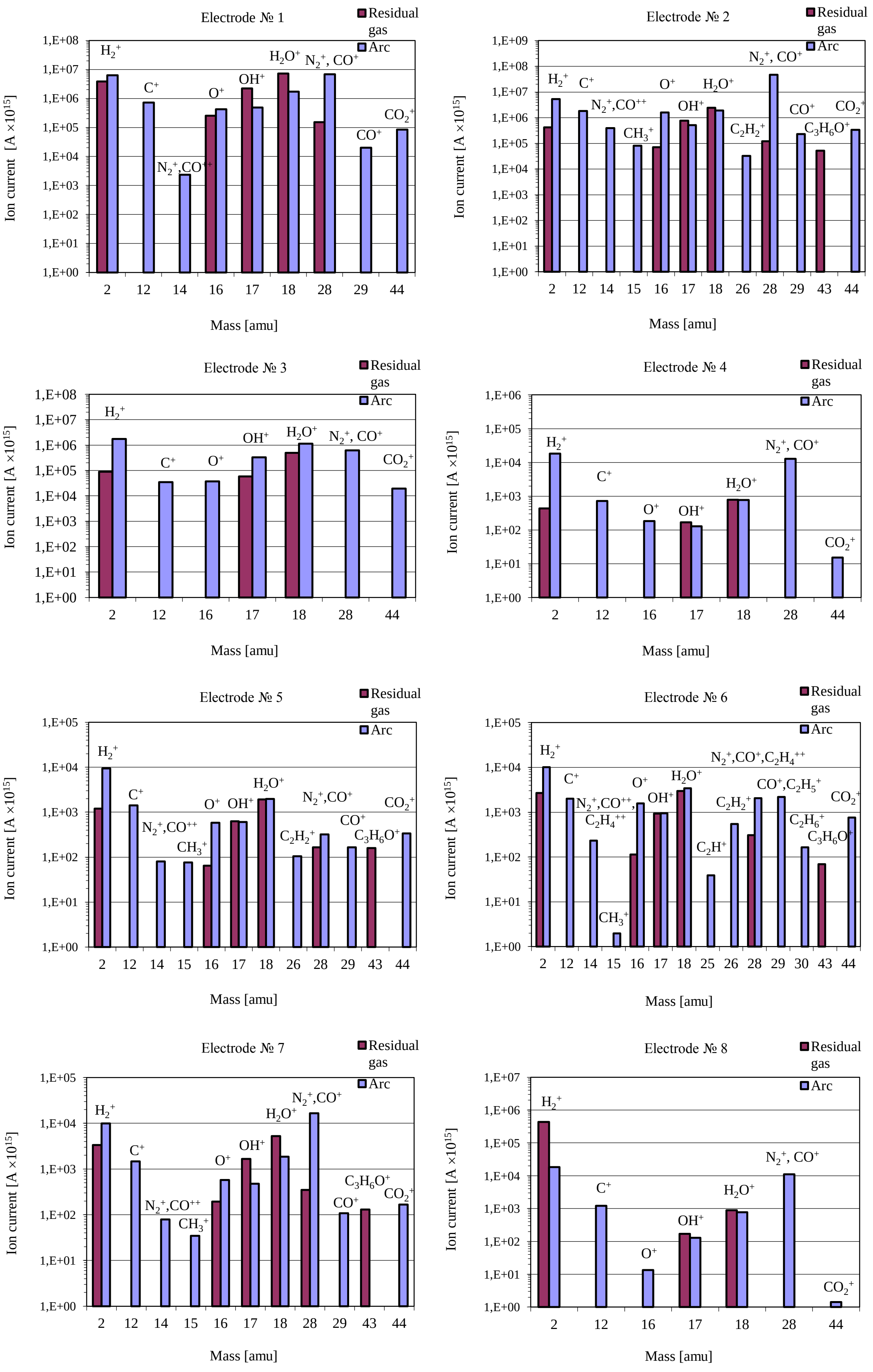

Fig. 8.7: *Mass–spectra for different electrodes taken during the residual gas composition measurements and during the arc deposition.*

As one can see, there is a significant difference between the electrodes and their gas composition. All the measurements were done with the same initial vacuum conditions, and there is a difference also in the measured peaks intensities. This fact can be explained by the difference in electrodes manufacturing processes. Some electrodes have higher purity and less porosity than the others. For the further deposition we choose electrodes with the number 8 due to the lowest vacuum contamination. These electrodes were the spectrographic graphite rods *Ringsdorff™ RW003* from *RINGSDORF – Werke GmbH*.

8.1.3 Influence of Deposition Parameters on Plasma Properties

8.1.3.1 Mass-spectroscopy During Magnesium Film Deposition

The deposition process was monitored using *QMS-200 Prisma* by *Balzers™*. Fig. 8.8 shows a characteristic residual gas spectrum before deposition and it is similar to Fig. 8.1.

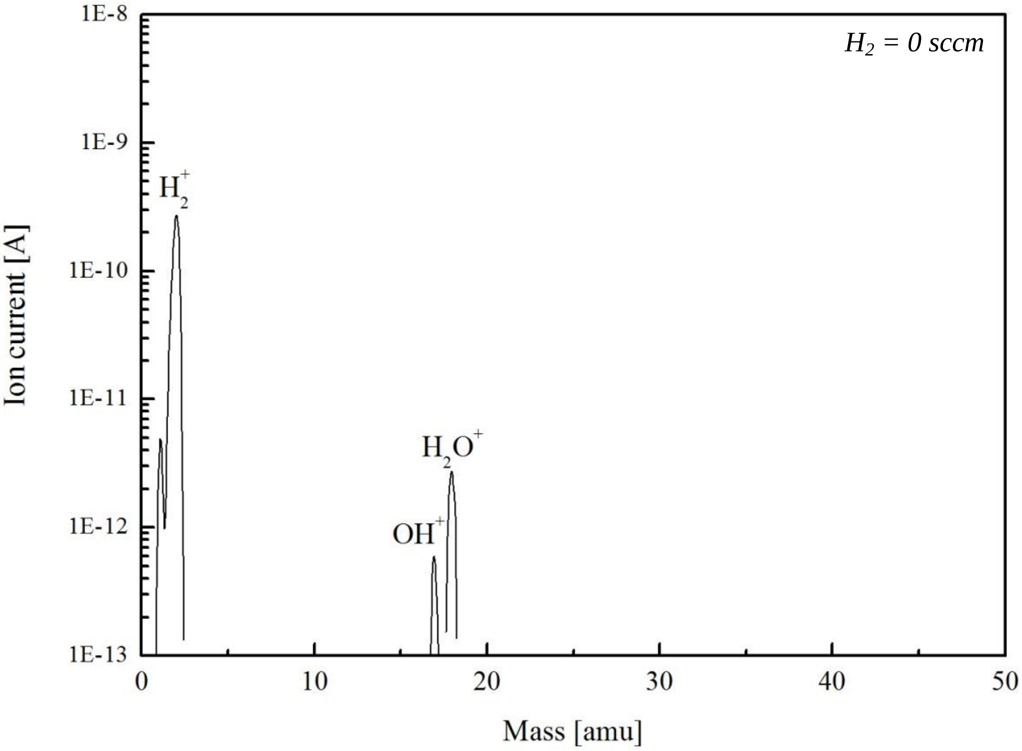

Fig.8.8: *Residual gas mass-spectrum before magnesium deposition.*

Fig. 8.9 shows the mass-spectrum during *Mg* deposition with *220 sccm* hydrogen flow rate at 1×10^{-4} *mbar*.

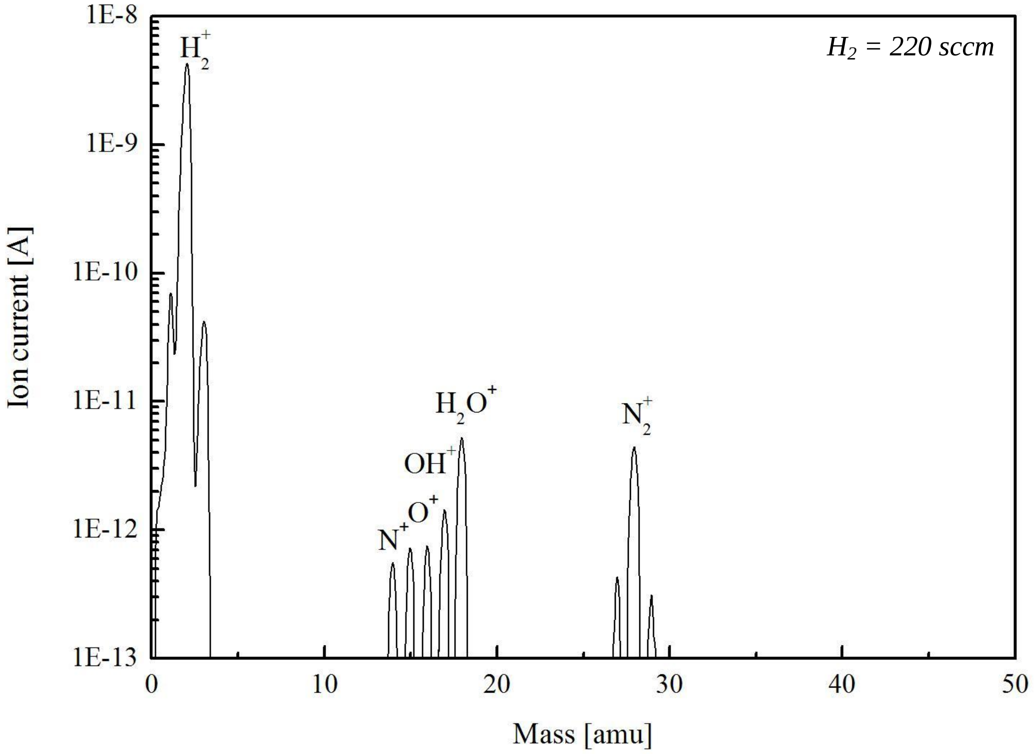

Fig. 8.9: *Working atmosphere mass-spectrum.*

As one can see, the presence of the nitrogen peak is stipulated by surface adsorption of nitrogen during chamber operation at the atmospheric pressure. The absence of argon and oxygen peaks at *40* and *32 amu* correspondingly also prove that there is no leak or contamination coming from the gas transport system. The absence of a magnesium peak means that on the way to the mass-spectrometer all magnesium ions condensed on the walls.

8.1.4 Particle Energy Measurement During DLC Film Deposition

The particle energy is a crucial parameter which determines the physical and chemical properties of the growing films. Knowing this parameter is necessary to understand the processes happening in the plasma and responsible for the film formation. In this work the ion energy was measured using retarding field energy analyzer.

8.1.4.1 Influence of Different Arc Modes on the Ion Energy

The transition between different arc modes is the easiest way to influence the particle energy. In order to distinguish this effect the ion energy measurements were performed without hydrogen admixture to the plasma. This transition was possible due to the variation of the electrode diameter ratio $\varnothing_A/\varnothing_C$. It was found that in the "anodic" arc mode ($\varnothing_A/\varnothing_C = 1/3$) the particles have the lowest energy $E_i = 7.3\ eV$, the highest particle energy have ions in the "cathodic" arc mode ($\varnothing_A/\varnothing_C = 3/1$) $E_i = 23\ eV$. The results of the ion current measurements (blue curve) and derived ion energy (red curve) are shown below in Fig. 8.10 – 8.12.

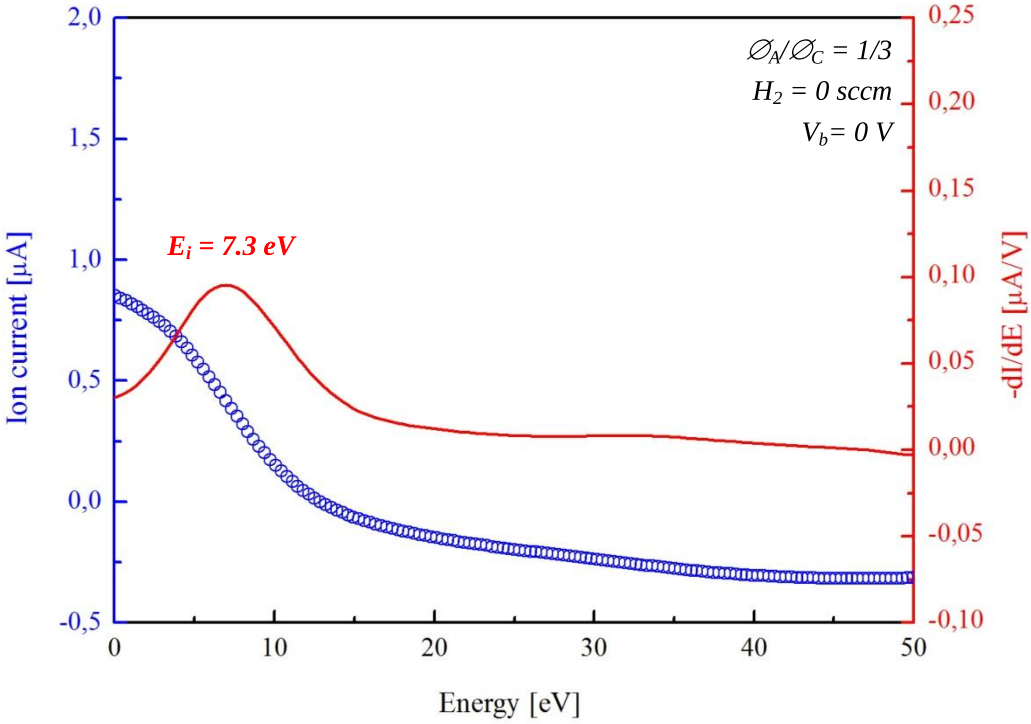

Fig. 8.10: *Measured ion current and derived ion energy for DLC coating with: "anodic" arc mode $\varnothing_A/\varnothing_C = 1/3$, 0 V bias voltage and 0 sccm hydrogen flow rate.*

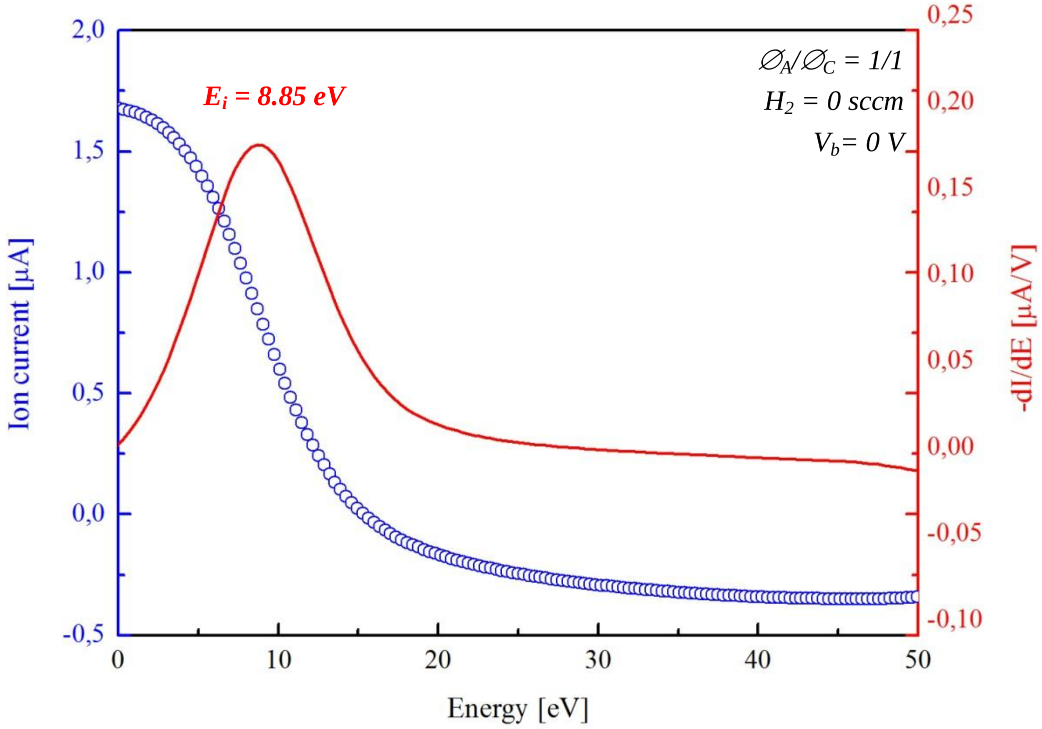

Fig. 8.11: *Measured ion current and derived ion energy for DLC coating with: “transition” arc mode* $\varnothing_A/\varnothing_C$ *= 1/1, 0 V bias voltage and 0 sccm hydrogen flow rate.*

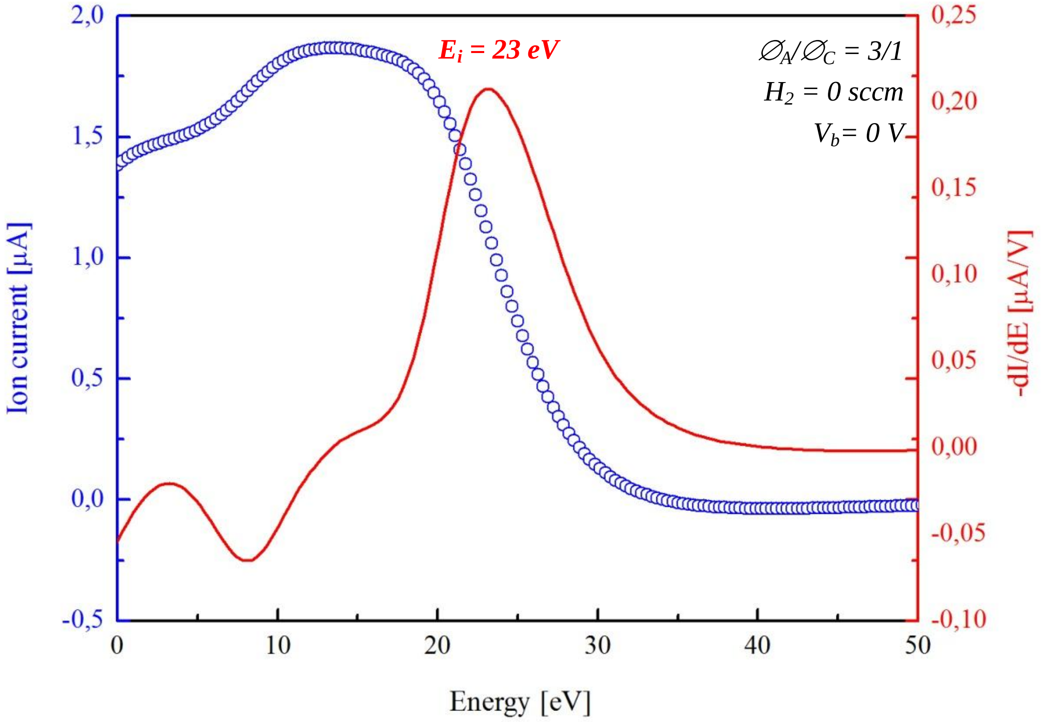

Fig. 8.12: *Measured ion current and derived ion energy for DLC coating with: “cathodic” arc mode* $\varnothing_A/\varnothing_C$ *= 3/1, 0 V bias voltage and 0 sccm hydrogen flow rate.*

In the “cathodic” arc mode two ion peaks at $E_i = 23\ eV$ and $E_i = 3.25\ eV$ were found. The presence of the second ion peak is explained by the existence of the twice ionized ions, while the main part of the ions have energy $E_i = 23\ eV$.

The measured ion energies respective to the arc modes are shown below in the Fig. 8.13.

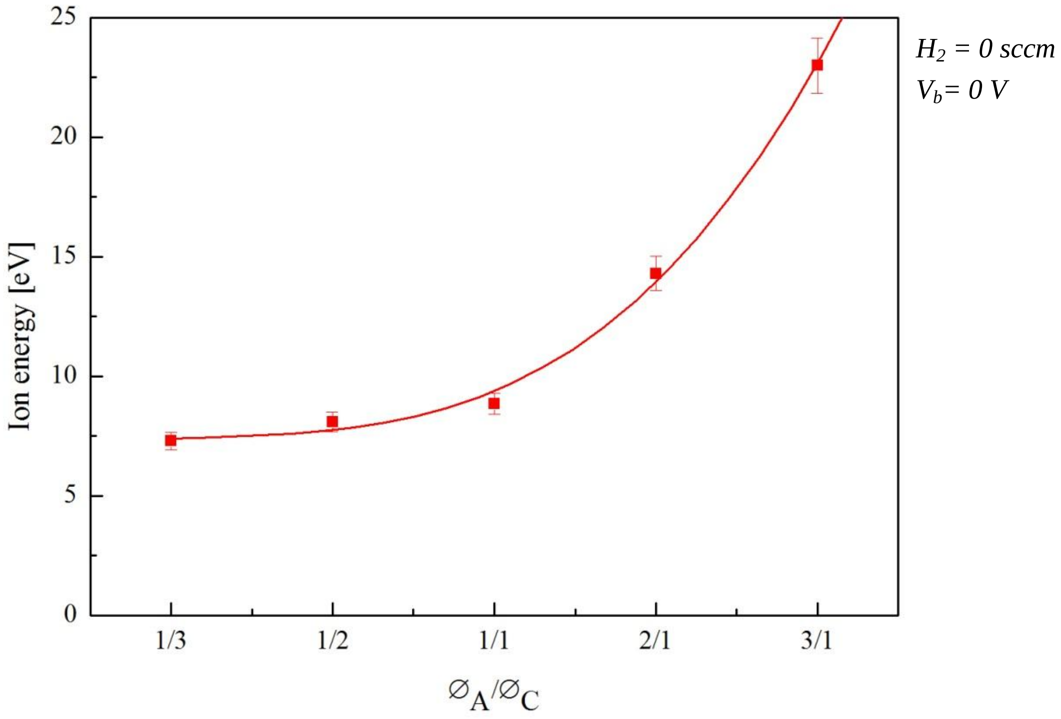

Fig. 8.13: *Variation of the carbon ion energy as a function of transition from “anodic” to “cathodic” arc modes.*

One can see that only by the variation of the electrode diameter ratio it was possible to have strong influence on particle energy and therefore film properties [Stamm09]. Each arc mode is characterized by the different particle energy. This aspect will be discussed below in the *Chapter 8.2*.

8.1.4.2 Influence of Different Hydrogen Flow Rates on the Ion Energy

It was found that the introduction of hydrogen into the plasma has a strong impact on to the particle energy. Fig. 8.14 shows the measured carbon ions energy depending on the hydrogen flow rate.

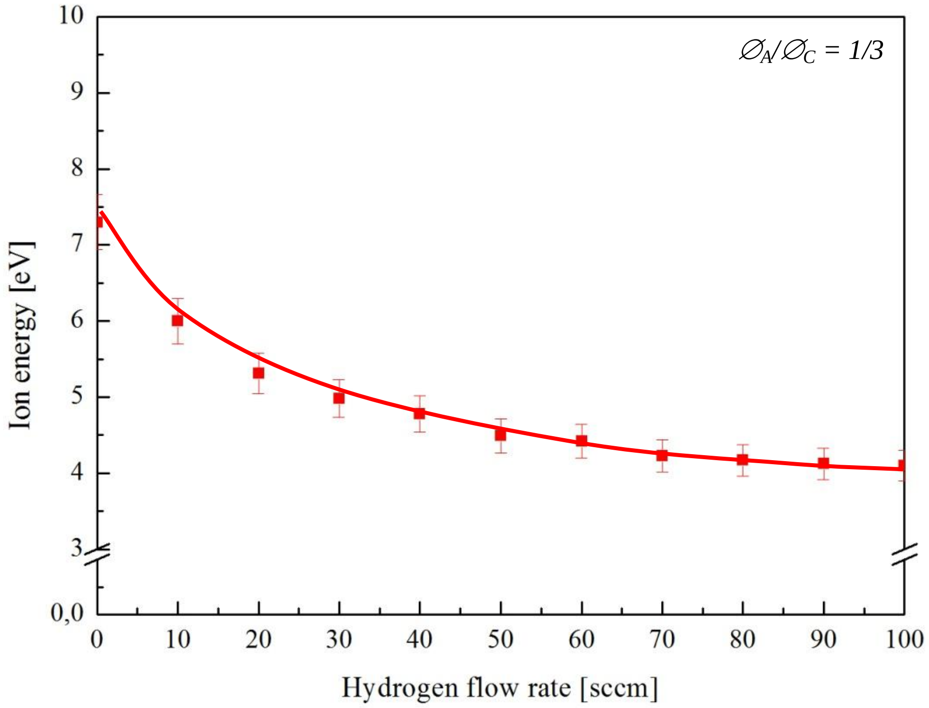

Fig. 8.14: *Measured ion energy of the deposited carbon ions as a function of the hydrogen flow rate variation.*

The increase of hydrogen flow rate leads to decrease of C^+_{12} ions energy from *7,3 eV* to *4,1 eV*. Such effect can be caused by two main parameters: change of the mean free path of the carbon ions and plasma chemistry. Ions now should experience more collisions on the way to the substrate, so they thermalize to lower energy. Due to the plasma chemistry carbon ions react with hydrogen ions on the way to the substrate and as a product of such reaction they may form hydrocarbons. Atomic hydrogen also interacts with carbon and can cause chemical etching of the growing carbon film. It could also terminate or saturate the chemical bonds between carbon – carbon atoms and change the film chemical structure.

8.1.4.3 Degree of Ionisation as a Function of Different Arc Modes

In order to control the film properties it is necessary to have a possibility to influence the particles arriving to the growing film surface. Such control is only possible on charged particles (ionized particles). The amount of ionized particles is the crucial parameter. So it means that the more ionized particles there are in the incident flux to the surface, the more control on the growing film properties we have.

The degree of ionisation Q – is the ratio of the amount of neutral particles to ionized ones, which arrive to a certain surface through a certain period of time.

Ion flux density j_i:

$$j_i = \frac{I_{isat}}{eA_k}; \tag{8.1}$$

I_{isat} – ion sturation current (ion current to the collector at $0\ V$),

e - elementary charge,

A_k – ion collector surface ($0.1257\ cm^2$), $d_k = 4\ mm$.

Using density of mass flux j_m we could calculate the particle flux density j_t, consisting of neutrals and ions.

$$j_t = \frac{j_m}{m_c}. \tag{8.2}$$

Density of mass flux j_m is a mass growth per time Δt, $\Delta t = 180\ s$ was used; it corresponds to the deposition time for every experiment.

$$j_m = \frac{\Delta m}{\Delta t A_{sub}}; \tag{8.3}$$

Δm – mass of the deposited film, A_{sub} – coated substrate surface ($8.0425\ cm^2$).

Degree of ionisation:

$$Q = \frac{j_i}{j_t} 100\%. \tag{8.4}$$

Fig. 8.15 shows the degree of ionisation calculated according to the equation *(8.4)* for the different arc modes.

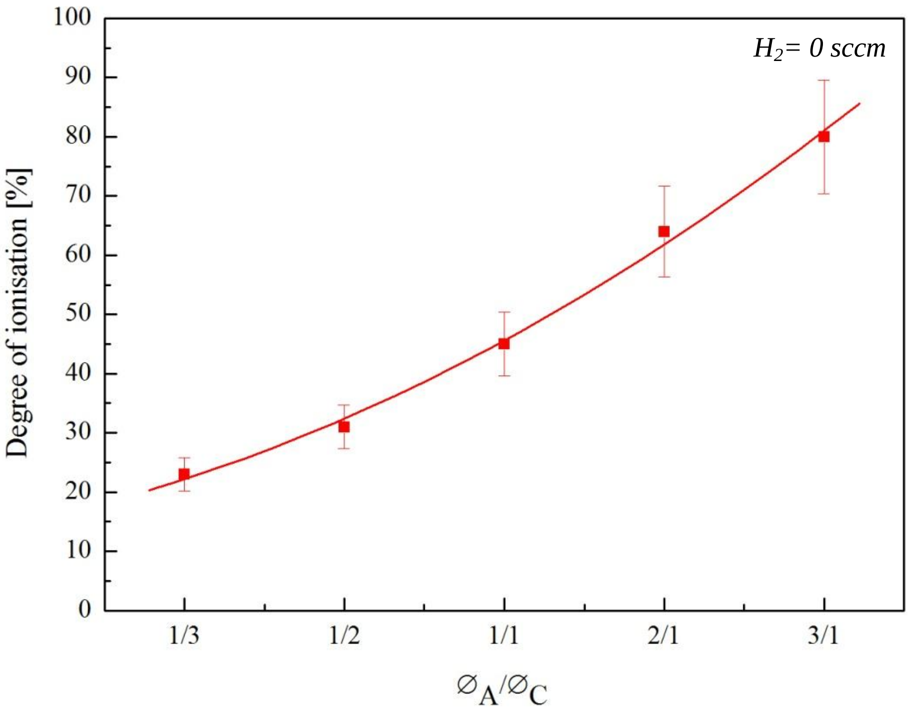

Fig. 8.15: *Degree of ionisation as a function of the transition from "anodic"* (*$\varnothing_A/\varnothing_C$ = 1/3*) *to "cathodic"* (*$\varnothing_A/\varnothing_C$ = 3/1*) *arc modes.*

The cathodic arc mode is characterized by the highest degree of ionisation among the other arc modes. The measurements show that it is possible to change the particle energy just by variation of the electrode diameter ratio. The difference in the particle energies is rather significant. Using this effect it is possible to influence on the film properties. The particles produced by "cathodic" arc mode have the highest ion energy $E_i = 23\ eV$ and degree of ionisation $Q = 80\ \%$.

8.1.5 Particle Energy Measurement During Magnesium Film Deposition

In this chapter, the influence of hydrogen admixture (different hydrogen flow rates) to the plasma on magnesium ion energy was investigated.

8.1.5.1 Influence of Different Hydrogen Flow Rates on the Ion Energy

The results of the ion current measurements (blue curve) and derived ion energy (red curve) are shown below in Fig. 8.16 a) and 8.16 b).

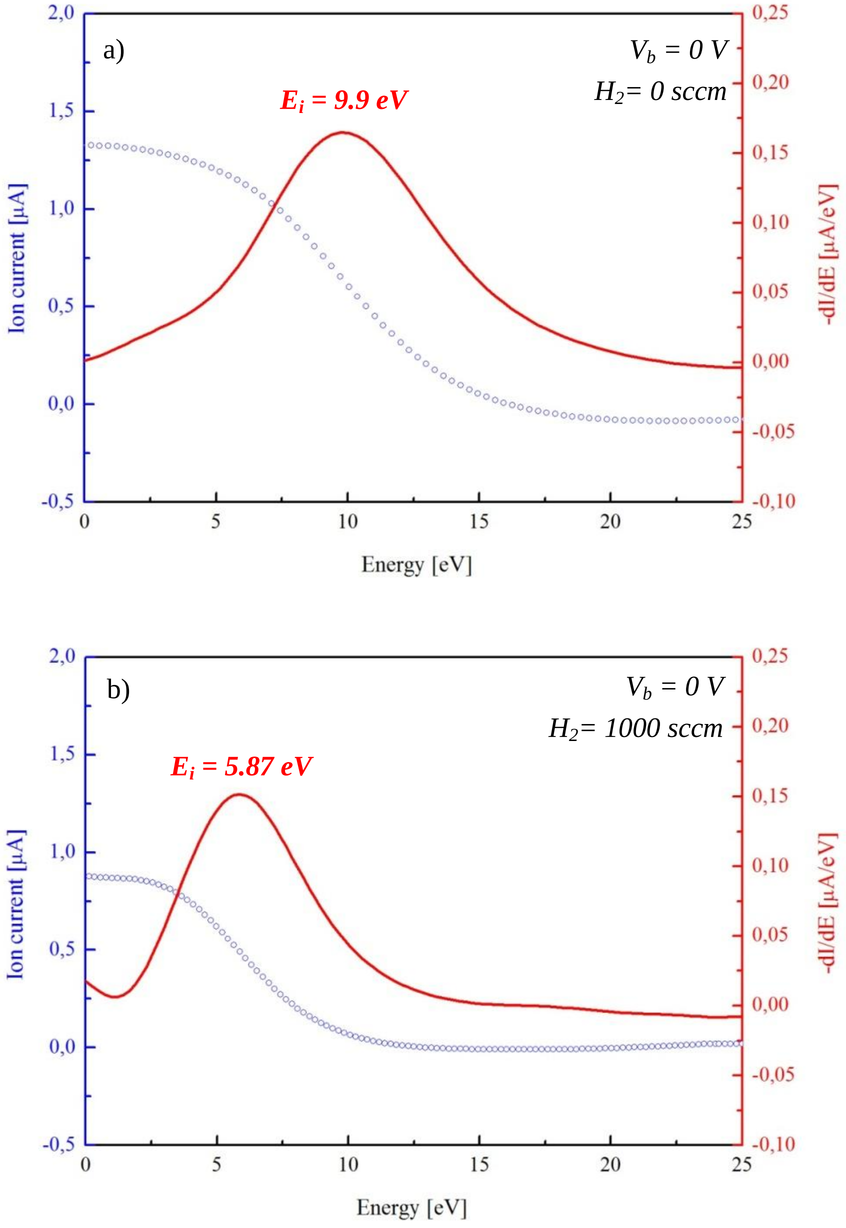

Fig. 8.16: *Measured ion current and derived ion energy for magnesium coating with:*

a) 0 V bias voltage and 0 sccm hydrogen flow rate;

b) 0 V bias voltage and 1000 sccm hydrogen flow rate.

Fig. 8.17 shows the measured magnesium ions energy depending on the hydrogen flow rates.

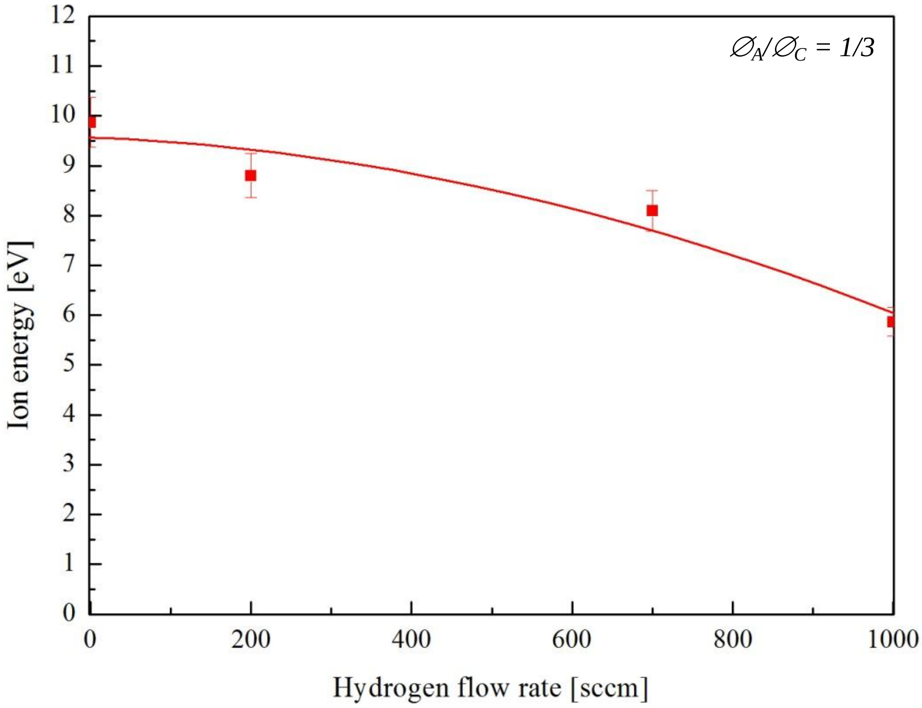

Fig. 8.17: *Measured ion energy of deposited Mg ions as a function of hydrogen flow rate.*

It was found that due to the introduction of hydrogen, the ion energy changes. Hydrogen flow is increased from *0 sccm* to the *1000 sccm* energy of Mg^+ ions decreases from *9,9 eV* to *5,9 eV*.

The increase of hydrogen flow rate leads to increase of working pressure, see Table 7.2. This changes the mean free path of magnesium ions. Ions now should experience more collisions with hydrogen atoms on the way to the substrate, so they thermalize to lower energies.

8.2 Film Diagnostics

Alongside with the plasma diagnostics it is also necessary to fulfil the film diagnostics. It is necessary to have complete information from these two sources to understand the influence of particle fluxes on the film properties.

Every plasma discharge is characterized by different parameters such as plasma composition, particle energy, working pressure, etc. These parameters were investigated in the plasma diagnostic chapter (*Chapter 8.1*), but other parameters like deposition rate, chemical composition are related to film diagnostics.

8.2.1 Arc Modes

In order to investigate different arc modes a vacuum arc plasma source adjustable from “cathodic” to “anodic” arc mode was used. Since vacuum arcs belong to the field of PVD techniques, it is necessary to know the electrode material consumption during the deposition process. Before each experiment, the weight of every graphite electrode was measured. After the deposition, the weight of the same electrode was measured again and the resulting mass difference or mass flow from each electrode was plotted. Such weight measurements were performed for each electrode diameter ratio. The results are shown in Fig. 8.18.

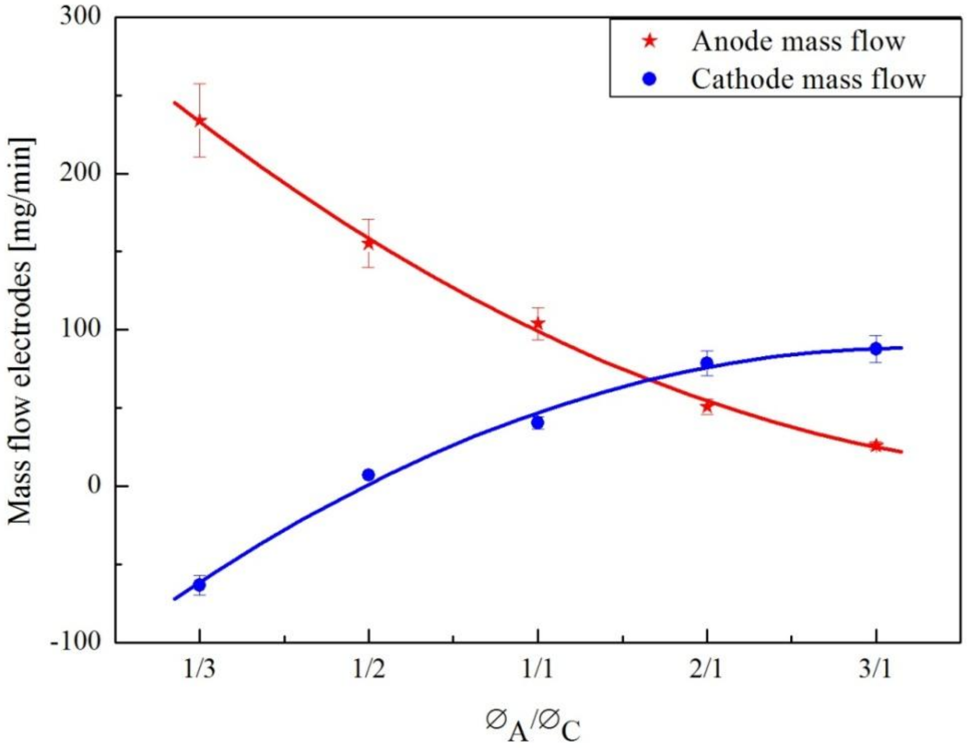

Fig. 8.18: *Electrodes mass flow as a function of the vacuum arc mode [Filipov05].*

During the anodic arc mode the mass flow from the anode (red curve) is the dominating flow. It is so high that it also leads to the fact that cathode is covered by the anode material; the cathode mass flow (blue curve) is negative. It means that weight of the cathode before the deposition is less than after the deposition. Such effect reaches its largest value at the electrode diameter ratio $\varnothing_A/\varnothing_C = 1/3$. The most of the deposited material is coming from the anode and therefore such mode is called "anodic". By the decrease of the cathode electrode diameter and the increase of the anode diameter, the mass flow from the cathode starts to increase and from the anode starts to decrease but it never reaches negative values. And at the electrode diameter ratio $\varnothing_A/\varnothing_C = 3/1$, the arc burns in "cathodic" mode where most of the evaporated material comes from the cathode.

Due to the high mass flow from the anode a few unexpected effects were observed. After long deposition time, the cathode is completely covered with the anode material so the influence of the cathode material on the film composition becomes negligibly small. Another effect of the high mass flow from the anode is that at the cathode edge, material evaporated from the anode, starts to form a 3-dimentional structure which is changing the electrode diameter ratio $\varnothing_A/\varnothing_C = 1/3$ or $\varnothing_A/\varnothing_C = 1/2$ toward $\varnothing_A/\varnothing_C = 1/1$, see Fig. 8.19 a). This effect leads to changes in the particle energy and therefore film properties. Such formations can be easily removed by mechanical treatment before every deposition experiment.

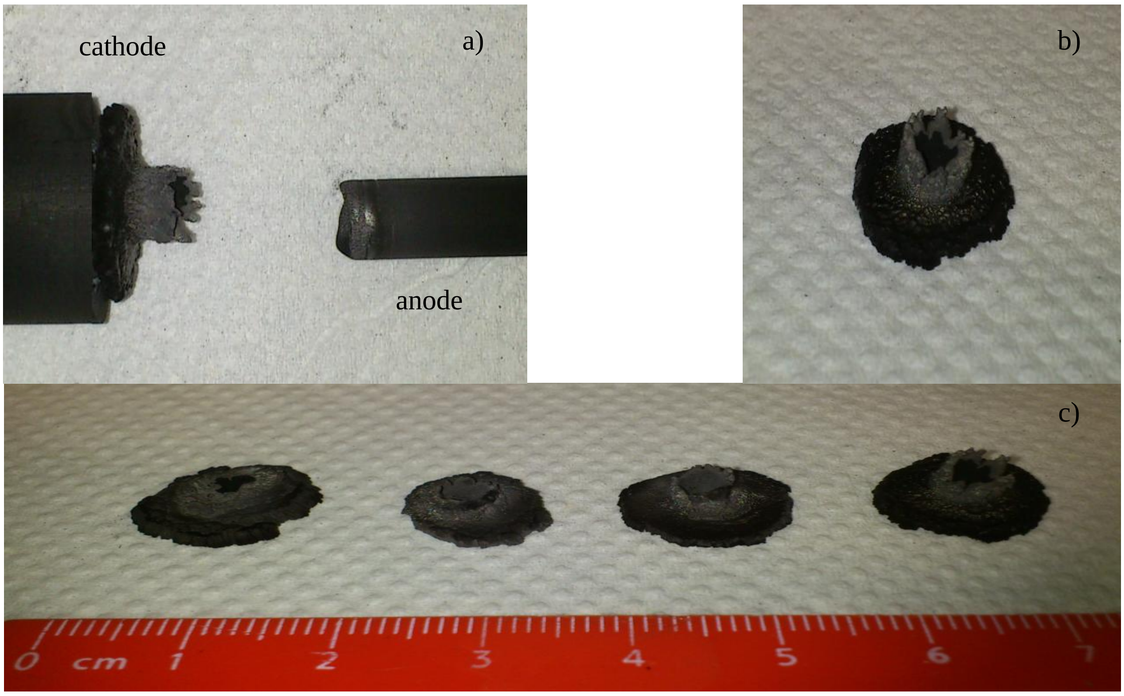

Fig. 8.19: *3-dimentional structures on the cathode edge.*

8.2.2 Deposition Rate

Deposition rate is the parameter characterized by the thickness of the condensed material per unit of time. The film thickness was measured by the *Dektak™ 6 Stylus Profilometer.* In Fig. 8.20 one can see the measured deposition rate as a function of different arc deposition modes without hydrogen admixture and at *0 V* bias voltage.

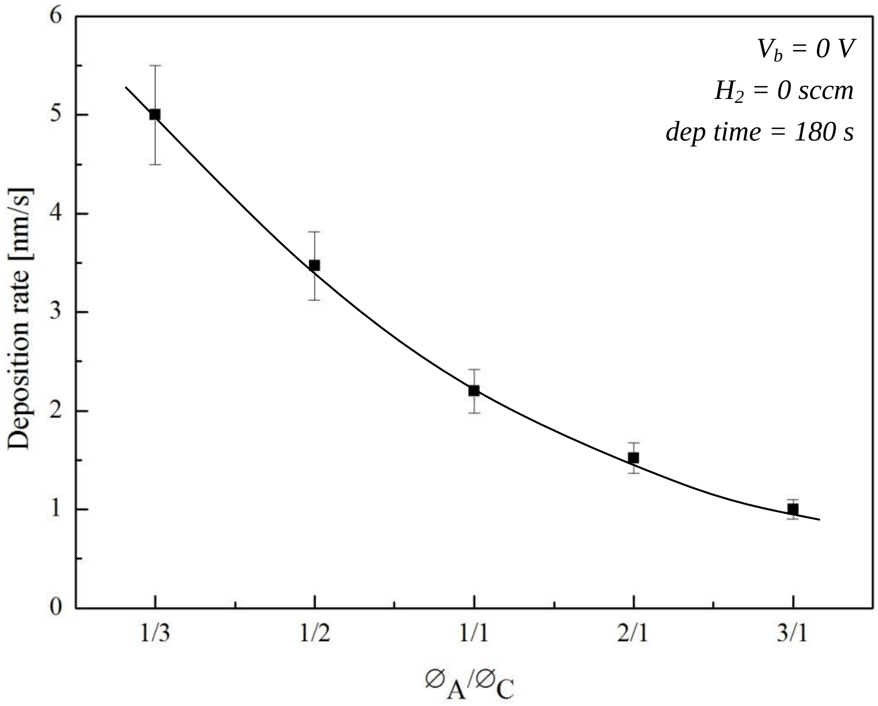

Fig. 8.20: *Deposition rate as a function of a vacuum arc mode.*

In the plasma diagnostics chapter (*Chapter 8.1.4*) the cathodic arc mode has shown the highest particle energy, degree of ionisation, but this mode has the lowest deposition rate *1 nm/s* in comparison to the "anodic" arc mode, where deposition rate is around 5 *nm/s*. Such difference can be explained by the difference in the electrode erosion process (electrode mass flow, see Fig. 8.18).

8.2.3 Structural Properties

One of the main parameter defining the thin film application area is their structural properties. Especially this fact is very important for DLC films. As mentioned above DLC is a whole class of carbon based coatings, which properties are widely varied according to their structure. But these properties are mostly determined by the plasma deposition process and the particle energy. There are several ways to influence the particle energy in the plasma: first – plasma discharge itself (by selection of an appropriate discharge type [Raizer01]), second – biasing the substrate, third – selecting working gas. In this chapter the influence of particle energy onto structural film properties will be shown.

8.2.3.1 Film Morphology

The film morphology is the first and an easily measured parameter which can immediately provide information about the influence of the deposition parameters onto film properties and its further sphere of application. The films with flat and smooth surface can be used as protective coatings, where the friction plays an important role and should be as small as possible. In turn films with high surface roughness can be used as an intermediate layer to improve adhesion between this film and subsequent one (sandwich structure).

For thin film analysis microscopic methods (*SEM* and *AFM*) are used to investigate film morphology and surface roughness. Optical microscopy is no longer the research routine in thin films technology due to the small film thickness and low resolution of an optical microscope.

To investigate film morphology a scanning electron microscope *ESEM Quanta 400 FEG* by *FEI Company* was used. The pictures were taken with *15 kV* acceleration voltage and with different magnifications of *20000* and *100000* times.

For further film morphology investigation it was necessary to use AFM technique. This method is alongside with SEM and can provide us very detailed information about surface roughness. For the surface roughness evaluation was used AFM *Veeco Dimension 3100* microscope. AFM was operated in the non-contact tapping mode. The square area of $5\ \mu m \times 5\ \mu m$ typical for AFM measurements was used.

8.2.3.1.1 Influence of Different Arc Modes on Film Morphology

At the beginning, the influence of transition from cathodic to anodic arc mode on the *DLC* film morphology was investigated. As it was described above the films were deposited onto double-side polished $2\ cm \times 1\ cm$ *Si* $\langle 100 \rangle$ wafers. The transition from the “cathodic” to the “anodic” arc mode was performed by variation of the electrode diameter ratio $\varnothing_A/\varnothing_C$. During the experiments no macroparticle filters were used. In the case when electrode ratio is $\varnothing_A/\varnothing_C = 3/1$ arc operates in “cathodic” mode, when ratio is $\varnothing_A/\varnothing_C = 1/3$ it was the “anodic mode”. The terms “anodic” or “cathodic” are used to describe which electrode is active and emits more particles. For each experiment the certain anode to cathode electrode diameter ratio was used, with the same deposition parameters, without working gas and bias voltage, as shown in a Table 8.4.

Table 8.4: *Deposition parameters during the cathodic to anodic arc transition experiment.*

Working pressure	5×10^{-6} *mbar*
Deposition time	*120 s*
Graphite electrodes	*RW 003, quality RW*
$\varnothing_A/\varnothing_C$	*3/1, 2/1, 1/1, 1/2, 1/3*

Typical SEM pictures of the deposited films are shown in Fig. 8.21. These images demonstrate the film morphology of the deposited DLC films by transition from “cathodic” arc mode to the “anodic” one.

In Fig. 8.21 *a)* and *b)* one can see the films deposited which were produced with an anode to cathode diameter ratio $\varnothing_A/\varnothing_C = 3/1$, in which the arc is running in a pure “cathodic” mode. This mode is characterized by low deposition rate (see Fig.8.20 in *Chapter 8.2.2*) and high macroparticle content in the films deposited. SEM image a) was taken with magnification of *20000* and image b) with magnification of *100000* times. Using the SEM images it was possible to evaluate macroparticle size distribution typical for this mode, which lies in a range from *100 nm* to *600 nm*.

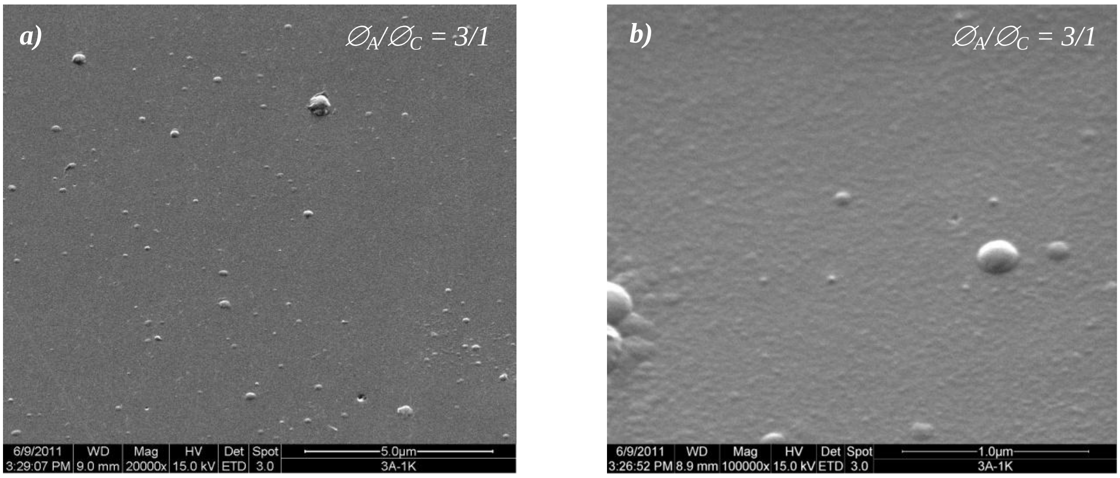

Fig. 8.21: *Typical SEM images of the DLC films deposited at "cathodic" mode, with electrode ratio* $\varnothing_A/\varnothing_C = 3/1$.

Fig. 8.22 demonstrates SEM images of the DLC films deposited at "transition" mode, where electrode diameter ratio is $\varnothing_A/\varnothing_C = 1/1$. This mode is characterized by higher deposition rate than at cathodic mode (see Fig. 8.20 in *Chapter 8.2.2*) and lower macroparticle content in the deposited films. Using the SEM images it was possible to evaluate macroparticle size distribution typical for this mode, which lies in a range from *100 nm* to *400 nm*.

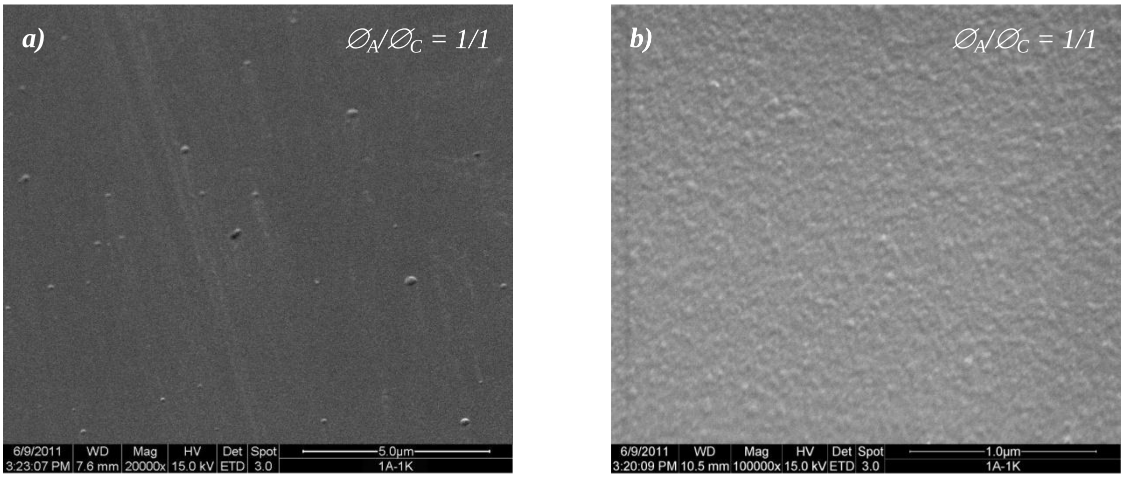

Fig. 8.22: *Typical SEM images of the DLC films deposited at "transition" mode, with electrode ratio* $\varnothing_A/\varnothing_C = 1/1$.

Fig. 8.23 demonstrates SEM images of the DLC films deposited at "anodic" mode, where electrode diameter ratio is $\varnothing_A/\varnothing_C = 1/3$. This mode is characterized by the highest deposition rate (see Fig.8.20 in *Chapter 8.2.2*) and almost no macroparticles inclusions in the deposited films. Using the SEM images it was possible to evaluate macroparticle size distribution typical for this mode, which lies in a range from *30 nm* to *70 nm*.

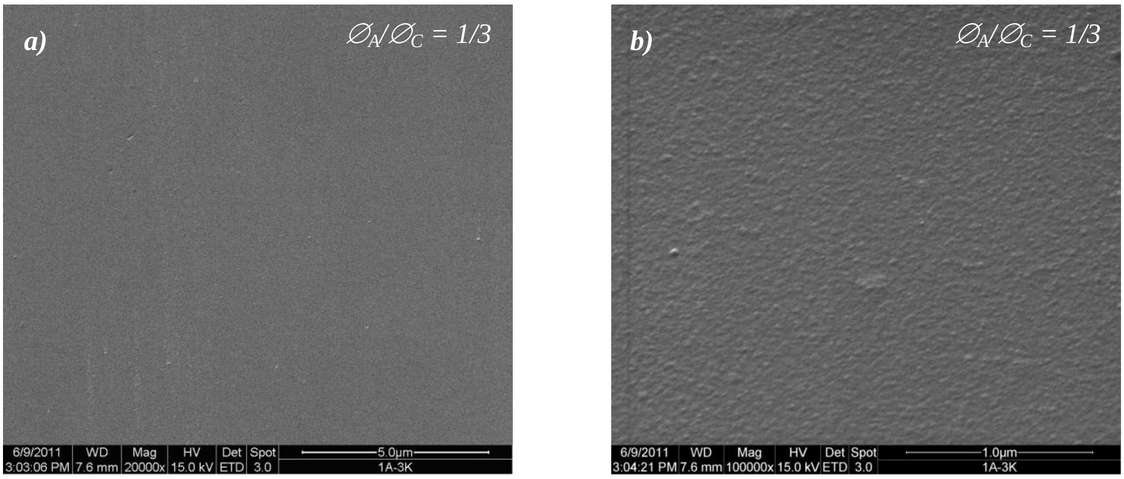

Fig. 8.23: *Typical SEM images of the DLC films deposited at "anodic" mode, with electrode ratio* $\varnothing_A/\varnothing_C = 1/3$.

As one can see, film morphology of the DLC films deposited strongly depends on the vacuum arc mode. By variation of the electrode diameter ratio it was possible to influence the particle energy (as shown in *Chapter 8.1.4*) and to affect film structural properties.

Due to the fact that the DLC films which were deposited during the anodic mode have shown the lowest roughness it was decided to use such type of DLC films in further experiments. The AFM [Eaton10] measurement results were evaluated using WSxM 3.1 Nanotech Electronica S.L. software [Horcas07]. This software was also used to obtain the 3D images of the scanned surface. For each AFM image (see Fig. 8.24) the evaluation parameters are shown in the corresponding table. The RMS (Root Mean Square) parameter was used to evaluate the surface roughness. The resulting substrate roughness dependence is shown in Fig 8.25.

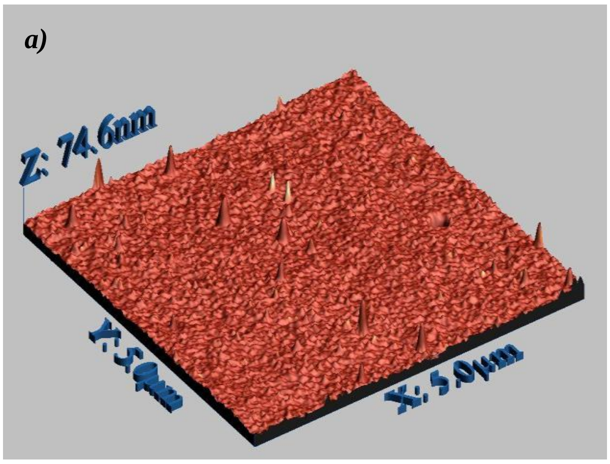

$\varnothing_A/\varnothing_C$	*3/1*
maximum height	*74.6 nm*
average height	*53.1 nm*
RMS roughness	*1.771 nm*

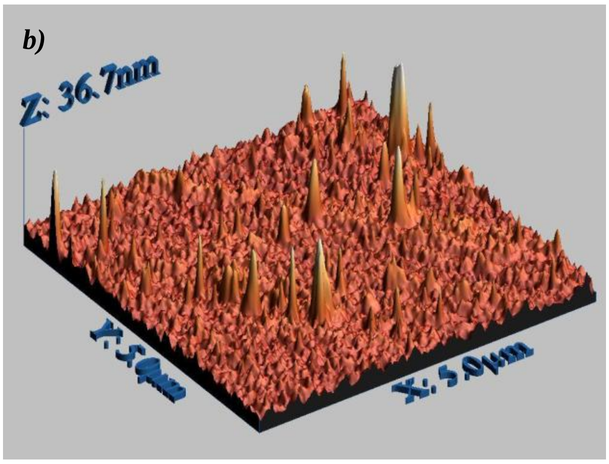

$\varnothing_A/\varnothing_C$	*1/1*
maximum height	*36.7 nm*
average height	*4.87 nm*
RMS roughness	*1.612 nm*

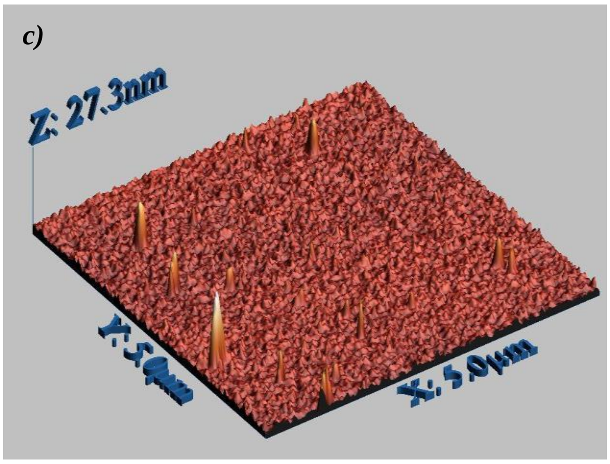

$\varnothing_A/\varnothing_C$	*1/3*
maximum height	*27.3 nm*
average height	*4.01 nm*
RMS roughness	*1.453 nm*

Fig. 8.24: *Typical AFM images of the DLC films deposited at different arc modes, with different electrode ratio a)* $\varnothing_A/\varnothing_C$ *= 3/1, b)* $\varnothing_A/\varnothing_C$ *= 3/1, c)* $\varnothing_A/\varnothing_C$ *= 3/1.*

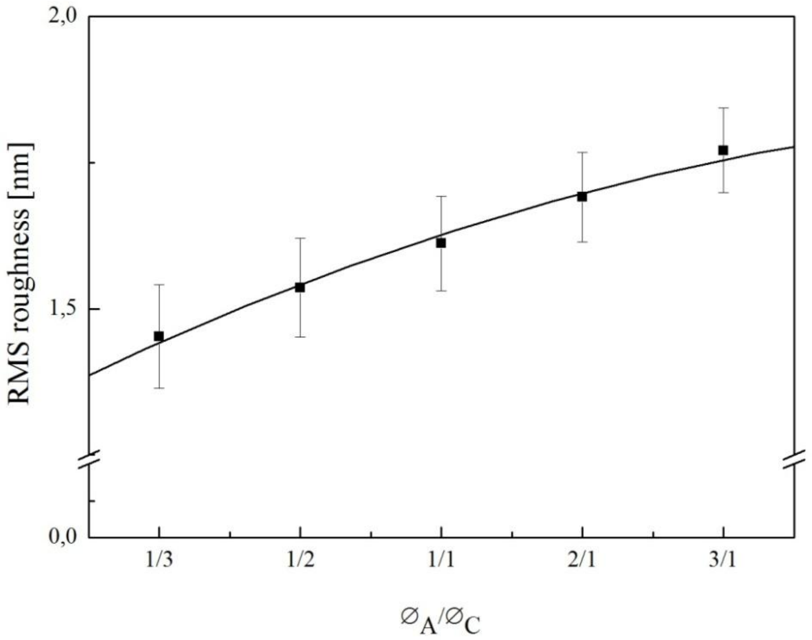

Fig. 8.25: *RMS roughness of DLC films with the electrode diameter variation.*

As in the case of SEM evaluation the AFM images also confirm the tendency of surface roughness reduction with the transition from the “cathodic” to “anodic” arc mode. But the measured values are lower than the substrate roughness measured via SEM due to the fact that for AFM evaluation only $5\ \mu m \times 5\ \mu m$ square area was used. Such a small area can not represent the whole substrate surface. The presence of graphite clusters and macroparticles in films deposited at “cathodic” mode leads to deterioration of their structural properties. Such deposition mode requires improvements concerning macroparticle filtering systems, like it was mentioned in *Chapter 5.2*.

8.2.3.1.2 Influence of Bias Voltage on Film Morphology

At the beginning of this chapter the influence of different arc modes on film morphology was shown. Now the influence of another parameter on film morphology – bias voltage to the substrate, will be investigated. As it was mentioned above, carbon is the chemical element properties are mostly dependent on particle energy. A negative DC bias was applied to the substrate in order to change the energy of particles arriving the substrate surface. During this experiment the anode to cathode electrode diameter ratio was kept constant at $\varnothing_A/\varnothing_C = 1/3$ (arc was operated in “anodic” mode). The only variable was negative bias voltage to the substrate from *0 V* to – 2*00 V* with *50 V* steps, as shown in Table 8.5.

Table 8.5: *Deposition parameters during anodic arc mode with different bias voltage.*

Bias voltage	*0 – 200 V*
Deposition time	*180 s*
Graphite electrodes	*RW 003, quality RW*
$\varnothing_A/\varnothing_C$	*3/1, 2/1, 1/1, 1/2, 1/3*

Typical SEM picture of the DLC films deposited under different bias voltages are shown in Fig. 8.26. Fig. 8.26 a) and b) show the film morphology of DLC films deposited at *0 V* bias, as one can see these samples are very smooth. In Fig. 8.26 e) and f) one can see that films deposited at – *200 V* bias have retained their smoothness and SEM images are not able to give more detailed information about the surface roughness.

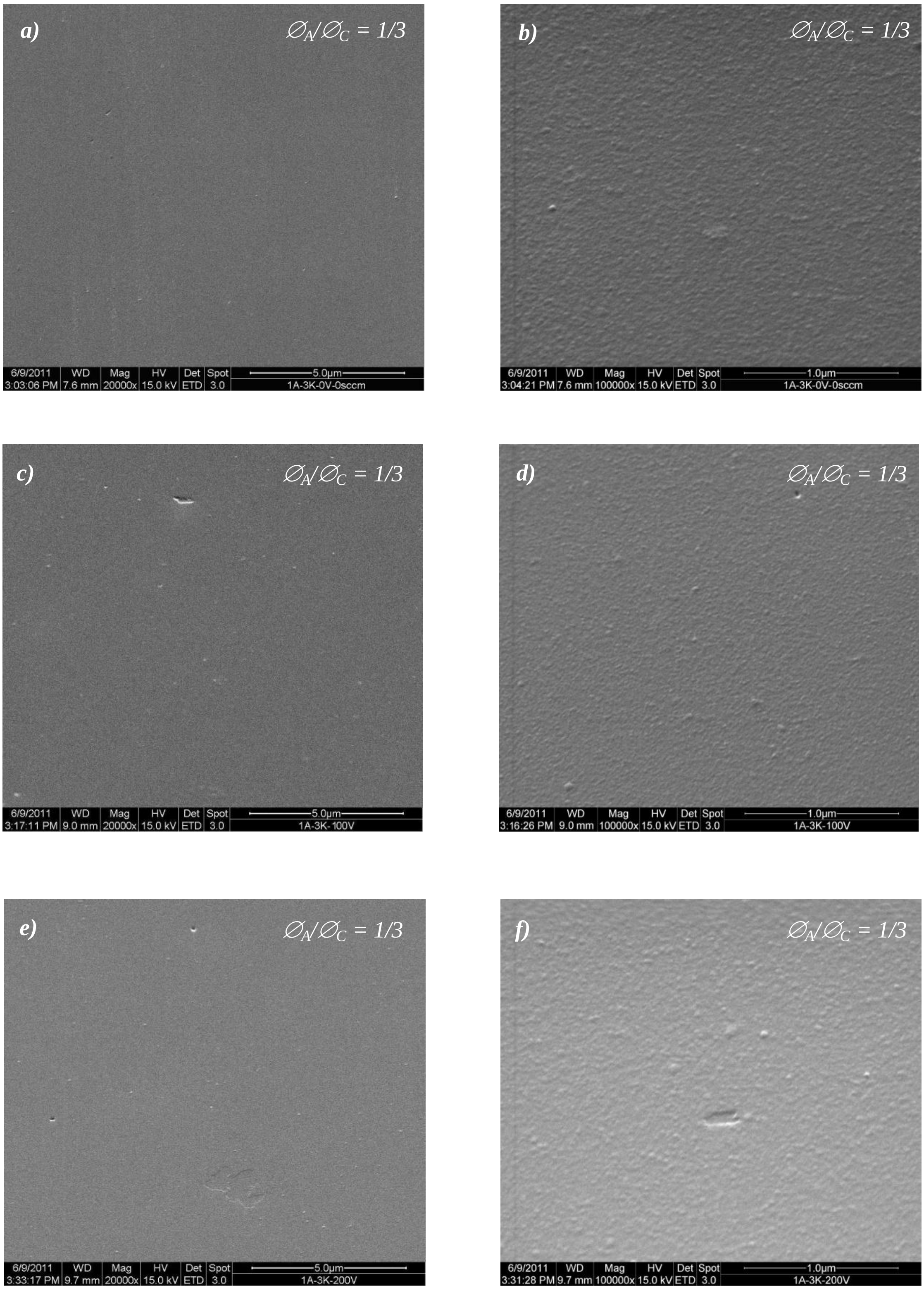

Fig. 8.26: *Typical SEM images of the DLC films deposited with the "anodic" arc with: a),b) 0 V bias voltage; c),d) „- 100“ V bias voltage; e),f) „- 200“ V bias voltage.*

For further information AFM images were used to evaluate the surface roughness.

Fig. 8.27 shows typical AFM images with their corresponding deposition parameters. One can see an increase of bias voltage leads to decrease of the surface roughness. The resulting substrate surface roughness dependence is shown in Fig. 8.28.

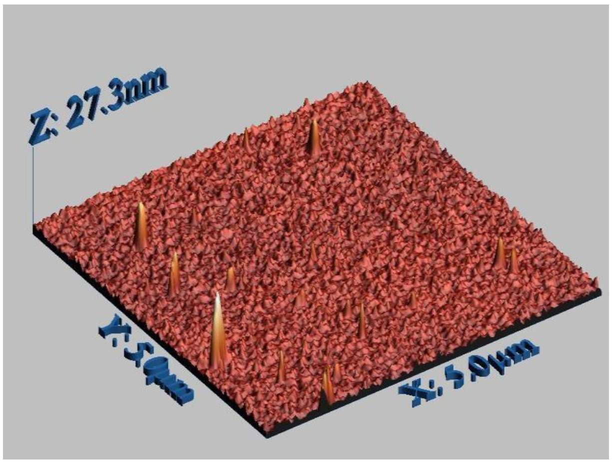

$\varnothing_A/\varnothing_C$	*1/3*
bias voltage	*0 V*
maximum height	*27.3 nm*
average height	*4.01 nm*
RMS roughness	*1.453 nm*

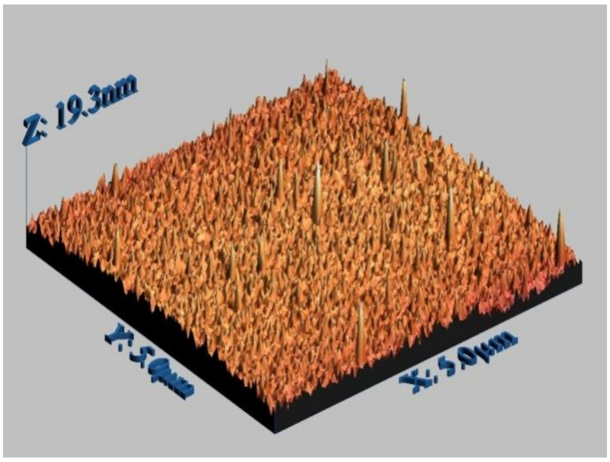

$\varnothing_A/\varnothing_C$	*1/3*
bias voltage	*- 100 V*
maximum height	*19.3 nm*
average height	*3.41 nm*
RMS roughness	*1.43 nm*

b)

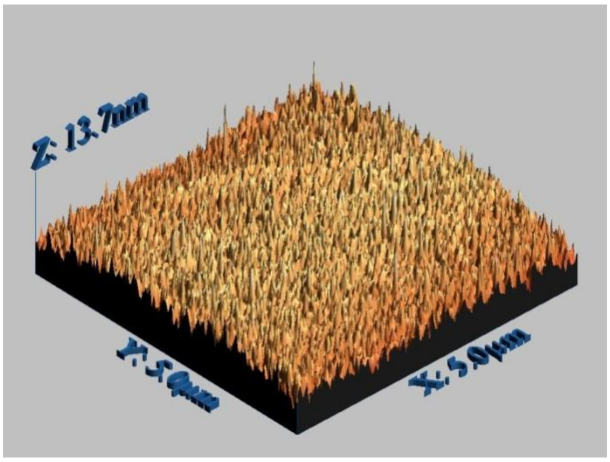

$\varnothing_A/\varnothing_C$	*1/3*
bias voltage	*- 200 V*
maximum height	*13.7 nm*
average height	*3.132 nm*
RMS roughness	*1.39 nm*

Fig. 8.27: *Typical AFM images of the DLC films deposited at "anodic" arc mode, with different bias voltages.*

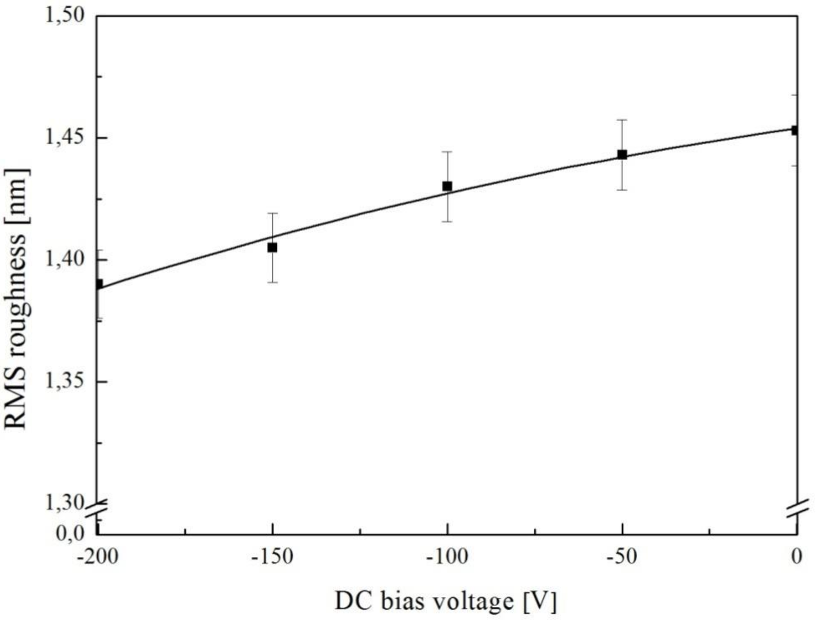

Fig. 8.28: *RMS roughness of DLC films as a function of the applied bias voltage.*

The film roughness decreases monotonically with an increase of the negative DC bias. The minimum surface roughness was observed on the coatings deposited at "*– 200" V* bias voltage, see Fig. 8.27c), it was *1,39 nm*.

8.2.3.1.3 Influence of Different Hydrogen Flow Rates on Film Morphology

The next important deposition parameter is working gas. In our experiments hydrogen with the purity grade 5 was used as a working gas. Hydrogen plays a key role during the DLC films growth [Lifshitz99, Robertson02]. Using different hydrogen flow rates it was possible to change the deposited film structures and structural properties. During this set of experiments the anode to cathode electrode diameter ratio was kept constant at $\varnothing_A/\varnothing_C = 1/3$ (arc was operated in "anodic" mode), the only variable was hydrogen flow rate from *0 sccm* to *100 sccm* with *10 sccm* steps, as shown in Table 8.6.

Table 8.6: *Deposition parameters during anodic arc mode with different hydrogen flow rates.*

Hydrogen flow rate	*0 sccm – 100 sccm*
Deposition time	*180 s*
Graphite electrodes	*RW 003, quality RW*
$\varnothing_A/\varnothing_C$	*1/3*

Typical SEM pictures of the DLC films deposited under different hydrogen flow rates are shown in Fig. 8.29.

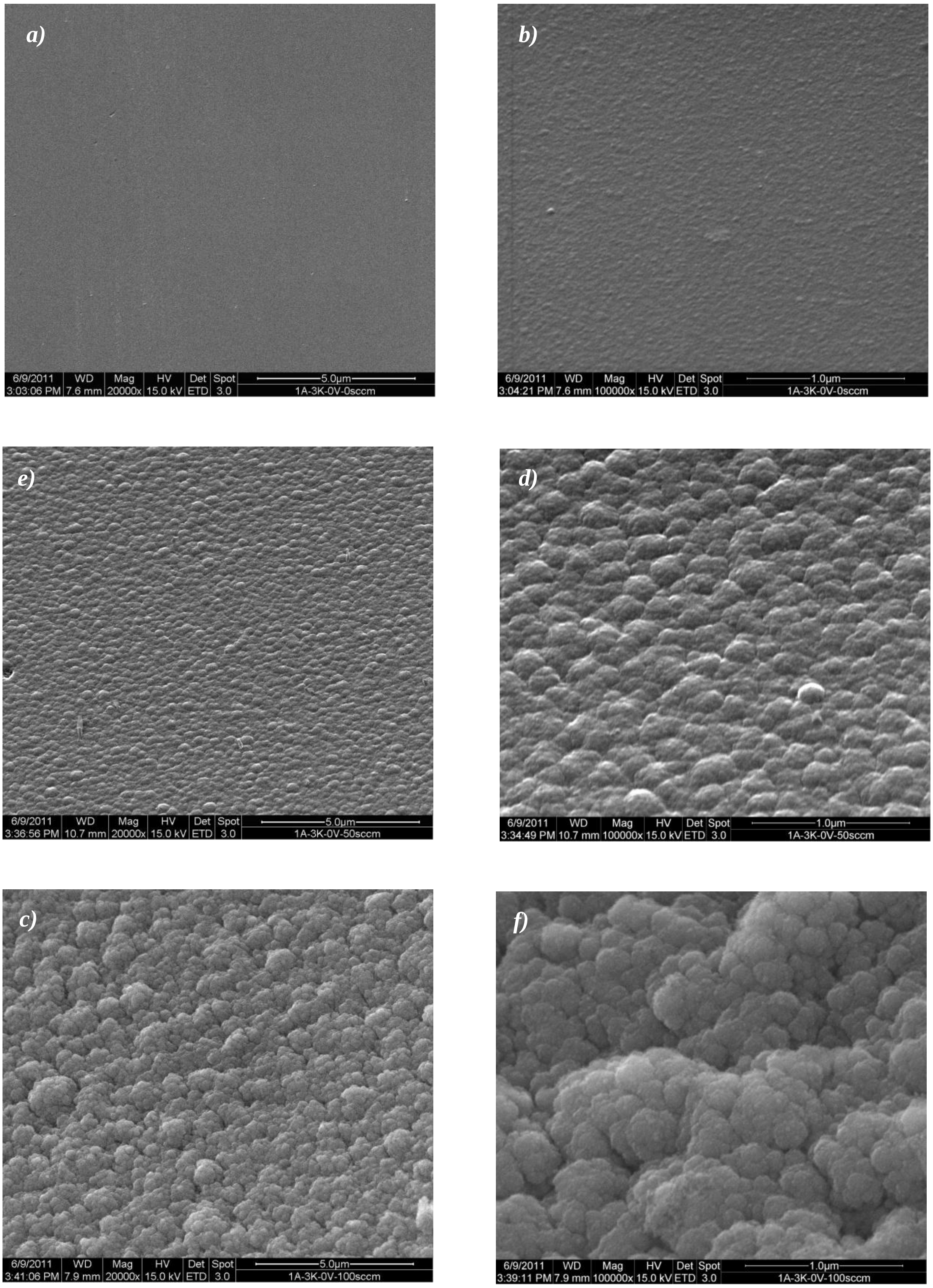

Fig. 8.29: *Typical SEM images of the DLC films deposited at "anodic" mode, with electrode ratio* $\varnothing_A/\varnothing_C = 1/3$*, at different* H_2 *flow rates a)and b) – 0 sccm, c)and d) – 50 sccm, e)and f) – 100 sccm.*

Fig. 8.29 a) and b) show the film morphology of DLC films deposited at *0 sccm* hydrogen flow rate, these images demonstrate that the samples have a very smooth surface and low roughness. In Fig. 8.29 c) and d) one can see that films deposited at *50 sccm* hydrogen flow rate become more rough. DLC films deposited at *100 sccm* hydrogen flow rate are shown in Fig. 8.29 e) and f), they demonstrate the maximum roughness among all the films deposited. Compared with other SEM images DLC films deposited without any working gas are uniform and have very low roughness.

Fig. 8.30 shows typical AFM images of the measured substrates and their evaluation parameters in the corresponding table.

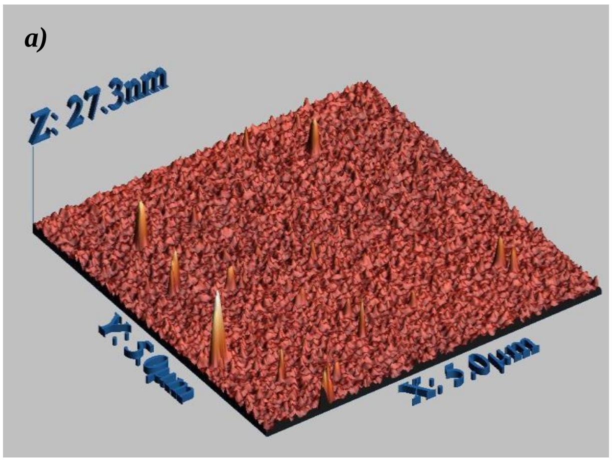

$\varnothing_A/\varnothing_C$	*1/3*
hydrogen flow rate	*0 sccm*
maximum height	*27.3 nm*
average height	*4.01 nm*
RMS roughness	*1.453 nm*

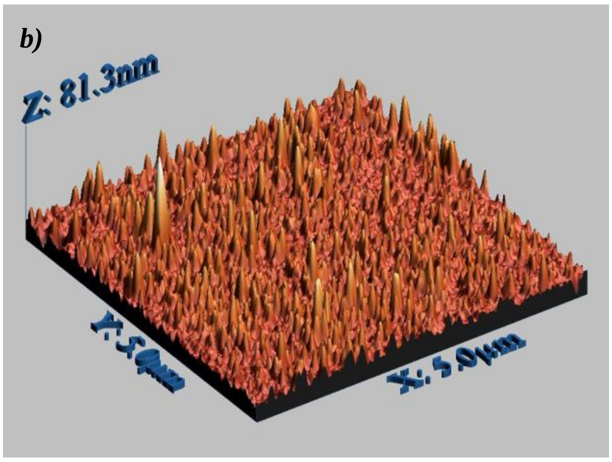

$\varnothing_A/\varnothing_C$	*1/3*
hydrogen flow rate	*50 sccm*
maximum height	*81.35 nm*
average height	*16.76 nm*
RMS roughness	*5.21 nm*

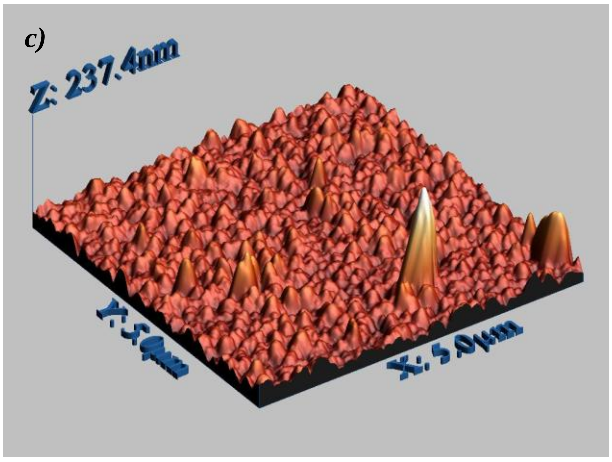

$\varnothing_A/\varnothing_C$	1/3
hydrogen flow rate	*100 sccm*
maximum height	*237.4 nm*
average height	*34.89 nm*
RMS roughness	*15.11 nm*

Fig. 8.30: *Typical AFM images of the DLC films deposited at different hydrogen flow rates a) 0 sccm, b) 50 sccm, c) 100 sccm.*

Fig. 8.30 a) corresponds to the films deposited without any working gas, so it shows the lowest roughness within these experiments. Like the SEM images the AFM images confirms an increase of the surface roughness due to the higher hydrogen flow rate. The film roughness increases monotonically with increasing hydrogen flow rate. The maximum surface roughness was observed for the coatings with *100 sccm* H_2 flow rate, see Fig. 8.30 c). The resulting substrate roughness dependence is shown in Fig. 8.31.

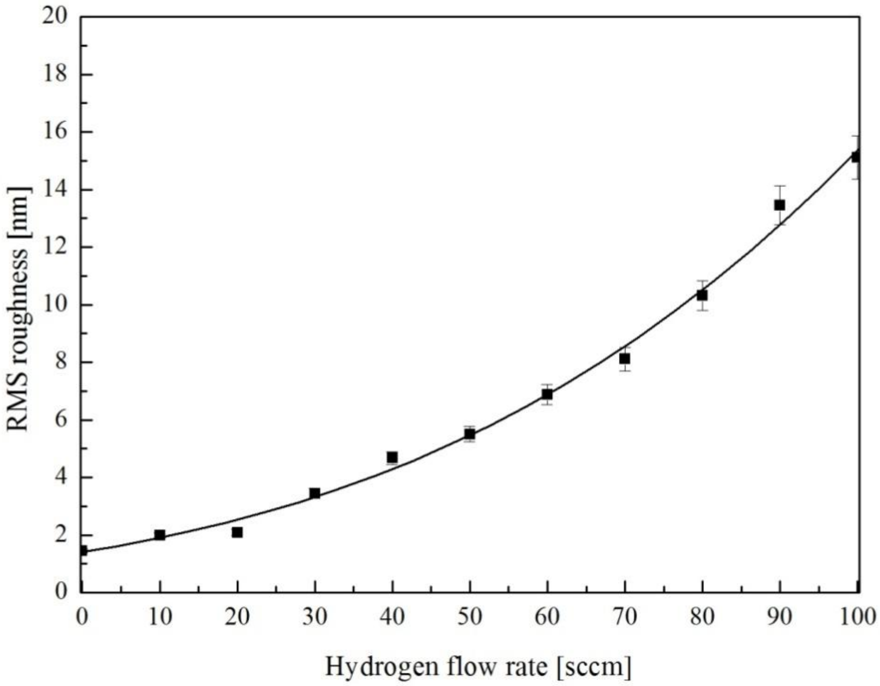

Fig. 8.31: *RMS roughness of DLC films as a function of hydrogen flow rate.*

Both, SEM and AFM images have shown the influence of deposition parameters on film surface morphology. The summarized substrate roughness dependence as a function of all deposition parameters is shown in Fig. 8.32.

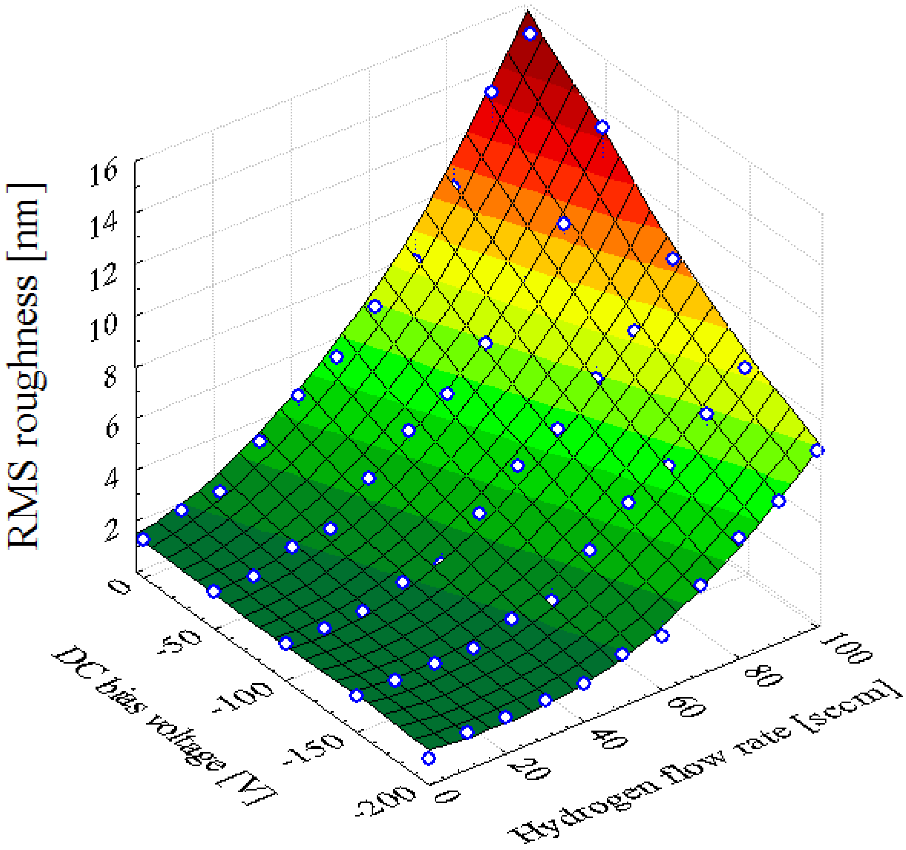

Fig. 8.32: *The film roughness as a function of bias voltage and hydrogen flow rate.*

DLC films deposited by "anodic" arc mode at "*– 200" V* bias voltage have shown the best smoothness and almost no macroparticle presence in the deposited films. As it was shown the variation of hydrogen flow rate has stronger influence on the film morphology than the other deposition parameters.

8.2.3.2 Hydrogen Content in the DLC Film

8.2.3.2.1 Hydrogen to Carbon Ratio

As it was mentioned above, hydrogen atoms play a key role in DLC coatings. They determine the physical and chemical properties of the deposited films. In order to continue film evaluation, it is necessary to know the hydrogen to carbon atoms *H/C* ratio. To evaluate this ratio a non-destructive spectroscopic method was used. Before the evaluation it is necessary to know the amount of hydrogen atoms in the vacuum chamber. The chamber is a vessel with known volume and some residual pressure. To know the hydrogen vapour pressure exactly, it is necessary to know the hydrogen partial pressure inside the chamber. This information can be obtained from residual gas analyzer software from *QMS-200 Prisma by Balzers*™ mass-spectrometer, see Fig. 8.4. According to the kinetic theory of gases, the average molecular kinetic energy is proportional to the absolute temperature:

$$\overline{E_{kin}} = \frac{mv^2}{2} = \frac{3}{2}k_BT, \tag{8.5}$$

where T is a gas temperature, k_B is the Boltzmann's constant ($k_B = 1.38 \cdot 10^{-23} J/K$) and $\overline{v}$ is the mean particle velocity perpendicular to the wall.

Therefore the number of impacts per area and time is:

$$Z = \frac{n}{6}v, \tag{8.6}$$

where $n = N/N_A$, N_A is Avogadro's number ($N_A = 6.022 \cdot 10^{-23} mol^{-1}$). According to the ideal gas law:

$$p = nk_BT. \tag{8.7}$$

Then:

$$n = p/k_BT \tag{8.8}$$

using υ from equation (8.5) and n from equation (8.8) it is possible to replace them in equation (8.6):

$$Z_H = \frac{1}{6}\frac{p}{k_BT}\sqrt{\frac{3k_BT}{m}} \tag{8.9}$$

To evaluate the amount of deposited carbon particles, it is necessary to know the deposition rate of carbon per area and per time. In order to calculate this amount, the films were obtained with deposition time $t_{dep} = 180\ sec$ onto round glass substrates with $d_{sub} = 25\ mm$ and corresponding surface area $A = \pi \cdot r^2$ where $A = 4.91 \times 10^{-4}\ m^2$. The substrate weight was measured before and after the deposition using a micro balance, and after substrate mass subtraction the mass of the deposited film – *m* was obtained.

It is known that:

$$1\ Mol\ C = 12g \qquad (8.10).$$

For a single carbon atom:

$$m_C = \frac{12}{6.022\times10^{-23}}\,g = 20.106\times10^{-27}\ kg \qquad (8.11)$$

When the deposited mass is known one can calculate the amount of the deposited carbon atoms at the whole substrate area. Then, dividing it by the deposition time and surface area, one can calculate the amount of deposited carbon atoms per area per second.

In order to estimate the number of carbon atoms in the deposited film, it was necessary to make the assumption that deposited film contains only carbon atom. But this assumption is inaccurate due to the fact that the deposited film contains not only carbon atoms but also hydrogen atoms. In fact, the deposited films contain some amount of hydrogen atoms in addition to carbon atoms with mass $m_C = 12\ amu$ when the hydrogen atom mass m_H is only *1 amu*. Even if one assume that in deposited film there is an equal amount of carbon and hydrogen atoms the error in the calculations is still less than *10%*.

The next assumption is that the adhesion coefficient of all particles coming to the surface is equal to one.

In the following Table 8.7, the calculated hydrogen to carbon atoms ratio for different films depending on the deposition parameters is given:

Table 8.7 *Calculated hydrogen to carbon atoms ratio*

Bias voltage [V]	0	100	200	100	200	0	100
H_2 flow rate [sccm]	10	10	10	50	50	80	80
H_2 part. pres. [Pa]	0.41	0.37	0.39	2.52	2.50	9.97	10
Deposition time [s]	180	180	180	180	180	180	180
Mass deposited [kg]	1.04×10^{-6}	1.06×10^{-6}	9.03×10^{-7}	1.44×10^{-6}	1.09×10^{-6}	2.02×10^{-6}	1.35×10^{-6}
Film thickness [m]	1.09×10^{-6}	9.63×10^{-7}	8.86×10^{-7}	1.44×10^{-6}	1.16×10^{-6}	2.47×10^{-6}	1.44×10^{-6}
Z_H [at $\cdot m^{-2}\cdot s^{-1}$]	4.50×10^{22}	4.06×10^{22}	4.28×10^{22}	2.77×10^{23}	2.74×10^{23}	1.09×10^{24}	1.10×10^{24}
Z_C [at $\cdot m^{-2}\cdot s^{-1}$]	5.88×10^{23}	5.98×10^{22}	5.08×10^{22}	8.13×10^{23}	6.12×10^{23}	1.14×10^{24}	7.60×10^{24}
$Z_H/(Z_H+Z_C)$ [%]	7	6	8	25	31	49	59

As one can see the concentration of hydrogen atoms in the deposited films is proportional to the hydrogen flow rate and also depends on the applied bias voltage. These results are shown in Fig. 8.33.

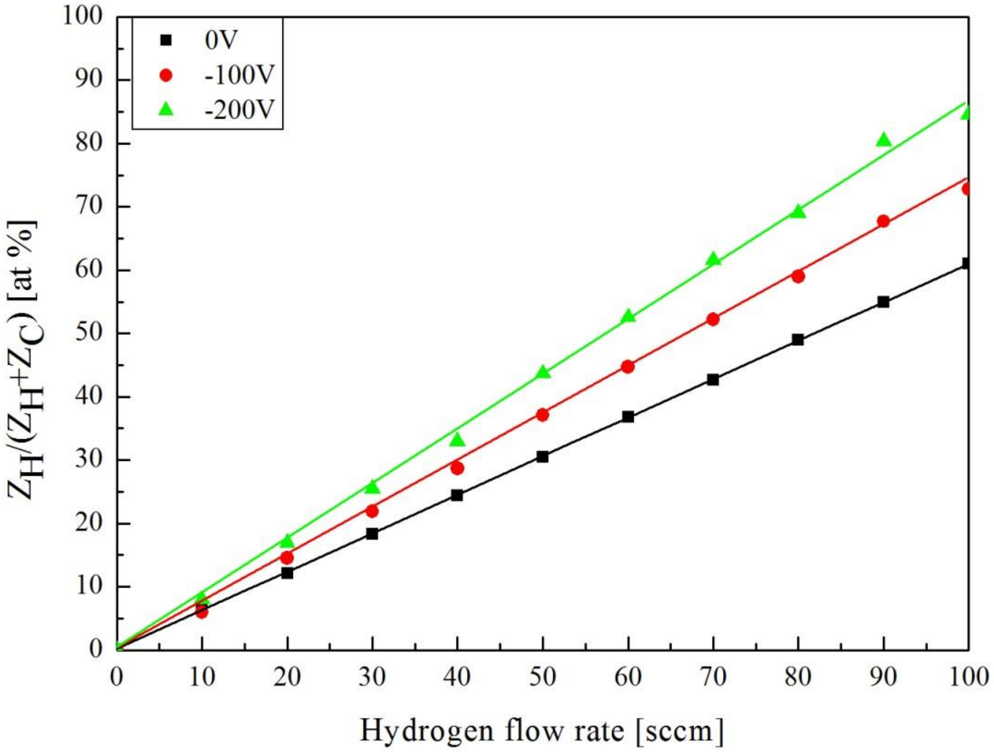

Fig. 8.33: *Calculated hydrogen concentration in deposited DLC films as a function of different hydrogen flow rates.*

Hydrogen and water are the typical residual gases in every vacuum deposition method, and always present during the plasma deposition and desired or undesired interact with the depositing ions and by-turn affects resulting film properties.

To understand and to take into account this influence it is necessary to evaluate the hydrogen concentration in the deposited film. Usually for this purpose different analytical methods were used elastic recoil detection analysis (*ERDA*) [Zou89], secondary ion mass-spectrometry (*SIMS*) [Madronero95] and nuclear reaction analysis (*NRA*) [Lanford95]. But all these methods are expensive and destructive. In this work was made an attempt to replace such methods with non-destructive spectroscopic technique.

8.2.3.2.2 Nuclear Reaction Analysis (NRA)

NRA method is used to obtain the information about hydrogen concentration in the deposited films. The samples with defined deposition parameters were chosen to obtain the information about hydrogen concentration, and then these data were used to calibrate spectroscopic results. Fig. 8.34 shows the measured by NRA hydrogen concentration for the substrates deposited at the different hydrogen flow rates.

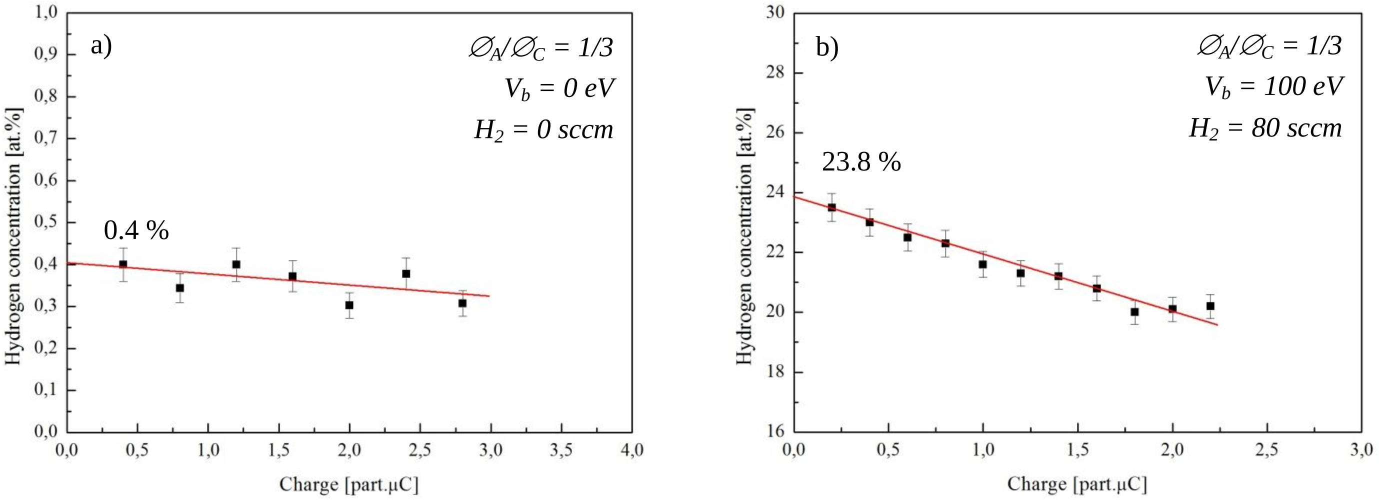

Fig.8.34: *The NRA hydrogen concentration as a function of the deposited charge for different hydrogen flow rates: a) 0 sccm, b) 80 sccm.*

The loss of hydrogen due to the radiation impact is measured as a function of the deposited charge; extrapolation to zero charge gives the actual hydrogen concentration. As one can see that variation of hydrogen flow rate have strong influence on hydrogen concentration in the deposited DLC films. According to the NRA measurements the assumption that DLC films deposited without hydrogen are “hydrogen-free” is wrong. The films deposited at the working pressure $< 10^{-6}$ *mbar* still contain very small amount of hydrogen. This can be explained by the fact that residual gas atmosphere in the vacuum chamber always contains hydrogen, see Fig. 8.1.

The hydrogen concentration determined by NRA is listed in the Table 8.8 and plotted in Fig. 8.35 as a function of the deposition parameters.

Table 8.8: *Measured by NRA hydrogen concentration*

Bias voltage [V]	*0*	*0*	*100*	*200*	*100*	*200*	*0*	*100*
H_2 flow rate [sccm]	*0*	*10*	*10*	*10*	*50*	*50*	*80*	*80*
Z_H by NRA [at %]	*0.4*	*7.9*	*9.6*	*8.4*	*15*	*17*	*21.4*	*23.8*

Using the results from the NRA measurements it was possible to determine the hydrogen concentration for different deposition parameters, see Fig. 8.35.

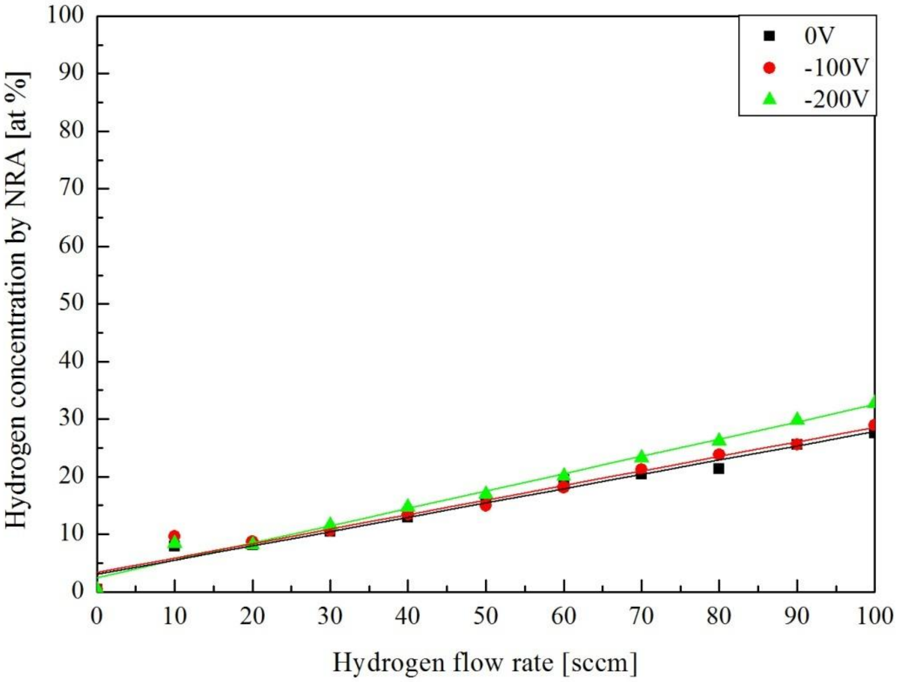

$\varnothing_A/\varnothing_C = 1/3$

Fig.8.35: *Variation of hydrogen concentration with variation of deposition parameters.*

Fig. 8.35 shows that films deposited at bias voltage “- *200 V”* have higher hydrogen concentration than film deposited without bias voltage. These results confirm spectroscopic calculations made to evaluate hydrogen to carbon atom ratio in the deposited films, see Fig. 8.33. This can be explained by the fact that bias voltage influencing only charged particles. In the plasma only carbon and hydrogen ions are present. The hydrogen ions are lighter than carbon ions so they are easier to control, therefore more hydrogen ions reaches a biased substrate.

8.2.3.2.3 Adhesion Coefficient

Knowing the hydrogen concentration in the deposited films the adhesion coefficient was obtained, see Fig. 8.36.

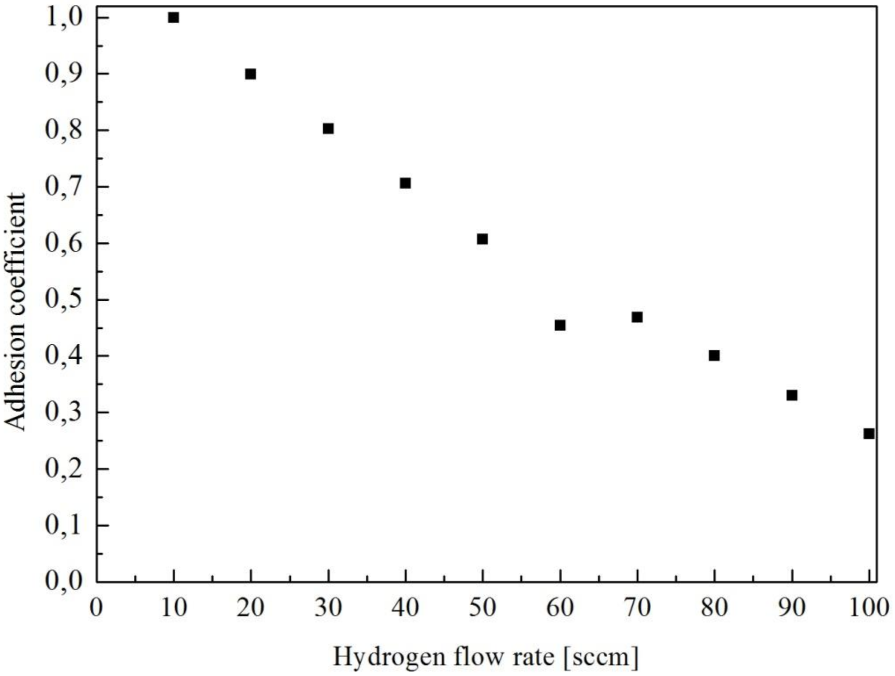

Fig. 8.36: *Adhesion coefficient for different hydrogen flow rates.*

Using this adhesion coefficient the hydrogen content in the deposited films can be determined without any structural analysis only by using spectroscopic techniques.

8.2.4 Optical Properties and Electronic Structure of DLC Films

In order to obtain the information about DLC film structure and chemical composition the non-destructive spectroscopic methods are used. In this work, an *ex-situ UV-VIS* spectroscopy was used in order to investigate the optical properties of the DLC films. Using spectroscopic data, it is possible to get information about the electronic structure of the films.

The optical spectra were recorded in a range from *200* to *2000 nm* using *UV-VIS-NIR Lambda-9 PerkinElmer* spectrometer. The spectrometer was operated in transmittance mode.

8.2.4.1 Film Transmittance

8.2.4.1.1 Influence of Different Arc Modes on Film Transmittance

Different arc modes are characterized by different particle energies and degree of ionisation, see *Chapter 8.1.4*. Therefore it is very important to investigate the optical properties of the DLC films to get to know the arc mode parameters. In order to visualize the effect of particle energy the films were additionally biased from *0 V* to "*– 1000 V*". All films were deposited in a vacuum without working gas. The first investigated parameter is the film transmittance. In Fig. 8.37 and Fig. 8.38 one can see measured optical spectra as a function of "anodic" to "cathodic" arc modes transition.

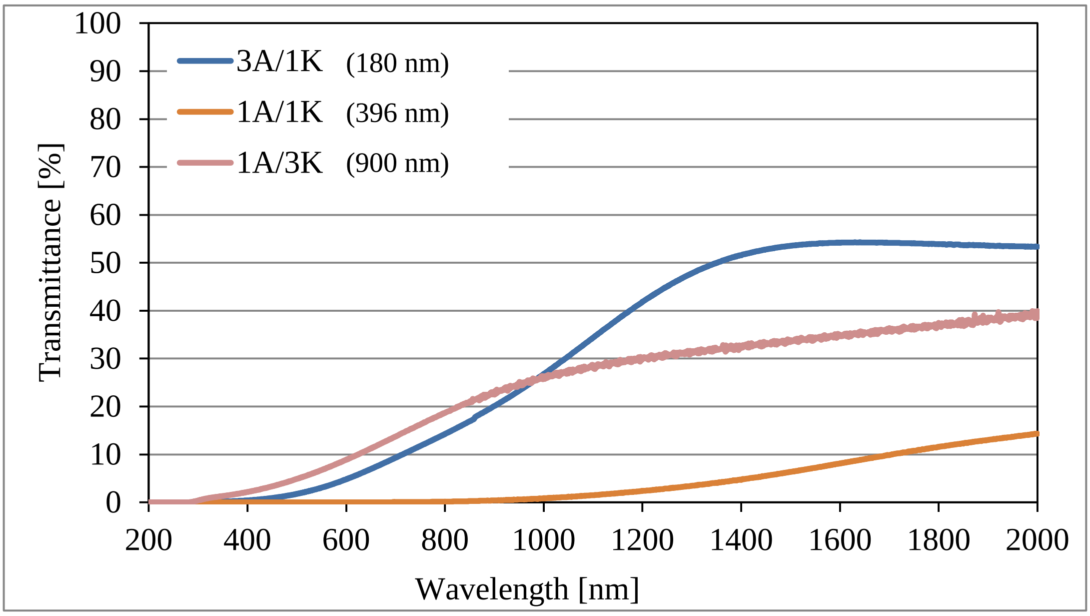

Fig. 8.37: *Measured film transmittance in a range from 200 to 2000 nm for deposited films according to the different electrode diameter ratios* $\varnothing_A/\varnothing_C$*, without hydrogen admixture.*

The film thickness is the main parameter determining the film transmittance. As it was shown before every mode is characterized by the different deposition rates (*Chapter 8.2.2*), which determine the film thickness.

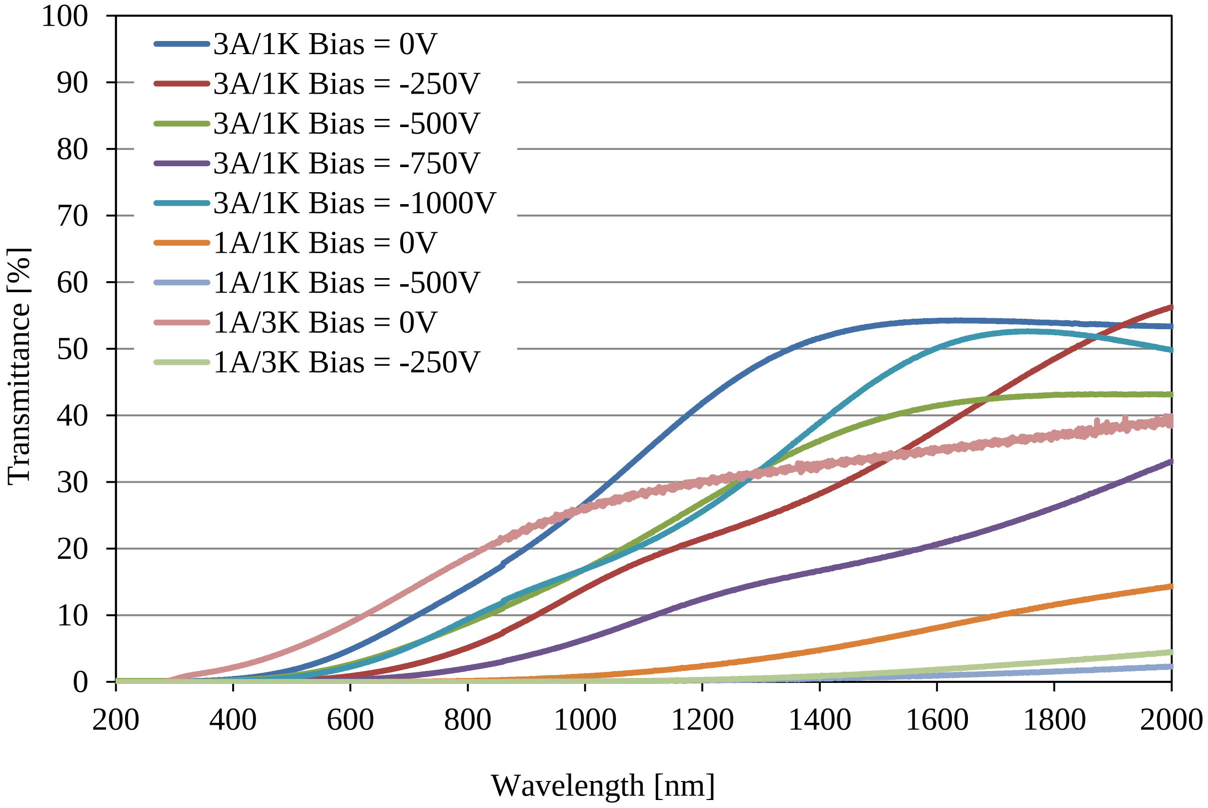

Fig. 8.38: *Measured film transmittance for deposited films according to the different electrode ratios and different bias voltages, without hydrogen admixture [Khlopyanova12].*

One can see that the film transmittance differs for each arc mode. Second – all films, deposited at different arc modes and bias voltages, show low film transmittance. Some of the films have very low transmittance but such effect is caused mainly by the different film thickness. As it was shown in *Chapter8.2.2*, each arc mode is characterized by different deposition rates, so the films deposited by the cathodic mode were the thinnest and therefore have the higher transmittance.

According to the measured film transmittance, there is a strong absorption range in a spectral range between *200 nm – 400 nm (2.6 eV – 6.2 eV)*, therefore this range was excluded from dielectric function calculation. The imaginary part ε_2 of the dielectric function for all deposited films was shown in a range from *0.6 eV to 2.6 eV*.

In order to obtain the imaginary part ε_2 of the dielectric function, all measured spectra were simulated by the commercial *SCOUT 3.6 ™* program, where for every measured spectrum the dielectric function was simulated for the whole measured spectral range.

8.2.4.1.2 Influence of Different Hydrogen Flow Rates on Film Transmittance

In Fig. 8.39 one can see measured optical spectra as functions of hydrogen flow rate.

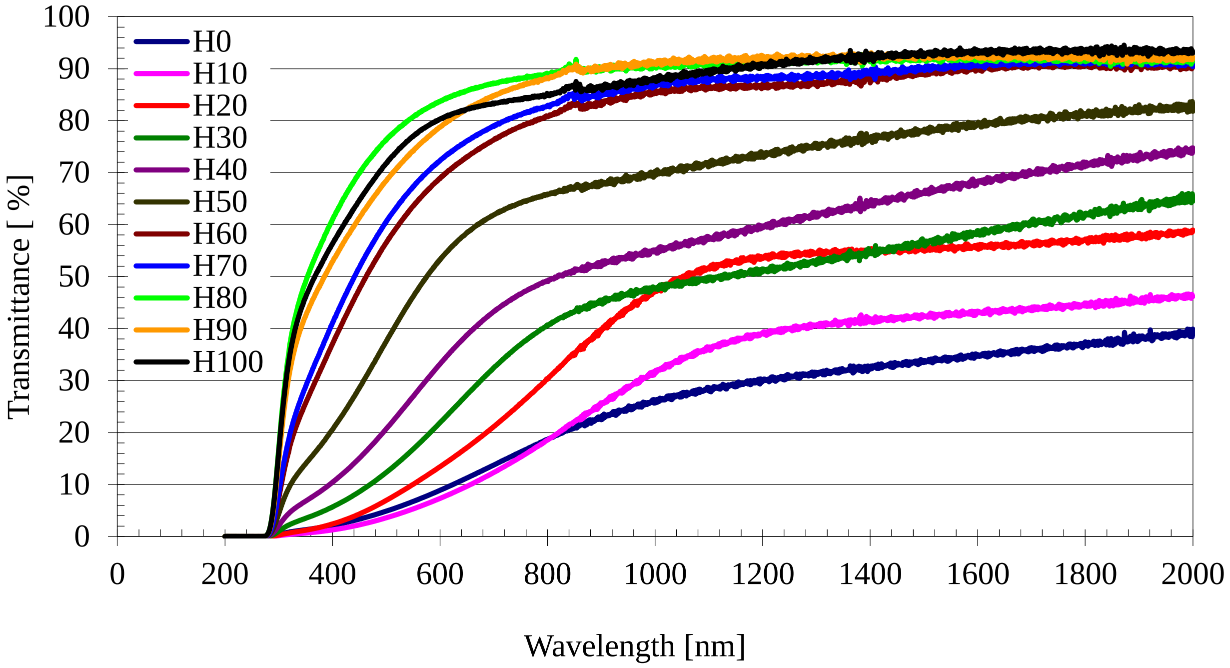

Fig. 8.39: *Measured film transmittance in a range from 200 to 2000 nm for deposited films according to the different hydrogen flow rates from 0 sccm to 100 sccm,* $\varnothing_A/\varnothing_C = 1/3$ *and 0 V bias voltage.*

The dielectric function was calculated in the range *200 nm* to *2000 nm*. As the transmittance appears below a wavelength of *400 nm*, the dielectric function in this region is more or less arbitrary. Therefore, it is shown in the following figures only in the range *400 nm* to *2000 nm*.

It was found that the film transmittance strongly depends on the deposition parameters – especially the hydrogen flow rate. According to the *NRA* measurements the higher hydrogen flow rates lead to higher hydrogen concentration in the deposited films which in turn leads to the higher film transmittance.

In order to demonstrate energy dependence the obtained optical spectra they were converted from *nm* to cm^{-1} by commercial *SCOUT 3.6™* simulation program. Such conversion also allows direct interpretation in the band model. For every measured spectrum the dielectric function was simulated for the whole measured spectral range. In this dielectric function, one harmonic oscillator for interband transitions was used. For the band gap calculation the *OJL* (*O'Leary, Johnson, Lim*) interband transition model for amorphous materials was used

[O’Leary97]. In the *OJL* model, the expressions for the *DOS* (density of states) are given for the optical transition from the valence band to the conduction band. The dielectric function parameters were continuously varied till the simulated curve has no, or very negligible deviation from the measured curve. In Table 8.9 one can see the main fitting parameters which were used in the model.

Tab. 8.9.*The dielectric function parameters received by using SCOUT 3.6™ program simulation for DLC film obtained at 0 V bias voltage and 50 sccm hydrogen flow rate.*

	Parameter	*Value*
1	***a-CH:band gap:*** *gamma_v*	*10436.4* cm^{-1}
2	***a-CH:band gap:*** E_0	*148357* cm^{-1}
3	***a-CH:band gap:*** *mass*	*0.0737* cm^{-1}
4	***a-CH:band gap:*** *decay*	*6264.2* cm^{-1}
5	***a-CH:H.O:*** *resonance frequency*	*39592.9* cm^{-1}
6	***a-CH:H.O:*** *oscillator strength*	*67808.1* cm^{-1}
7	***a-CH:H.O:*** *damping*	*3410.6* cm^{-1}
8	***a-CH:DB:*** *imaginary part*	*0.2215* cm^{-1}
9	***Stack 1 Layer 2 a-CH:*** *Layer thickness*	*0.165* μm

Where *gamma* determines the width of the band tails, E_0 defines the gap between the band edges, *mass* is a scaling coefficient determining the shape of the *DOS*, *decay* determines the way how the imaginary part of the dielectric function decays to zero for high frequencies [Gordijn04].

In Fig. 8.40 one can see the measured spectrum (red line) and the fitted one (blue).

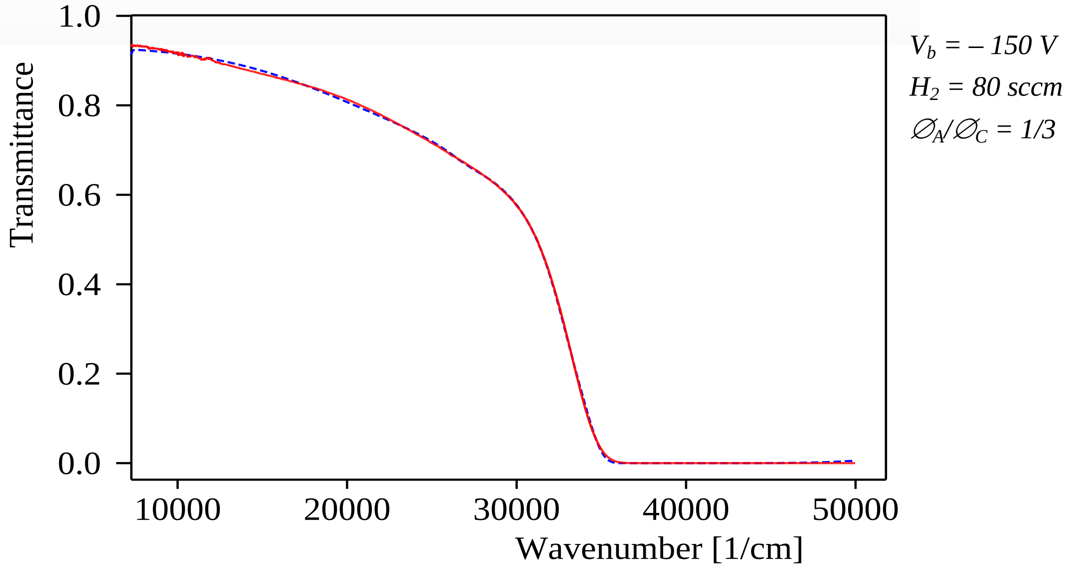

Fig. 8.40: *Measured and simulated film transmittance for deposited films. Red curve corresponds to the measured spectrum, blue to the fitted one.*

In the Fig. 8.41 one can see measured and simulated film transmittance curves for DLC films obtained at different deposition conditions (hydrogen flow rates: *20*, *50* and *80 sccm* correspondingly) in a range from *200* to *2000 nm* (*50000* to *5000* cm^{-1}) with corresponding band gap.

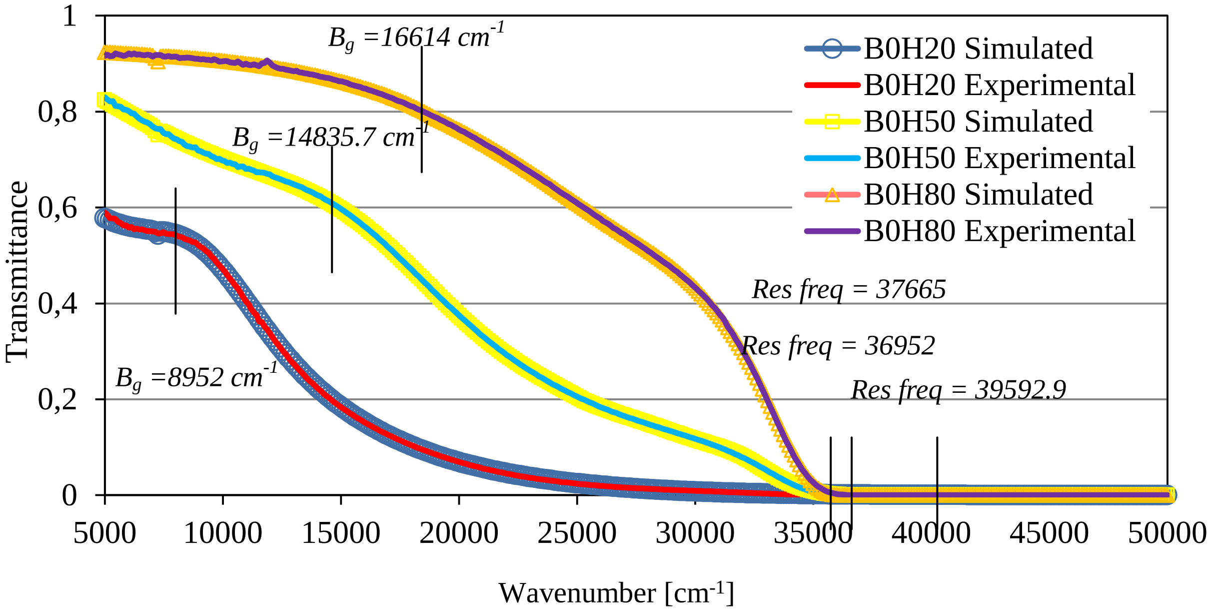

Fig. 8.41: *Measured and simulated film transmittance spectra for different deposited films at various hydrogen flow rates.*

For a more precise fitting, film thickness was also measured by a *Dektak 6M* profilometer, and used as a starting value for the *SCOUT 3.6 ™* simulations. In order to prove the applicability of the fitting model the film thicknesses d_{prof} measured by the *Dektak 6M* profilometer and film thickness calculated in the model d_{opt} were compared. In Fig. 8.42 one can see film thicknesses measured by profilometer d_{prof} plotted against the calculated d_{opt} from the *SCOUT 3.6 ™*.

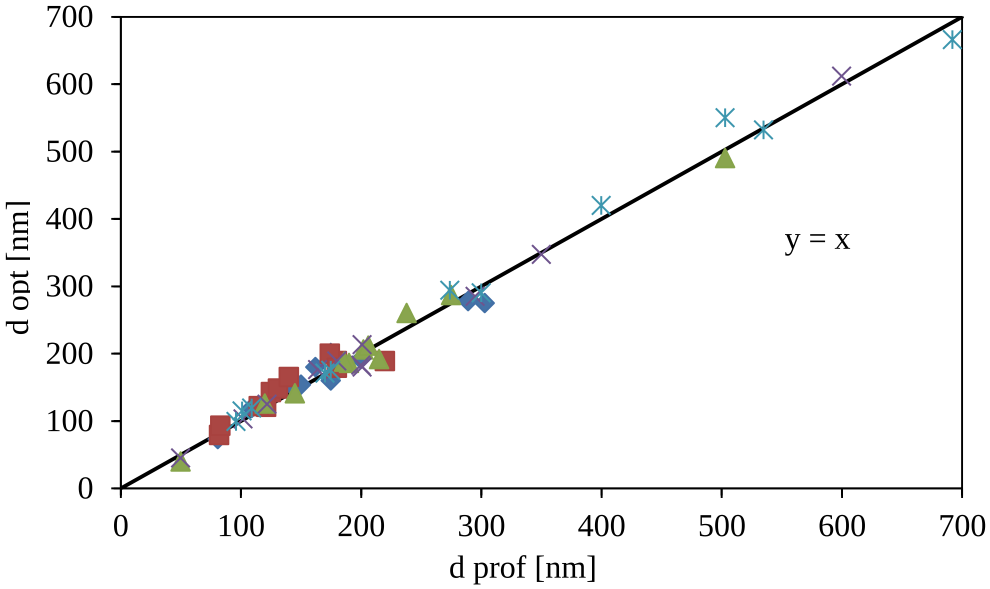

Fig. 8.42: *Film thickness measured by profilometer* d_{prof} *and obtained from SCOUT 3.6 ™ program* d_{opt}.

The straight line at the diagram with slope equal to 1 shows there is very small discrepancy between measured and calculated film thicknesses, less than *10 %*. The resulting diagram confirms the correctness of the fitting model.

8.2.4.2 The Optical Band Gap

The optical band gap is the main parameter determines the optical properties of any material. In this chapter the influence of deposition parameters on the band gap for deposited DLC films is shown.

8.2.4.2.1 Influence of Different Arc Modes on the Band Gap

In Fig.8.43 one can see the diagram of the optical band gap E_g from the *SCOUT 3.6* ^{TM} as a function of the deposition parameters $\varnothing_A/\varnothing_C$ and bias voltage without hydrogen admixture to the plasma.

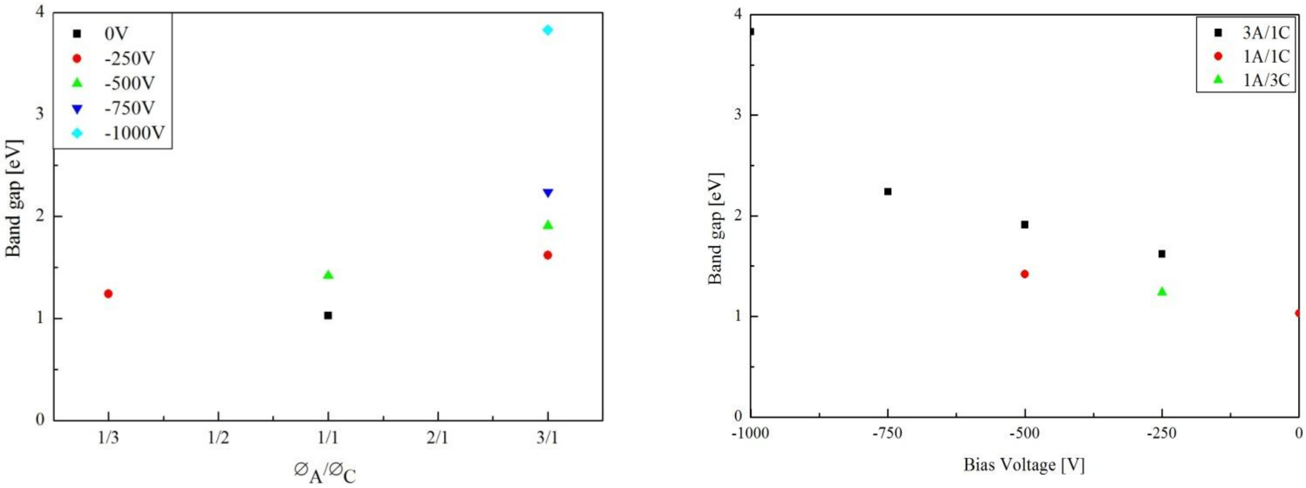

Fig. 8.43: *Dependence of the band gap of DLC films on arc mode and bias voltage.*

In Fig.8.43 one can see, the films deposited at “cathodic” arc mode ($\varnothing_A/\varnothing_C = 3/1$) have the biggest optical band gap among all arc modes. The smallest band gap have films deposited at “anodic” mode ($\varnothing_A/\varnothing_C = 1/3$). By increase of bias voltage the optical band gap also increase, and stays the biggest for films deposited at cathodic arc mode. As it was shown in *Chapter 8.1.4*, the arc mode and the bias voltage both are influencing the ion energy. The ion energy is one of the main parameters which influence the sp^3/sp^2 – ratio in the films. This ratio is closely related to the optical band gap [Ferrari00]. The “cathodic” arc mode is characterized by high degree of ionisation and high ion energy ($E_i \approx 20\ eV$), while in the “anodic” mode the carbon ions have energy $E_i \approx 7\ eV$, as shown in *Chapter 8.1.4*. The correlation between the optical band gap and sp^3/sp^2 – ratio will be discussed below.

8.2.4.2.2 Influence of Different Hydrogen Flow Rates on the Band Gap

In Fig. 8.44 one can see the diagram of the optical band gap E_g from the *SCOUT 3.6* ^{TM} as a function of hydrogen flow rate and bias voltage.

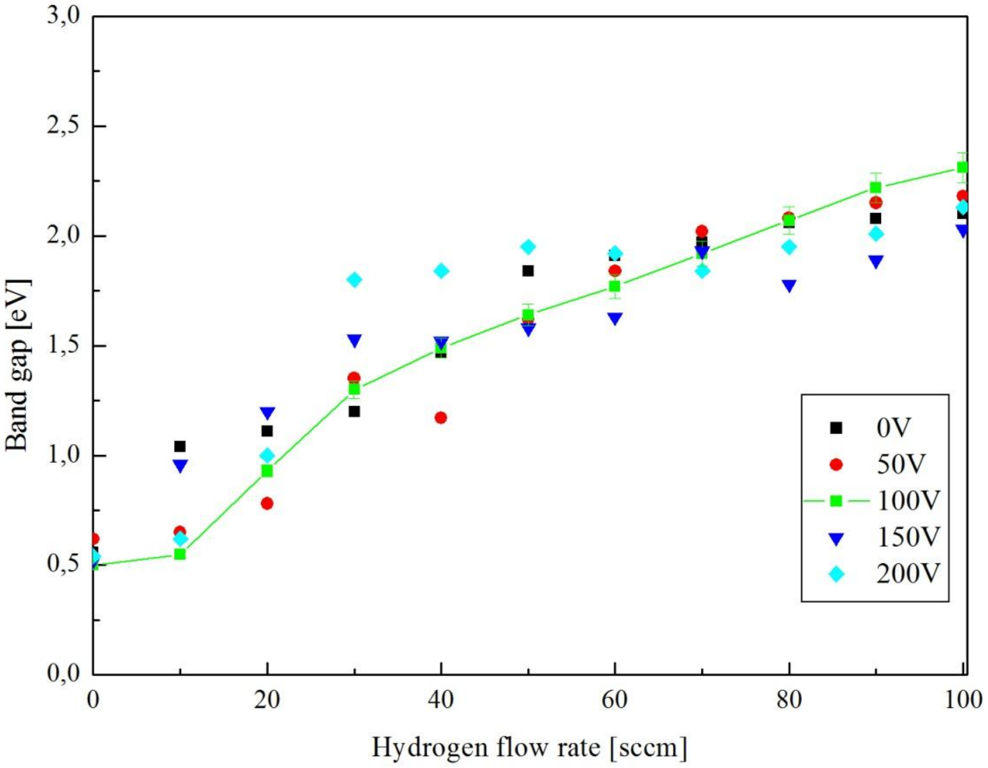

Fig. 8.44: *Dependence of the band gap* E_g *of DLC films on the deposition parameters.*

In Fig.8.44 one can see that the hydrogen flow rate (hydrogen content) has a strong effect on the optical band gap E_g. An increase of hydrogen concentration leads to an increase of the optical band gap E_g. The obtained results are in good agreement with the literature values and confirm other experimental works [Robertson02]. The effect of applied negative bias voltage is much weaker than the effect of hydrogen concentration.

8.2.4.3 DLC Band Model

Due to the presence of σ and π electrons in DLC, their electronic structure consists of two valence and two conduction bands. The valence bands correspond to σ and π bonding states and conduction bands correspond to σ^* and π^* anti-bonding states. The density of states (*DOS*) corresponding to this situation is schematically depicted in Fig.8.45. The *DOS* distributions of σ and π valence electrons are parabolic (rigid-band model [Stern67]).

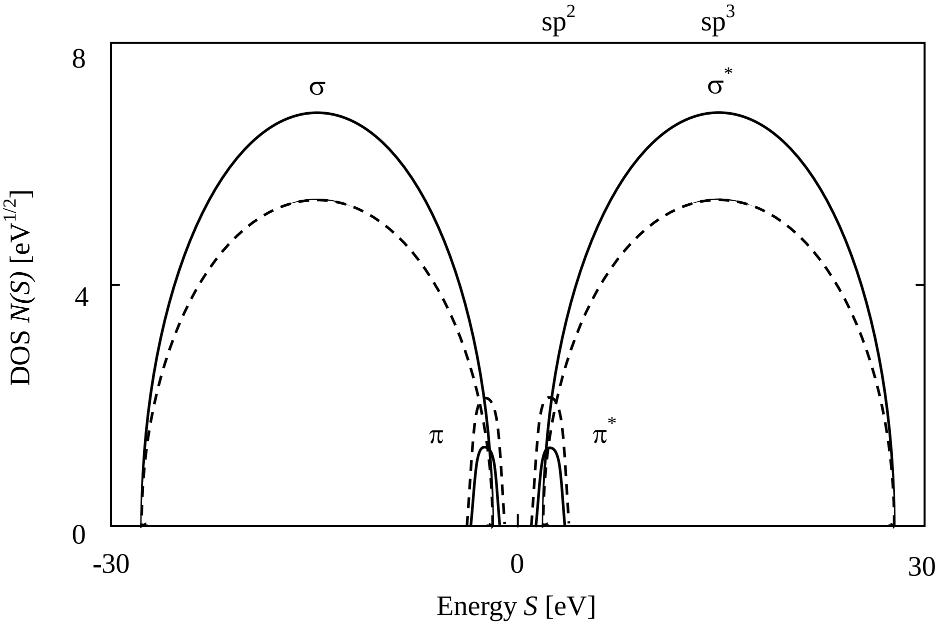

Fig. 8.45: *Schematic densities of states of two DLC films cf. [Franta07]*

π - $\pi^* \cong sp^2$ *and* σ - $\sigma^* \cong sp^3$.

In this model the effective band gap is decreased with an increase of the density of π and π^* states. Even if the real *DOS* is very complicated, there is an empirical correlation between sp^2 – bonded carbon atoms content and Tauc gap [Adamopoulos04]. Where sp^2 – bonded carbon atoms give π and π^* states and sp^3 – bonded carbon atoms give σ and σ^* states correspondingly, usually the sp^1– bonded carbon atoms can be neglected. Fig. 8.46 shows variation of the experimentally determined optical band gap against the sp^2 – bonded carbon atoms content for different types of DLC films.

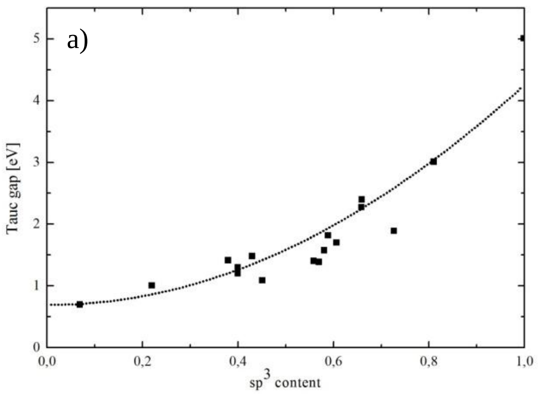

Fig. 8.46 a): *Optical band gap vs. sp*^{3} *– bonded carbon fraction (by NMR and EELS) for different diamond-like carbon coatings deposited by various techniques. The dotted line is a quadratic fit to the data cf. [Ferrari00].*

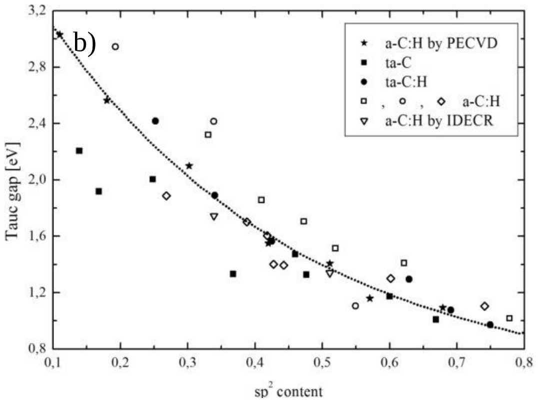

Fig. 8.46 b): *Empirically obtained variation of optical band gap vs. sp*^{2} *– bonded carbon atoms fraction (by EELS) for different diamond-like carbon coatings deposited by various techniques. The dotted line is an exponential fit to the data cf. [Adamopoulos04].*

In Fig. 8.46 one can see that the optical band gap for different types of DLC films, regardless of the type (hydrogenated or non-hydrogenated), changes in a similar way with *sp*^{2} – bonded carbon fraction, showing that optical band gap in the first place depends on the *sp*^{2} – carbon hybridization.

The value of the band gap in DLC films is determined by the density of the π states of the *sp*^{2} – bonded carbon sites. The *sp*^{2} – bonded carbon fraction is a very important parameter which determines the electronic and optical properties of deposited DLC films. The films with the low *sp*^{2} – content have high optical band gap and the films with high *sp*^{2} content have low optical band gap.

The dotted line represents the fitted mean value for the obtained results. By the help of this dependence and using the optical band gap obtained from the *SCOUT 3.6™* simulation program it was possible to determine the *sp*^{2} content in the deposited films. In order to do this it was necessary to represent this dependence in a form of *sp*^{2} content as a function of optical band gap see Fig. 8.47.

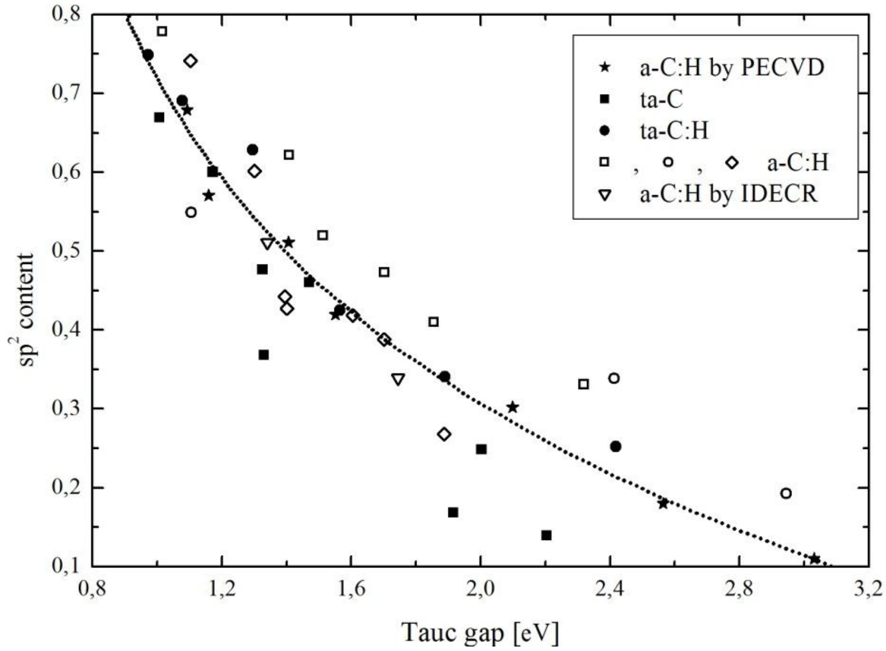

Fig. 8.47: *The sp^2 content as a function of optical band gap cf. [Ferrari00].*

Combining optical band gap dependence from Fig. 8.44 and the data from Fig. 8.46 for the band gap, one can plot them together and immediately obtain the information which will help to sort deposited films according to the conventional classification.

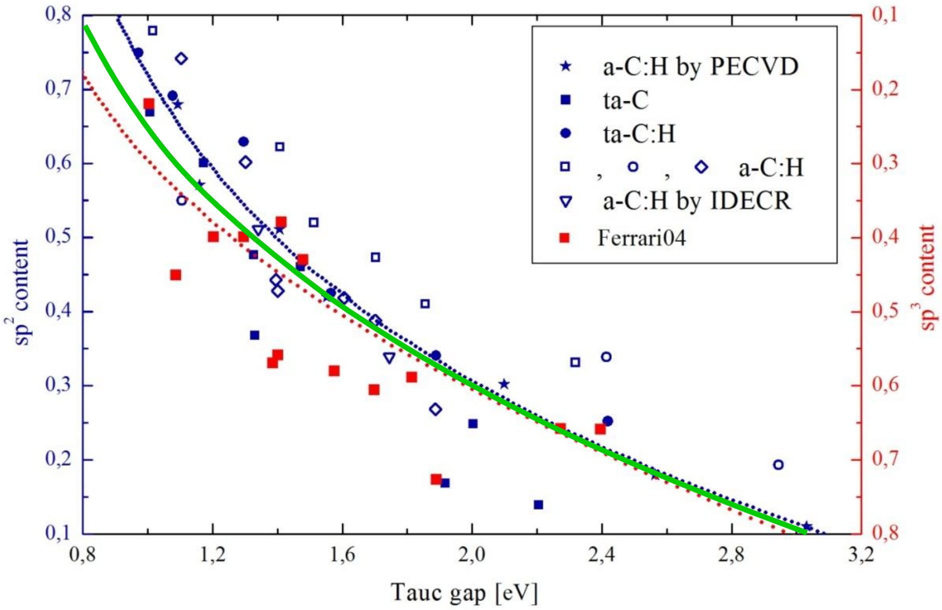

Fig. 8.48: *Dependence of the optical band gap E_g of DLC films on the deposition parameters and sp^3/ sp^2 bonded carbon content in the deposited films (red curve is the fit to the experimental data of [Ferrari00] blue one is the fit to the experimental data of [Adamopoulos04], green curve is the mean value which were used for evaluation).*

From Fig. 8.48 one can obtain not only information about the influence of deposition parameters onto the optical band gap but also get additional information about *sp*^{3} – bonded carbon atoms content and its variation with main deposition parameters. The *sp*^{3} and *sp*^{2} contents can be deduced from the Tauc gap.

8.2.4.4 The sp^3 Content in DLC Film as a Function of Deposition Parameters

The *sp*^{3} content in DLC film is a crucial parameter, responsible for mechanical properties of DLC films. But it also connected with other parameters in the DLC films, and such correlation can be observed.

8.2.4.4.1 Influence of Different Arc Modes on sp^3 Content

The results obtained from Fig. 8.48 and Fig. 8.44 are plotted in a diagram as a function of different arc modes and bias voltage are shown in Fig. 8.49.

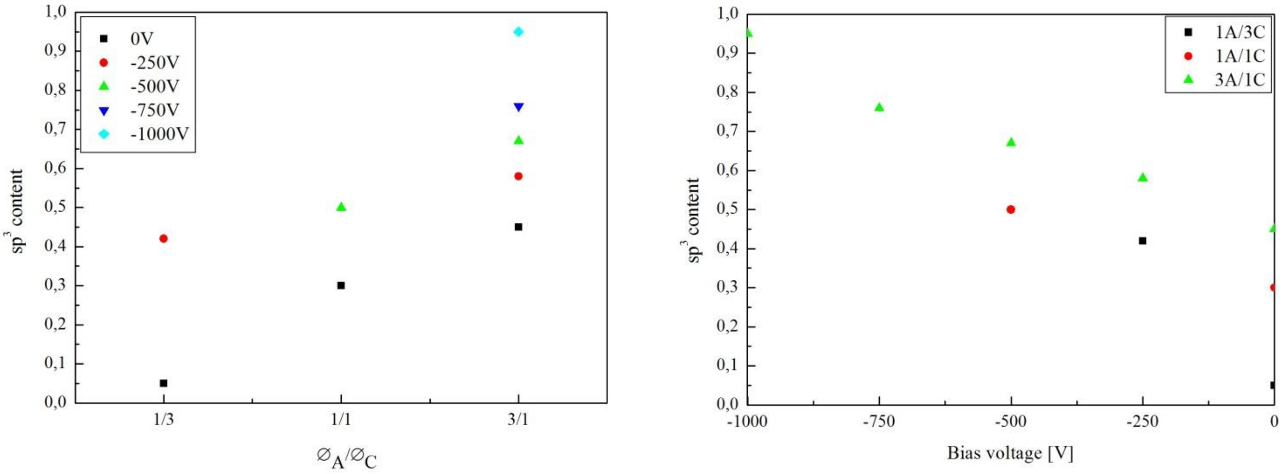

Fig. 8.49: *sp*^{3} *content in DLC films as a function of arc mode and bias voltage.*

Fig 8.49 shows, the films deposited at “cathodic” arc mode ($\varnothing_A/\varnothing_C = 3/1$) have the highest concentration of *sp*^{3} bonded carbon atoms and this concentration decrease with transition to “anodic” mode ($\varnothing_A/\varnothing_C = 1/3$). From Fig. 8.49 one can see, the *sp*^{3} content in DLC films is depends on the bias voltage.

8.2.4.4.2 Influence of Different Deposition Parameters on sp^3 Content

Using the same procedure one can estimate also the correlation between hydrogen flow rate and the sp^3 content in the films. In order to do it the films were deposited at “anodic” mode (electrode diameter ratio $\varnothing_A/\varnothing_C = 1/3$) with different bias voltages and various hydrogen flow rates, see Fig. 8.50.

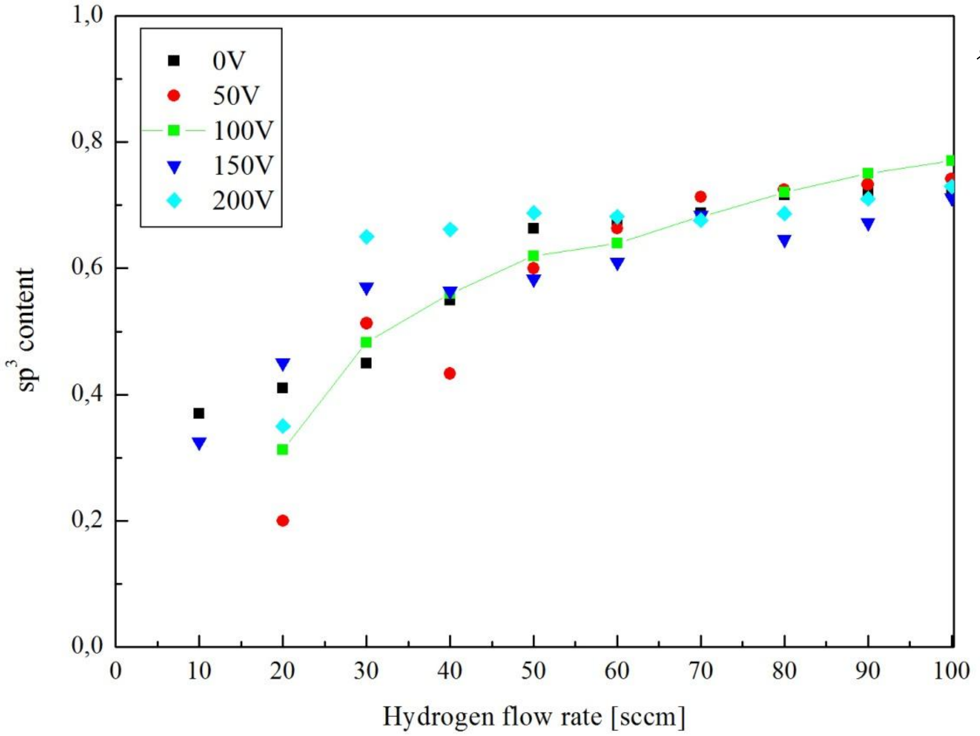

$\varnothing_A/\varnothing_C = 1/3$

Fig. 8.50: *sp^3 content in DLC films as a function of deposition parameters deduced from optical band gap.*

In Fig. 8.50 one can see that there is a good correlation between hydrogen concentration in the deposited films and sp^3 content. The films with low hydrogen concentration have low sp^3 content, with increasing hydrogen concentration the sp^2 content decreases and thereby the sp^3 content increases. The influence of bias voltage on sp^3 content is clear at low hydrogen flow rates $<$ *50 sccm*, the highest sp^3 content have the DLC films deposited at “- *200 V*”. By increase of hydrogen flow rates over *50 sccm* the influence of bias voltage become less clear. At he high flow rates the amount of sp^3 bonded carbon atoms basically defined by hydrogen content.

8.2.4.5 The Complex Dielectric Function

Using measured and simulated optical spectra of DLC films, one can obtain very significant information about the electronic structure of DLC films.

The most important information is the complex dielectric function, which consists of real ε_1 and imaginary ε_2 parts:

$$\varepsilon = \varepsilon_1 + i\varepsilon_2, \tag{8.12}$$

where

$$\varepsilon_1 = n^2 - k^2 \tag{8.13}$$

$$\varepsilon_2 = 2nk \tag{8.14}$$

and n is the refractive index and k is the extinction coefficient [Born02].

The imaginary part ε_2 of the dielectric function is the main information obtained from the *SCOUT 3.6 ™* optical simulation program; it characterizes the electronic structure of deposited films and can be used to understand the influence of deposition parameters onto film properties. ε_1 spectrum can be obtained from the ε_2 spectra by the Kramers-Kronig relations [Kramers27, Kronig26, Toll56].

According to the measured film transmittance, a strong absorption area lies in a spectral range between *200 nm – 285 nm (4.3 eV – 6.2 eV*) correspondingly. The details of the dielectric function in this region are not supported by features in the transmittance curve. Therefore, we plot the obtained dielectric function only in the range *0.6 eV* to *4.3 eV*.

In Fig. 8.51 one can see the spectral dependence of the imaginary part ε_2 of the dielectric function obtained from the *SCOUT 3.6 ™* simulation program. In this spectral dependence two characteristic areas can be observed. The first area is located between *1* and *2 eV* and the second area lies around *4 eV*. These areas are closely related to the dielectric function. Such behaviour of the imaginary part ε_2 of the dielectric function is also confirmed by other experimental results [Aksenov93, Paret98].

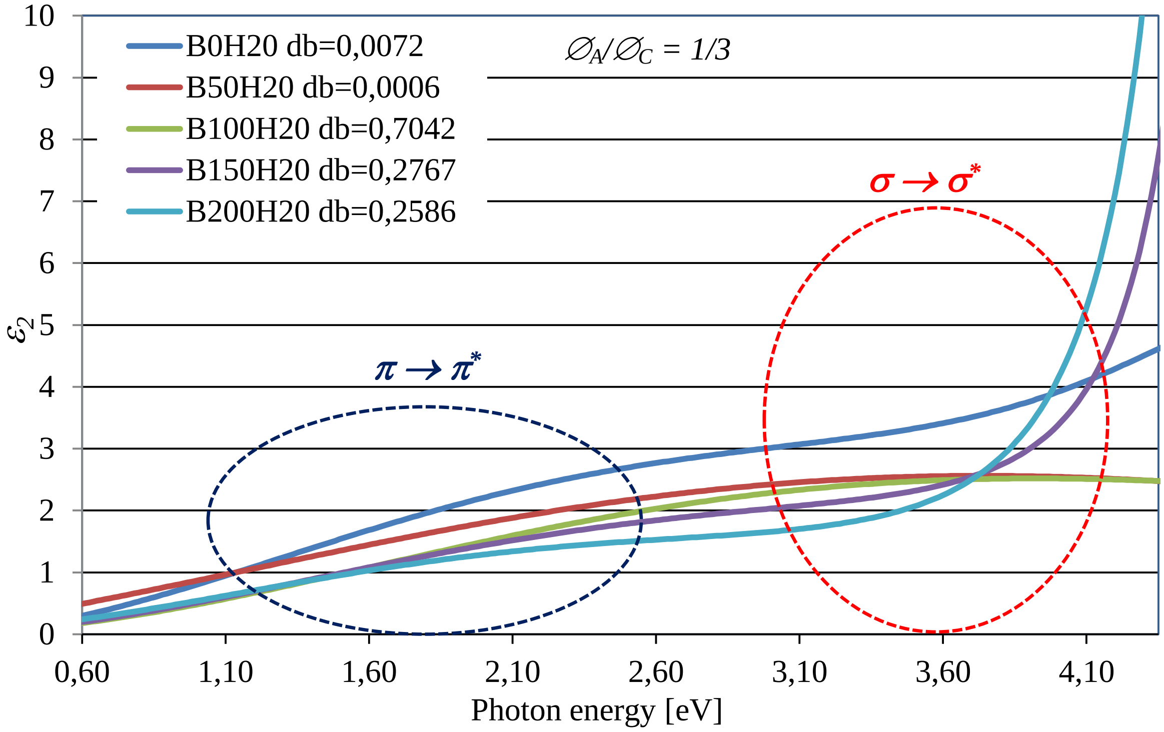

Fig. 8.51: *Spectral dependences of the imaginary part ε_2 of the dielectric function for deposited DLC films at constant hydrogen flow 20 sccm and bias voltage variation from 0 V to -200 V.*

According to Pparameterization of Density of States (*PDOS*) model [Franta06], the $\pi \rightarrow \pi^*$ and $\sigma \rightarrow \sigma^*$ interband transitions give two separate contributions to the ε_2 spectra. The transitions $\sigma \rightarrow \pi^*$ and $\pi \rightarrow \sigma^*$ are less probable due to the high localization of π electrons and therefore cannot be observed. In this model, the spectral dependence of imaginary part of the dielectric function ε_2 is calculated numerically as a convolution of *DOS* belonging to both the valence and conduction bands. According to such model, the first region in the spectral dependence of the imaginary part ε_2 of the dielectric function occurs due to the $\pi \rightarrow \pi^*$ interband transitions, and another one due to the $\sigma \rightarrow \sigma^*$ interband transitions.

In order to normalize the imaginary part ε_2 of the dielectric function and due to the strong light dispersion, it was necessary to subtract the dielectric background from the calculated imaginary part ε_2 of the dielectric function. In Fig. 8.52 one can see the unnormalized imaginary part ε_2 of the dielectric function and in Fig. 8.53 normalized ε_2 by dielectric background subtraction.

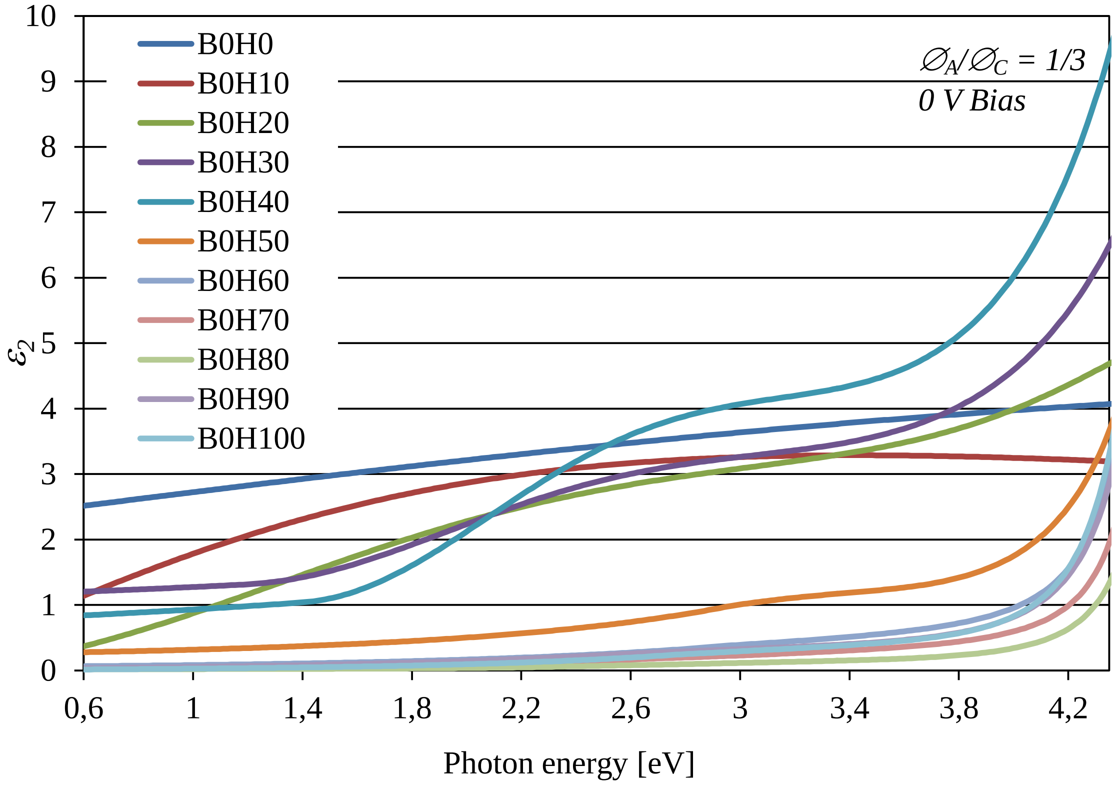

Fig. 8.52: *Spectral dependences of unnormalized imaginary part* ε_2 *of the dielectric function at 0 V bias voltage and different hydrogen flow rates from 0 sccm to 100 sccm.*

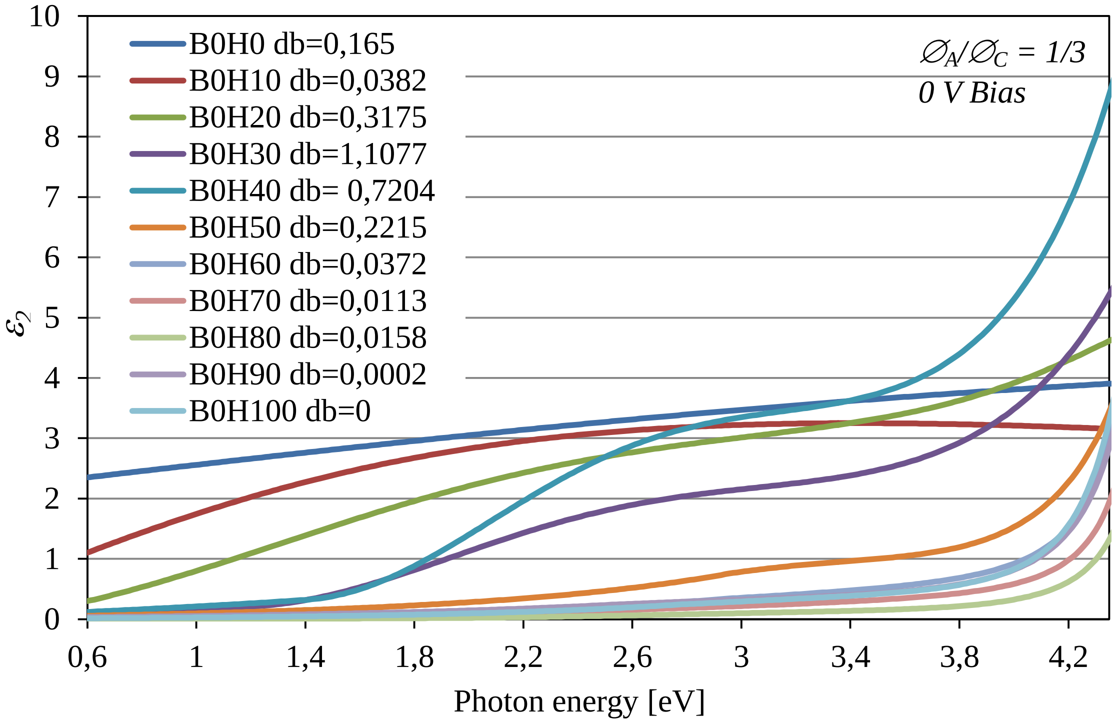

Fig. 8.53: *Spectral dependences of* ε_2 *normalized by dielectric background subtraction at 0 V bias voltage and different hydrogen flow rates from 0 sccm to 100 sccm.*

.

After normalization, the influence of deposition parameters on the imaginary part ε_2 of the dielectric function becomes clearer. The influence of deposition parameters on the dielectric function is shown below.

In order to understand the influence of the deposition parameters on the dielectric function and in turn onto film properties we need to examine all spectral dependences of the imaginary part ε_2 of the dielectric function. All calculated spectral dependencies can be found in *Appendix I*.

8.2.4.5.1 Influence of Different Arc Modes on ε_2

In this chapter, the influence of two main deposition parameters, chemistry (hydrogen flow rate) and particle energy on the DLC films optical properties was investigated. In Fig. 8.54 one can see the spectral dependence of the imaginary part ε_2 of the dielectric function obtained from the *SCOUT 3.6™* simulation program for DLC films deposited without hydrogen admixture to the plasma at different arc modes.

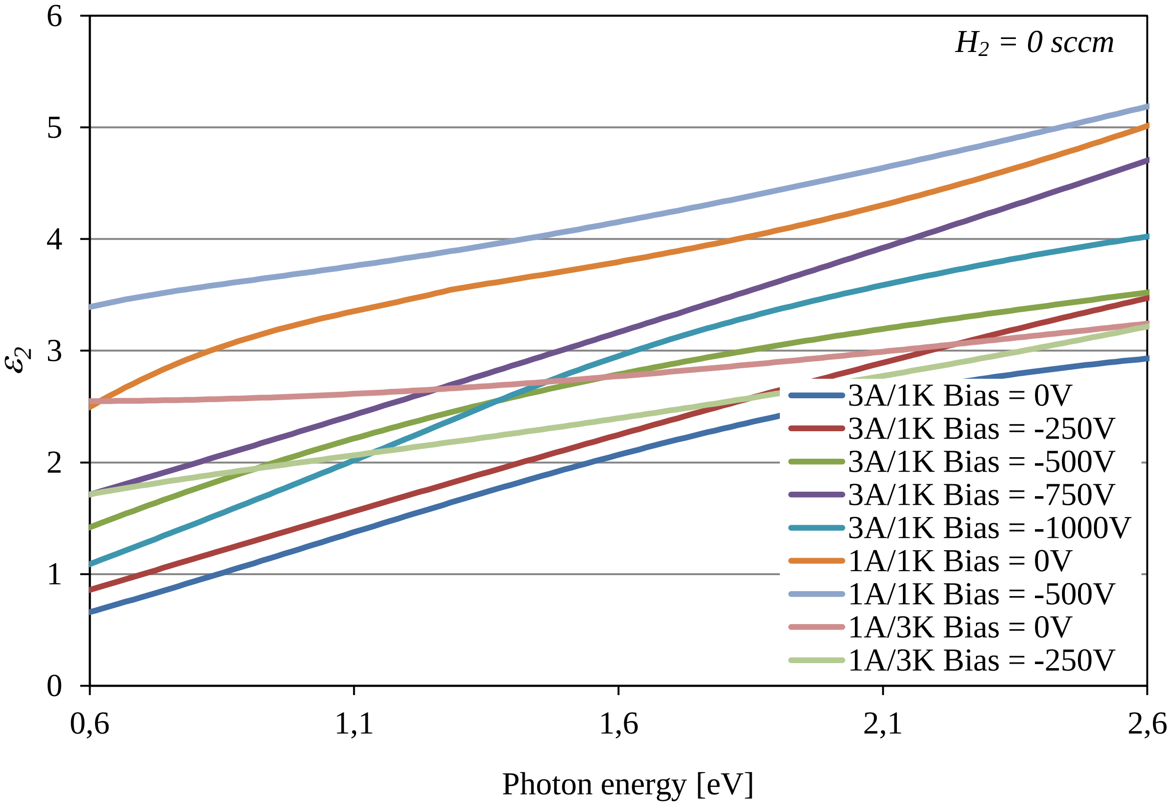

Fig. 8.54: *Spectral dependences of the imaginary part ε_2 of the dielectric function for DLC films deposited at different anode to cathode diameter ratios and different bias voltages [Khlopyanova12].*

All dielectric functions show a similar behaviour. In the case of *0 V* bias voltage the effect of different arc modes can be seen. The films deposited at cathodic arc mode have the smallest

$\pi \rightarrow \pi^*$ bonds concentration what means the lowest sp^2 carbon atoms content. The $\sigma \rightarrow \sigma^*$ bonds are not shown in this spectral dependence due to the strong absorption in the energies over *2.6 eV*. By the increase of the bias voltage the $\pi \rightarrow \pi^*$ bonds concentration decrease but above a certain value of the bias voltage the $\pi \rightarrow \pi^*$ bonds concentration starts to grow. This fact can be explained by the influence of the particle energy. After certain energy value the particles arriving the substrate cause damage to the film structure and lead to the sp^2 bonded carbon atoms formation.

8.2.4.5.2 Influence of Different Hydrogen Flow Rates on ε_2

To demonstrate the influence of hydrogen flow rate on the imaginary part ε_2 of the dielectric function the measured spectra for different hydrogen flow rates at constant bias voltage were examined. Such spectral dependence is shown in Fig. 8.55. The negative substrate bias voltage was set to *"– 50 V"* and hydrogen flow rate was varied in *10 sccm* steps from *0 sccm* till *100 sccm*.

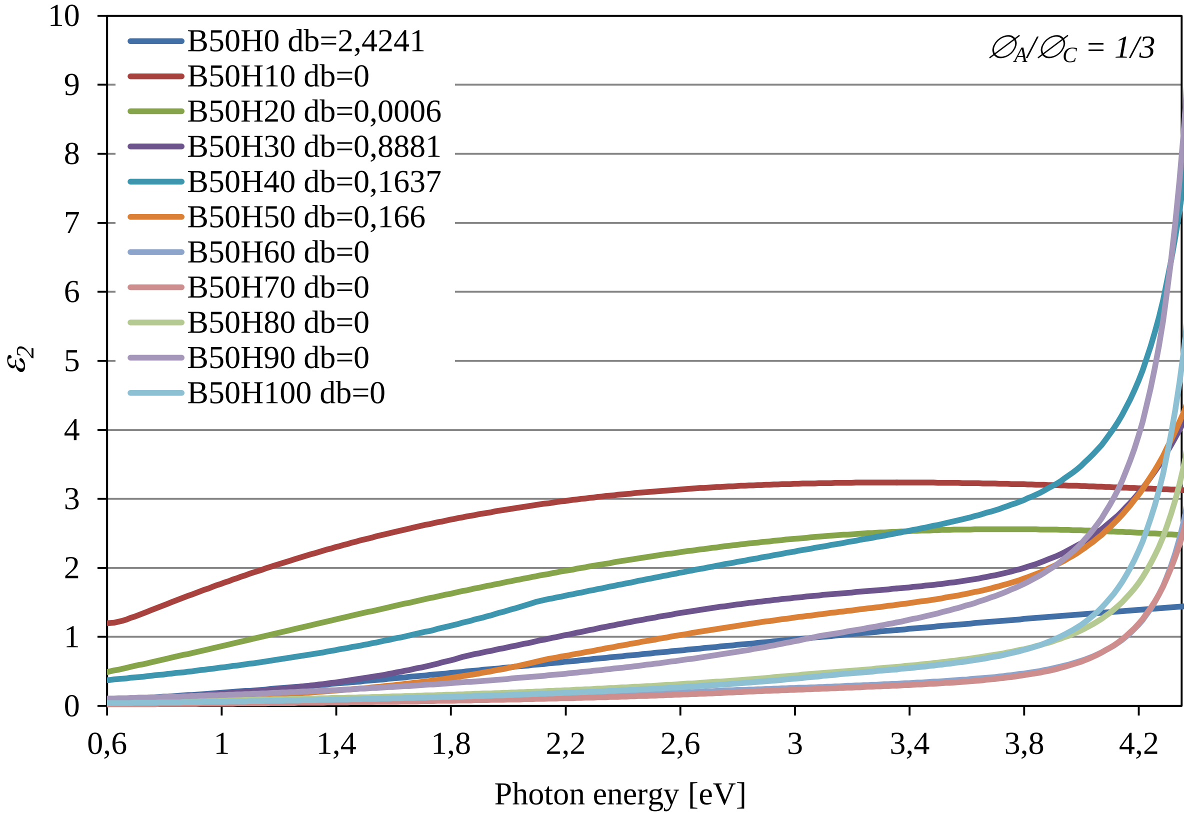

Fig. 8.55: *Spectral dependences of the imaginary part ε_2 of the dielectric function for deposited DLC films at different hydrogen flow rates. The bias voltage to the substrate was kept at "– 50 V".*

The first sign demonstrating the influence of hydrogen flow rate on the dielectric function is that the imaginary part ε_2 changes its shape only due to the variation of hydrogen flow rate.

According to the shape, all spectral dependencies of the imaginary part ε_2 of the dielectric function can be divided in few groups as a function of the hydrogen flow rate and correspondingly hydrogen concentration in the deposited films:

a) *H0 – H20* – very low hydrogen content (*[H] ≤ 10 at. %*),

b) *H30 – H*50 – low hydrogen content (*10 at. % < [H] ≤ 20 at. %*),

c) *H60 – H100* – intermediate hydrogen content (*20 at. % < [H] < 40 at. %*).

The hydrogen content determination of the deposited DLC films was carried out by nuclear reaction analysis (*NRA*), and it was discussed in *Chapter 8.2.3.2.*

Such correlation between the hydrogen flow rate and the shape of the imaginary part ε_2 of the dielectric function was also observed for all films independently from the applied bias voltage, see *Appendix I.*

Another sign of the influence of the hydrogen flow rate on the imaginary part ε_2 of the dielectric function is that for films deposited at the residual hydrogen atmosphere (working pressure $< 10^{-6}$ *mbar*) spectrum is located above all other spectra. And increase of hydrogen flow rate leads to a decrease in the values of the spectra of the imaginary part ε_2 of the dielectric function, see Fig. 8.55.

In regard to the $\pi \rightarrow \pi^*$ and $\sigma \rightarrow \sigma^*$ bonds, one can say that $\pi \rightarrow \pi^*$ bonds in the first region of the imaginary part ε_2 of the dielectric function are reduced by an increase of hydrogen flow rate from *0 sccm* to *50 sccm* and $\sigma \rightarrow \sigma^*$ bonds in the second region on the contrary are increased. At flow rates above *50 sccm* $\pi \rightarrow \pi^*$ bonds reduced even stronger than at small flow rates, and $\sigma \rightarrow \sigma^*$ bonds also start to reduce but very slowly in comparison to the $\pi \rightarrow \pi^*$ bonds.

Such behaviour of π and σ bonds can be explained as follows. The DLC films deposited at small hydrogen flow rates < 30 *sccm* have high amount of sp^2 – hybridized carbon atoms and have a small optical band gap. The films deposited at flow rates of *30 – 50 sccm* show presence of both sp^2 and sp^3 – hybridized carbon atoms in similar amounts, and low concentration of hydrogen. And in the films deposited at flow rates > 50 *sccm* the content of sp^2 – hybridized carbon atoms becomes very small (optical band gap increases), Fig. 8.44 and the content of sp^3– hybridized carbon atoms increases strongly (Fig. 8.50), but hydrogen concentration in such films is also increased. Such assumptions are in good agreement with the literature [Casiragi05]. In most types of *DLC* films, an increasing content of sp^3 – bonded carbon atoms correlates with increasing hydrogen content. Hydrogen saturates $C = C$ bonds by transformation of sp^2 carbon sites into $sp^3 = CH_2$ and $\equiv CH$ sites. This increase the amount of all sp^3 bonds but not the $C = C$

sp^3 bonds. The *a-C:H* films with a small band gap have a high sp^2 content. The *a-C:H* films with high hydrogen concentration have high sp^3 content and a broad optical band gap $B_g > 2\ eV$ [Robertson02].

8.2.4.5.3 Influence of Bias Voltage on ε_2

In order to demonstrate the influence of bias voltage on the imaginary part ε_2 of the dielectric function, the bias voltage to the substrate was varied in *50 V* steps from *0 V* to "*– 200 V*". To separate the influence of the bias voltage on the imaginary part ε_2 of the dielectric function from hydrogen flow rate the spectral dependence at different bias voltages but at constant hydrogen flow rate were considered. Such spectral dependence is shown in Fig. 8.56. The hydrogen flow rate was set to *30 sccm*. The spectral dependencies with different flow rates can be found in *Appendix I*.

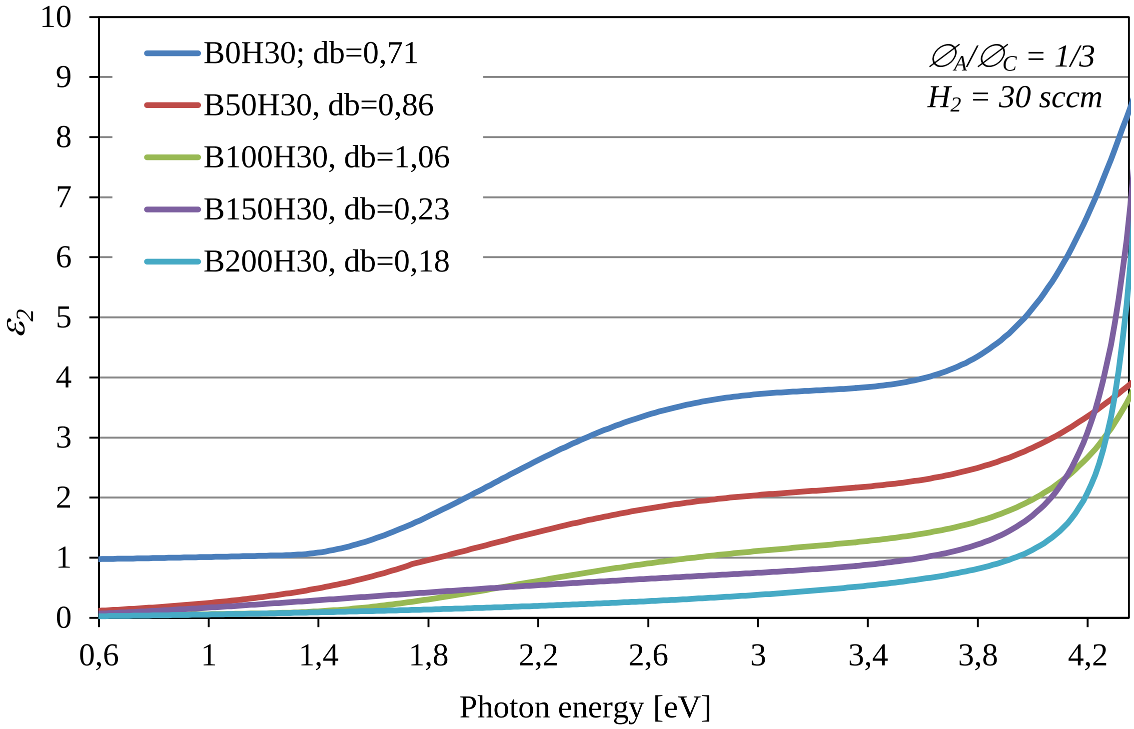

Fig. 8.56: *Spectral dependences of the imaginary part ε_2 of the dielectric function for deposited DLC films at different bias voltages from 0 V to 200 V, but at constant hydrogen flow rate 30 sccm.*

The influence of bias voltage on the imaginary part ε_2 of the dielectric function is also noticeable. At *0 V* bias voltage one can see the presence of both, $\pi \rightarrow \pi^*$ and $\sigma \rightarrow \sigma^*$ bonds. The values of the imaginary part ε_2 of the dielectric function are the highest in comparison to other spectra with the same hydrogen flow rate. By increase of bias voltage, the imaginary part ε_2 of the dielectric function in a region of *1 – 2 eV* decreases strongly, what means that $\pi \rightarrow \pi^*$ bonds become smaller, therefore concentration of sp^2 – hybridized carbon atoms is decreased. Such results are also in good agreement with the literature [Robertson02].

The influence of bias voltage on the imaginary part ε_2 of the dielectric function in the region around *4 eV* is not as noticeable as in the region *1 – 2 eV*, but the value of $\sigma \rightarrow \sigma^*$ bonds is proportional to the bias voltage. Fig. 8.57 shows the influence of the deposition parameters (hydrogen flow rate and bias voltage) on the imaginary part ε_2 of the dielectric function at *3.3 eV*.

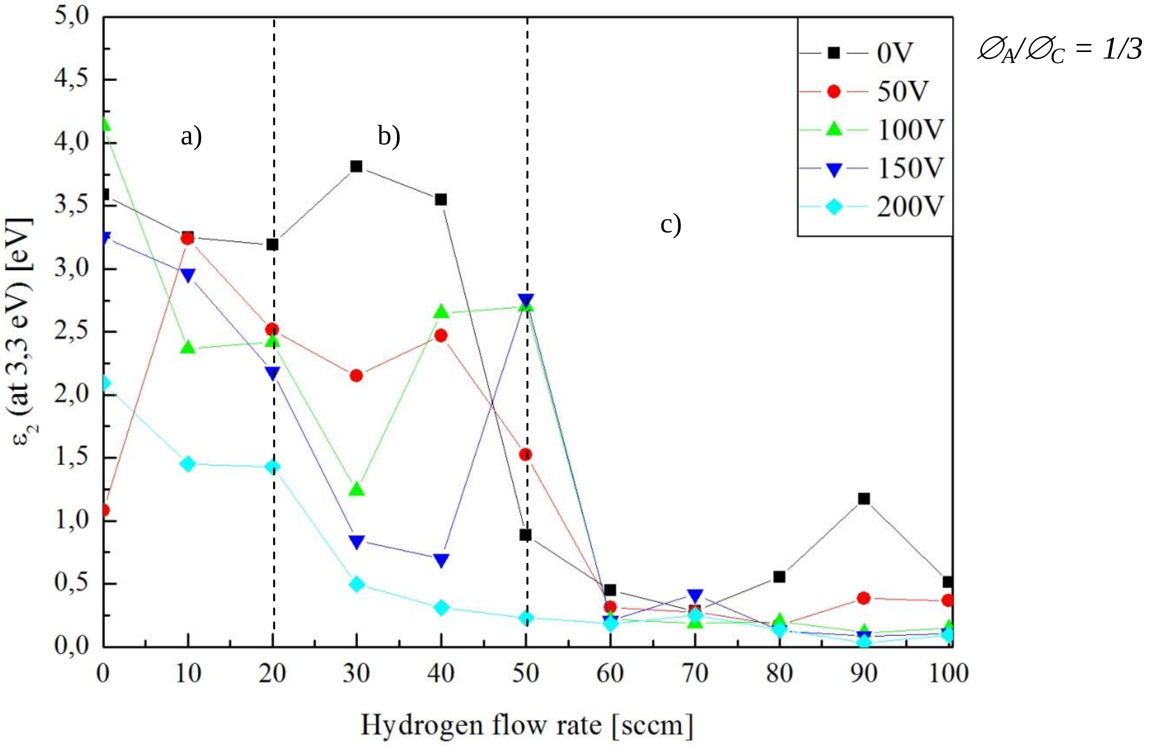

Fig. 8.57: T*he imaginary part ε_2 of the dielectric function for deposited DLC films at 3.3 eV as a function of bias voltage and hydrogen flow.*

The value of the imaginary part ε_2 of the dielectric function at *3.3 eV* decrease with an increase of hydrogen flow rate. According to the behaviour of ε_2, in Fig. 8.57 three regions can be observed. In the region *a)* films have high concentration of sp^2 – hybridized carbon atoms and low of sp^3. With increase of hydrogen flow rate the sp^3– hybridized carbon atoms content starts to grow and ε_2 decreases. In the region *b)* there is transition from graphitic structure to amorphous carbon structure is occurred. In this region the influence of bias voltage becomes significant. The ε_2 decreasing with increase of the bias voltage. The amount of the sp^2 –

hybridized carbon atoms starts to decrease and content of the sp^3 – hybridized carbon atoms increases. In the region *c)* a polymerization of DLC films occur. The behaviour of the imaginary part ε_2 of the dielectric function at *3.3 eV* is characteristic for DLC films deposited at high hydrogen flow rare and high bias voltage [Aksenov93] (very low values of ε_2).

Conclusion

Both deposition parameters (hydrogen flow rate and negative bias voltage to the substrate) demonstrate strong influence on the imaginary part ε_2 of the dielectric function. By *PDOS* (parameterization of density of states) model, this influence can be interpreted in terms of sp^2 and sp^3 – hybridized carbon atoms concentration.

The influence of hydrogen on the dielectric function is much stronger than the influence of the negative bias voltage. According to the results the DLC films deposited at low hydrogen flow rate $< 30\,sccm$ and bias voltage less than *50 V* demonstrate high concentration of sp^2 bonded carbon atoms and have small optical band gap. Increase of bias voltage leads to a decrease of sp^2 bonded carbon atoms content.

By increasing of hydrogen flow rate from *30 sccm* to *50 sccm*, the concentration of sp^2 bonded carbon atoms decreases and sp^3 content increases which leads to an increase of the optical band gap. A hydrogen flow rate of *50 sccm* corresponds to *20 at.%* of hydrogen concentration in DLC. This is the determinative flow rate, responsible for the changes in the structure of DLC films. It can be seen in the spectral dependence of the imaginary part ε_2 of the dielectric function.

At high hydrogen flow rates $> 50\,sccm$ the content of sp^3 bonded carbon reaches its maximum and films have the biggest band gap among the DLC films deposited in these experiments. Using the experimental data, the band gap and the hydrogen content were plotted together with the results from other authors [Casiragi05, Poukhovoi11], see Fig. 8.58.

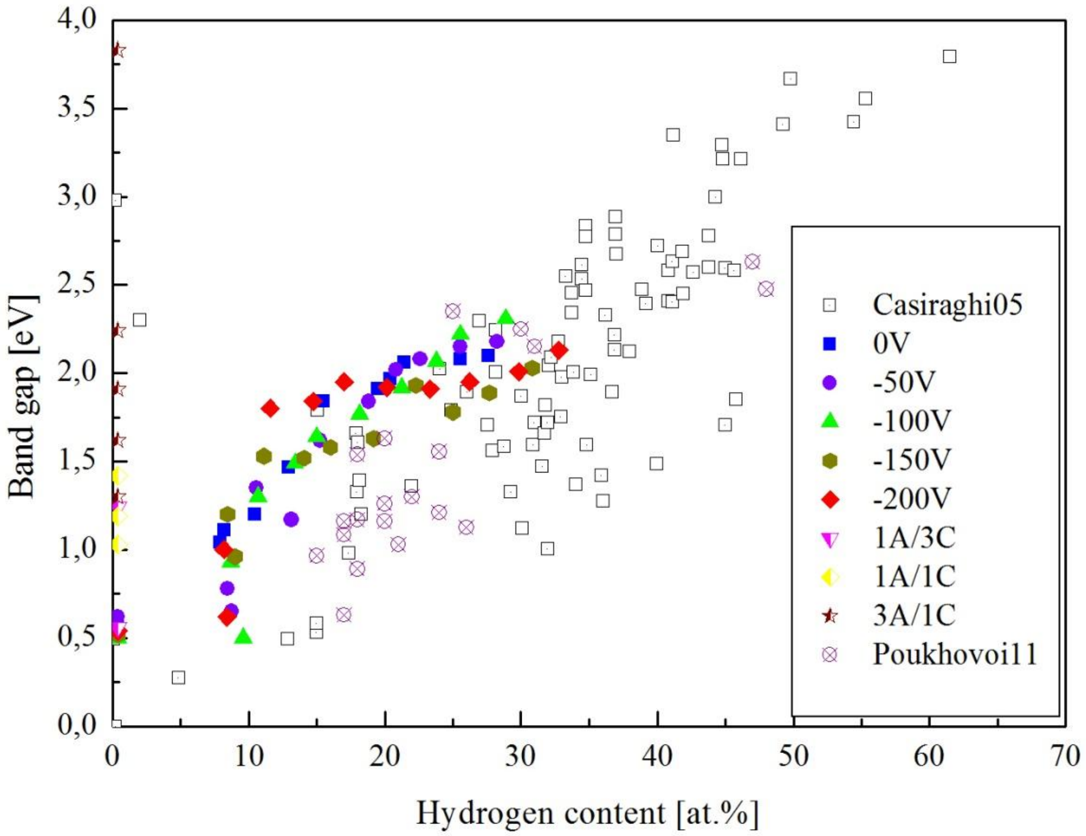

Fig. 8.58: *Measured optical band gap and hydrogen content in comparison to the experimental data [Casiragi05, Poukhovoi11].*

According to Fig. 8.58 the results obtained in this work are in a good agreement with the literature. There is a correlation between hydrogen content in deposited DLC films and the optical band gap.

8.2.5 Raman Spectroscopy

In case of DLC coatings, Raman spectroscopy is a commonly used analytical method to obtain information about carbon hybridisation state. A significant number of experimental results based on different analytical techniques including Raman spectroscopy which were summarized by Robertson and co-workers [Robertson91, Ferrari00]. But the interpretation of Raman spectra is rather complicated and cannot be used solely without any other analytical methods. Raman spectroscopy is rather an additional method to confirm previous results and to complete the films analytical results. Using these results, it is possible to classify the deposited DLC films and to determine their electronic structures. Due to the fact that Raman spectroscopy for sp^2 – hybridized carbon atoms is *50 – 230* times more sensitive than for sp^3 – hybridized carbon atoms (due to the higher cross section), this method does not provide direct evaluation of sp^3/sp^2 – hybridized carbon atoms content. Such information can be indirectly derived from Raman spectroscopy.

In order to obtain reliable information from Raman spectra, a multiwavelength micro-Raman by *Jobin Yvon™* was used. Measurements were taken with *100×* objective. In order to prevent the damage of the DLC film caused by the laser, the measurements were taken using *0.6* diaphragm (*25%* transmittance). Raman spectra were recorded using two lasers: *Ar* laser with the wavelength $\lambda_1 = 514\ nm$ and *He-Ne* laser with the wavelength $\lambda_2 = 633\ nm$. To evaluate the measured spectra it is necessary to use such parameters as peak position (*G*-peak position), peak intensity ratio (I_D/I_G), full width at half maximum of the G-peak (*FWHM G*), the *G*-peak dispersion ($Disp_G$). Fig. 8.59 shows measured at *633 nm* Raman spectra for DLC films deposited at “anodic” mode (electrode diameter ratio $\varnothing_A/\varnothing_C = 1/3$) with various hydrogen flow rates. The first thing needs to be mentioned is a photoluminescence (*PL*) background. The presence of photoluminescence in visible Raman spectra is the characteristic feature for hydrogenated carbon films. The higher hydrogen content in the DLC film the bigger is photoluminescence [Casiragi05].

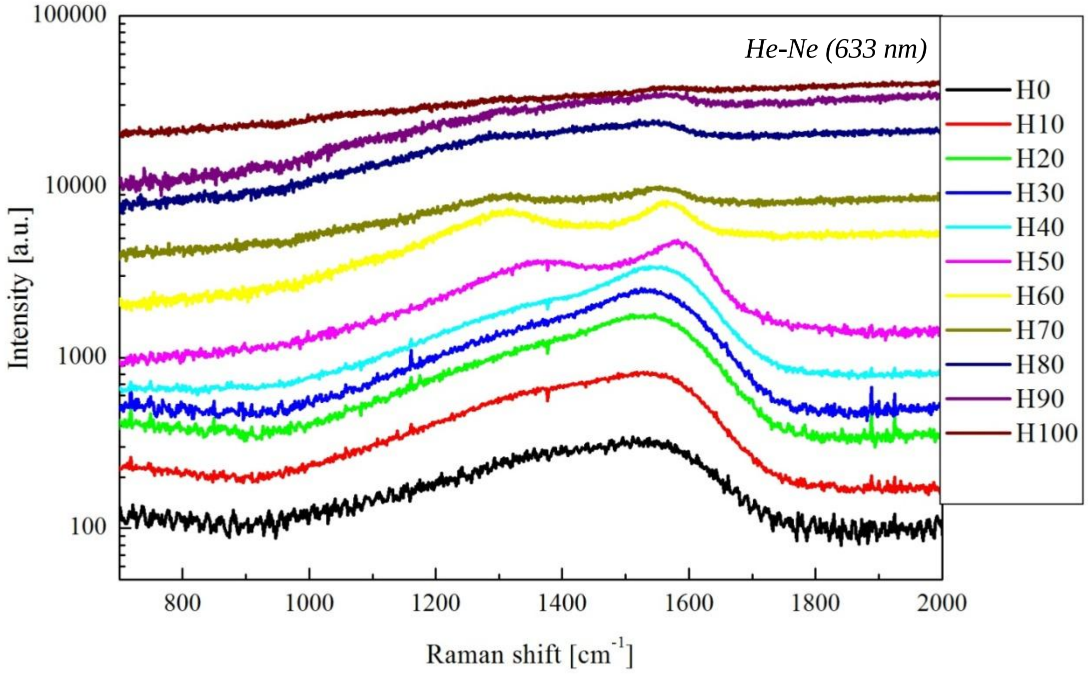

$\varnothing_A/\varnothing_C = 1/3$

Fig. 8.59: *Raman spectra for DLC films deposited at "anodic" mode (*$\varnothing_A/\varnothing_C = 1/3$*) with various hydrogen flow rates, 0 V bias voltage.*

In Fig. 8.59 one can see that DLC films deposited at hydrogen flow rates between *0 sccm* and *50 sccm* show no photoluminescence background, since their spectra have no slope. The influence of photolumincence background only takes place at high hydrogen flow rates, higher than *60 sccm*, what corresponds to hydrogen contents over *20 at.%*, see *Chapter 8.2.3.2*.

8.2.5.1 The G-Peak Position

The *G*-peak position is one of the main parameters which is used in Raman spectra evaluation. It is strongly connected to the graphitic components of the deposited DLC films and not to sp^3 – hybridized carbon atoms content. Therefore it is marked as "graphite", the information about *G*-peak position is also connected to the breathing mode of sp^2 – hybridized carbon atoms organized in the rings [Ferrari00]. It is possible, that DLC films with different sp^3 – hybridized carbon atoms content demonstrate similar Raman spectra. Therefore evaluation of the *G*-peak position can be performed only in combination with other Raman parameters.

In order to understand the influence of various deposition parameters on Raman spectra it is necessary to investigate them separately. The first parameter discussed below is the transition from "anodic" to "cathodic" arc mode.

8.2.5.1.1 Influence of Different Arc Modes on the G-Peak Position

Fig. 8.60 shows the G-Peak position as a function of electrode diameter ratios $\varnothing_A/\varnothing_C$ without working gas.

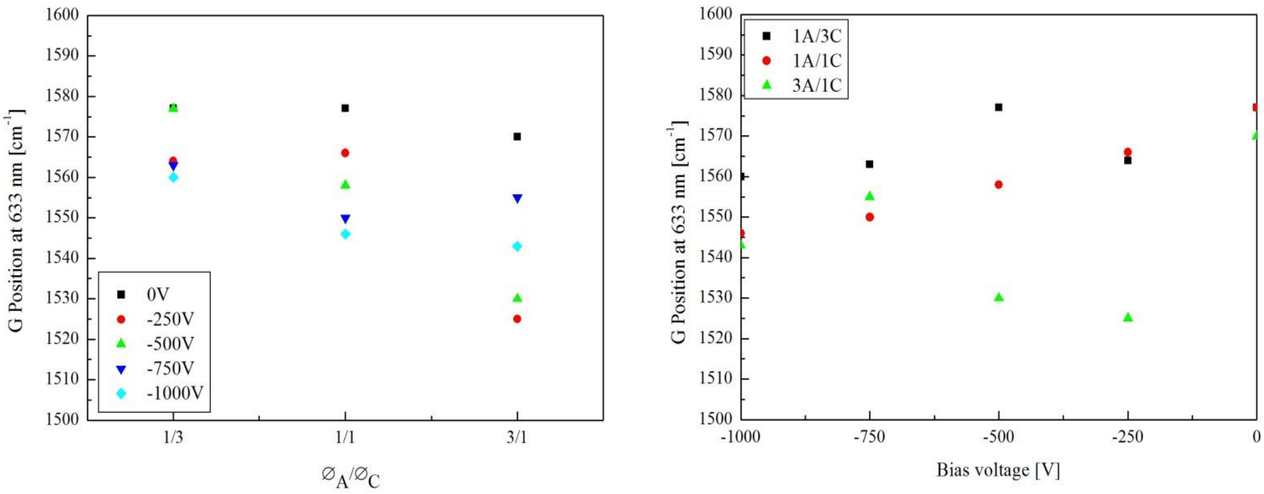

Fig. 8.60: *The G-peak position for DLC films deposited at different electrode diameter ratios $\varnothing_A/\varnothing_C$ and different substrate bias voltages without hydrogen taken at 633 nm [Khlopyanova12].*

For DLC films deposited at the electrode diameter ratio $\varnothing_A/\varnothing_C = 3/1$ “cathodic” mode, the G-peak was found at the lowest position $1526\ cm^{-1}$. During transition to the “anodic” mode an increase in the G-peak position can be seen ($1560\ cm^{-1}$ in a case of $\varnothing_A/\varnothing_C = 1/3$). The G-peak shifts toward smaller values with increasing bias voltage.

8.2.5.1.2 Influence of Bias Voltage and Different Hydrogen Flow Rates on the G-Peak Position

In this part of the work the DLC films were deposited at “anodic” mode (electrode diameter ratio $\varnothing_A/\varnothing_C = 1/3$) with different bias voltages and various hydrogen flow rates. The resulting *G*-peak position variation for two working wavelengths can be seen in Fig. 8.61.

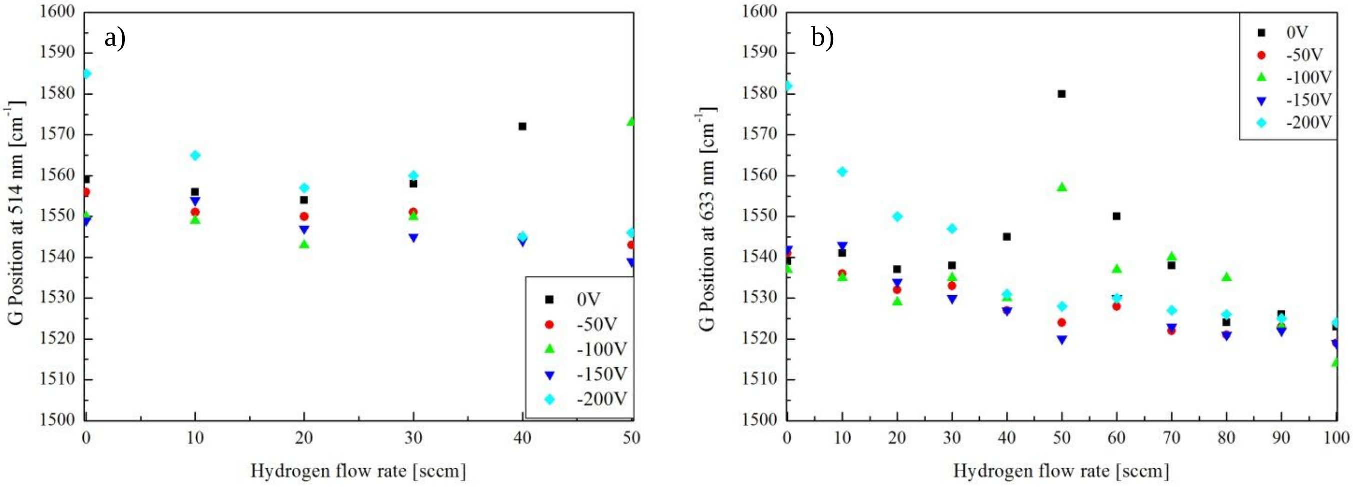

Fig. 8.61: *The G-peak position variation as a function of the deposition parameters measured at different laser wavelengths a) at 514 nm, b) at 633 nm.*

In Fig. 8.61, one can see strong influence of hydrogen flow rate on the *G*-peak position. An increase in hydrogen flow rate leads to a decrease of the *G*-peak position. In the case of *50 sccm* hydrogen flow rate, there is an increase of the G-peak position, but such effect was observed for the DLC films deposited at *“0 V”* and *“– 100 V”* bias voltages only.

Using the results obtained from the *NRA* and *UV-VIS* spectroscopy (see *Chapters 8.2.3.2* and *8.2.4*), the data can be summarized in one diagram, see Fig. 8.62.

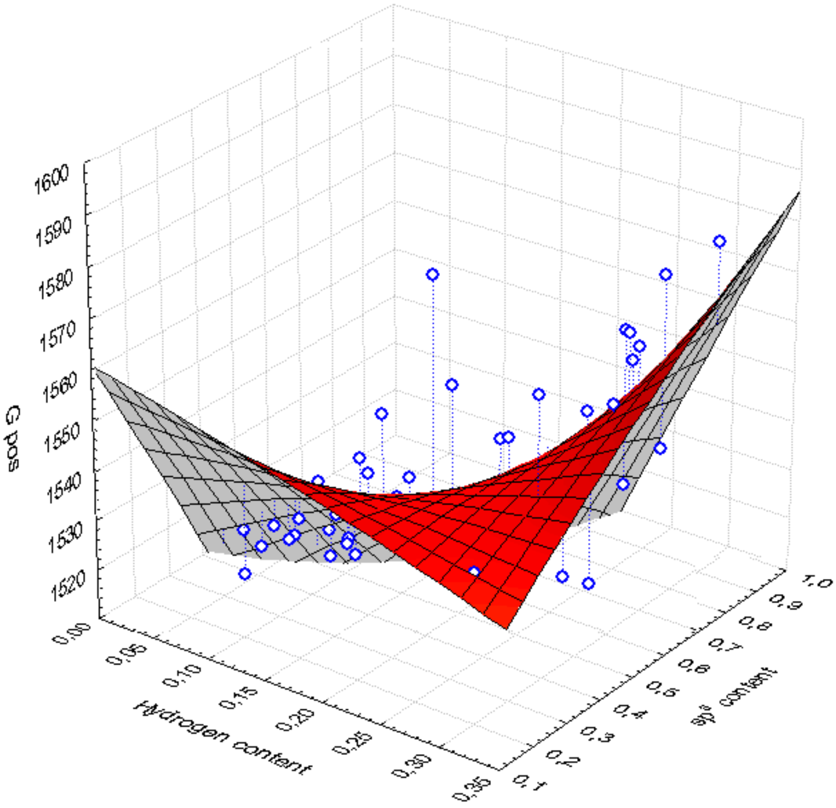

Fig.8.62: *The G-peak position variation as a function of the hydrogen concentration and* sp^3 *content in the deposited films.*

In Fig. 8.62 one can see that the surface of the graph has two slopes one is for hydrogenated films another slope is for hydrogen free films, see Fig. 8.63. Due to the high discrepancy in the experimental results, the *G*-peak position parameter cannot be used for sp^3 – hybridized carbon content determination. To do this, it is also necessary to know the hydrogen content to define the sp^3 content more precisely.

8.2.5.2 The I_D/I_G Ratio

The ratio of the *D* and *G* band peaks (I_D/I_G) is a measure of the size of the sp^2 bonded carbon atoms organized in rings. Together with other Raman parameters it is used to evaluate the sp^3/sp^2 content in the deposited DLC films. Usually, the experimental data from Robertson co-workers are used as reference. The evaluation of DLC coatings by Raman spectroscopy is common and for films with rather high hydrogen content (more than *20 at.%*), such method is able to provide reliable information about sp^3/sp^2 content [Casiragi05]. In the work [Irmer05] it was found that there is a strong influence of the hydrogen content on the behaviour of the *D* and *G* bands respectively, see Fig. 8.63.

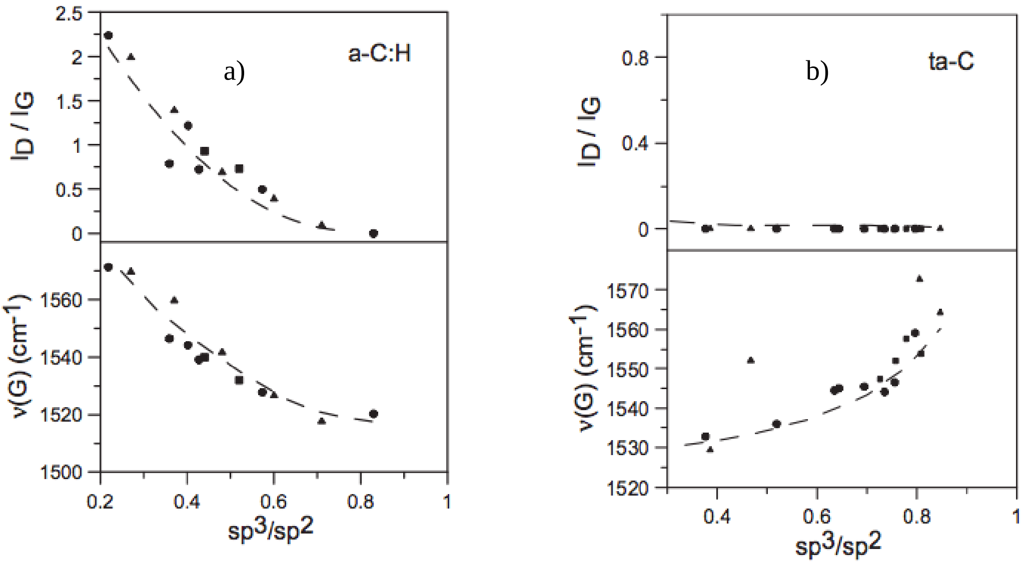

Fig.8.63: *Raman frequency of the G band and the* I_D/I_G *ratio in dependence on the* sp^3/sp^2 *ratio for different types of DLC films hydrogenated (a-C:H) and hydrogen free (ta-C) [Irmer05].*

According to the different experimental results summarized by [Irmer05], it was found that parameters such as the I_D/I_G ratio and the *G*-peak position have different behaviour for different types of DLC films. Fig. 8.63 a) shows their behaviour in the case of hydrogenated DLC films. Both parameters, the I_D/I_G ratio and the *G*-peak position, decrease with increasing sp^3 – carbon content. But for the “hydrogen-free” films, Fig. 8.63 b), these parameters have shown different behaviour: I_D/I_G stays constant at small values with an increase of content of sp^3 – carbon atoms and the *G*-peak position is going towards high values with an increase of sp^3 – carbon content.

8.2.5.2.1 Influence of Different Arc Modes on the I_D/I_G Ratio

The influence of the deposition parameters like $\varnothing_A/\varnothing_C$ ratio (different arc modes) and bias voltage on the measured parameter the I_D/I_G is shown in Fig. 8.64. The DLC films were deposited without hydrogen addition.

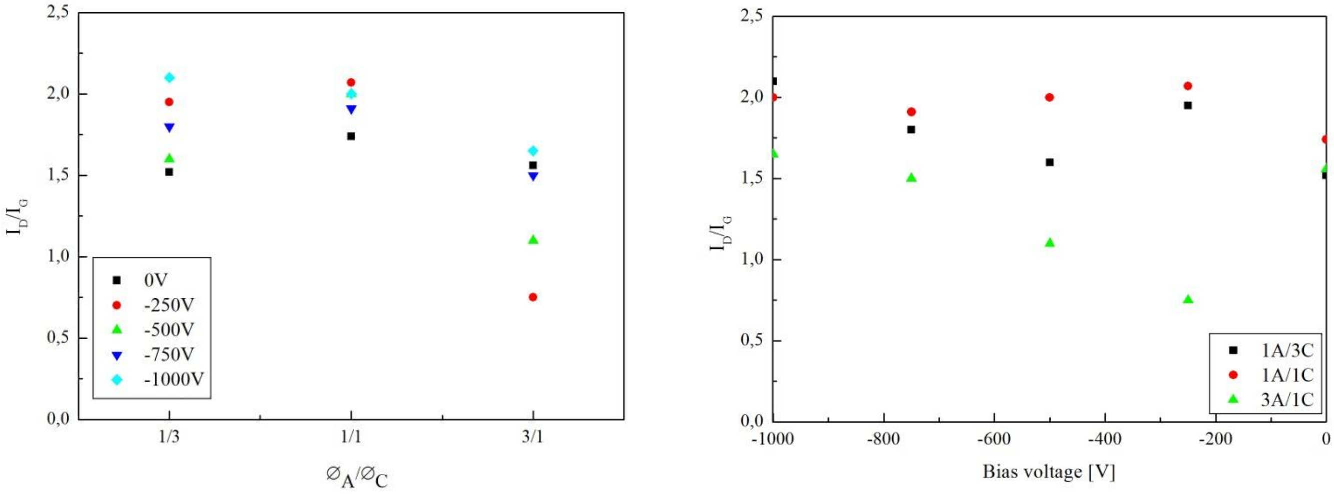

Fig. 8.64: *Variation of I_D/I_G for DLC films deposited at different electrode diameter ratios $\varnothing_A/\varnothing_C$ and different substrate bias voltages without hydrogen addition taken at 633 nm [Khlopyanova12].*

In Fig. 8.64 one can see that the I_D/I_G ratio for “hydrogen-free” films is much bigger than in the literature, Fig. 8.63 b). It reaches the maximum for the DLC films deposited at “anodic” mode ($\varnothing_A/\varnothing_C = 1/3$) and decrease with the transition to the “cathodic” arc mode ($\varnothing_A/\varnothing_C = 3/1$). An increase of bias voltage leads to slight increase in I_D/I_G ratio.

8.2.5.2.2 Influence of Bias Voltage and Different Hydrogen Flow Rates on the I_D/I_G Ratio

The influence of bias voltage and different hydrogen flow rates on the I_D/I_G ratio for DLC films deposited at “anodic” mode ($\varnothing_A/\varnothing_C = 1/3$) is shown in Fig. 8.65.

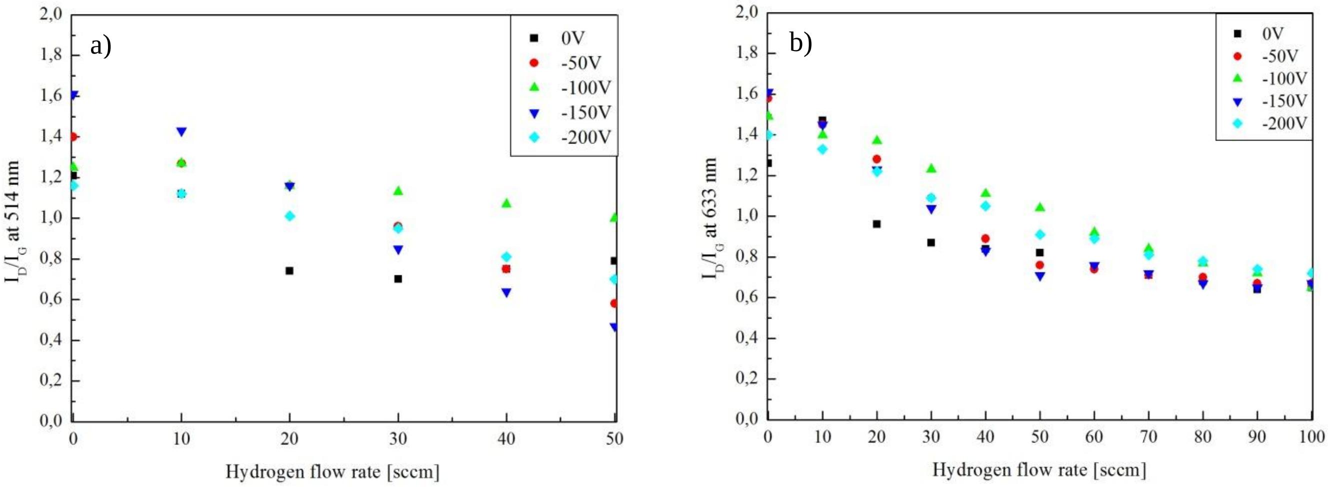

Fig. 8.65: *Variation of I_D/I_G as a function of bias voltage and different hydrogen flow rates measured at different laser wavelengths a) at 514 nm, b) at 633 nm.*

Fig. 8.65 shows that the I_D/I_G ratio decreases with increasing hydrogen flow rate. But the influence of bias voltage on this parameter is less strong. In order to have more detailed view, the results were summarized in the following diagram, Fig. 8.66.

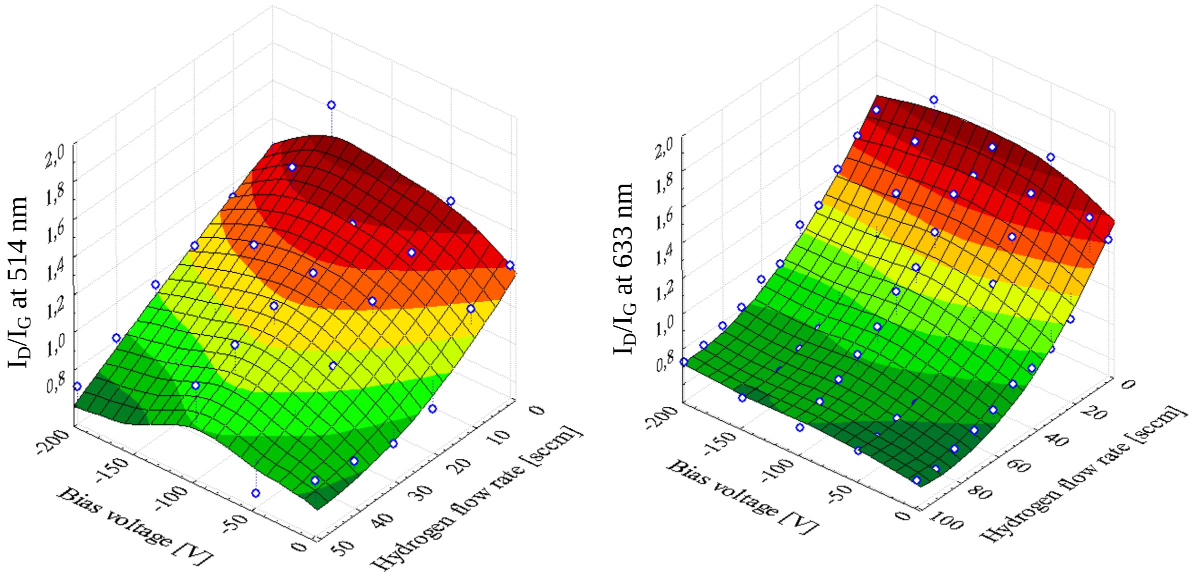

Fig. 8.66: *Summarized variation of the I_D/I_G as a function of hydrogen flow rate and bias voltage measured at different laser wavelengths a) at 514 nm, b) at 633 nm.*

One can see that an increase of bias voltage leads to a small increase of the I_D/I_G ratio, but this effect is much weaker than effect of hydrogen flow rate. Using the results obtained from hydrogen concentration measurements, see *Chapter 8.2.3.2* and evaluation of the optical spectra, see *Chapter 8.2.4* it was possible to plot a summarized 3D-diagram, see Fig. 8.67.

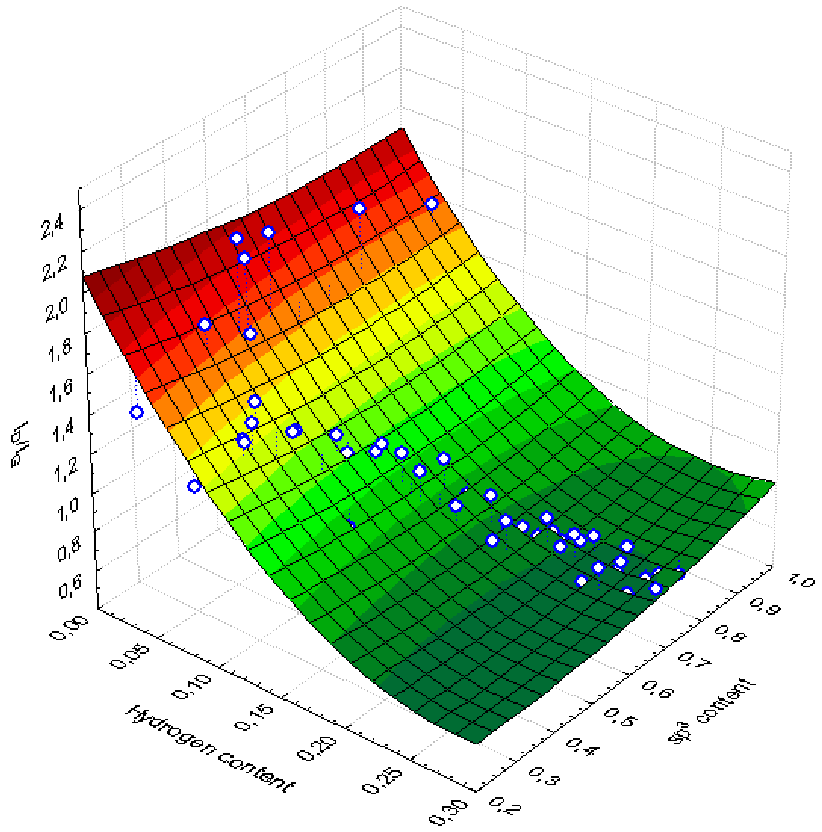

Fig. 8.67: *Variation of the I_D/I_G ratio as a function of the hydrogen concentration and sp^3 content deduced from band gap evaluation in the deposited films.*

Fig. 8.67 shows that hydrogen content in the deposited DLC films has strong influence on the I_D/I_G ratio. The behaviour of the I_D/I_G ratio in the dependence of the sp^3/sp^2 ratio is rather different for hydrogenated and hydrogen-free coatings, see Fig. 8.63. But it was found that even for the films with very low hydrogen content, around *0.4 at.%*, the I_D/I_G ratio is far away from the near zero values as shown by [Irmer05]. The term hydrogen-free coatings means that even such values around *0.4 at.%* are still to high to consider them as hydrogen-free coatings. To produce really hydrogen-free coatings in the regular plasma deposition systems is not possible or very complicated. In fact for the regular plasma systems the hydrogen content around *3 at.%* was observed. There are no reliable sources concerning Raman behaviour for the hydrogen poor coatings with hydrogen concentration around few percents. Therefore application of Raman spectroscopy for the evaluation of so-called “hydrogen-free” coatings – without confirmation that they are really hydrogen-free – is not possible.

8.2.5.3 The Full Width at Half Maximum of G-Peak (FWHM G)

The *FWHM G* is the parameter which is influenced by the structural disorder of sp^2 – bonded carbon atoms. The *FWHM G* parameter is a measure of structural disorder [Casiragi05]. Structural disorder originates from bond length distortion and bond angle. It is also used to evaluate the cluster size of the sp^2 – bonded carbon atoms.

8.2.5.3.1 Influence of Different Arc Modes on FWHM G

The influence of the deposition parameters $\varnothing_A/\varnothing_C$ ratio and bias voltage on the measured parameter I_D/I_G is shown in Fig. 8.68. The DLC films were deposited without hydrogen admixture to the plasma.

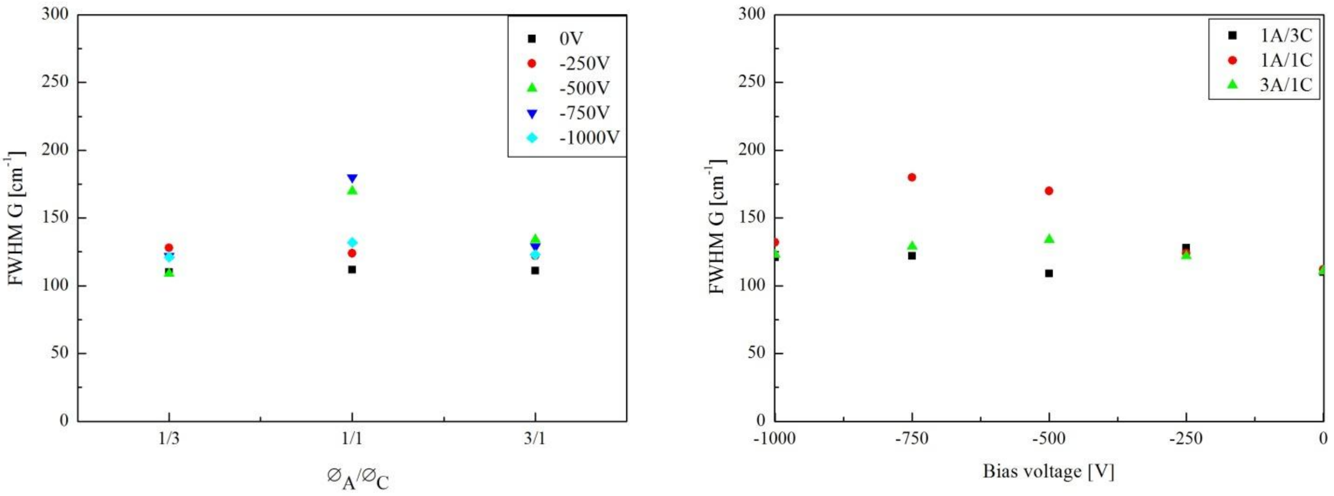

Fig. 8.68: *Variation FWHM G for DLC films deposited at different electrode diameter ratios* $\varnothing_A/\varnothing_C$ *and different substrate bias voltages without hydrogen taken at 633 nm [Khlopyanova12].*

As one can see, the different arc modes have small influence on the *FWHM G* parameter. The films deposited at “anodic” mode ($\varnothing_A/\varnothing_C = 1/3$) have the smallest *FWHM G*. The films deposited at “cathodic” mode ($\varnothing_A/\varnothing_C = 3/1$) have nearly the same *FWHM G*. In the case of “transition” mode ($\varnothing_A/\varnothing_C = 1/1$), there is an increase of the *FWHM G*, but such effect was observed for the DLC films deposited at *“– 500 V”* and *“– 750 V”* bias voltage only. In turn increase of bias voltage leads to increase of *FWHM G*. The DLC films deposited at *0 V* bias voltage have the smallest *FWHM G*.

8.2.5.3.2 Influence of Bias Voltage and Different Hydrogen Flow Rates on FWHM G

The influence of bias voltage and different hydrogen flow rates on the *FWHM G* parameter for DLC films deposited at “anodic” mode ($\varnothing_A/\varnothing_C = 1/3$) is shown in Fig. 8.69.

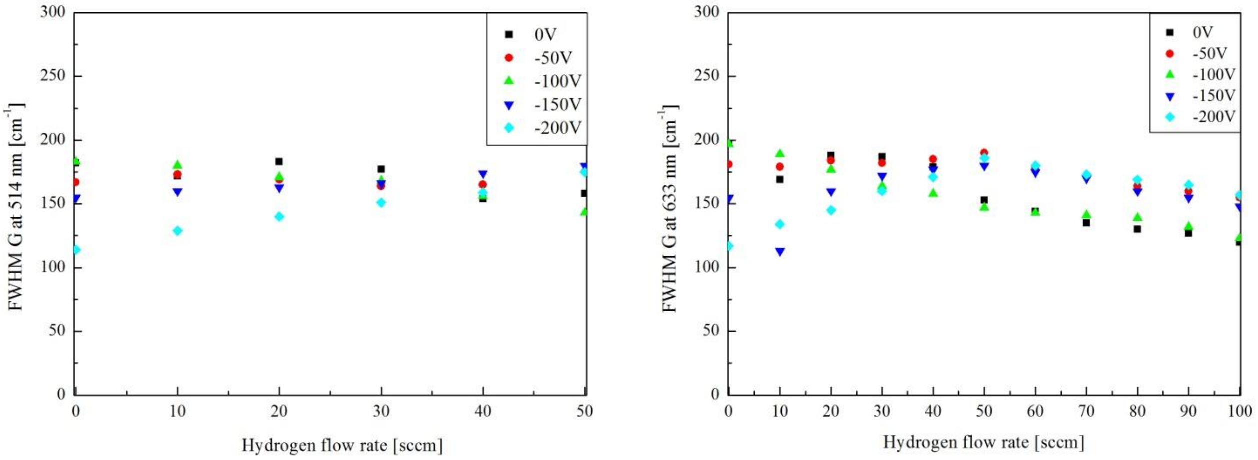

Fig. 8.69: *Variation of FWHM G as a function of the deposition parameters measured at different laser wavelengths a) at 514 nm, b) at 633 nm.*

Fig. 8.69 shows that *FWHM G* is influenced mostly by the hydrogen flow rate. It is shown that value of *FWHM G* increase with increase of the hydrogen flow rate and after *50 sccm* it slightly decreases with the increase of hydrogen flow rate. Using data from [Ferrari04] Fig. 8.70 it was possible to estimate the cluster size of the sp^2 – bonded carbon atoms. In this work, the deposited DLC films have cluster size around *1 nm* to *2 nm*. Increase of hydrogen content in the deposited DLC films leads to increase of cluster size.

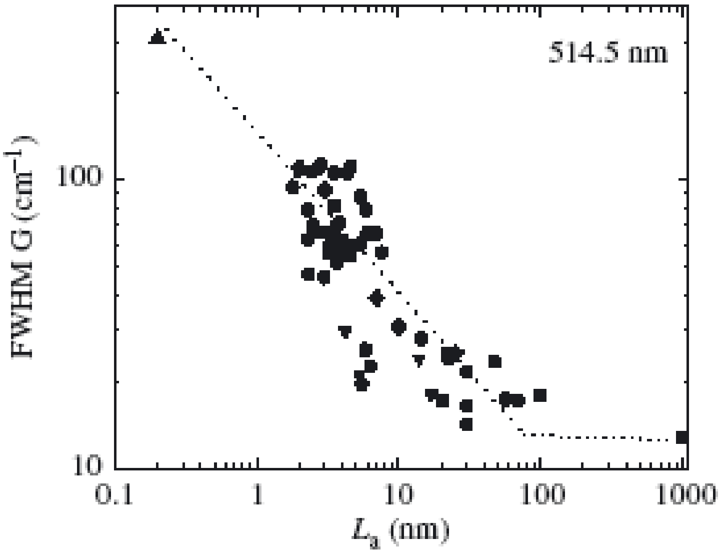

Fig.8.70: *Variation of FWHM G with the cluster size of the sp^2 – bonded carbon atoms L_a [Ferrari04].*

8.2.5.4 The G-Peak Dispersion ($Disp_G$)

The G-peak dispersion *($Disp_G$)* is very sensitive to the evolution of the sp^2 – carbon atoms phase and related to the optical properties and hydrogen content. This parameter determines topological disorder. It originates from size and shape distribution of sp^2– bonded carbon atoms [Casiragi05]. It gives information of how sp^2– carbon atoms are organised in the films (rings or chains), see Fig. 8.71. $Disp_G$ is linked to the total $(C-C + C-H)$ sp^3 – hybridized carbon fraction, hydrogen content, band gap and mechanical properties.

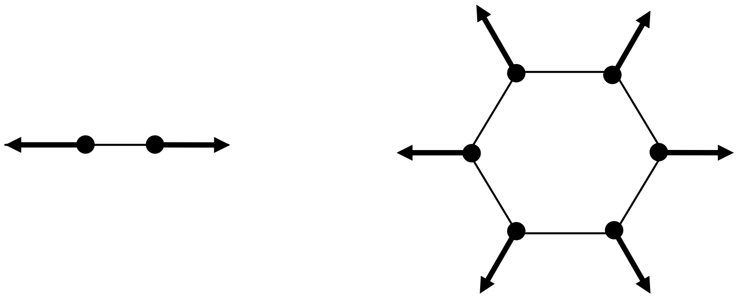

Fig. 8.71: *Eigenvectors of the Raman G and D modes in DLC.*

In order to determine the G-peak dispersion, a multi-wavelength Raman spectroscopy was used. At the beginning, the G-peak position was measured using *Ar* laser radiation with excitation wavelength $\lambda_1 = 514\ nm$, and then *He-Ne* laser with excitation wavelength $\lambda_2 = 633\ nm$, see Fig. 8.72.

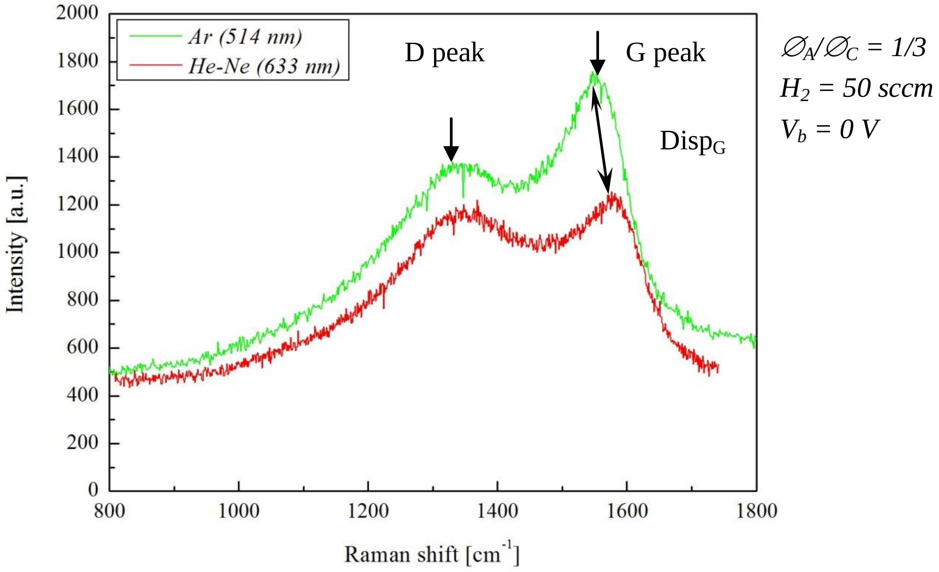

Fig. 8.72: *Raman spectra measured at different laser wavelengths, 514 nm and 633 nm, for DLC films deposited at electrode diameter ratio $\varnothing_A/\varnothing_C = 1/3$, 0 V bias voltage, 50 sccm hydrogen flow rate.*

The G-Peak dispersion $Disp_G$ is defined by the equation:

$$Disp_G = \frac{G_{pos}(\lambda_1)-G_{pos}(\lambda_2)}{(\lambda_1-\lambda_2)} \qquad (8.15)$$

In Fig. 8.73 one can see the influence of bias voltage and hydrogen flow rate on the G-peak dispersion deposited at “anodic” mode ($\varnothing_A/\varnothing_C = 1/3$).

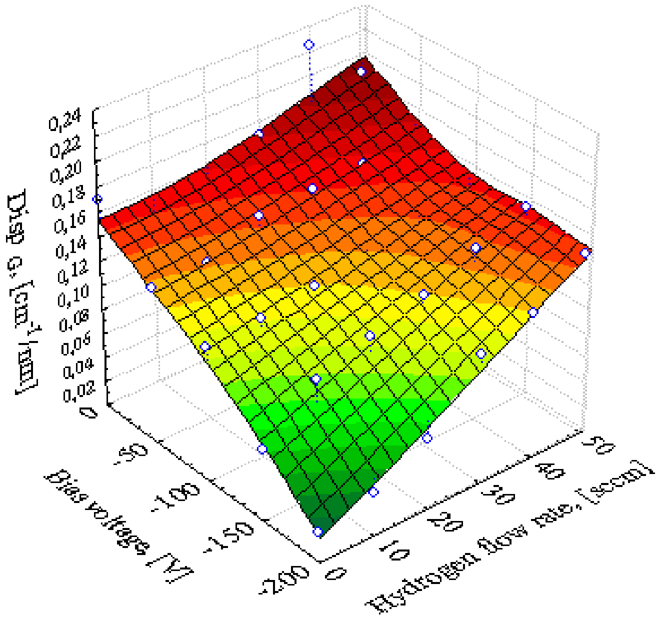

Fig.8.73: *The G-peak dispersion as a function of deposition parameters.*

Comparison to the Robertson data [Robertson02] suggests information on the organisation of sp^2 – bonded carbon atoms. In the films which demonstrate high dispersion, the sp^2 – bonded carbon atoms exist in chains. And for the DLC films with very low dispersion, the sp^2 – bonded carbon atoms form mostly rings.

One can see that an increase of the negative bias voltage leads to a decrease of G-peak dispersion. The G-peak dispersion increases linearly with increasing of hydrogen content, while the *FWHM G* shows a maximum at *50 sccm* hydrogen flow rate and then decreases.

8.2.5.5 Correlation between Results from Raman and UV-VIS Spectroscopy

In this chapter the attempt to find the correlation between the data evaluated from *UV-VIS* spectra and the results obtained from Raman spectra is shown.

8.2.5.5.1 The Optical Band Gap and Raman parameters

Fig. 8.74 shows variation of the *G*-peak position and the I_D/I_G ratio with optical band gap.

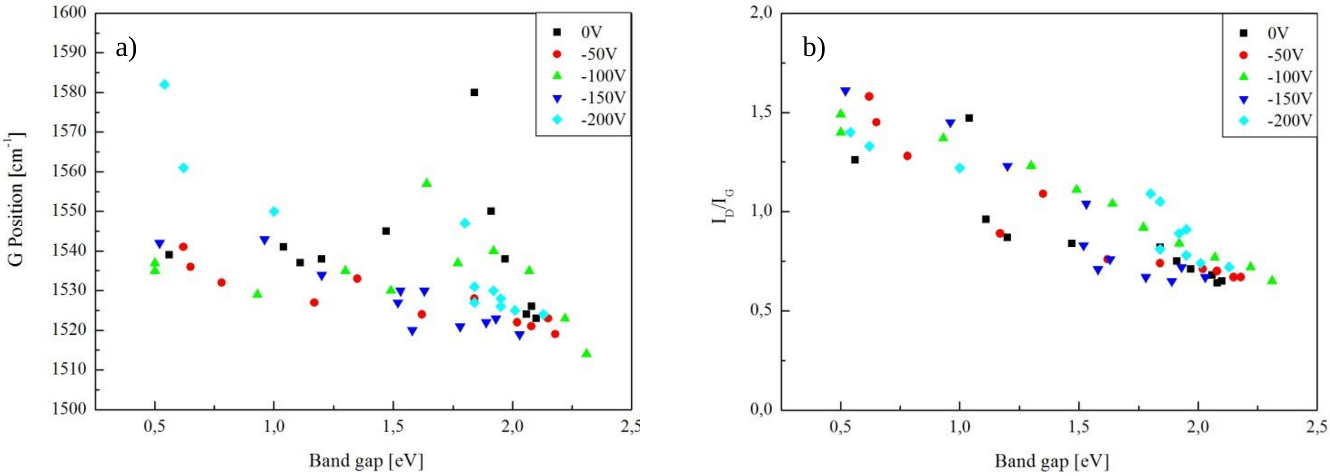

Fig. 8.74: *a) The G-peak position variation with the band gap, and b) variation of the I_D/I_G ratio with the band gap, for DLC films deposited at anodic mode ($\varnothing_A/\varnothing_C$ = 1/3).*

From Fig. 8.74 a) one can see that the *G*-peak position shifted to the lowest values with the increase of the optical band gap in the films. In the range between *1.5 eV – 2 eV*, there is an increase of the *G*-peak position. Such increase can be explained by the change in the DLC film structure by the transition from one type of DLC films to another.

From Fig. 8.74 b) one can see that the I_D/I_G ratio also decreases with the increase of the optical band gap in the films.

Using information from these two parameters [Ferrari00] one can conclude that the decrease of *G*-peak position and decrease of the I_D/I_G ratio caused by an increase of sp^3-content in the DLC films. The growth of the band gap with increase of sp^3-content correlates with experimental results shown in this work. The data obtained from two independent measurement techniques are in good agreement with each other.

8.2.5.5.2 The Imaginary Part ε_2 of the Dielectric Function and Raman Parameters

Fig. 8.75 shows variation of the *G*-peak position and I_D/I_G ratio with the imaginary part ε_2 of the dielectric function measured at *3.3 eV*.

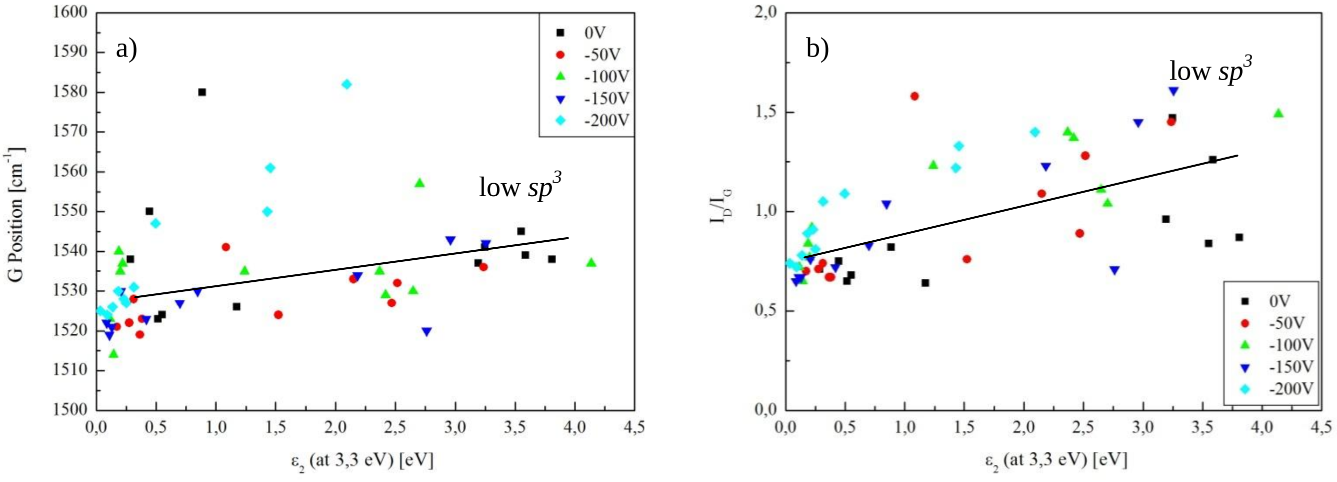

Fig. 8.75: *a) The G-peak position variation with the imaginary part ε_2 of the dielectric function, and b) variation of the I_D/I_G ratio with the imaginary part of the dielectric function for DLC films deposited at anodic mode ($\varnothing_A/\varnothing_C = 1/3$).*

One can see that both parameters increase with an increase of the imaginary part ε_2 of the dielectric function.

In order to evaluate the influence of the imaginary part ε_2 of the dielectric function on both Raman parameters it is necessary to use data from *Chapter 8.2.4.5*, where the influence of deposition parameters on the imaginary part ε_2 of the dielectric function is discussed. As it is shown above, the behaviour of the imaginary part ε_2 of the dielectric function at *3.3 eV* is described by $\sigma \rightarrow \sigma^*$ band transitions between sp^3-hybridized carbon atoms. The DLC films with low sp^3-content have high values of the imaginary part ε_2 of the dielectric function (*2 eV – 4 eV*). By increase of sp^3-content in the films the imaginary part ε_2 of the dielectric function decreases to values around *0.5 – 0.1 eV*, see Fig. 8.57. The higher sp^3-content in the DLC films, the lower values has the imaginary part ε_2 of the dielectric function.

Evaluation of the Raman spectra shows that an increase of *G*-peak position and I_D/I_G ratio caused by an decrease of sp^3-content in the DLC films. Again, both spectroscopic methods Raman spectroscopy and UV-VIS spectroscopy have shown correlation between obtained results. Which can be explained in consistent way.

8.2.6 Mechanical Properties

8.2.6.1 Residual Stress Measurements

The residual stress in the DLC films plays the key role and determines the mechanical properties of the DLC films. The residual stress measurements were performed by *ESMA* technique. The main components to the residual stress in the DLC films is the thermal stress σ_{th} and intrinsic stress σ_{int}. The lattice mismatch component can be also neglected due to the fact that DLC films are amorphous [Robertson02].

8.2.6.1.1 Thermal Stress

In this work, the thermal stress σ_{th} component from *Eq. (6.9)* can be neglected due to the low deposition temperature (the substrate was mounted onto a copper water-cooled holder) and 20 cm working distance, as is shown in Fig. 8.76.

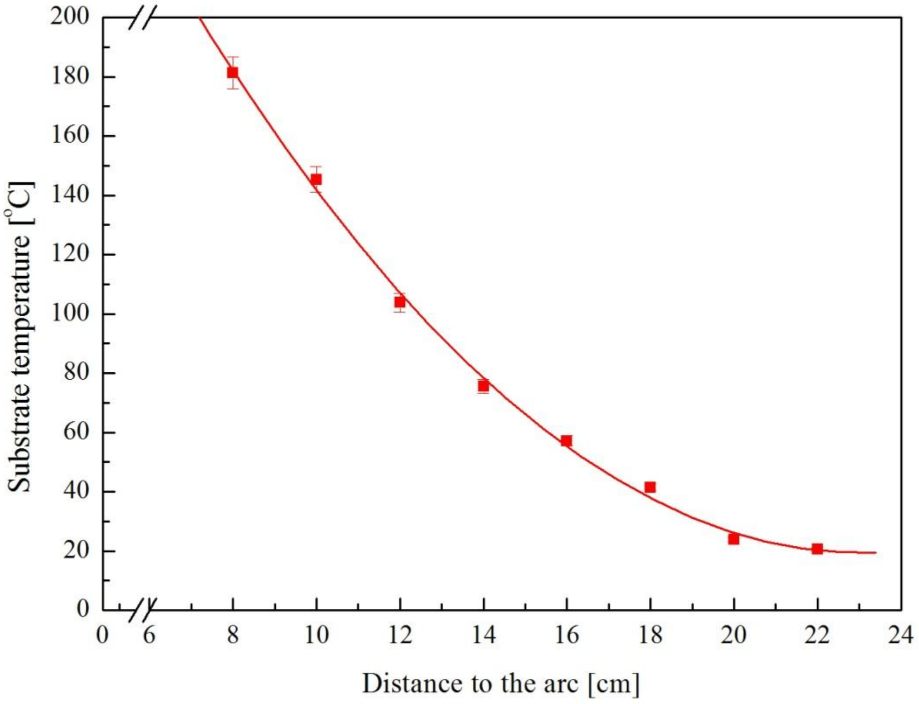

Fig. 8.76: *Substrate temperature as a function of the distance between substrate and plasma.*

As one can see during the deposition the substrate temperature was kept near the room temperature.

8.2.6.1.2 Influence of Different Arc Modes on Residual Stress

As it was shown above, particle energy (ion energy) is a crucial parameter characterizing different arc modes, see *Chapter 8.1.4*. And by-turn this parameter defines also not just chemical and electronic properties of the deposited DLC films but also their mechanical properties, especially intrinsic stress. In this chapter, the influence of different arc modes on residual stress is investigated. According to substrate curvature, it is necessary to mention that compressive stress defined as negative and tensile stress as positive.

In Fig. 8.77 one can see the influence of different arc modes on intrinsic stress in the DLC film. The films were deposited without hydrogen gas.

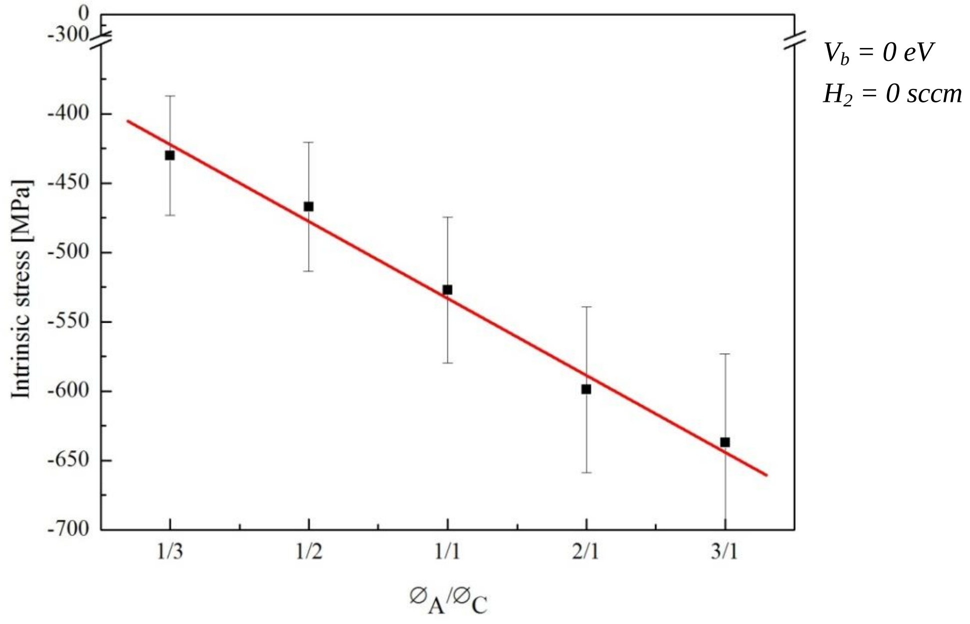

Fig. 8.77: *Intrinsic stress in the deposited DLC films as a function of the different arc modes.*

One can see that all the DLC films deposited by the vacuum arc are found to be under compressive stress. Such results are in good agreement with literature [Robertson02]. The films deposited at the “cathodic” arc mode ($\varnothing_A/\varnothing_C = 3/1$) have shown the highest values of the compressive stress – *640 MPa*, and films deposited at the “anodic” mode ($\varnothing_A/\varnothing_C = 1/3$) have the lowest stress level – *426 MPa*. There is a correlation between particle energy and the film stress, see Fig.8.78.

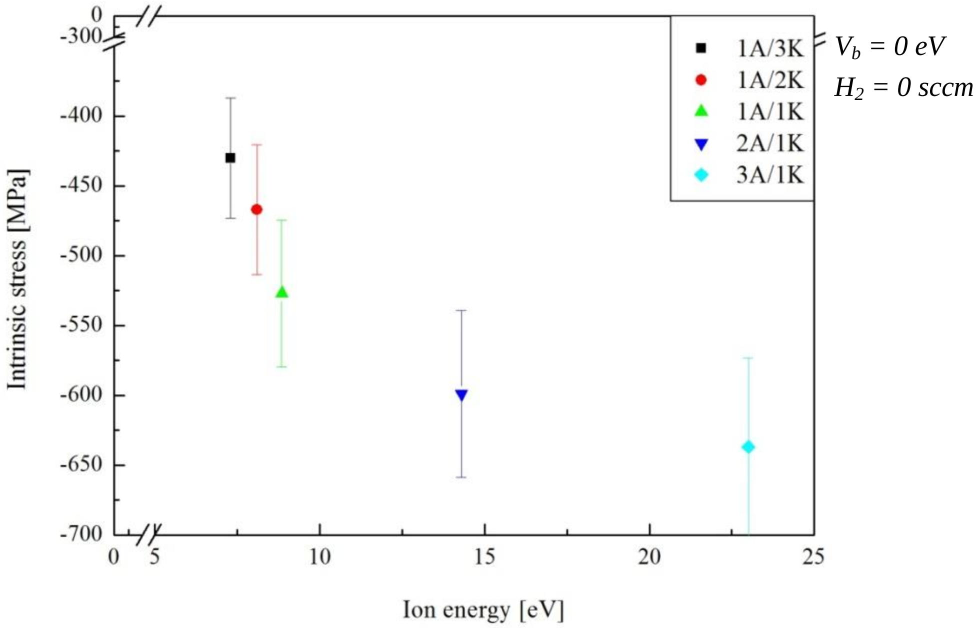

Fig. 8.78: *Intrinsic stress as a function of the ion energy for different arc modes.*

Fig. 8.78 shows the influence of the ion energy on the mechanical stress in the deposited DLC films. The films deposited at the electrode diameter ratio $\varnothing_A/\varnothing_C = 3/1$ “cathodic” mode with particle energy $E_i = 23\ eV$ have the highest mechanical stress, - *640 MPa*. The reduction in the ion energy results in a change in the film structure and stress reduction from – *640 MPA* to a to – *430 MPa*.

8.2.6.1.3 Influence of Bias Voltage on Residual Stress

The negative bias voltage to the substrate is used to increase the energy of the incident ions to the substrate surface. And as it was shown, residual stress is proportional to the particle energy and an increase of the particle energy leads to an increase of the mechanical stress. In order to investigate influence of this parameter, films were deposited at $\varnothing_A/\varnothing_C = 1/3$ and without hydrogen admixture to the plasma, see Fig. 8.79.

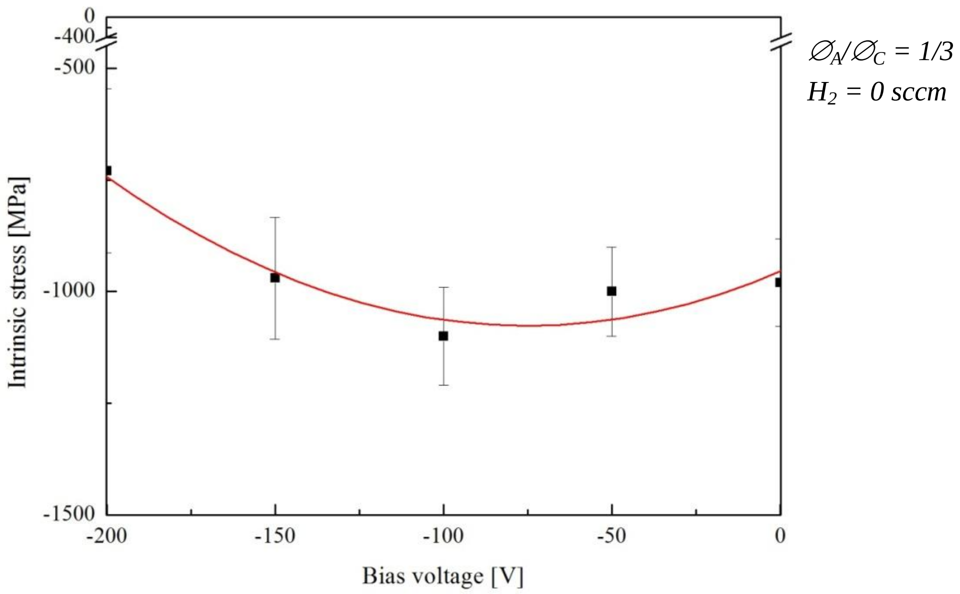

Fig. 8.79: *Variation of the mechanical stress as a function of the bias voltage for DLC films deposited at* $\varnothing_A/\varnothing_C = 1/3$ *without hydrogen admixture to the plasma.*

From Fig. 8.79 one can see that there is a maximum in the compressive stress (negative values) which corresponds to the *"– 100 V"* bias voltage. Such result is in agreement with literature [Robertson02].

8.2.6.1.4 Influence of Different Hydrogen Flow Rates on Residual Stress

Another parameter influencing the film properties is the plasma chemistry. The gas admixture to the plasma has also strong influence onto residual stress. The hydrogen admixture into the carbon plasma leads to the formation of the various hybridized carbon atoms and carbon hydrogen bonds, characterized by different mechanical properties [Grill99]. The admixture of hydrogen into the plasma leads to the changes in the particle energy due to the chemical reactions in the plasma and particle collisions due to the decrease of the mean free path of the carbon atoms.

Fig. 8.80 shows the measured residual stress in DLC films deposited at $\varnothing_A/\varnothing_C = 1/3$ "anodic" mode, without bias voltage at different hydrogen flow rates.

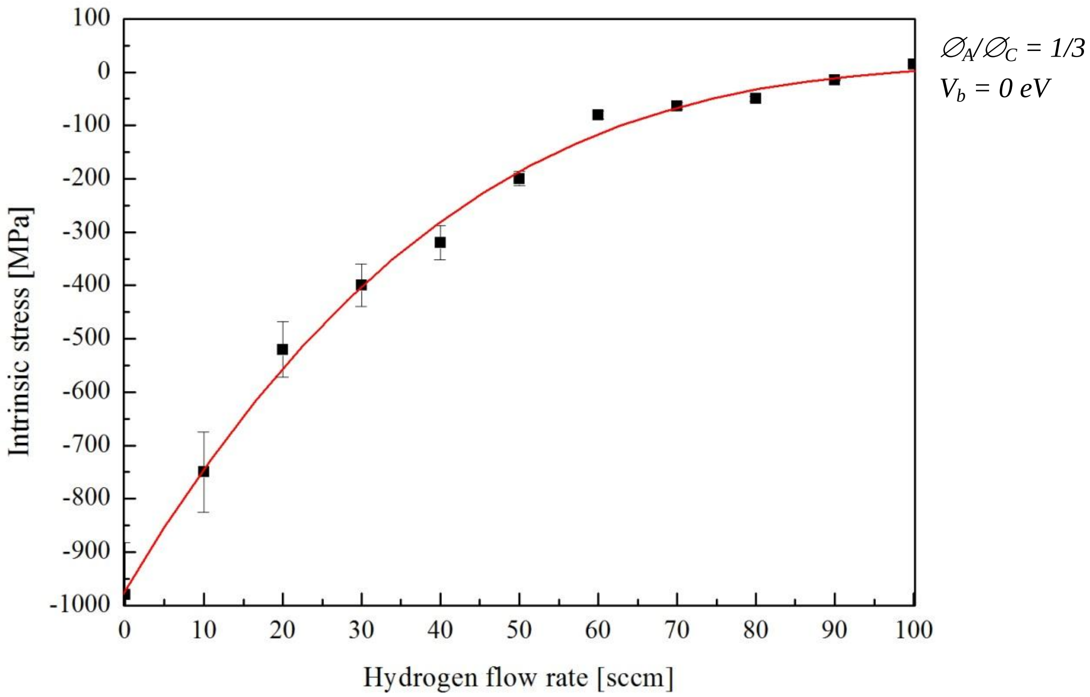

Fig. 8.80: *Influence of the hydrogen flow rate on the residual stress in the deposited DLC films.*

Hydrogen has also strong influence on the intrinsic film stress, but as opposed to the bias voltage, the increase of the hydrogen flow rate leads to stress reduction. Such effect takes place due to the decrease of the ion energy in the plasma and hydrogen incorporation in the growing films. This changes the structure of the growing films. At certain flow rates, the type of stress can be changed from compressive to tensile. Using the measured particle energy from *Chapter 8.1.4.2* and data from the intrinsic stress measurements, one can demonstrate the correlation between particle energy and intrinsic stress at different hydrogen flow rates. In order to do this the DLC films were deposited at $\varnothing_A/\varnothing_C = 1/3$ electrode ratio “anodic mode” and *0 V* bias voltage. The influence of hydrogen flow rate on ion energy and intrinsic stress is shown in Fig. 8.81.

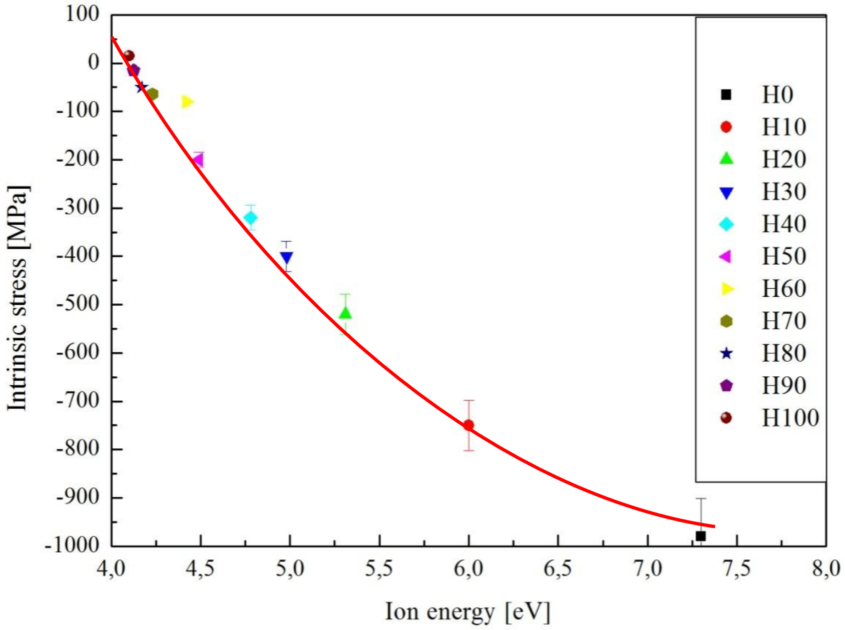

$\varnothing_A/\varnothing_C = 1/3$

$V_b = 0$ eV

Fig. 8.81: *Intrinsic stress as a function of the ion energy at different hydrogen flow rates.*

As one can see, DLC films deposited at high hydrogen flow rates (low energetic ions) have low intrinsic stress. At *100 sccm* hydrogen flow rate, tensile stress (*15 MPa*) was observed. The highest stress of *-980 MPa* was measured for the films deposited at *0 sccm* hydrogen flow rate. In order to summarize the influence of all deposition parameters on intrinsic stress, the data were plotted in a 3D diagram, see Fig. 8.82.

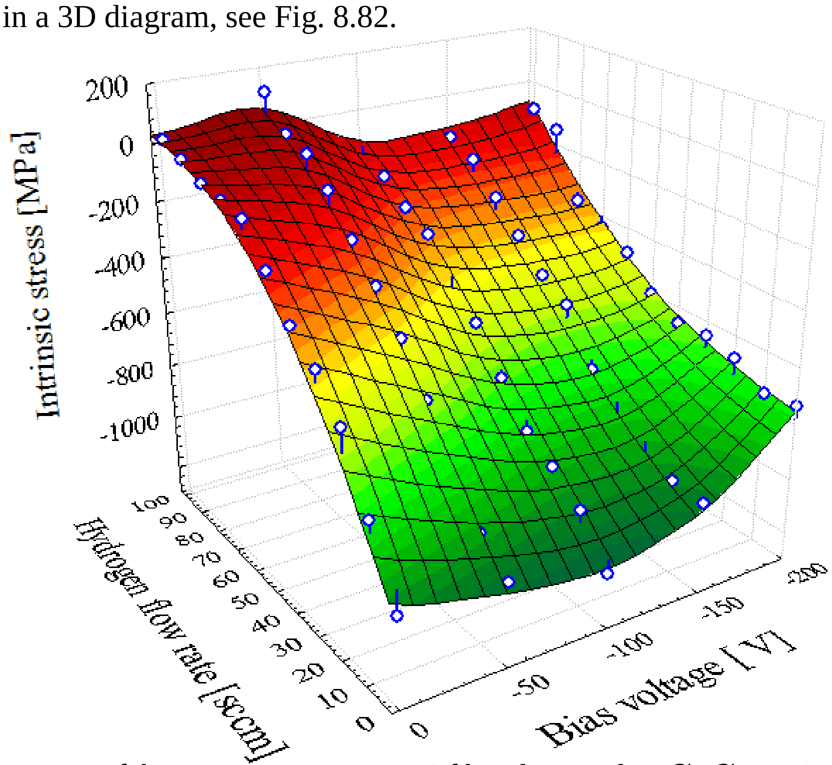

$\varnothing_A/\varnothing_C = 1/3$

Fig. 8.82: *Variation of the intrinsic stress in DLC films deposited at* $\varnothing_A/\varnothing_C = 1/3$ *as a function of bias voltage and hydrogen flow rate.*

In a case of DLC films deposited without working gas an increase of the bias voltage till *"– 100 V"* leads to an increase of the residual film stress. Such effect can be explained by the increase of the $C = C$ sp^3 – hybridized carbon atoms content (the amount of stress is proportional to the sp^3 content, as explained by "subplantation model" [Robertson99]). Further increase of bias voltage leads to the reduction of the intrinsic stress.

For the DLC films deposited in hydrogen atmosphere the increase of the hydrogen flow rate leads to "stress termination", it saturates carbon bonds and prevents formation of the $C = C$ sp^3– hybridized carbon atoms. Presence of hydrogen leads to formation of soft polymeric $sp^3 = CH_2$ and $\equiv CH$ sites, (see Chapter 8.2.4.4.2) which are responsible for poor mechanical properties of such DLC films.

8.3 DLC Film Classification

All films deposited can be divided in few classes according to size of the optical band gap, hydrogen concentration and sp^2 and sp^3 bonded carbon atoms content. In order to categorize the films investigated in this work the ternary phase diagram can be used [Casiragi05], see Fig. 8.83. The films according to their properties can be divided in few types.

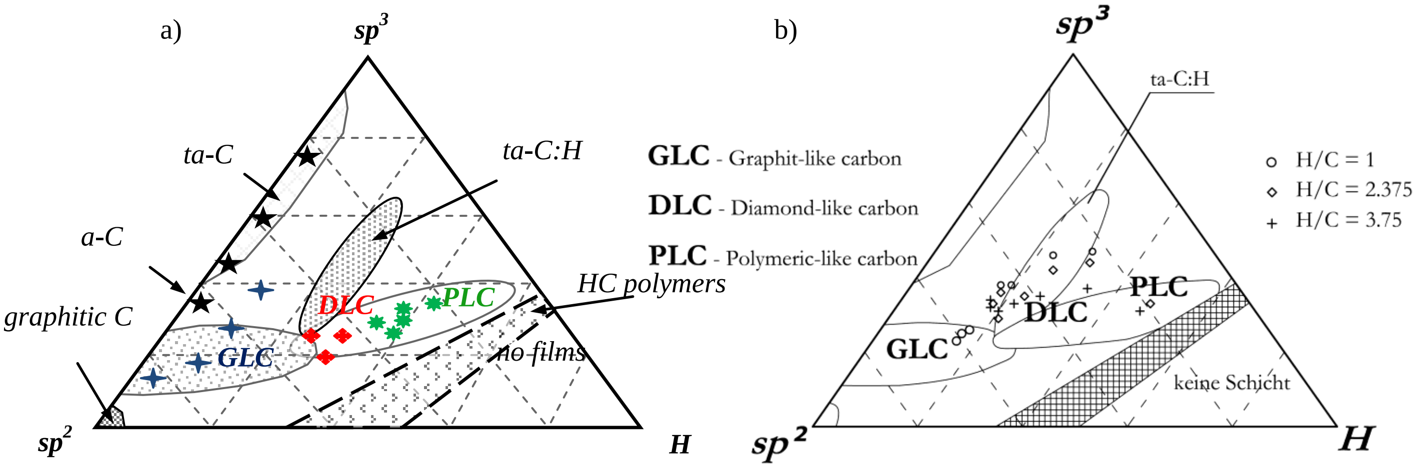

Fig. 8.83: *a) Ternary phase diagram for DLC films produced in this work. Various points – films deposited in this work according to their classification, where* ***GLC*** *– graphite-like carbon,* ***DLC*** *– diamond-like carbon and* ***PLC*** *– polymer-like carbon,* ***TAC*** *– tetrahedral amorphous carbon. b) Ternary phase diagram for the DLC films from [Poukhovoi11].*

As one can see, in this work it was possible to deposit DLC films in a wide range of film properties by variation of deposition parameters. The films deposited at residual gas vacuum have negligible hydrogen concentration ($[H] \sim 0.4\ at.\%$). They have very high content of sp^3– bonded carbon atoms, big optical band gap $E_g \geq 2\ eV$. Such films can be characterized as *ta-C* tetrahedral amorphous carbon – ***TAC***. Such films were deposited at “cathodic” arc mode without hydrogen admixture to the plasma. The films deposited at “anodic” arc mode have lower sp^3– content, smaller optical band gap $1\ eV < B_g < 2\ eV$. They can be described as *a-C* amorphous carbon films and they were also obtained without hydrogen admixture.

The films with relatively high hydrogen concentration ($[H] > 20\ at.\ \%$) can have up to $70\%\ sp^3$– bonded carbon atoms (but all bonds are hydrogen terminated) and are characterized by big optical band gap $E_g \approx 2\ eV$, low density, poor mechanical properties and high transparency in the visible range of the electromagnetic spectrum. Usually DLC films of such type belong to the polymer-like DLC – ***PLC***. Such films were deposited at high hydrogen flow rates over *50 sccm* in “anodic” arc mode.

The *a-C:H* films with low hydrogen concentration ($10\ at.\ \% < [H] \leq 20\ at.\ \%$) have lower content of sp^3– bonded carbon atoms than polymer-like DLC but the concentration of $C-C\ sp^3$ bonds is higher. Therefore they have higher density and their mechanical properties are much better than for ***PLC***. Their optical transmittance is lower than for polymer-like films and their optical band gap is narrower $1\ eV < B_g < 2\ eV$. The films with such properties are common for DLC *a-C:H* films – ***DLC***. Such films were deposited at the hydrogen flow rates between *30* and *50 sccm* in “anodic” arc mode.

DLC films with low hydrogen content ($[H] \leq 10\ at.\ \%$) are usually characterized by high sp^2– bonded carbon atoms concentration. They have narrow band gap $B_g \leq 1\ eV$, low transmittance and poor mechanical properties. Such films are usually called – graphite-like *a-C:H* films – ***GLC***. Such films were deposited at the hydrogen flow rates below *30 sccm* in “anodic” arc mode.

Comparing the films deposited in this work by vacuum arc Fig. 8.83a) and the films deposited by *ICP/CCP* plasma source [Poukhovoi11] Fig. 8.83b), one can see that both plasma sources are working in the same particle energy range from several *eV* till *100 eV*. Such similarity is also confirmed by the ternary phase diagrams obtained in this work and in the work [Poukhovoi11]. Both plasma sources are able to produce DLC coatings in a wide range of the film classes. But there is a difference mainly originated from the differences between CVD and PVD deposition techniques. By the CVD system, it was possible to deposit *ta-C:H* films but such class of coatings was not possible to obtain by PVD method in this work. However the CVD system is not able to produce DLC coatings with low hydrogen content or “hydrogen-free” coatings.

8.4 Magnesium Film Deposition

The results shown in this chapter are presented in [Filipov09, Filipov12].

In this chapter were investigated, the magnesium films deposited on steel substrates using experimental setup equipped with anodic vacuum arc with hydrogen admixture to the plasma, see *Chapter 7.2*. The aim is to show the influence of deposition parameters (particle energy, bias voltage and hydrogen admixture) on the Mg grain size in the deposited films. Magnesium grain size is the main parameter responsible for hydrogen storage in the Mg film. The influence of hydrogen admixture on the ion energy was shown in *Chapter 8.1.5*.

8.4.1 Energy Dispersive X-Ray Spectroscopy (EDX)

EDX is widely used analytical technique to identify elemental composition of materials. It is used in conjunction with the scanning electron microscopy (*SEM*). It allows to perform elemental composition analysis at any investigated by SEM sample.

Before deposition it was necessary to know the elemental composition of magnesium used. In the deposition Mg with *99 %* purity was used. In Fig. 8.84 one can see SEM image of magnesium used for the deposition.

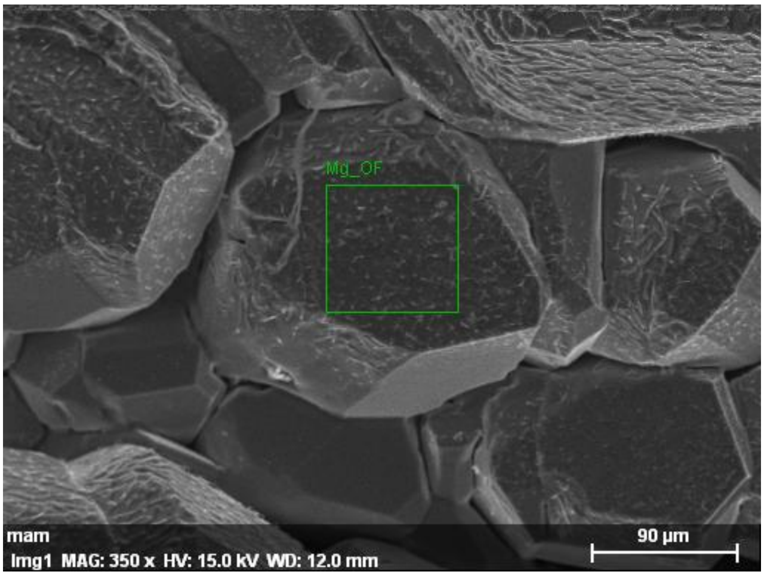

Fig. 8.84: *SEM image of magnesium surface.*

The EDX spectrum for magnesium specimen is shown in Fig. 8.85.

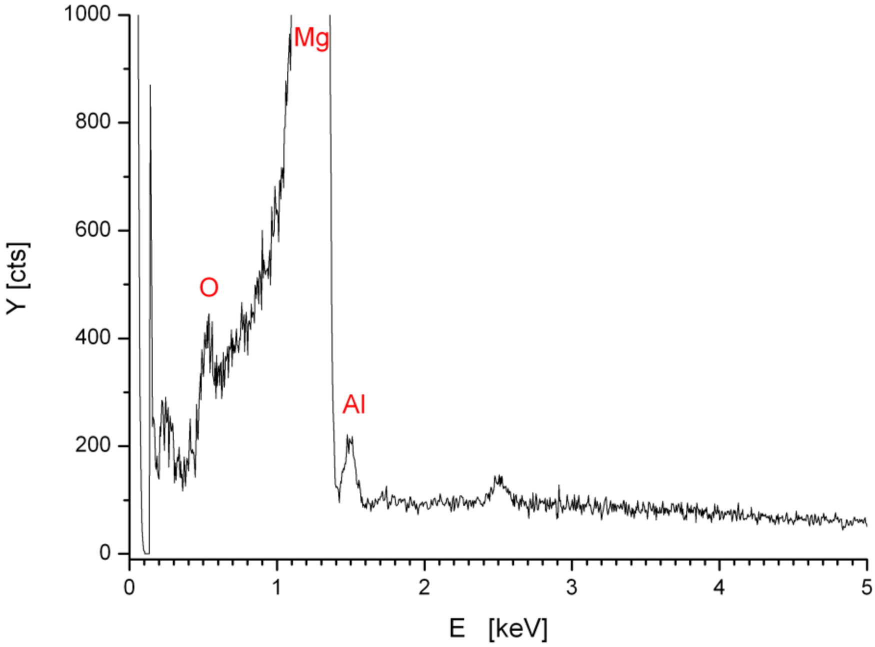

Fig. 8.85: *EDX spectrum of magnesium specimen.*

In EDX spectrum the strongest peak belongs to magnesiumg. Some minor impurities can be observed in EDX spectrum of magnesium. First impurity detected is the oxygen. Oxygen peak is coming from the magnesium surface due to the strong oxidation of alkaline earth metal. The next peak belongs to the aluminium. The presence of Al can be explained by impurities in magnesium itself due to insufficient purification of Mg during production. The remaining peaks cannot be identified. But their intensity is rather low and their influence on magnesium purity can be neglected.

Before magnesium deposition it is necessary to know the elemental composition in the steel substrate. EDX measurements were performed on a scanning electron microscope *Quanta 400 FEG* equipped with EDAX analyse system type “*Genesis 4000*”, see Fig. 8.86.

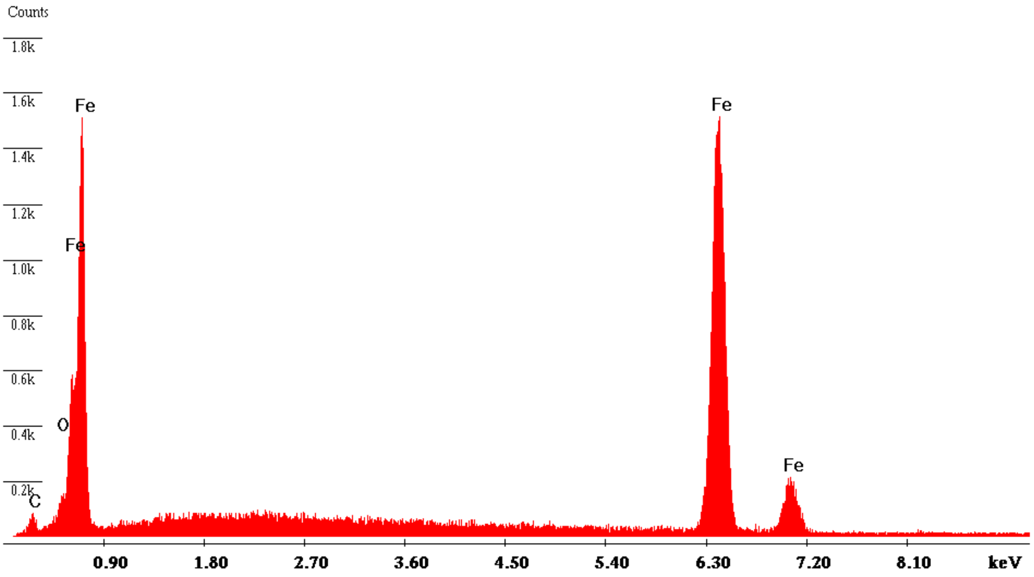

Fig. 8.86: *EDX spectrum of uncoated steel substrate.*

In Fig. 8.86 one can see that main peaks coming from steel. A small peak of oxygen can be explained by oxide layer on the steel surface. Carbon peak is also coming from steel. After magnesium deposition the EDX was used to control the Mg film elemental composition, see Fig. 8.87.

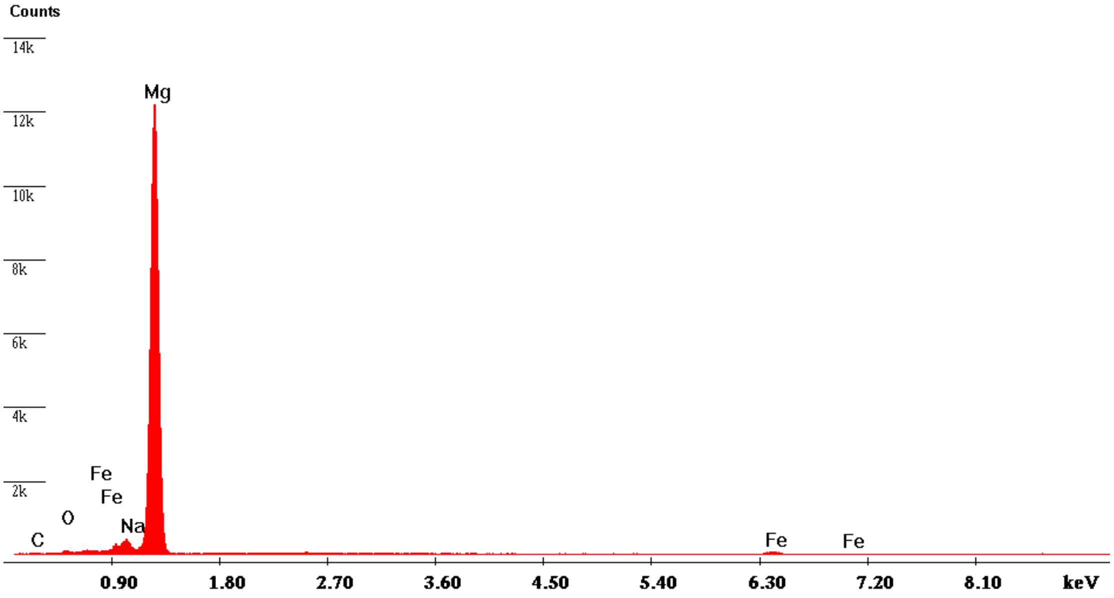

Fig. 8.87: *EDX spectrum of magnesium coated steel substrate.*

In EDX spectrum of magnesium coated steel substrate a signal from Fe become weaker due to thick magnesium film on the substrate. Fig. 8.87 shows that a small peak appears around *1 keV*. This peak can be attributed to Zn and Cu (or to Na impurities of the magnesium used for coating).

As it was mentioned above, the anodic arc is characterized by very high deposition rate. Due to high deposition rate even the cathode can be coated with material coming from anode crucible. In order to demonstrate such effect the cathode disc was examined after the deposition. Fig. 8.88 shows picture of brass cathode disc and SEM image of the eroded cathode. Fig. 8.89 demonstrates EDX spectrum of the brass cathode surface after magnesium deposition.

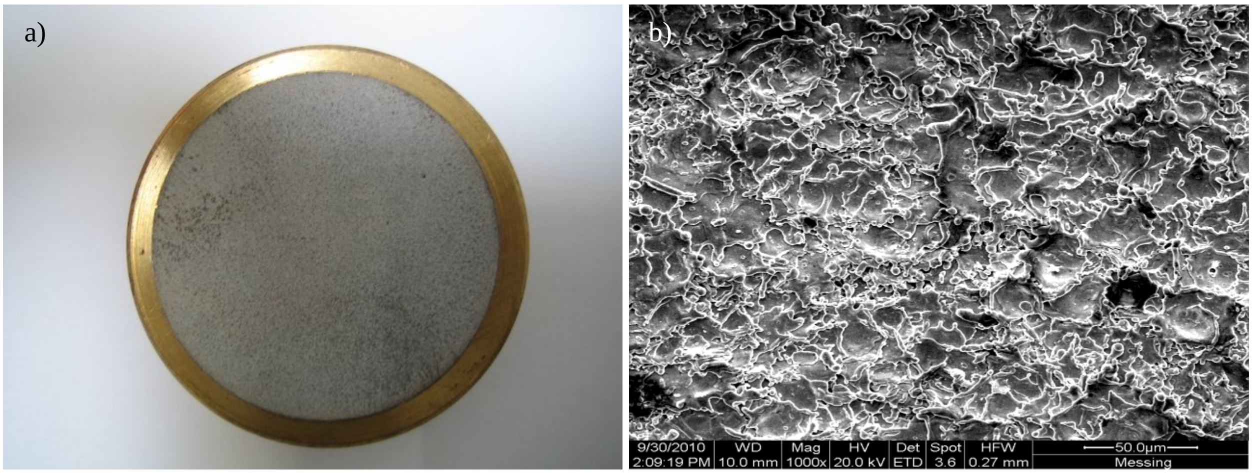

Fig. 8.88: a) *Picture of the brass cathode disc, b) SEM picture of the eroded cathode disc.*

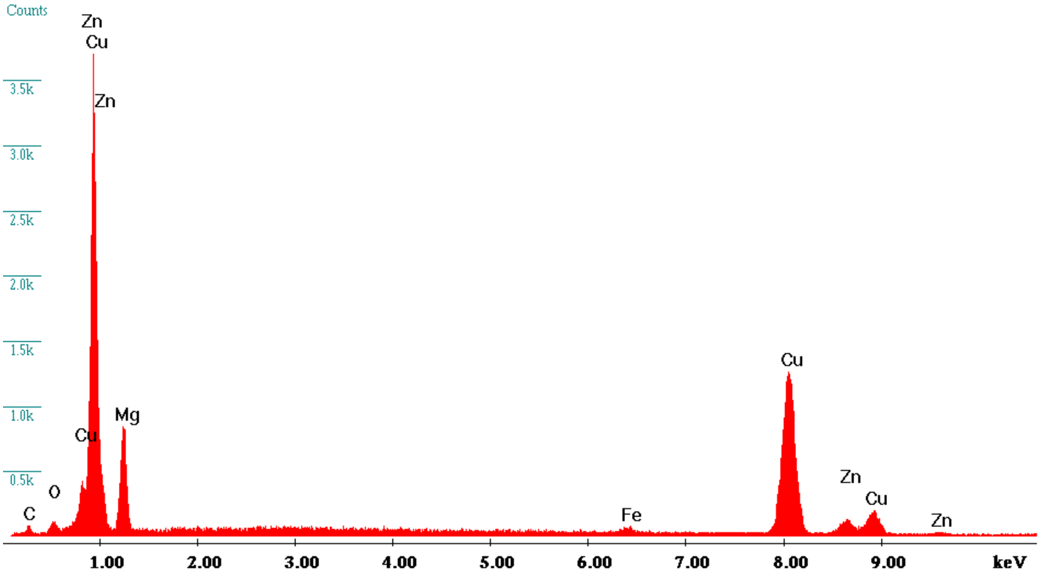

Fig. 8.89: *EDX spectrum of magnesium coated cathode.*

In Fig. 8.89 one can see typical EDX spectrum for brass mainly Cu and Zn. The presence of the Mg peak in Fig. 8.89 indicates that evaporated anodic material is also deposited onto the cathode surface, what decreases plasma and film contamination by the cathode material.

8.4.2 The Grain Size by SEM

To investigate film morphology of the deposited magnesium films a scanning electron microscope ESEM Quanta 400 FEG by FEI Company was used. Fig. 8.90 shows magnesium films on steel substrates deposited under various deposition parameters. Using SEM picture (Fig.8.90) one can estimate the grain size of deposited magnesium crystallites.

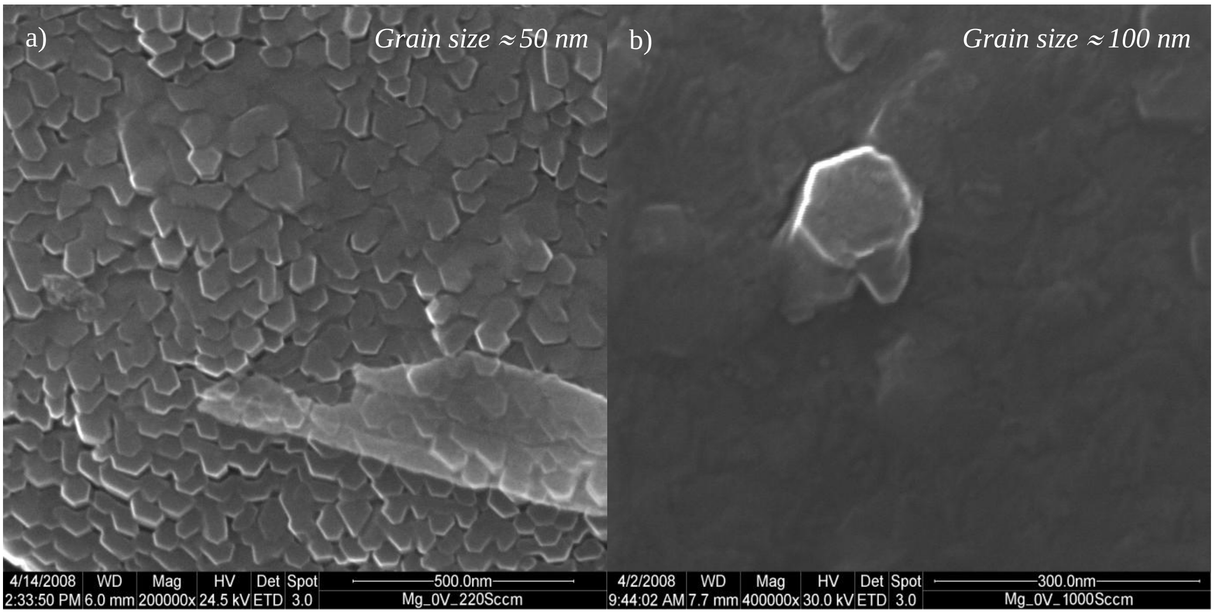

Fig. 8.90: *SEM pictures of the coated specimen: a) bias 0V, working pressure:* 1×10^{-4} *mbar, b) bias 0V, working pressure:* 1×10^{-3} *mbar.*

The increase of hydrogen flow rate leads to an increase of Mg grain size. According to the *SEM* images one can estimate magnesium grain size for coated samples. The grain size of specimen coated at working pressure 1×10^{-4} *mbar* sample a) is around *50 nm*, for sample b) coated at working pressure 1×10^{-3} *mbar* it is around *100 nm*. In the next chapter magnesium grain size obtained from *SEM* evaluation will be compared with the grain size evaluation from *XRD* (x-ray diffraction) patterns.

8.4.3 The Grain Size by XRD

XRD was used to determine the Mg grain size of the coatings. The x-ray diffraction profiles were recorded with a *Bruker AXS D8* diffractometer using CuK_α radiation. The crystallite size G can be calculated from the intercept by using already known values of k and λ, see *Chapter 6.2.3*. Fig. 8.91 shows the XRD spectrum for a magnesium coated steel substrate. Fig. 8.92 shows the evaluation of XRD profiles using a Williamson-Hall plot, see *Chapter 6.2.3*.1. From that one can deduce the grain size.

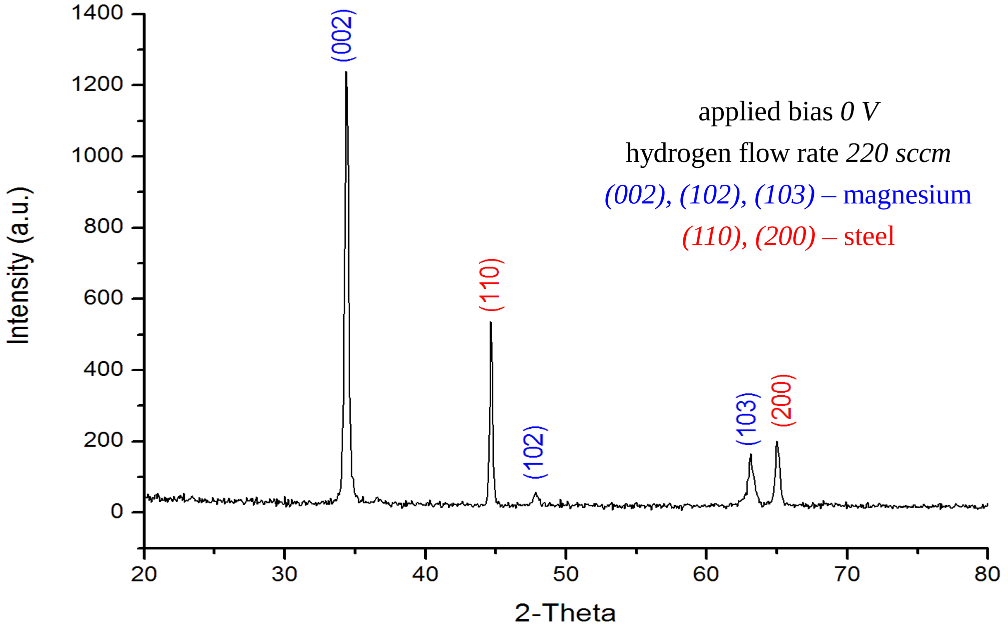

Fig. 8.91: *XRD pattern of magnesium coated steel specimen, with peaks evaluation [Filipov12].*

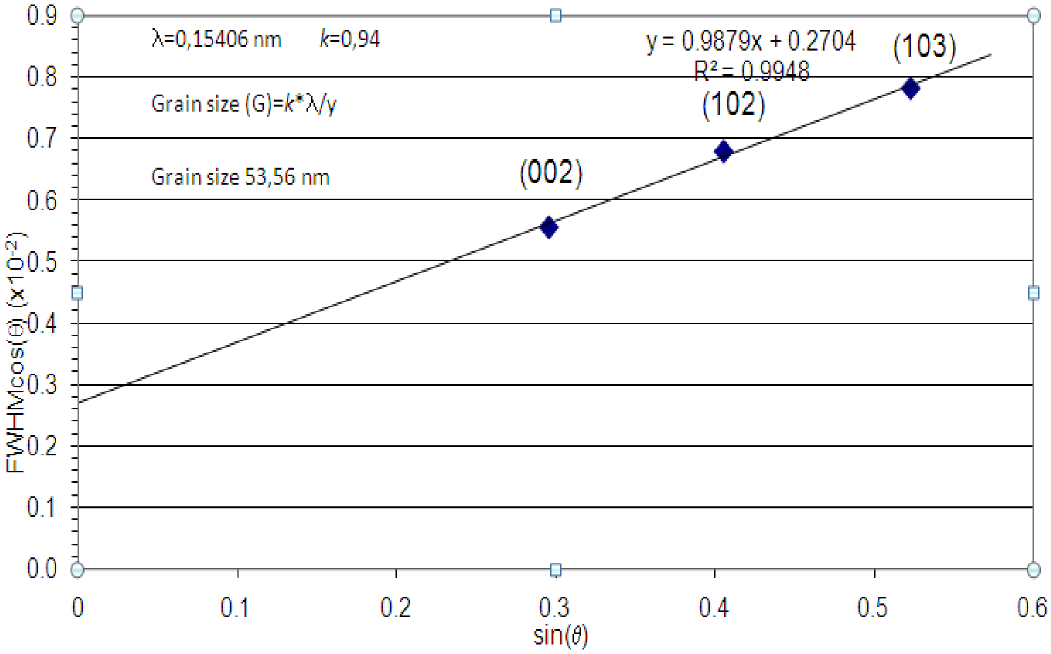

Fig. 8.92: *Williamson-Hall plot [Filipov12].*

Fig.8.93 shows a summarized 3D-diagram of Mg grain size as a function of applied bias voltage and actual hydrogen flow rate.

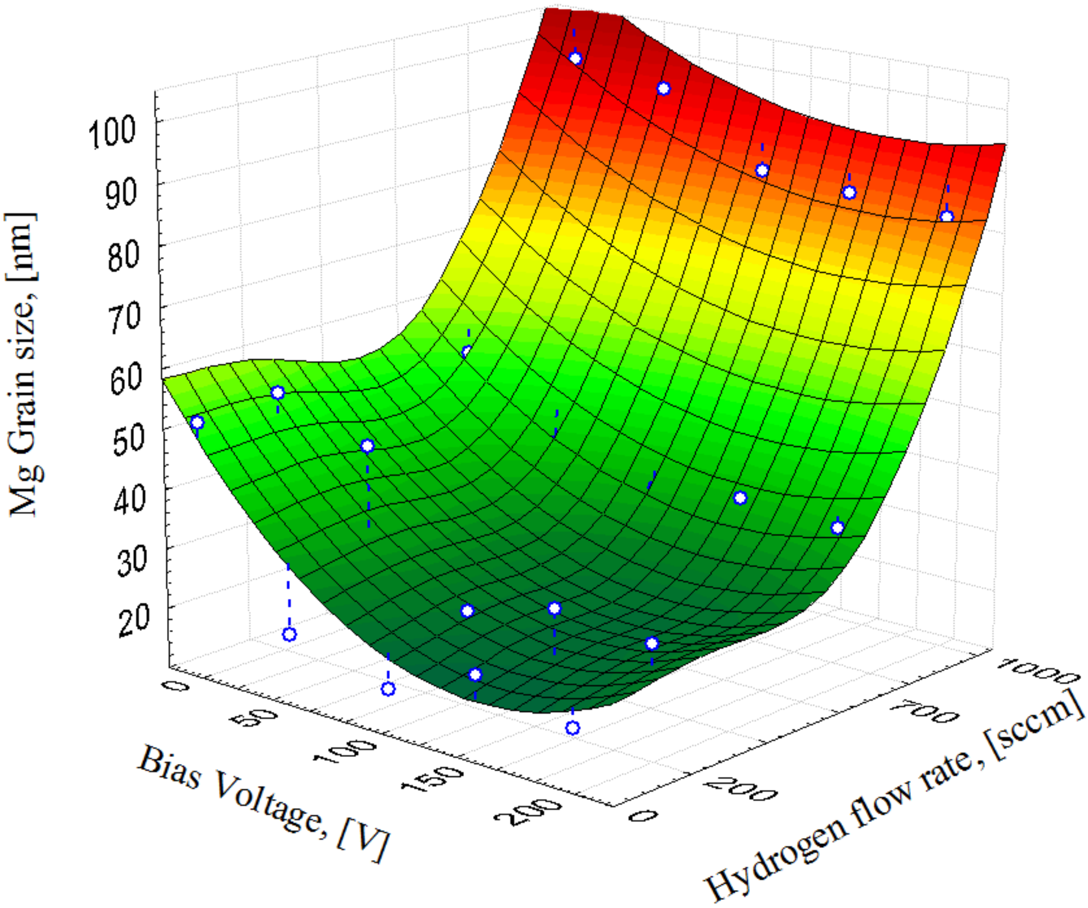

Fig. 8.93: *Magnesium grain size as a function of deposition parameters.*

According to the Fig. 8.93, the grain size in the deposited magnesium films can be varied from *18 nm* to *100 nm* just by variation of the deposition parameters. These data are in a good agreement with the magnesium grain size evaluation by SEM. As one can see in Fig. 8.93, the applied bias voltage leads to a reduction of the crystallite size due to ion peening. On the other hand, increasing hydrogen pressure leads to growth of Mg grain size (due to the thermalization). The increase of hydrogen pressure leads to hydrogen incorporation in the growing magnesium film which increases magnesium grain size but reduces the scope of hydrogen kinetics.

Diamond-like carbon is a whole class of carbon based materials which properties can be adjusted in a wide range. In order to investigate the influence of deposition parameters on DLC film properties, it is necessary to separate them from each other. An arc plasma source adjustable from “cathodic” to “anodic” arc modes allows independently tune plasma parameters to investigate their influence on DLC film properties. For the first time, the role of different arc modes and the transition between “cathodic” and “anodic” arc modes on film properties was shown.

The big advantage of the vacuum arc deposition technique is that it can be operated without working gas. Such characteristic allows to influence the plasma chemistry by addition of desired working gas. In this work, the properties of the DLC coatings were controlled by arc plasma source adjustable from “cathodic” to “anodic” mode. In addition, properties of the DLC films were investigated as a function of different hydrogen flow rates.

Hydrogen is a crucial parameter for DLC film deposition. There is a strong correlation between the properties of DLC films and hydrogen content. It influences film structure (a-C or a-C:H) and thereby changes their properties. Thus, the knowledge of hydrogen concentration in the deposited film is very important to have control over chemical, optical, electronic and mechanical properties of the DLC films. Admixture of hydrogen into the plasma gives another possibility to control film properties additionally by its influence on plasma chemistry.

First, the plasma parameters (ion energy and plasma composition) were investigated. Then chemical, optical and electronic properties of the obtained DLC films were analysed *ex-situ* by the means of spectroscopic methods. Furthermore, the influence of plasma parameters on the mechanical properties of the DLC films was also studied.

The study of the influence of various arc modes and deposition parameters on the film properties by independent examination of the deposition parameters particle energy, bias voltage and hydrogen admixture was performed.

The particle energy (ion energy) shows strong influence on DLC film properties an increase of the ion energy leads to decrease of surface roughness, increase of the film stress and optical band gap. The role of the hydrogen admixture and the influence of the hydrogen flow rate on the DLC growth process were investigated and it was shown that an increase of the hydrogen content in the film leads to an increase of the optical band gap, surface roughness and decrease of the intrinsic film stress. However, an increase of the bias voltage leads to a decrease of the surface roughness and an increase of the residual stress in the film. All these parameters can be separately adjusted in order to obtain desired film properties. As one can see, the influence of deposition parameters on film properties is very important for controlled deposition of DLC films.

By plasma diagnostic, it was shown that each arc mode is characterized by the individual set of parameters (particle energy, deposition rate) and differs from each other. The "anodic" arc mode is characterized by the highest deposition rate *5 nm/s* but it produces the ions with the lowest particle energy $E_i \approx 7\ eV$, among other arc modes. The film analysis shows, the DLC films deposited at this mode have the lowest surface roughness *1.45 nm*, moderate intrinsic stress *– 426 MPa*, narrow optical band gap $1\ eV < B_g < 2\ eV$ and content of sp^3- bonded carbon atoms around *40%*.

In contrast to the "anodic" mode the "cathodic" arc mode has the lowest deposition rate around *1 nm/s*, but the highest measured particle energy $E_i \approx 23\ eV$. DLC films deposited under such mode show the biggest optical band gap $B_g > 2\ eV$ highest intrinsic stress *640 MPa* and sp^3-content around *70%*.

By hydrogen admixture into the plasma, it was possible to change all these parameters and adjust them in a wide range.

By the help of NRA technique it was possible to calibrate mass-spectroscopic data and to show that the hydrogen content in the deposited films can be determined without any structural analysis by using only spectroscopic techniques. The investigation of the *UV-VIS* spectra provides information about optical and electronic properties of the deposited DLC films. The correlation between plasma parameters and film properties is also discussed. As it was shown by the Raman spectroscopy, the hydrogen admixture into the plasma changes the chemical composition and the film structure. The content of sp^3- hybridized atoms and hydrogen content growth with the increase of hydrogen admixture in the plasma. It should be mentioned, there are no reliable sources concerning Raman behaviour for the coatings with hydrogen concentration around few percents. Therefore application of Raman spectroscopy for the evaluation of so-called "hydrogen-free" coatings – without confirmation that they are really hydrogen-free – is not possible.

The correlation between the results obtained from spectroscopic methods is observed. The data obtained from two independent spectroscopic measurement techniques (Raman spectroscopy and *UV-VIS* spectroscopy) are in good agreement with each other.

The stress measurements in the deposited DLC films have shown that the mechanical stress in films can be influenced and adjusted according to the deposition parameters.

In this work, the ability to deposit DLC films in a wide range of film properties and variation of deposition parameters by arc plasma source adjustable from cathodic to anodic mode was shown. The influence of deposition parameters on DLC film properties and possibility to tailor them according to the functional properties was demonstrated.

The arc plasma source adjustable from “cathodic” to “anodic” mode is a promising deposition technique which is able to deliver DLC films in a wide range of properties with controlled structure and characteristics. Therefore, it would be interesting to extend the range of investigated parameters, especially mechanical properties (hardness,...), and produce DLC films with very low, but controlled hydrogen content; and to continue the research on the topic discussed in this work.

References

[Adamopoulos04] G. Adamopoulos, J. Robertson, N. A. Morrison and C. Godet: *Hydrogen content estimation of hydrogenated amorphous carbon by visible Raman spectroscopy*, Journ. Appl. Phys. Vol. 96, No. 11 (2004).

[Aksenov78] I.I. Aksenov, V.A. Belous, V.G. Padalka and V.M. Khoroshikh: *Transport of Plasma Streams in a Curvilinear Plasma – Optics System*, Sov. J. Plasma Phys. **4** (1978), 425.

[Aksenov93] I. I. Aksenov, S. I. Vakula and V. E. Strel’nitskij: *Optical spectra of diamond-like carbon films in the energy region between 1 and 13 eV*, Diam. Relat. Mater. 2 (1993), 1387-1390.

[Anders99] A. Anders: *Approaches to Rid Cathodic Arc Plasmas of Macro- and Nanoparticles a Review*, Surf. Coat. Technol. **120–121** (1999), 319.

[Angus88] J. C. Angus and F. Jansen: *Dense “Diamond-like” Hydrocarbons as Random Covalent Networks*, J. Vac. Sci. Tech. **A6** (1988), 1778.

[Angus91] J. S. Angus: *Diamond and Diamond-like Phases*, Diamond Relat. Mater. 1 (1991), 61.

[Balandin08] A. A. Balandin, S. Ghosh, W. Bao, I. Calizo, D. Teweldebrhan, F. Miao and C. N. Lau: *Extremely High Thermal Conductivity of Graphene: Experimental Study*, Nano Letters, Vol. 8, No. 3, (2008), 902-907.

[Bogdanovic85] B. Bogdanovic: *Catalytic synthesis of Organolithium and organomagnesium compounds and of lithium and magnesium hydrides - applications in organic synthesis and hydrogen storage*, Angewandte Chemie International Edition in English **24** (1985), 262–273.

[Born02] M. Born and E. Wolf: *Principles of Optics*, 7th Edition Cambridge University Press (2002).

[Bovchar73] D. Bovchar and E. Galperin: Academy of Science Reports. **209**. (1973), 610-612.

[Boxman95] R. L. Boxman, D. S. Sanders, P. J. Martin and J. M. Lafferty: *Handbook of Vacuum Arc Science and Technology – Fundamentals and Applications*, Noyes Publications, Park Ridge (1995).

[Bragg13] W. L. Bragg: *The Diffraction of Short Electromagnetic Waves by a Crystal*, Proceedings of the Cambridge Philosophical Society **17** (1913), 43–57.

[Buck91] V. Buck, J. Bur am Orde, M. Mausbach: *Deposition of Diamondlike Carbon Films by Anodic Arc Technique*, Materials Science and Engineering A14O, (1991), 770.

[Buck93] V. Buck: *Microanalysis and Modelling of Tribological Coatings*, Surface and Coatings Technology 57, (1993), 163.

[Buck06] V. Buck, N. Wöhrl, A. Poukhovoi, O. Filipov, M. Haase and Y.-Ch. Lee: Adjusting Residual Stress, *Adhesion, Tribological Performance and Wettability of Nanocrystalline and Diamondlike Hard Carbon Coatings, in: Application of Nanocrystalline Diamond and Diamondlike Carbon Materials*, in N.R. Ray (Ed.): “Application of Nano-crystalline Diamond and Diamond like Carbon Materials”, Kolkata (2006), 57.

[Buck06] V. Buck: *Lecture materials,* (2006).

[Bunch07] J. S. Bunch:. *Electromechanical Resonators from Graphene Sheets*, Science 315, 490 (2007).

[Casiragi05] C. Casiraghi, A.C. Ferrari and J. Robertson: *Raman Spectroscopy of Hydrogenated Amorphous Carbons*, Phys. Rev. **B72** (2005), 085401.

[Cowley75] John M. Cowley: *Diffraction physics,* North-Holland, Amsterdam (1975).

[Darriet80] B. Darriet, M. Pezal: *Application of magnesium rich rare-earth alloys to hydrogen storage,* Int. J. Hydrogen Energy **5**(2) (1980), 173.

[Dillon97] A. C. Dillon, K. M. Jones, T. A. Bekkedahl, C. H. Kiang, D. S. Bethune and M. J. Heben: *Storage of hydrogen in single-walled carbon nanotubes,* Nature **386** (6623), (1997), 377-379.

[Dillon01] A. C. Dillon, M. Heben: *Hydrogen storage using carbon adsorbents: past, present and future,* J. Appl. Phys. A: Mater. Sci. Process. **72** (2001), 133-142.

[Eaton10] P. Eaton, P. West: *Atomic Force Microscopy,* Oxford University Press, (2010), 256.

[Eckhardt75] G. Eckhardt: *Interpretation of data on cathode erosion and efflux from cathode spots of vacuum arcs,* J. Appl. Phys. **46**, (1975), 3282.

[Ehrich88a] H. Ehrich: *The anodic vacuum arc. I. Basic construction and phenomenology,* J. Vac. Sci. Technol. A **6**(1) (1988), 134-138.

[Ehrich88b] H. Ehrich, B. Hasse, M. Mausbach, K. G. Mueller, R. Schmidt: *The anodic vacuum arc. II. Experimental study of arc plasma*, J. Vac. Sci. Technol. A **6**(4) (1988) 2499-2503.

[Ehrich90] H. Ehrich, B. Hasse, M. Mausbach and K. G. Mueller: *The anodic vacuum arc and its application to coating*, J. Vac. Sci. Technol. A **8**(3) (1990), 2160-2164.

[Ferrari00] A.C. Ferrari and J. Robertson: *Interpretation of Raman Spectra of Disordered and Amorphous Carbon*, Phys. Rev. **B61** (2000), 14095.

[Ferrari04] A.C. Ferrari and J. Robertson: *Raman Spectroscopy of Amorphous Nanostructured Diamond-like carbon and Nanodiamond*, Phil. Trans. R. Soc. Lond. **A362** (2004), 2477.

[Filipov05] O. Filipov, N. Wöhrl, S. Reuter and V. Buck: *Correlation of plasma parameters and diamond-like carbon films properties*, DPG Berlin spring meeting 2005.

[Filipov09] O. Filipov, V. Buck: *Deposition of Magnesium Films Using an Anodic Arc Plasma Source*, XVI Workshop Plasmatechnik, Ilmenau (2009).

[Filipov12] O. Filipov, S. Schipporeit, V. Buck: *Anodic arc evaporation of nanocrystalline Mg films*, J. Optoelectron. Adv. Mater. **14** (2012), 418.

[Franta06] D. Franta, D. Necas, L. Zajickova and V. Bursikova: *Modelling of DLC Optical Properties Based on Parametrization od Density of States*, IWAncDLC (2006), 39-50.

[Franta07] D. Franta, D. Necas and L. Zajickova: *Models of dielectric response in disordered solids, Optics Express*, Vol. 15, No. 24, (2007).

[Gordijn04] A. Gordijn, J. K. Rath, and R. E. I. Schropp: *Thickness determination of very thin amorphous and microcrystalline silicon layers using reflection/transmission measurements,* Appl. Phys. Let. Vol.85, No21 (2004), 5096-5098.

[Grill99a] A. Grill: *Diamond-like Carbon: State of the Art*, Diamond Relat. Mater. **8** (1999), 428.

[Grill99b] A. Grill: *Electrical and Optical Properties of Diamond-like Carbon*, Thin Solid Films **355-356** (1999), 189.

[Grill03] A. Grill: *Diamond-like Carbon Coatings as Biocompatible Materials-an Overview,* Diamond Relat. Mater. **12** (2003), 166.

[Hasse92] B. Hasse: *Untersuchung des anodischen Vakuumbogens*, PhD thesis, Essen (1992).

[He11] Y. Y. He, G. F. Zhang, V. Buck: *Effects of reactors on the deposition of DLC films using liquid electrochemical technique*, Diam and Relat. Mater.: Vol 20 **2** (2011), 97-100.

[Hirscher01] M. Hirscher, M. Becher, M. Haluska, U. Dettlaff-Weglikowska, A.Quintel, G. S. Duesberg, Y. M. Choi, P. Downes, M. Hulman, S.Roth, I. Stepanek, P. Bernier: *Hydrogen storage in sonicated carbon materials,* Appl. Phys. A: Mater. Sci. Process. **72** (2001), 129-132.

[Hoffman76] R. W. Hoffman: *Stresses in thin films: The relevance of grain boundaries and impurities*, Thin Solid Films 34, (1976), 185.

[Horcas07] Horcas, R. Fernandez, J.M. Gomez-Rodriguez, J. Colchero, J. Gomez-Herrero, A. M. Baro, Rev. Sci. Instrum. 78, 013705, (2007).

[Huot01] J. Huot, G. Liang, R. Schulz: *Mechanically alloyed metal hydride systems,* Appl. Phys. A: Mater. Sci. Process. **72** (2001), 187-195.

[Iijima91] S. Iijima: *Helical Microtubules of Graphitic Carbon*, Nature 354 (1991), 56.

[Imamura10] H. Imamura, S. Nakatomi, K. Tanaka, Y. Hashimoto, Y. Sakata: *Magnesium-based nanocomposites synthesized by high-energy ball milling for hydrogen storage,* Proceedings WHEC2010 (2010), 319-322.

[Ingram88] S. G. Ingram, N. St. J. Braithwaile: *Ion and electron energy analysis at a surface in an RF discharge,* J. Phys. D. Appl. Phys. **21** (1988), 1496.

[Irmer05] G. Irmer and A. Dorner-Reisel: *MicroRaman Studies on DLC Coatings,* Adv. Eng. Mater. **7**, No. 8, (2005).

[Jaeger98] S. Jaeger, B. Szyszka, J. Szczyrbowski, G. Brauuer: *Comparison of transparent conductive oxide thin films prepared by a. c. and d. c. reactive magnetron sputtering*, Surface and Coatings Technology **98** (1998), 1304-1314.

[Jüttner01] B. Jüttner: *Cathode spots of electric arcs*, J. Phys. D: Appl. Phys. 34, (2001), 103.

[Kadetov04] V. A. Kadetov: *Diagnostics and Modeling of an Iductively Coupled Radio Frequency Discharge in Hydrogen*, PhD thesis, Bochum (2004).

[Karpov97] D.A. Karpov: *Cathodic Arc Sources and Macroparticle Filtering*, Surf. Coat. Technol. **96** (1997), 22.

[Khlopyanova12] V. Khlopyanova: *Erzeugung und Untersuchung wasserstoffarmer Kohlenstoffschichten*, Dipl. thesis, Duisburg (2012).

[Kramers27] H.A. Kramers :*La diffusion de la lumiere par les atomes*. Atti Cong. Intern. Fisica, (Transactions of Volta Centenary Congress) Como **2**: (1927), 545–557.

[Kronig26] R de L. Kronig: *On the Theory of Dispersion of X-Rays,* JOSA, Vol. 12, Issue 6, (1926), 547-556.

[Kroto85] H. W. Kroto, J. R. Heath, S. C. O’Brien, R. F. Curl and R. E. Smalley: *C60: Buckminsterfullerene,* Nature 318 (1985), 162.

[Lanford95] W. A. Lanford: *Nuclear Reactions for Hydrogen Analysis,* Handbook of Modern Ion Beam Analysis ed. By J. Tesmer and M. Nastasi, Materials Research Society (1995), 193.

[Lifshitz99] Y. Lifshitz: *Diamond-like carbon – present status,* Diam and Relat Mater 8 (1999), 1659-1676.

[Madronero95] A. Madroñero and M. Verdú: *Hydrogen Content Evaluation in Vapour-grown Carbon Fibres by SIMS, Carbon* **33** (1995), 247.

[Musa94] G. S. Musa, H. Ehrich, M. Mausbach: *Studies on Thermoionic Cathode Anodic Vacuum Arcs,* J. Vac. Sci. Technol. A **12** (1994), 2887.

[Musa97] G. S. Musa, H. Ehrich, J. Schuhmann: *Pure metal vapor plasma source with controlled energy of ions,* IEEE Transactions on Plasma science **23**(2) (1997), 386-391.

[Nijkamp01] M. G. Nijkamp, J. Raaymakers, A. J. van Dillen, K. P. de Jong: *Hydrogen storage using physisorption – materials demands,* Appl. Phys. A: Mater. Sci. Process. **72** (2001), 619-623.

[Novoselov04] K. S. Novoselov, A. K. Geim, S. V. Morozov, D. Jiang, Y. Zhang, S. V. Dubonos, I. V. Grigoriev and A. A. Firsov: *Electric Field Effect in Atomically Thin Carbon Films*, Science 306, (2004), 666.

[O’Leary97] S. K. O’leary, S. R. Johnson and P. K. Lim: *The Relationship Between the Distribution of Electronic States and the Optical Absorption Spectrum of an Amorphous Semiconductor: An Empirical Analysis*, J. Appl. Phys. **82** (1997), 3334.

[Osawa70] E. Osawa, *Kagaku*, Vol. 25, (1970), 854.

[Paret98] V. Paret, A. Sadki, Y. Bounouh, R. Alameh, C. Naud, M. Zarrabian, A. Seignac, G. Turban, M. L. Theye: *Optical investigations of the microstructure of hydrogenated amorphous carbon films*, Journ Non-Cryst. Solids 227-230 (1998), 583-587.

[Pierson93] H. O. Pierson: *Handbook of Carbon, Graphite, Diamonds and Fullerenes*, Noyes Publications, Park Ridge, (1993).

[Poukhovoi11] A. Poukhovoi: *Abscheidung von amorphen wasserstoffhaltigen Kohlenstoffschichten mittels neuartiger hybrider RF-Plasma-Quelle und deren spektroskopische Charakterisierung*, Phd. thesis, Verlag Dr. Hut, München (2011).

[Radushkevich52] L.V. Radushkevich, V. M. Lukyanovich, Phys. Chem 26 (1952), 89.

[Raizer01] Y. P. Raizer: *Gas discharge Physics*, Springler-Verlag, Berlin/New York (2001).

[Robertson87] J. Robertson and E.P. O'reilly: *Electronic and Atomic Structure of Amorphous Carbon*, Phys. Rev. **B35** (1987), 2946.

[Robertson02] J. Robertson: *Diamond-like Amorphous Carbon*, Mater. Sci. Eng., **R37,** (2002), 129.

[Rudy05] Rudy W. P. Wagemans, Joop H. van Lenthe, Petra E. de Jongh, A. Jos van Dillen, and Krijn P. de Jong: *Hydrogen storage in magnesium clusters: quantum chemical study*, J. Am. Chem. Soc. **127** (2005), 16675-16680.

[Scherrer18] P. Scherrer: *Bestimmung der Groesse und der inneren Struktur von Kolloidteilchen mittels Röntgenstrahlen,* Goettinger Nachrichten Gesell., **2** (1918), 98.

[Schimmel03] H. G. Schimmel, G. J. Kearley, M. G. Nijkamp, C. T. Visserl, K. P. de Jong, F. M. Mulder: *Hydrogen adsorption in carbon nanostructures: Comparison of nanotubes, fibers, and coals,* Chem.- A Eur. J. **9** (2003), 4764-4770.

[Schlapbach01] L. Schlapbach, A. Zuettel: *Hydrogen-storage materials for mobile applications,* Nature **414**(6861) (2001) 353-358.

[Schuhmann00] J. Schuhmann: *Metallisierung von Polymeren: Einfluss der Teilchen-, Schicht- und Substrateigenschaften auf die Adhaesion kondensierter Schichten,* Shaker Verlag, Aachen (2000).

[Schunk80] Schunk: *Carbon and Graphite,* Technical documentation (1980).

[Stamm09] B. Stamm, B. Kuezuen, O. Filipov, S. Reuter, I. Erdmann, F. Deuerler, D. Krix, K. Huba, H. Nienhaus, V. Buck: *Adjustment of wear particle size distribution of DLC coatings for tribological metal-on-metal pairing in artificial hip joints,* Mat.-wiss. u. Werkstofftech. No. 1-2, (2009), 40.

[Stephanakis68] J. D. Stephanakis, W. H. Bennet: *Electrostatic energy analyzer for studying gas-focused electron beams and their background media*, Rev. Sci. Instrum. 39 (1968), 1714.

[Stern67] E. A. Stern: *Ridgid-Band Model of Alloys*, Phys. Rev. 157, 544–551 (1967).

[Stoney09] G. G. Stoney: *The Tension of Metallic Films Deposited by Electrolysis*, Proc. R. Soc. London, Ser. A, 82, (1909), 172–175.

[Surdu-Bob07] C. Surdu-Bob, G. Musa, V. Buck, I. Mustata, O. Filipov and A. Poukhovoi: *Mass Spectrometry and Ion Energy Analysis of the Carbon TVA Plasma For the Synthesis of DLC Films*, J. Optoelectron. Adv. Mater. **9** (2007), 2657.

[Suryanarayana98] C. Suryanarayana, M. Grant Norton: *X-ray diffraction – a practical approach,* Plenum Press, New York (1998).

[Toll56] J. S. Toll: *Causality and the Dispersion Relation: Logical Foundation*, Phys. Rev. 104, (1956), 1760–1770.

[Varin06] R. A.Varin, T. Czujko and Z. Wronski: *Particle size, grain size and g-MgH$_2$ effects on the desorption properties of nanocrystalline commercial magnesium hydride (MgH$_2$) processed by controlled mechanical milling,* Nanotechnology **17** (2006), 3856–3865.

[Web12] http://upload.wikimedia.org/Wikimedia/commons/f/f8/Lichtbogen 3000 volt. jpg, (20.12.2012).

[Williamson53] G. K. Williamson and W. H. Hall: *X-ray line broadening from filed aluminium and wolfram,* Acta Metall. **1** (1953), 22.

[Windischmann91] H. Windischmann, G. F. Epps, Y. Cong, R. W. Collins*: Intrinsic stress in diamond films prepared by microwave plasma CVD*, J. Appl. Phys., Vol. 69, No. 4, (1991), 2231.

[Windischmann92] H. Windischmann: Critical Review in Solid State and Material Science 17(8) (1992) 547.

[Woehrl06] N. Wöhrl, V. Buck: *Zerstörungsfreie Bestimmung mechanischer Spannungen in nanokristallinen Diamantschichten,* Galvanotechnik 12, (2006), 3020-3029.

[Woehrl10] N. Woehrl: *Synthesis and Characterization of Nanocrystalline Diamond Films,* PhD thesis, Duisburg (2010).

[Zaluska99] A. Zaluska, L. Zaluski, J. O. Ström–Olsen: *Nanocrystalline magnesium for hydrogen storage,* J. Alloys Compd. **288** (1-2) (1999), 217-225.

[Zecchina05] A. Zecchina, S. Bordiga, J. G. Vitillo, G. Ricchiardi, C. Lamberti, G. Spoto, M. Bjorgen, K. P. Lillerud: *Liquid hydrogen in protonic chabazite,* J. Am. Chem. Soc. **127** (2005), 6361-6366.

[Zou89] J.W. Zou, K. Reichelt, K. Schmidt and B. Dischler: *The Deposition and Study of Hard Carbon Films*, J. Appl. Phys. **65**, (1989), 3914.

[Zuttel04] A. Zuettel: *Hydrogen storage methods,* Springer-Verlag Heidelberg, Naturwissenschaften **91**(4) (2004), 157-172.

Appendix I

The imaginary part ε_2 of the dielectric function

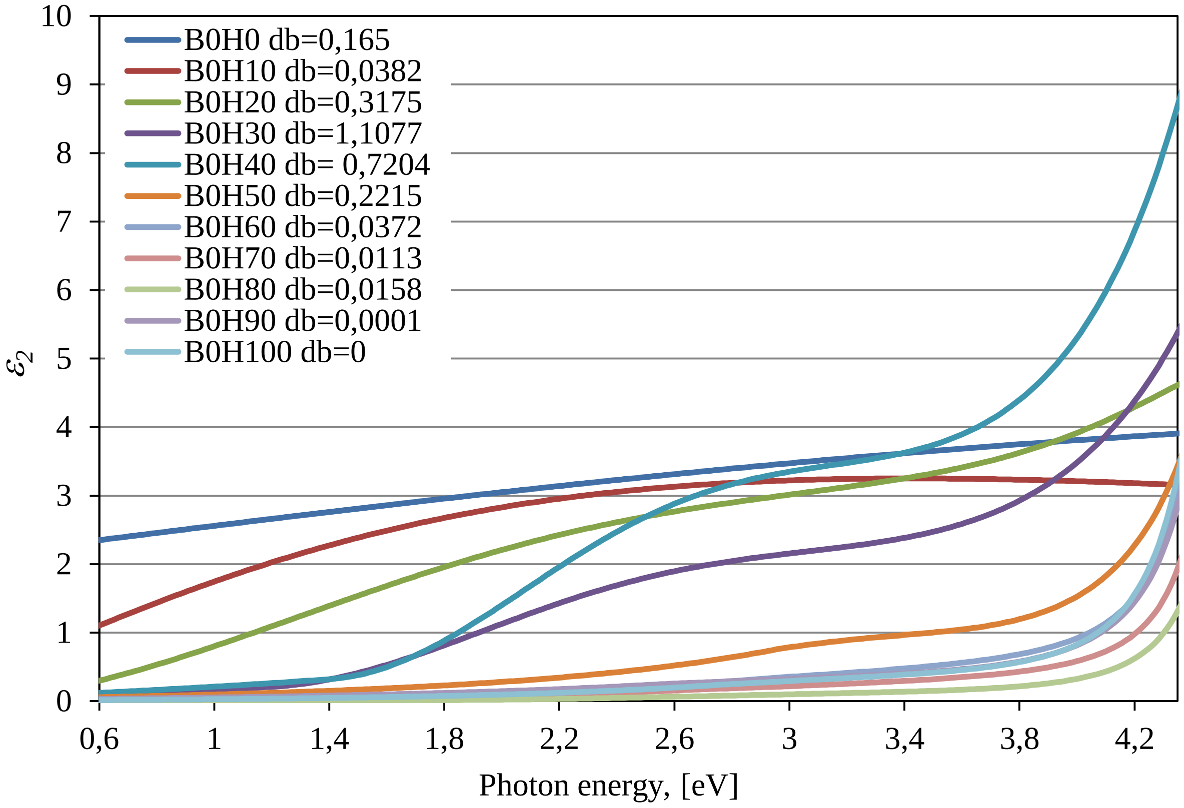

Fig. 9.1: *Spectral dependences of the imaginary part ε_2 of the dielectric function for deposited DLC films at the 0 V bias voltage.*

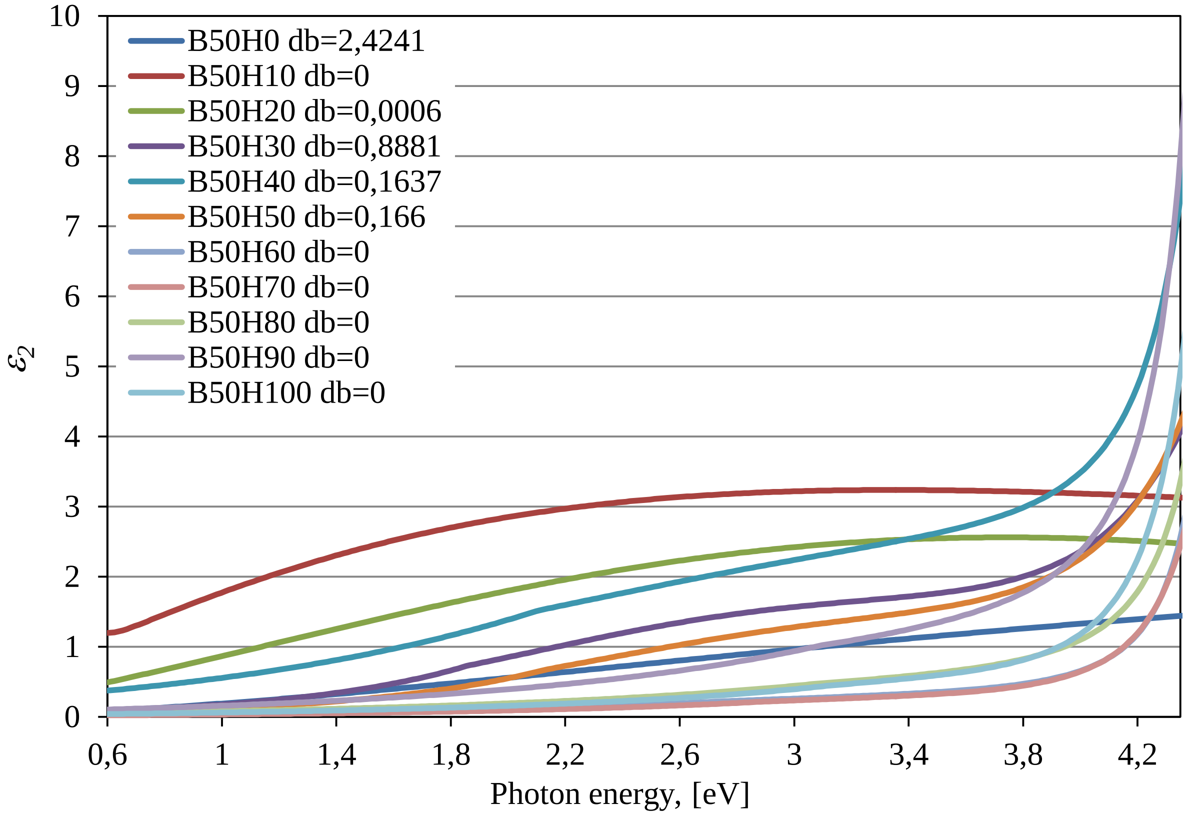

Fig. 9.2: *Spectral dependences of the imaginary part ε_2 of the dielectric function for deposited DLC films at the "– 50 V "bias voltage.*

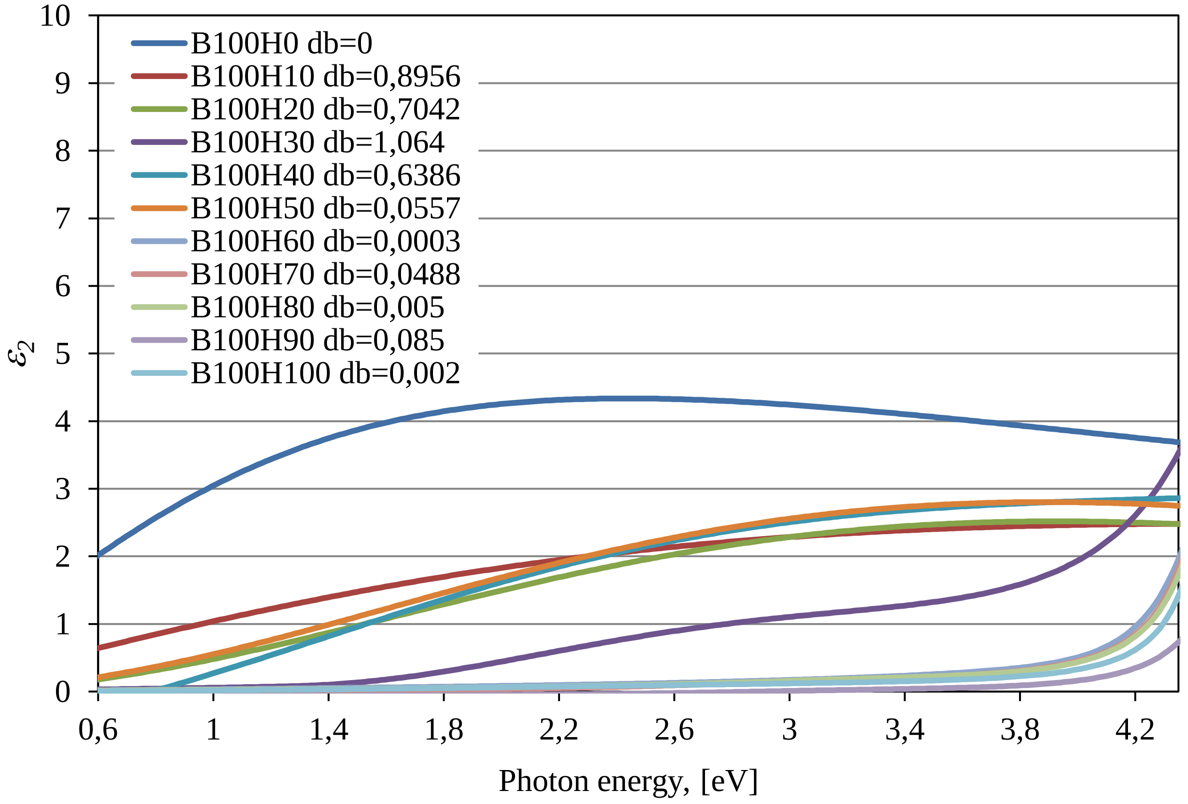

Fig. 9.3: *Spectral dependences of the imaginary part ε_2 of the dielectric function for deposited DLC films at the "– 100 V "bias voltage.*

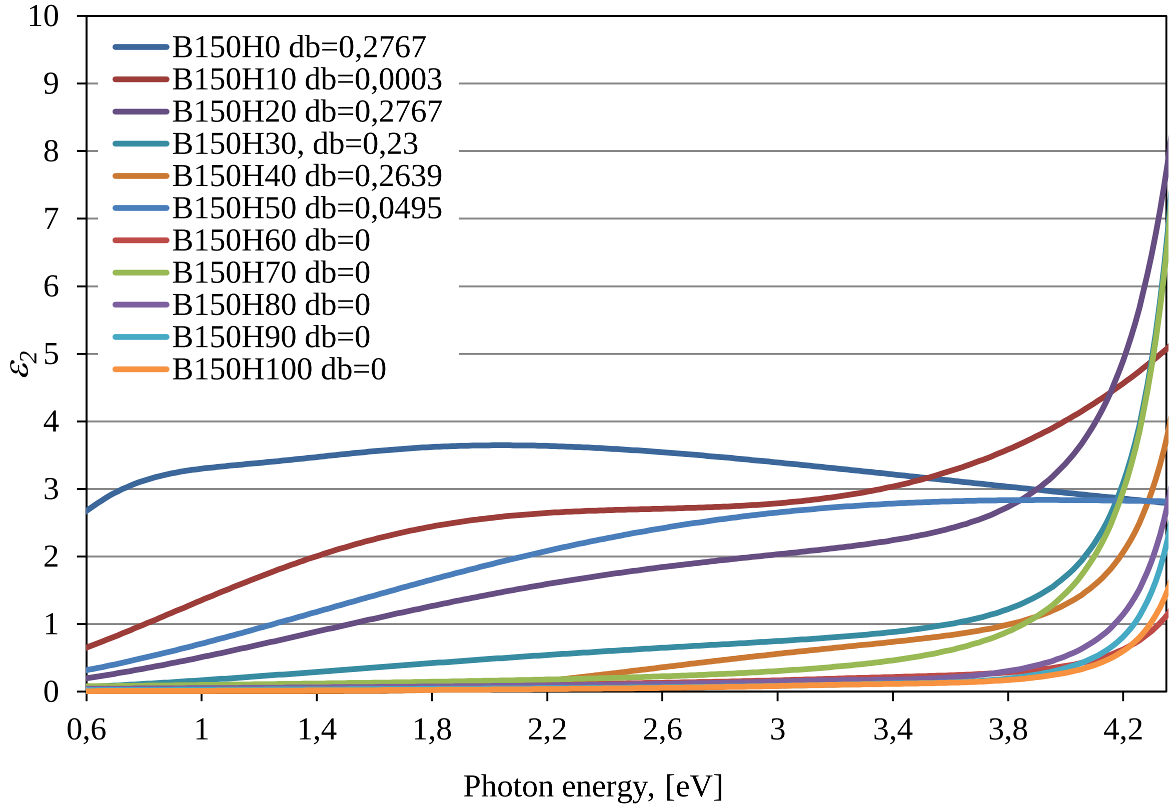

Fig. 9.4: *Spectral dependences of the imaginary part ε_2 of the dielectric function for deposited DLC films at the "– 150 V "bias voltage.*

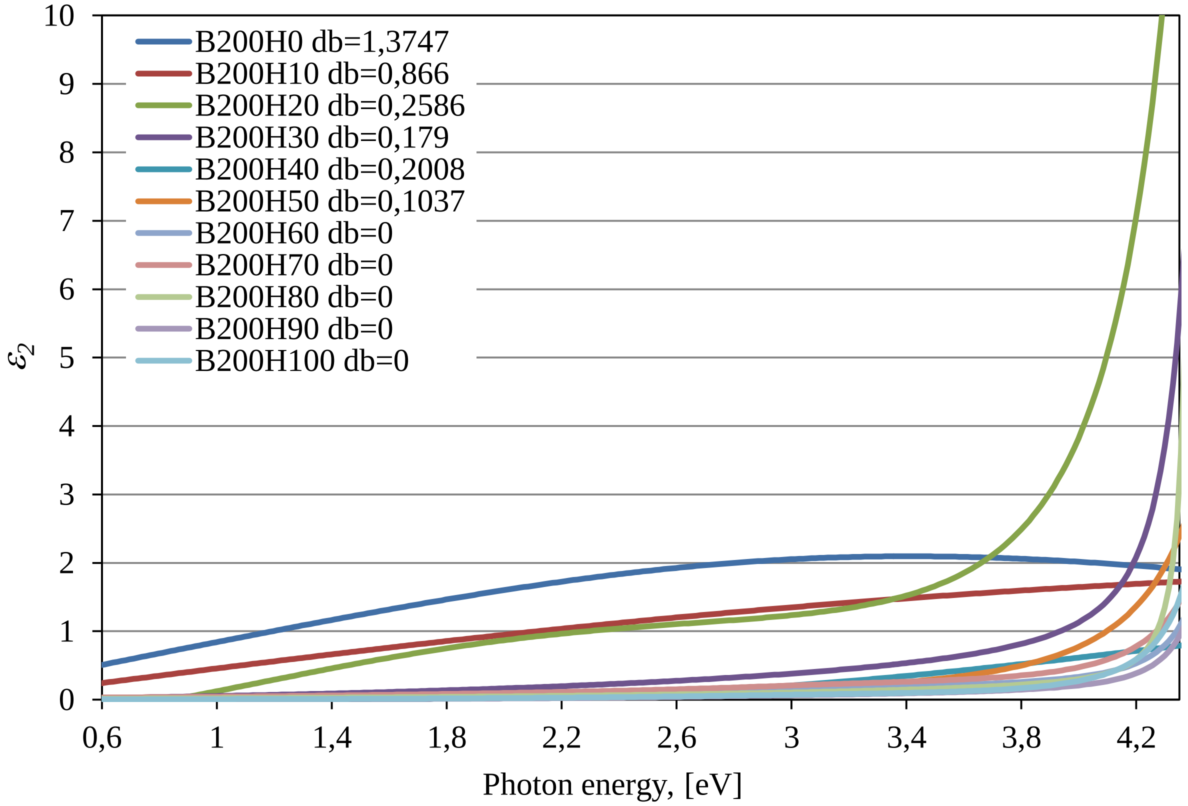

Fig. 9.5: *Spectral dependences of the imaginary part ε_2 of the dielectric function for deposited DLC films at the "– 200 V "bias voltage.*

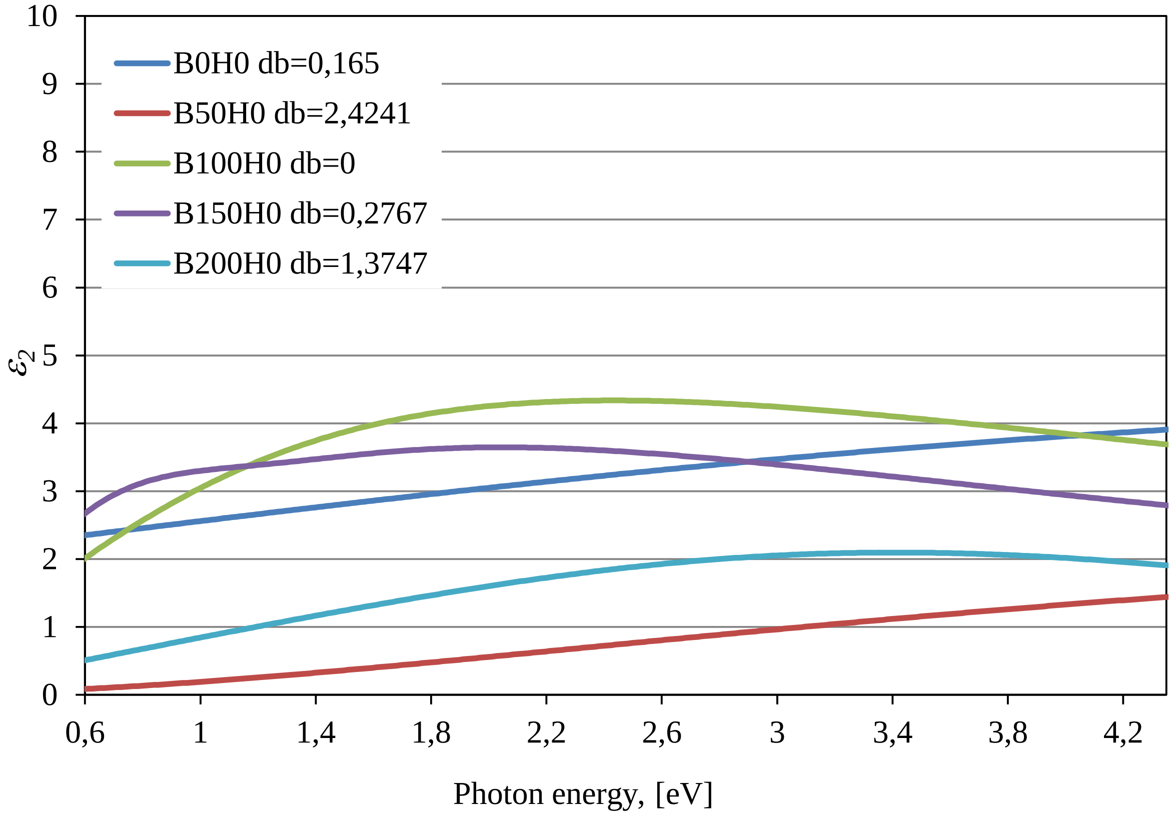

Fig. 9.6: *Spectral dependences of the imaginary part* ε_2 *of the dielectric function for deposited DLC films at the 0 sccm hydrogen flow rate.*

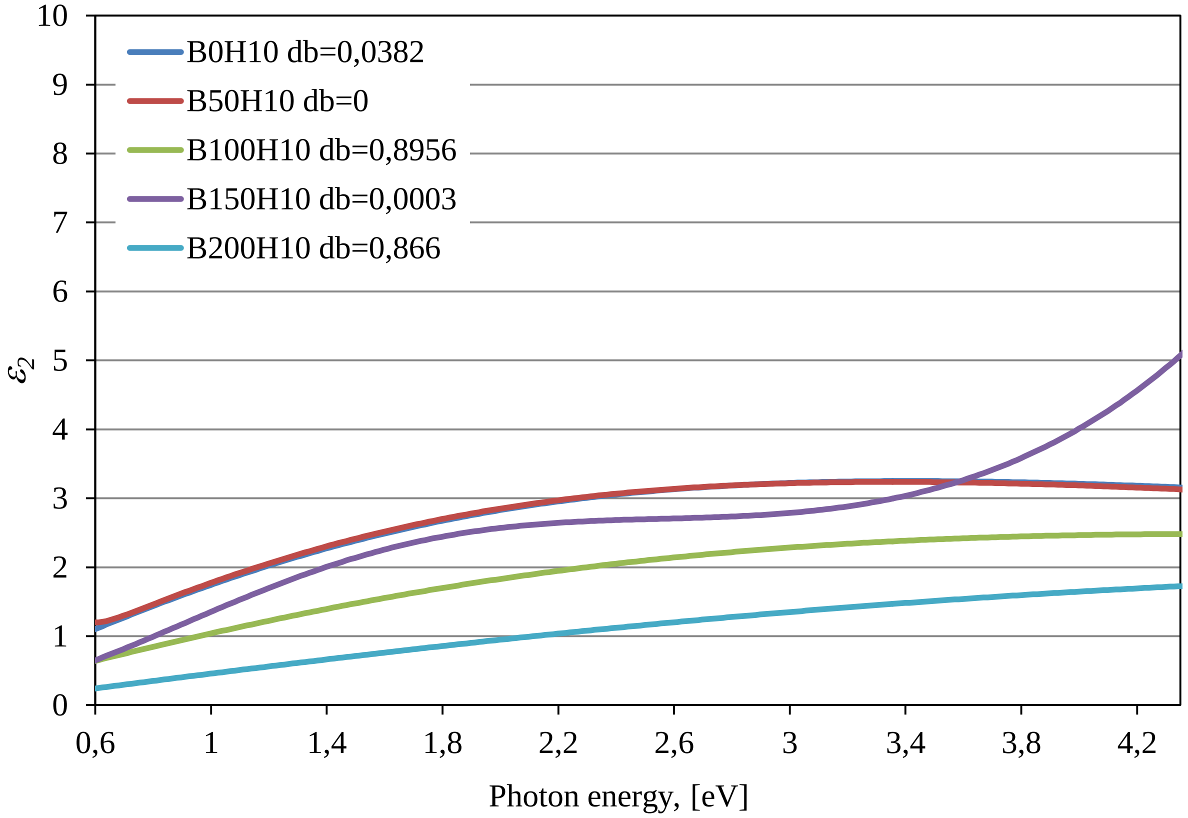

Fig. 9.7: *Spectral dependences of the imaginary part* ε_2 *of the dielectric function for deposited DLC films at the 10 sccm hydrogen flow rate.*

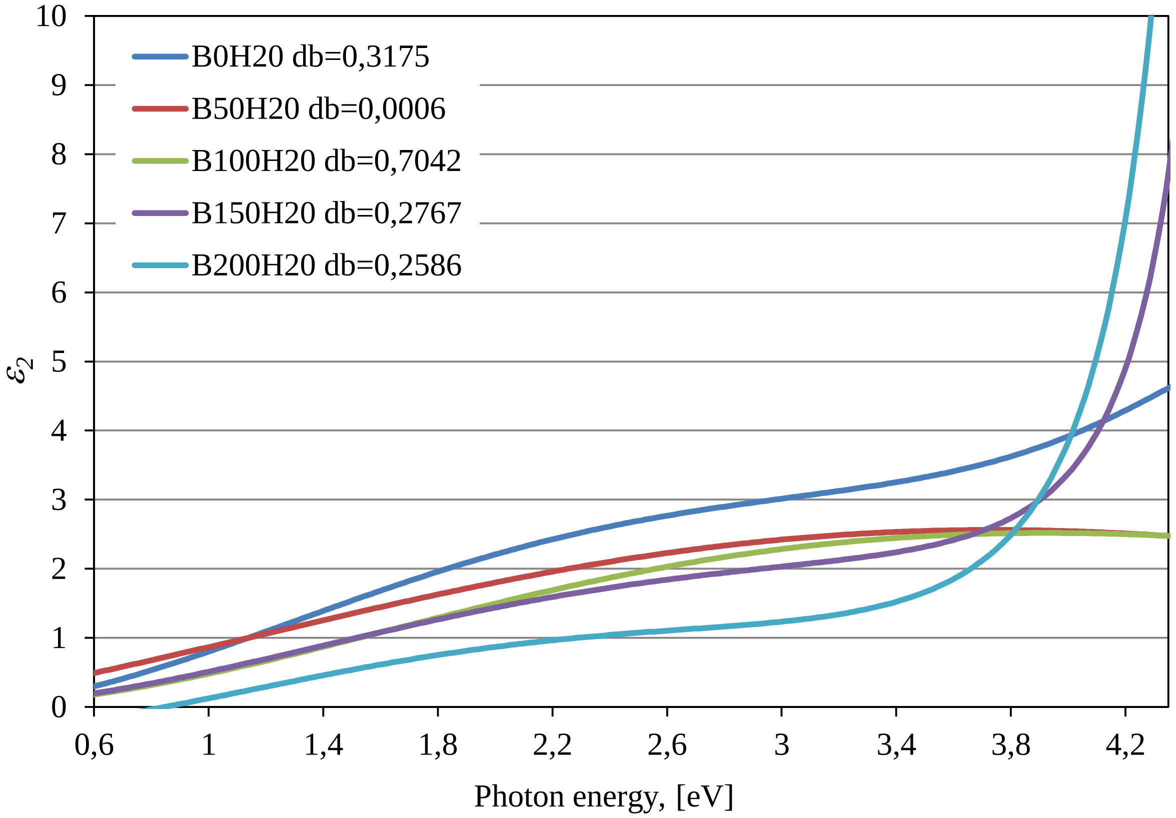

Fig. 9.8: *Spectral dependences of the imaginary part ε_2 of the dielectric function for deposited DLC films at the 20 sccm hydrogen flow rate.*

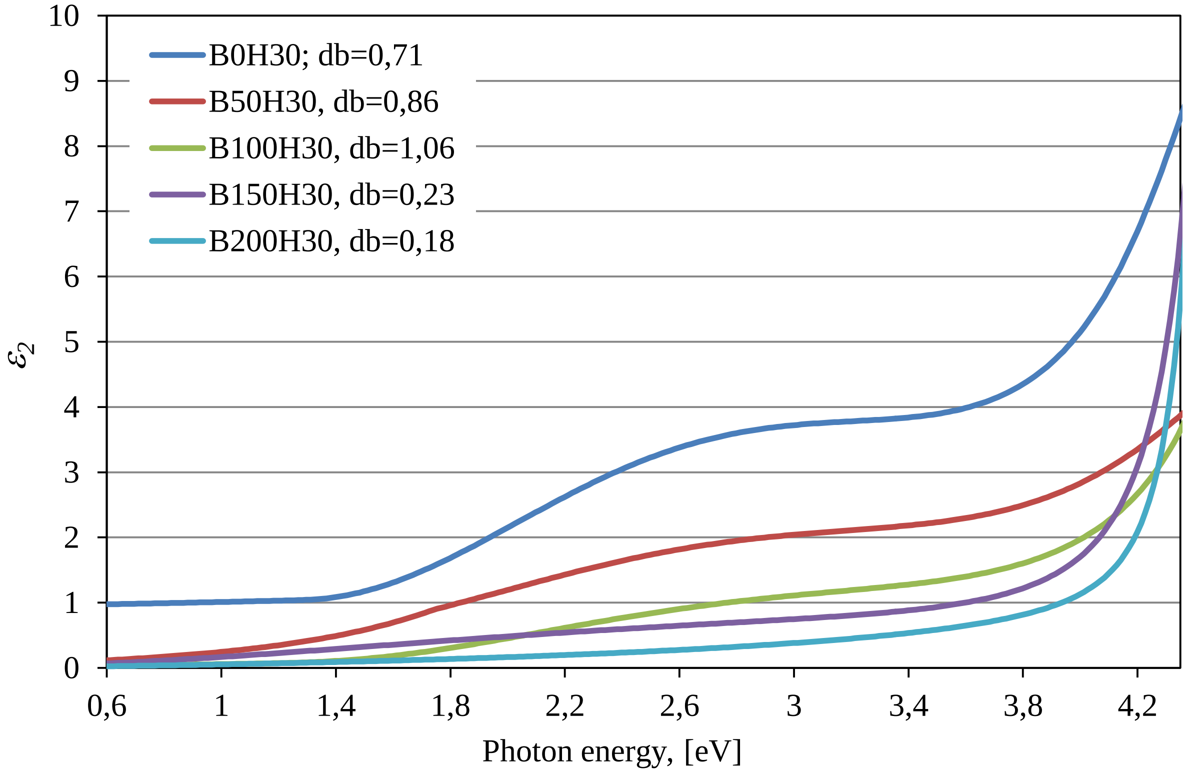

Fig. 9.9: *Spectral dependences of the imaginary part ε_2 of the dielectric function for deposited DLC films at the 30 sccm hydrogen flow rate.*

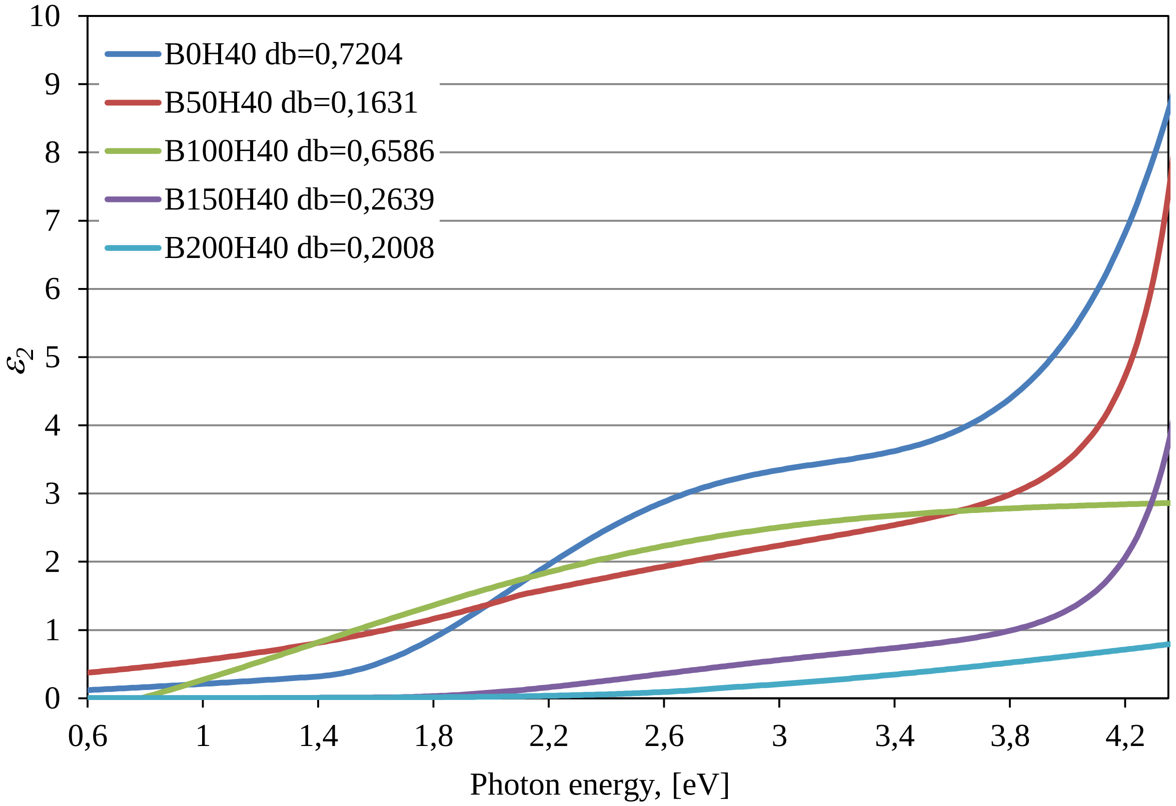

Fig. 9.10: *Spectral dependences of the imaginary part ε_2 of the dielectric function for deposited DLC films at the 40 sccm hydrogen flow rate*.

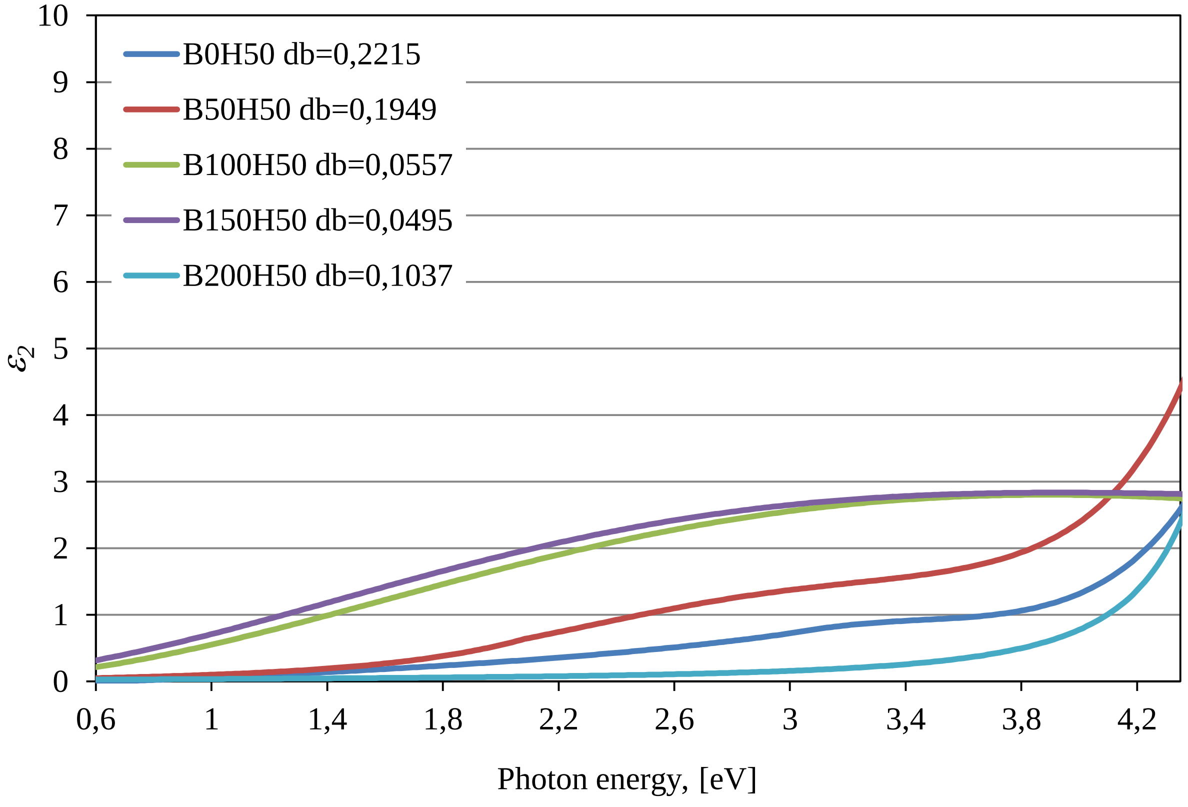

Fig. 9.11: *Spectral dependences of the imaginary part ε_2 of the dielectric function for deposited DLC films at the 50 sccm hydrogen flow rate*.

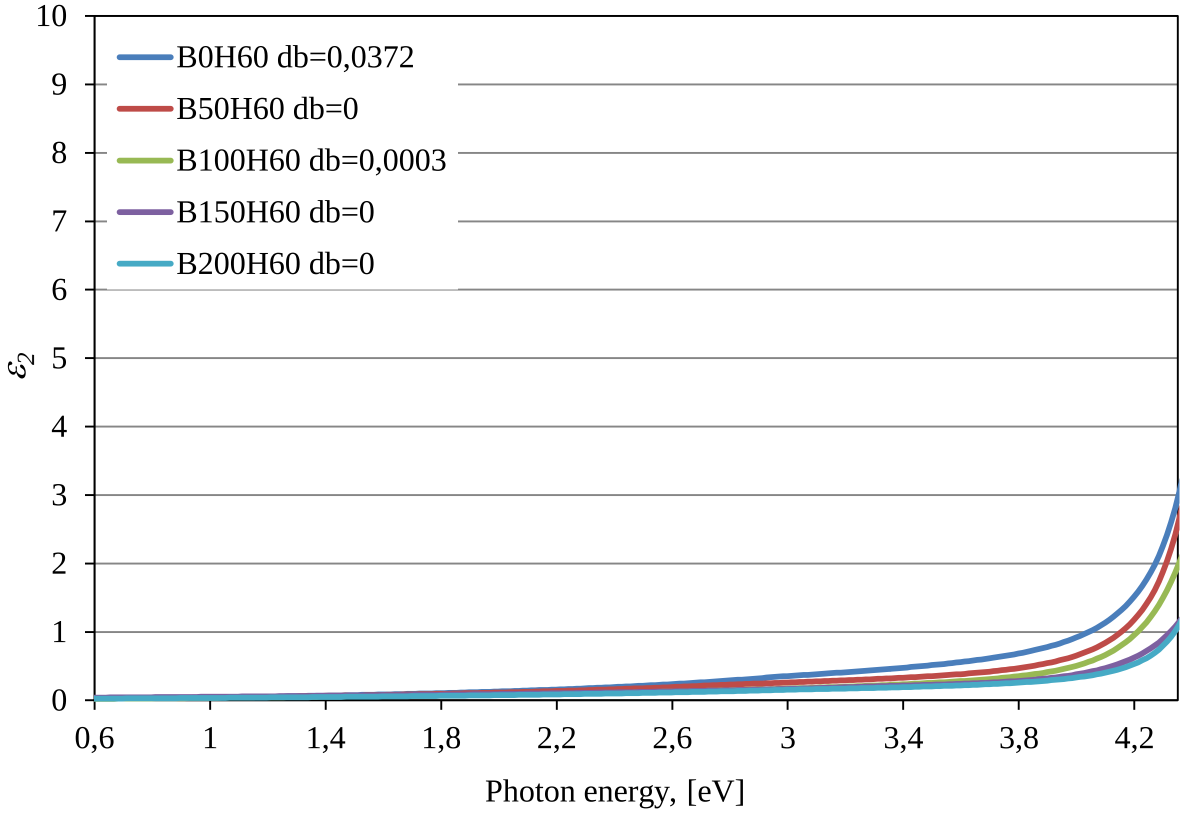

Fig. 9.12: *Spectral dependences of the imaginary part ε_2 of the dielectric function for deposited DLC films at the 60 sccm hydrogen flow rate.*

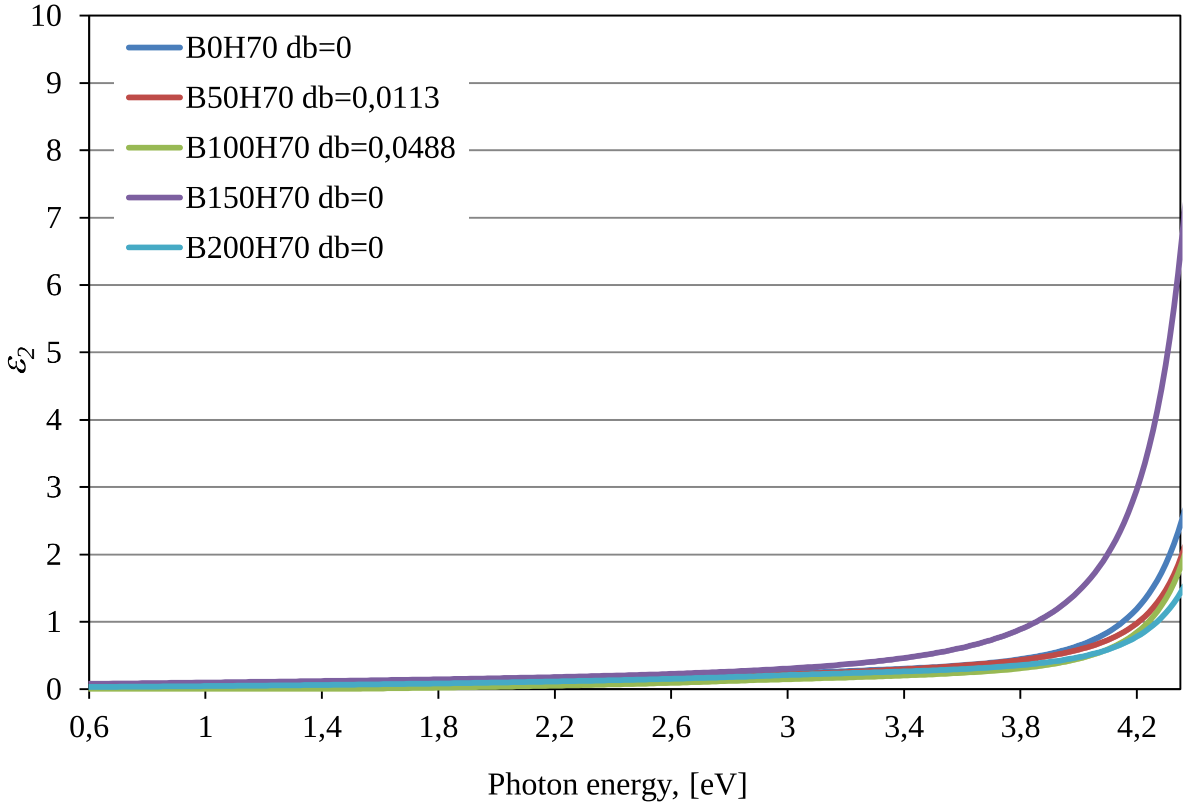

Fig. 9.13: *Spectral dependences of the imaginary part ε_2 of the dielectric function for deposited DLC films at the 70 sccm hydrogen flow rate.*

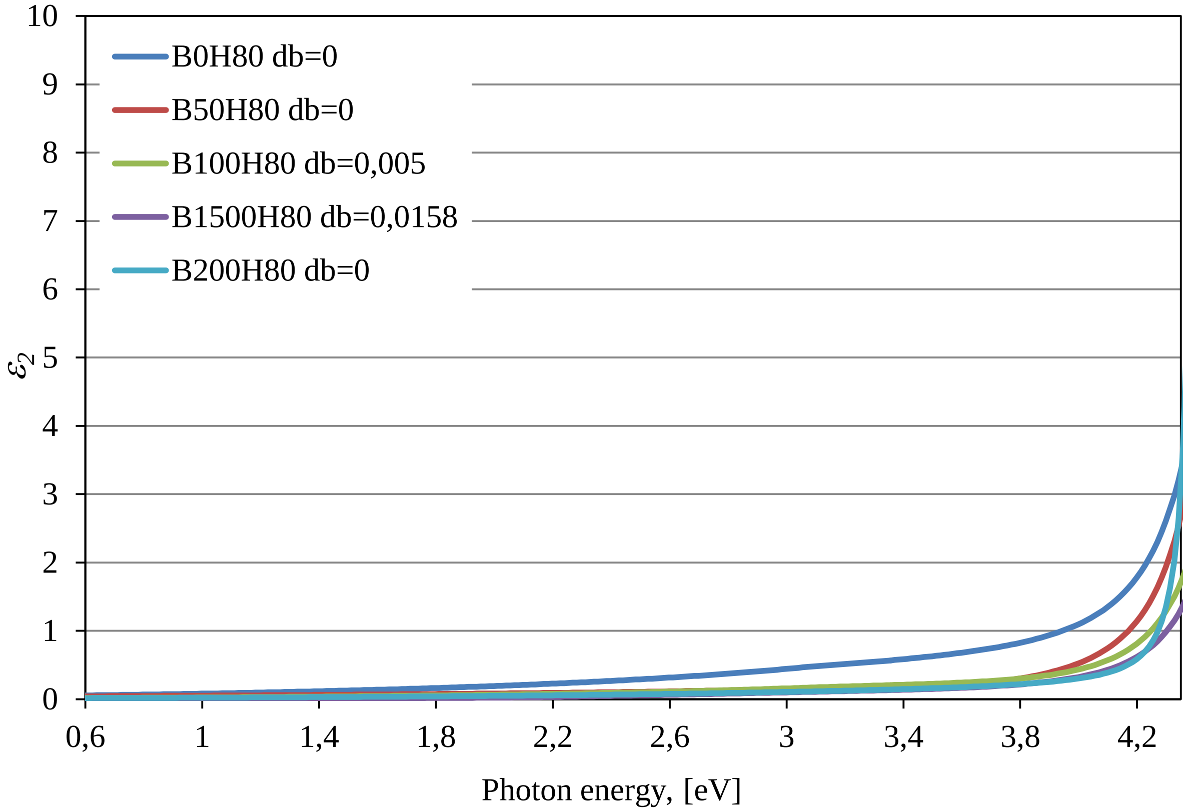

Fig. 9.14: *Spectral dependences of the imaginary part ε_2 of the dielectric function for deposited DLC films at the 80 sccm hydrogen flow rate.*

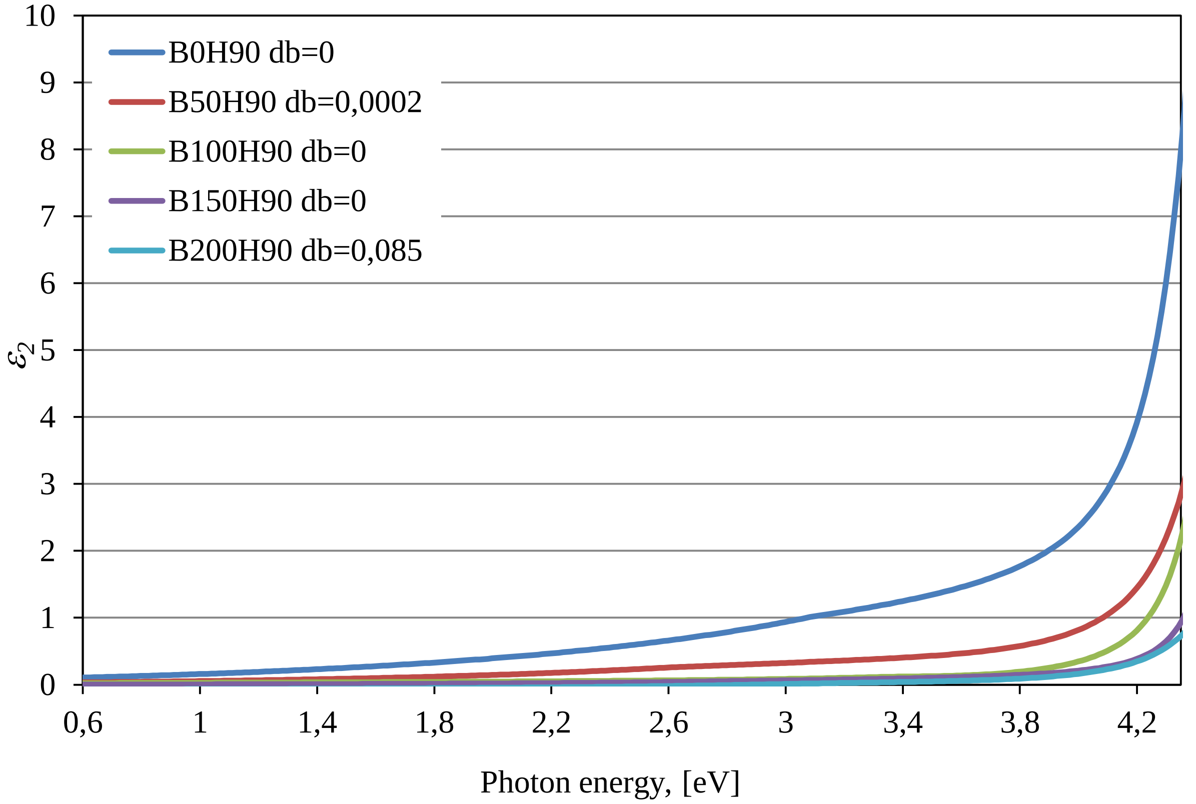

Fig. 9.15: *Spectral dependences of the imaginary part ε_2 of the dielectric function for deposited DLC films at the 90 sccm hydrogen flow rate.*

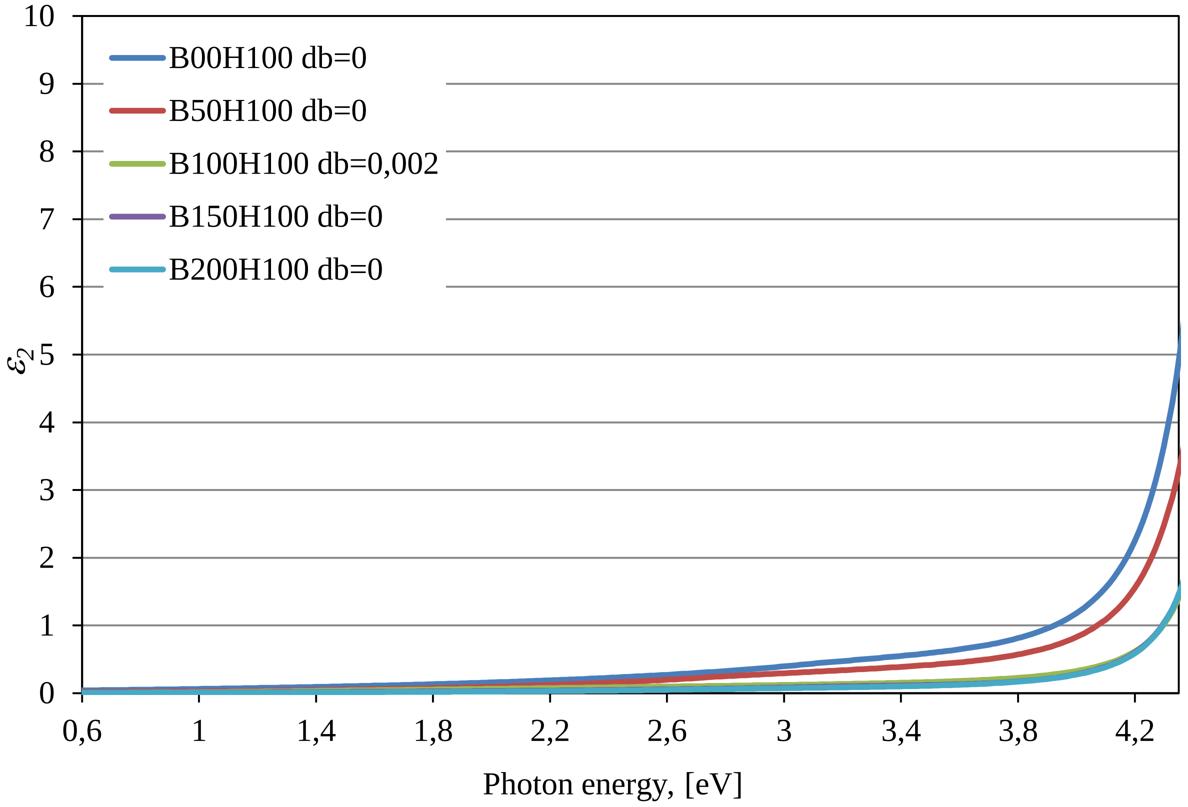

Fig. 9.16: *Spectral dependences of the imaginary part* ε_2 *of the dielectric function for deposited DLC films at the 100 sccm hydrogen flow rate*.